POLITECNICO
MILANO 1863

DIPARTIMENO DI ENERGIA

DOCTORAL PROGRAM IN ENERGY AND NUCLEAR SCIENCE AND TECHNOLOGY

CHARGE TRANSPORT IN PRINTABLE CARBON-BASED SEMICONDUCTORS

FROM SP^2-CONJUGATED MATERIALS TO SP-CARBON WIRES

Doctoral dissertation of:

STEFANO PECORARIO

Advisor:

Dr. Mario Caironi

Tutor:

Prof. Carlo S. Casari

The Chair of the Doctoral Program:

Prof. Vincenzo Dossena

Year 2023 – Cycle XXXIV

To my parents

Acknowledgements

This dissertation is the result of a long and exciting scientific journey. I feel incredibly lucky to have shared it with amazing colleagues, who are not only fantastic researchers, but true friends. Thus, a first special acknowledgement goes to the big family of the Center for Nanoscience and Technology (the one and only CNST). Thank you, guys!

I cannot find the words to express my gratitude to my supervisor, Mario. For all these years, you have been a role model under all points of view. Your always positive attitude, vision, and passion for our work is simply incredible. I could not have hoped for a better guidance and I will be always grateful for your smart advice, support and the countless things I learnt from you!

Also, I am deeply thankful to my tutor, Carlo. Your support and precious advice have been very important for my personal and professional growth.

I wish to acknowledge the amazing PME group, including former and present members, as well as the “FLEEP guys”. It has been a pleasure to share with you so many hours in the lab (and at the pub). The collaborative spirit of the group has been invaluable to grow as a researcher and to have fun while doing experiments. I learnt tons of things from you all, thank you.

I am particularly grateful to Alberto (aka Scacca), because your help and mentoring have been fundamental throughout my PhD. Also, I wish to thank Lorenzo, Mengting, Vito, Fabrizio, Francesco, Ivan and Pietro for the great collaborations in several projects. I would like to acknowledge my master thesis students, Stefano, Elda, Pierfrancesco and Andrea. It was a real pleasure to work with you. Also, I wish to thank the entire technical and administrative staff of the CNST, for your prompt help and rare sympathy.

Finally, I wish to thank my parents, Silvia and Agostino, and my family for your endless support and love. Knowing I can always count on you is a privilege that helps me facing any challenge with serenity.

Abstract

Solution processable organic semiconductors and semiconducting single-walled carbon nanotubes (SWCNTs) are at the heart of the emerging field of printed electronics. Flexible electronic circuits, wearable biosensors, semi-transparent solar panels, edible electronics and neuromorphic devices are only a few examples of the innovative applications made possible by the unique optoelectronic and mechanical properties of carbon-based semiconductors. Still, boosting charge transport in solution processed carbon-based semiconductors is necessary to compete with the electrical performance offered by inorganic semiconductors. In order to design organic semiconductors with enhanced charge mobility and functionalities, it is crucial to understand relationships between electrical and structural properties from the molecular level up to the macro-scale. Likewise in solution processed random networks of semiconducting SWCNT, understanding the effects of the network composition on charge transport is important to establish efficient processing standards leading to high-performance devices.

This thesis aims to shed light on the structure-property relationships in field-effect transistors based on thin films of three classes of printable semiconductors. The first study regards the effects of molecular encapsulation on the photophysical and charge transport properties of a high-mobility semiconducting polymer, PNDIT2, which is widely employed in n-type organic field effect transistors (OFETs) and as non-fullerene acceptor in organic photovoltaics.[1] Encapsulating macrocycles are covalently bonded to the thiophene units, while the naphthalenediimide (NDI) moieties are free to establish intermolecular interactions. Molecular encapsulation emerges as a promising approach to enforce planarization of the polymer backbone and to avoid coiling of the polymer chains in solution. Furthermore, the encapsulating rings promote crystalline packing through an intermolecular-lock mechanism. Due to the presence of the macrocycles the π-π stacking distance between NDI units increases with respect to the naked polymer, which is reflected in lower charge carriers mobility. Still, charge transport is remarkably preserved in the encapsulated PNDIT2, as demonstrated by ideal OFETs characteristics.

The second part of the thesis examines charge transport in field-effect transistors based on solution processed random networks of single-walled carbon nanotubes (SWCNTs).[2] Monochiral (6,5) SWCNT networks and multichiral networks containing five different semiconducting species with different band gaps are investigated by charge modulation

microscopy (CMM). CMM allows to map charge-induced optical features in the transistors channel with micrometric resolution. Hence, it is possible to visualize the distribution of the free carriers and identify correlations with local properties of the network, such as SWCNTs density and species composition. The CMM maps provide direct evidence that holes and electrons are transported preferentially through the same percolation paths. A dependence of the charge-modulated signal on the density of SWCNTs is observed for the monochiral network during the switching of the transistor. Moreover, it is found that the monochiral network presents less fragmented percolation pathways with respect to the multichiral network, which is in good agreement with the better performance of devices based on monochiral SWCNT.

Finally, molecules based on a linear backbone of sp-hybridized carbon atoms, namely cumulenic sp-carbon wires, are introduced as a novel class of conjugated semiconductors for organic electronics.[3] Solution-processed thin films of tetraphenyl[3]cumulene ([3]Ph) are deposited by a large-area meniscus-coating technique, and employed as active layers in OFETs. Optimized polycrystalline thin films of [3]Ph show ideal field-effect characteristics and hole mobility up to 0.1 $cm^2 V^{-1} s^{-1}$. Moreover, the devices display promising operational stability in air without specific encapsulation. A comprehensive spectroscopic and structural characterization, combined with DFT calculations, allow to correlate optical absorption features and charge transport properties with the thin film microstructure, thus providing guidelines for the molecular design of a whole new family of performant organic semiconductors with sp-hybridized backbone.

Table of Contents

Frequently Used Abbreviations

[3]Ph	Tetraphenyl[3]cumulene (aka, tetraphenylbutatriene)
CMS	Charge Modulation Spectroscopy
CMM	Charge Modulation Microscopy
DFT	Density Functional Theory
E-PNDIT2	Encapsulated poly-naphthalene diimide bithiophene
FET	Field-Effect Transistor
HOMO	Highest Occupied Molecular Orbital
LUMO	Lowest Unoccupied Molecular Orbital
NDI	Naphthalene diimide
OLED	Organic Light-Emitting Diode
OFET	Organic Field-Effect Transistor
OPV	Organic Photovoltaic
PNDIT2	Poly-naphthalene diimide bithiophene
SWCNT	Single-Walled Carbon Nanotube

1. Introduction

At the base of organic matter, carbon is a versatile chemical element whose valence electrons can take on many hybridization states and give rise to a vast range of allotropic forms, molecules, and nanostructures (**Figure 1**). Alkanes, alkenes, and alkynes present three-dimensional, planar and linear molecular structures, due to the sp^3-, sp^2-, and sp-hybridization of carbon atomic orbitals, respectively. Polymers are also grounded on carbon and on its capacity to bond with several heteroatoms, creating virtually infinite opportunities to tune the chemical, mechanical, thermal, optical and electrical properties. The most wide-spread polymers are based on sp^3-hybridized carbon atoms (*e.g.*, polyethylene, polystyrene, polyvinylchloride, …), which are electrically insulating due to the strong localization of the charge density in carbon-carbon single bonds. On the contrary, conjugated polymers feature a backbone based on sp^2-hybridized carbons where overlapping p-orbitals give rise to extended molecular orbitals. In these systems, π-electrons are delocalized and mobile, leading to semiconductive[4,5] and even conductive[6,7] materials.

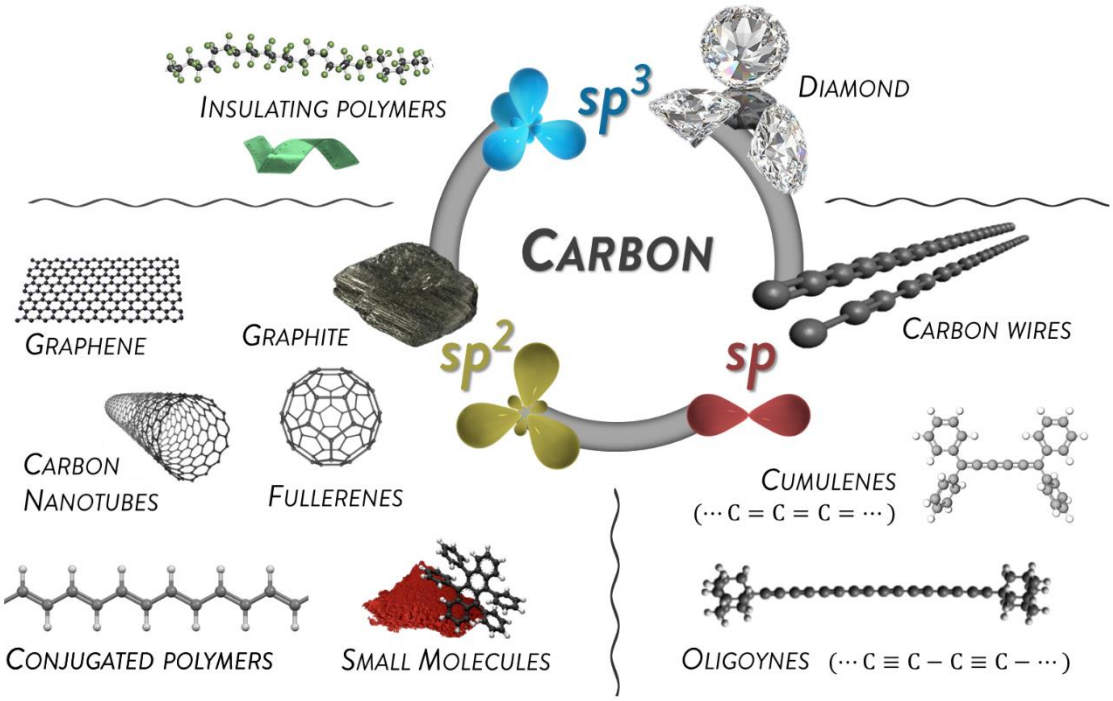

Figure 1. Carbon-based materials and nanostructures classified according to the predominant hybridization state.

Moving to condensed matter, diamond and graphite are crystals of sp^3- and sp^2-hybridized carbons, respectively. Additionally, sp^2-hybridized carbons permit π-conjugation and allow exceptional opto-electronic properties in low-dimensional carbon nanostructures such as graphene (two-dimensional, 2D), carbon nanotubes (quasi-one-dimensional, 1D) and fullerenes (quasi-zero-dimensional, 0D).

Graphene owns great potential for high-performance electronic applications because of ultrahigh charge carrier mobility ($\sim 10^5$ cm^2 V^{-1} s^{-1}) outperforming crystalline silicon (10^2 to 10^3 cm^2 V^{-1} s^{-1}).[8] However, being a semimetal (*i.e.*, a zero-gap semiconductor), it is challenging to build devices that can actually switch off.[9] Thus, strategies to open a bandgap (*e.g.,* the synthesis of graphene nanoribbons[10] and nanoporous graphene[11]) are required to enable applications such as field-effect transistors. Promising opportunities for the use of graphene and other 2D materials in solution-processed flexible electronics have been envisioned.[12,13] Yet, several challenges lie ahead, encompassing the formulation of high-quality 2D ink materials, their stability and reliability in air, along with device engineering for integration in complex circuits.[14]

Fullerenes have been widely employed as n-type semiconductors for OFETs[15], charge storage applications[16] and as acceptors in bulk-heterojunction solar cells[17]. Nowadays, they are being replaced by non-fullerene acceptors (conjugated small molecules and polymers), which provide facile tunability of functionalities and superior thermal and photochemical stability.[18,19]

Finally, single-walled carbon nanotubes (SWCNTs) are hollow cylindrical structures that are regarded as 1D materials due to their high aspect ratio (diameter ~0.5-5 nm, and lengths in the order of micrometres to centimetres). They can be described as rolled-up sheets of graphene, where the roll-up angle and diameter define the electronic properties of the tubes, determining above all if they are metallic or semiconducting. Aligned arrays and random networks of purely semiconducting SWCNTs are currently real rivals of silicon and other semiconductors as active layers in high-frequency circuits.[20] Moreover, networks of semiconducting single-walled carbon-nanotubes (SWCNTs) hold promise for applications in large-area, flexible and printed electronics.[21]

Besides sp^2-hybridization, also sp-hybridization can provide extended π-conjugated systems in the form of carbon atom wires.[22] The sp-allotropic form of carbon, the so-called "carbyne", is constituted by an infinite chain of sp-hybridized carbons. Despite elusive to be synthesized and stabilized because of the intrinsic reactivity of sp-carbons, extensive efforts are being addressed

towards the synthesis of longer and longer carbon atom wires to gain access to their outstanding predicted mechanical, optical and electrical properties.[23] Furthermore, there is a growing interest in the investigation of the semiconducting properties of short sp-carbon wires (*i.e.,* molecular systems). Yet, most studies focused either on molecular vibrational and optical properties, either on the measurement of single molecules conductance in molecular junctions, while investigation of thin film properties are scarce.[24]

The opportunities offered by chemically tuning the properties of semiconducting organic molecules and carbon nanostructures are practically limitless. Still, most opto-electronic devices rely on crystalline silicon and on other inorganic semiconductors. Aside from economic and technological aspects, the fundamental reason lies in the intrinsically different charge transport mechanisms in inorganic and organic semiconductors. Conventional inorganic semiconductors are ordered covalent crystals, where charge carriers are subjected to a periodic potential. Thus, charge carriers are fully delocalized and can be effectively described as Bloch waves propagating in a lattice (band transport model). Instead, organic semiconductors, as well as networks of semiconducting SWCNTs and molecular crystals of sp-carbon wires, are disordered materials where inter-molecular and inter-nanotubes interactions are ruled by weak Van der Waals forces. A high level of static (structural) and dynamic (vibrational) disorder alters the picture of free electrons propagating in a periodic potential, thus leading to charge carriers localization. Hence, charge transport proceeds by thermal activated polaron hopping and is much less efficient than in covalent crystals. However, these "soft" materials own great potential to fabricate devices with sufficient electrical performances to express the many advantages of carbon-based materials, such as nearly infinite possibility to tune functionalities, biocompatibility, mechanical flexibility, printability and ability to store and transport ions.[25] The success of organic light emitting diodes (OLEDs) represents an undoubtable example of the bright future expected for organic semiconductors as active materials for opto-electronic applications. A major advantage of carbon-based semiconductors is the possibility to deposit large-area thin films from solution onto flexible substrates, thus enabling the field of printed and flexible electronics. The applications include flexible electronic circuits[26,27], electronic skin[28], thermoelectric generators[29,30], semi-transparent and flexible organic photovoltaics (OPV)[31,32], biodegradable/edible electronics[33,34], neuromorphic devices[35] and biosensors[36–38].

To achieve such ambitious goals, it is essential to deeply understand the charge transport processes in carbon-based semiconductors, which depend both on intrinsic physicochemical properties of the materials and on extrinsic factors like the device architecture and the

processing conditions. The objective of this thesis is to shed light on the structure-property relations of three noticeable examples of solution processable carbon-based semiconductors, including an n-type conjugated polymer, networks of semiconducting SWCNTs and thin films of cumulenic sp-carbon wires. Different at first blush, these carbon-based semiconductors share similar charge transport mechanisms and can be employed as active layers to fabricate printed field-effect transistors with comparable performance.

The thesis is organized as follows:

Chapter 2 briefly describes the physical principles at the base of the charge transport properties of conjugated polymers and small molecules, SWCNTs, and sp-carbon wires. Also, it introduces the fundamental theories of charge transport in organic semiconductors.

Chapter 3 focuses on the main experimental highlights of this work, including the deposition of semiconducting thin films from solution, the engineering of organic field-effect transistors (OFETs) and the fundamentals of charge modulation spectroscopy and microscopy (CMS and CMM).

Chapter 4 delves into the effects of molecular encapsulation on the photophysical and charge transport properties of PNDIT2, a conjugated polymer that is widely employed in n-type organic field-effect transistors and as non-fullerene acceptor in organic solar cells.

Chapter 5 discusses on charge transport in field-effect transistors based on solution-processed random networks of semiconducting SWCNTs. In this study, the use of charge modulation microscopy provides insight about charge transport at the microscopic scale in networks composed of a single SWCNT chiral species and of a mix of five different species.

Chapter 6 presents the results on thin-films of solution-processed cumulenic sp-carbon wires employed as active layers in OFETs, which emerge as a new class of molecular semiconductors for large-area organic electronics.

The thesis concludes with an overview of the principal findings and with an outlook on future perspectives (**Chapter 7**).

2. Physical Principles

This chapter deals with a brief overview of the properties of carbon-based semiconductors (**Chapter 2.1**) and of the mechanisms ruling the charge transport in conjugated systems (**Chapter 2.2**). The aim is to illustrate common concepts and differences among three-main families of carbon-based semiconductors, and to highlight the principal advantages and drawbacks that they offer when employed as active layers in field-effect transistors.

2.1. Carbon-Based Semiconductors

2.1.1. Semiconducting Small-Molecules and Polymers

Both small-molecules and semiconducting polymers are π-conjugated systems composed of two main parts: a conjugated backbone and functional side-chains (**Figure 2**). The HOMO and LUMO frontier molecular orbitals are primarily located on the conjugated backbone. Their energies and spatial distribution are the main responsible for the absorption/emission properties of these materials, and for both intramolecular and intermolecular charge transport processes.[39] The energy of the HOMO level is strongly affected by the electron density and delocalization of the electrons along the conjugated core.

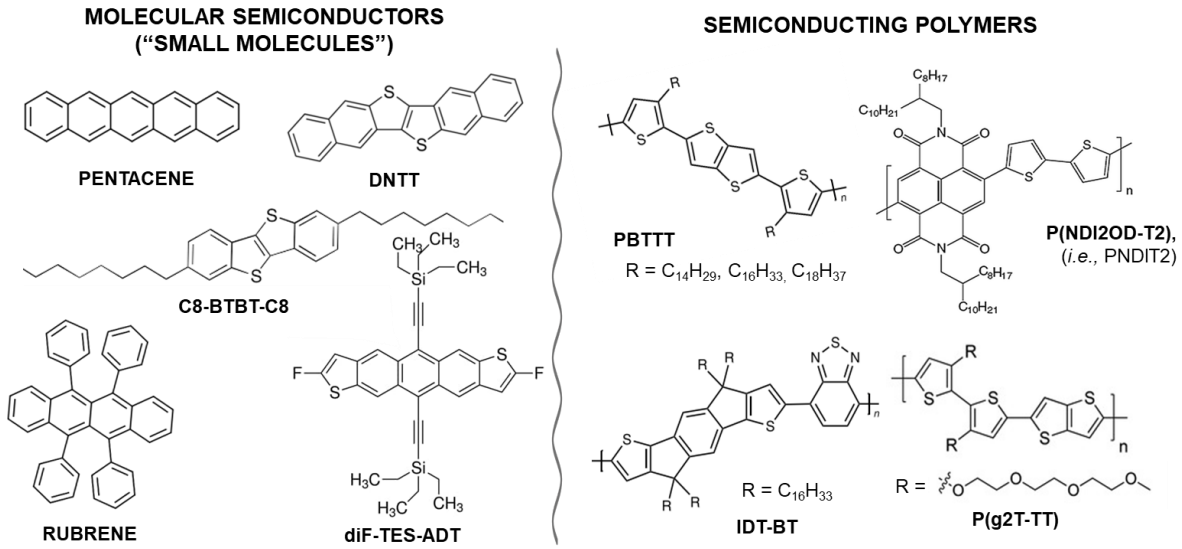

Figure 2. Representative examples of high-mobility molecular semiconductors and semiconducting polymers.

The more the conjugation of the system is extended, the more the electrons are delocalized on the whole molecule, inducing both an increase of the HOMO energy and a decrease of the LUMO energy. Thus, the HOMO-LUMO gap reduces and is manifested by a red-shifted optical absorption spectrum. Furthermore, the integration of electron donating groups (*e.g.,* N, O, S heteroatoms and alkyl chains R) usually increases the HOMO energy. Instead, the addition of electron-withdrawing groups (*e.g.*, -F, -C(O)OR, -C≡N) is adopted to decrease the energy of both HOMO and LUMO levels.[39] Tuning the frontier molecular orbitals energy levels is essential, for instance, to favour injection of holes to the HOMO level and of electrons to the LUMO level by matching the work function of metal electrodes. Moreover, to operate devices (OFETs, for example) in environmental conditions both the neutral and charged species must be stable against chemical reactions with atmospheric agents such as water, oxygen and moisture. This condition is usually reached for p-type transport when the ionization potential of the organic semiconductor is greater than 4.9 eV[40], and for n-type transport when the electron affinity is greater than ~4 eV[41].

The delocalization of HOMO and LUMO orbitals is generally positively associated with high hole and electron mobility, respectively. Still, the solid-state packing and the microstructure of molecular and polymeric semiconductors play a key role. Side-chains are often introduced to control the packing of small-molecules and polymers in thin films. Moreover, they are useful to improve the processability of organic semiconductors and to add functionalities. For instance, the addition of alkyl-chains increases the solubility in common organic solvents[42], while glycol side-chains permit water permeation in a polymeric matrix and boost the performance in organic electrochemical transistors (OECTs)[43].

While conventional semiconductors like silicon, germanium, and III-V semiconductors form covalent crystals, organic semiconductors arrange in Van der Waals solids, which are softer than crystals held by ionic or covalent bonds. The π-electrons in the molecular backbone effectively create a Wannier state, which is only weakly coupled to nearest neighbours through polarisation and van der Waals interactions. The eigenstates are short ranged and only (de)localized across one to a few sites. This results in a narrow bandwidth, which is a measure of the charge transfer integral between neighbouring molecules. Moreover, vibrational motions in these soft molecular solids lead to large fluctuations of the transfer integrals. Thus, as it will be discussed in details in Chapter 2.2, the charge transport mechanisms in organic semiconductors are based on polaron hopping and transient localization, rather than on band transport.[44]

Small-molecule organic semiconductors are prone to form ordered molecular crystals, with packing motifs that depend on the specific molecule and have a fundamental impact on the charge transport.[44,45] Furthermore, the processing conditions often lead to the formation of different polymorphs.[46–48] Small-molecule thin films have reached charge mobility in p-type field effect transistors in the range from 1 to 20 $cm^2 V^{-1} s^{-1}$,[49] with most performant molecules belonging to the families of fused acenes and heteroacenes (*e.g.* pentacene[50], rubrene[51], TIPS-pentacene[52], diF-TES-ADT[53]) or heteroarenes (BTBT[54], DNTT[55]). In these systems, a high-degree of backbone conjugation is combined with ordered π-stacking motifs (in particular, the Herringbone and the brick-wall packing), leading to high charge transfer integrals and low dynamic disorder.[25] The mobility in n-type OFETs lags behind compared to p-type devices. Indeed, it is more challenging to design stable n-type semiconductors with extensive delocalization of the LUMO level (required for high electron mobility). Along with fullerenes[15,56], the best results were achieved with n-heteropentacenes[57], and with naphthalene and perylene diimides (NDI and PDI)[58].

Thin films of conjugated polymers are intrinsically more disordered than molecular crystals. Still, state-of-the-art polymeric semiconductors can afford a sufficient degree of para-crystallinity and reach charge carriers mobility of 0.5 to 5 $cm^2 V^{-1} s^{-1}$.[59] Despite the lower mobility compared to best small molecules, they offer some remarkable advantages in terms of processability and of mechanical properties, particularly suitable to realize large-area flexible and stretchable OFETs.[60,61] Besides, the ability of certain conjugated polymers to store and transport ions, such as PEDOT:PSS[62], p(g2T-TT)[63], and other organic mixed ionic-electronic semiconductors (OMIECs)[64], has opened a plethora of opportunities for bioelectronics[65] and organic neuromorphic devices[35].

An important class of semiconducting polymers is the one of donor-acceptor (D-A) copolymers, featuring a backbone made of alternating electron-rich (donor) and electron-deficient (acceptor) units.[66] Despite their degree of crystallinity is generally lower than other conjugated polymers such as regioregular P3HT and PBTT, D-A copolymers achieve mobilities >1 $cm^2 V^{-1} s^{-1}$ in OFETs. This counterintuitive behaviour is attributed to a low degree of energetic disorder in these systems, which present highly planar and rigid backbones with low torsional angles between the donor and acceptor units.[67,68] Moreover, D-A copolymers are widely employed in OPV with many examples of power conversion efficiencies >5% in all-polymer solar cells.[69] Common building blocks of D-A copolymers include diketopyrrolopyrrole (DPP), indacenodithiophene (IDT), benzothiadiazole (BTZ),

thiophene (T), naphtalenediimide (NDI), cyclopentadithiophene (CDT), and isoindigo (IIT).[70–73] For example, Facchetti and collaborators[74] combined an NDI acceptor with two T donors to give birth to PNDIT2, one of the most successful high-mobility n-type polymers, which has been widely studied and employed in OFETs[75,76], OPV[77] and organic thermoelectrics[78].

In D-A copolymers, the charge density of the HOMO is manly distributed on the donor unit, while the LUMO level is located on the acceptor moiety. They present a characteristic broad, low-energy absorption band in the visible/near-infrared spectral range, which is assigned to the charge-transfer (CT) transition (**Figure 3a)**. As shown in **Figure 3b** for the representative case of the n-type copolymer PNDIT2, the CT transition mainly involves a redistribution of the charge density from the donor to the acceptor units along the backbone.[79]

Chapter 4 of this thesis delves with the investigation of the effects of molecular encapsulation on the charge transport and photophysical properties of PNDIT2 (**Figure 3c**).

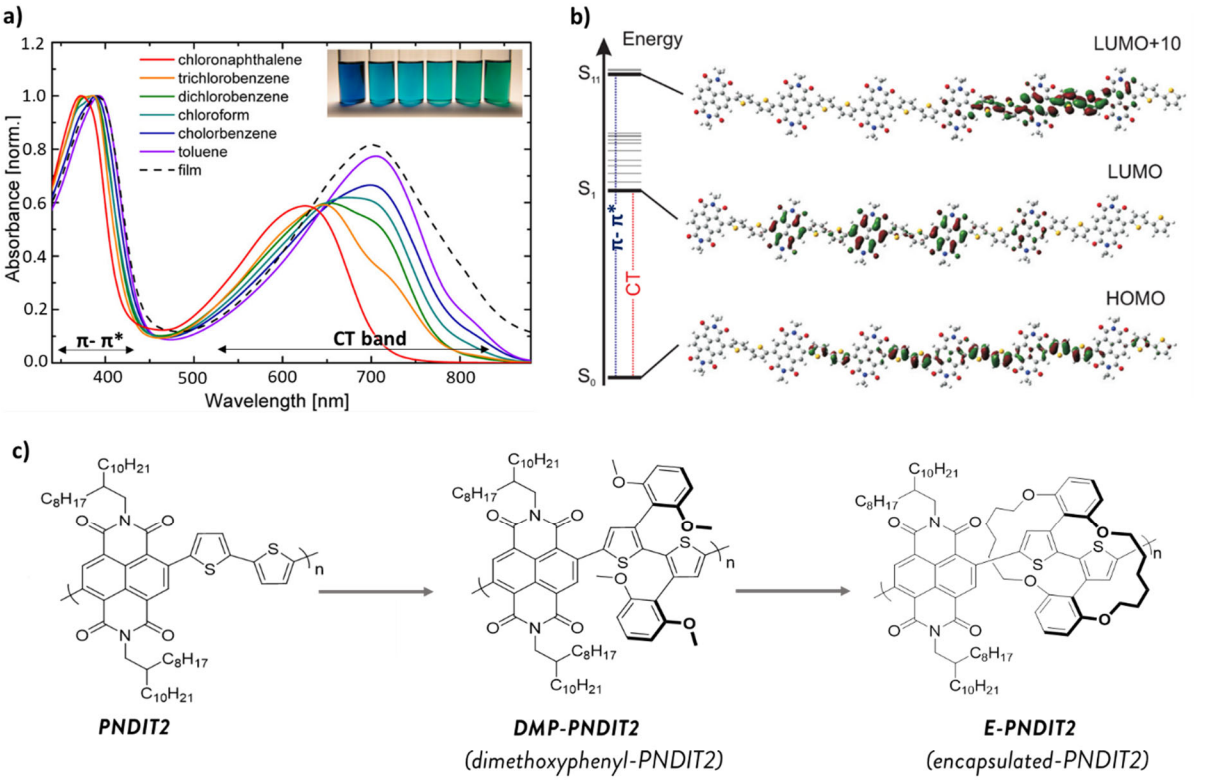

Figure 3. a) Absorption spectra of the D-A copolymer PNDIT2 dissolved in various solvents (full lines) and in thin film (dashed line). **b)** HOMO, LUMO and LUMO+10 which mainly contribute to the π-π* and charge transfer (CT) electronic transitions. **c)** The three polymers studied in Chapter 4 to investigate the effect of molecular encapsulation on the photophysical and charge transport properties of PNDIT2. a-b) Adapted with permission from Steyrleuthner *et al., J. Am. Chem. Soc.* 2012 (Ref.[79]), Copyright 2012 American Chemical Society.

Encapsulated conjugated polymers are attractive to investigate in isolation the role of inter- and intramolecular interactions on charge and exciton transport.[80–82] They can be prepared following either covalent or non-covalent (*i.e.*, rotaxanes-based) strategies.[83,84] In this work, encapsulating macrocycles are covalently bonded to the thiophene units (T2) with the aim to gain control over the thin film molecular packing while keeping the naphthalene diimide (NDI) units accessible for intermolecular interactions. The strong π-π interaction between the NDI moieties is indeed known to drive the coiling of individual PNDIT2 chains in common organic solvents and to play a major role in the solid-state packing and charge transport processes.[79,85,86] It is found that molecular encapsulation prevents the preaggregation of the polymer chains in solution, but allows π-stacking between the NDI moieties in solid state through an intermolecular locking mechanism. The electron transport is partially preserved, with OFETs demonstrating field-effect mobility of $\sim 10^{-3}$ cm^2 V^{-1} s^{-1}. The reduction in mobility with respect to pristine PNDIT2 (0.1-1 cm^2 V^{-1} s^{-1}) is attributed to the larger π-π spacing and to the loss of long-range energetic order in films of encapsulated PNDIT2. Moreover, the encapsulating rings promote a planarization of the backbone with a reduction of the torsional angle between the donor and acceptor parts, which results in a red-shift of the absorption spectrum. Molecular encapsulation emerges as a promising strategy for tuning the structural, optical and charge transport properties of donor-acceptor copolymers, with applications ranging from OFETs to OPV.

Key references:

- S. Pecorario, J. Royakkers, A. D. Scaccabarozzi, F. Pallini, L. Beverina, H. Bronstein, M. Caironi, Effects of Molecular Encapsulation on the Photophysical and Charge Transport Properties of a Naphthalene Diimide Bithiophene Copolymer, *Chem. Mater.* **2022**, *34*, 18, 8324–8335
- H. Bronstein, C. B. Nielsen, B. C. Schroeder, I. McCulloch, The role of chemical design in the performance of organic semiconductors, *Nat. Rev. Chem.* **2020**, *4*, 66
- Schweicher, G., Garbay, G., Jouclas, R., Vibert, F., Devaux, F., Geerts, Y. H., Molecular Semiconductors for Logic Operations: Dead-End or Bright Future?. Adv. Mater. 2020, 32, 1905909.
- R. Steyrleuthner, M. Schubert, I. Howard, B. Klaumünzer, K. Schilling, Z. Chen, P. Saalfrank, F. Laquai, A. Facchetti, D. Neher, Aggregation in a High-Mobility n-Type Low-Bandgap Copolymer with Implications on Semicrystalline Morphology, *J. Am. Chem. Soc.* **2012**, *134*, 18303.
- J. Royakkers, H. Bronstein, Macrocyclic Encapsulated Conjugated Polymers, *Macromolecules* **2021**, *54*, 1083.

2.1.2. Single-Walled Carbon Nanotubes

Single-walled carbon nanotubes (SWCNT) can be seen as rolled-up sheets of graphene (**Figure 4a)**. The rolling direction, the chirality and the diameter of a SWCNT are described by the so-called chiral vector $\overrightarrow{C_h}$:

$$\overrightarrow{C_h} \equiv n \cdot \overrightarrow{a_1} + m \cdot \overrightarrow{a_2}, \quad (1)$$

where $\overrightarrow{a_1}$ and $\overrightarrow{a_2}$ are the graphene unit cell vectors and (*n*, *m*) are a couple of positive integers, the so-called chiral indices. When the chiral vector is parallel to $\overrightarrow{a_1}$, zigzag carbon nanotubes are produced, described by (*n*, 0) chiral indices. The case of (*n*, *n*) indices lead to armchair nanotubes. All the other (*n*, *m*) result in chiral carbon nanotubes.

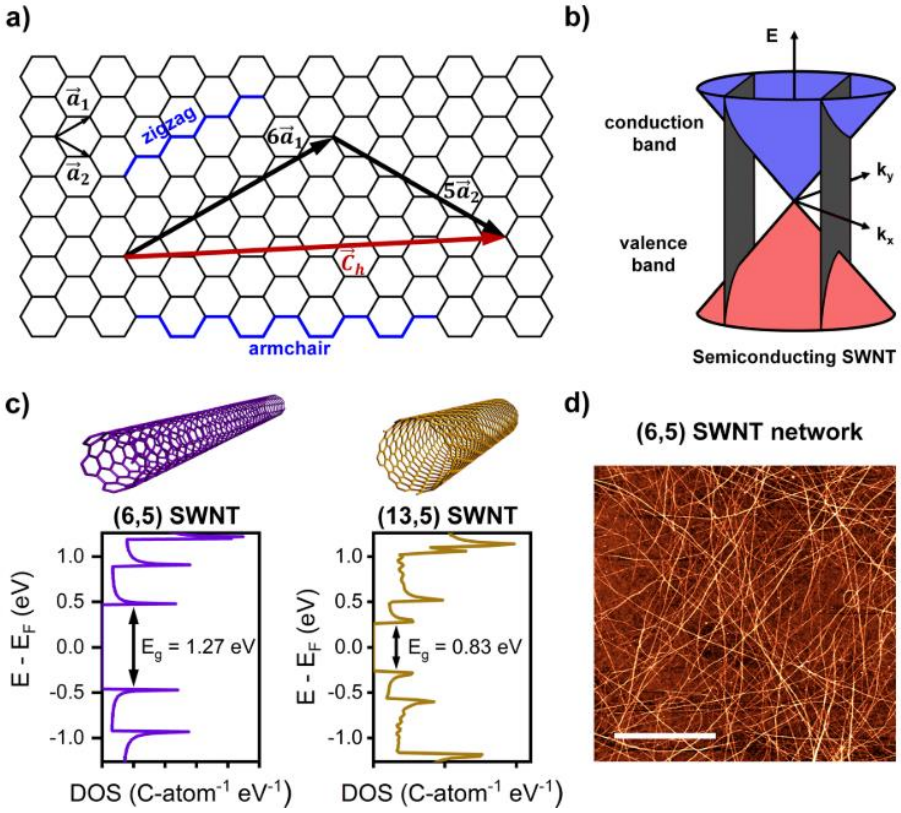

Figure 4. a) Conceptual construction of a (6,5) SWCNT by rolling up a sheet of graphene. **b)** One-dimensional carbon nanotube subbands visualized as cuts through the Dirac cone in the band structure of graphene, in agreement with the quantization of allowed wavevectors within the zone-folding approximation. **c)** Illustration of semiconducting (6,5) and (13,5) SWNTs and their corresponding DOS. **d)** Atomic force micrograph of a random network of (6,5) SWNTs deposited by spin-coating on SiO_2 (scale bar is 1 μm). Reprinted from Zorn N. F. and Zaumseil J., *Applied Physics Reviews*, 2021 (Ref.[87]) with the permission of AIP Publishing.

The chiral vector forms the circumference of the SWCNT. Thus, it also determines the diameter *d*:

$$d = \frac{|\overrightarrow{C_h}|}{\pi} = \frac{a\sqrt{n^2 + nm + m^2}}{\pi}, \quad (2)$$

with $a = |\overrightarrow{a_1}| = |\overrightarrow{a_2}| = 2.46$ Å. Note that, while the chiral indices define uniquely a SWCNT specie, different chiralities can have the same diameter. Typical SWCNTs have diameters in the range ~ 0.5-5 nm, while their length extends in the order of micrometres to centimetres. Hence, these cylindrical carbon nanostructures are regarded as 1D materials.

Within the zone folding approximation, the electronic band structure of SWCNT is derived from the knowledge of the first Brillouin zone of graphene with the addition of periodic boundary conditions to the electronic wavefunction ψ.[88] As a result of quantum confinement along the circumferential direction, the allowed wavevectors $\vec{Q}$ are determined as follows:

$$\psi(0) = \psi(\overrightarrow{C_h}) = \psi(0)e^{i\vec{Q}\cdot\overrightarrow{C_h}} \quad (3)$$

$$\Rightarrow \vec{Q} \cdot \overrightarrow{C_h} = 2\pi l \quad (4)$$

with l that is an integer. Therefore, the wavevectors $\overrightarrow{Q_\parallel}$ parallel to the circumferential direction must satisfy:

$$|\overrightarrow{Q_\parallel}| = \frac{2\pi}{|\overrightarrow{C_h}|} l = \frac{2}{d} l, \quad (5)$$

This equation implies that allowed wavevectors in the SWCNTs reciprocal space are quantized and form a discrete set of line cuts of the Brillouin zone of graphene separated by $2/d$. Thus, the SWCNT band structure can be derived as 1D cross-sections of the 2D band structure of graphene (**Figure 4b**). The band structure of graphene is characterized by the presence of Dirac cones, *i.e.*, the valence and the conduction bands touch at the K-points (Dirac points). Importantly, if one of the 1D line-cuts crosses a Dirac point, the SWCNTs presents a metallic behaviour, otherwise there exists an open bandgap implying semiconducting behaviour. Stemming from geometrical considerations, the metallic or semiconductive character of SWCNTs is determined by the following condition on the chiral indices:

$$|m - n| = 3q, \quad (6)$$

with q being an integer number. As a rule of thumb, this condition implies that approximately 1/3 of the possible SWCNTs are metallic and 2/3 are semiconductive.[88]

The density of states (DOS) of SWNTCs is characterized by sharp peaks named *Van Hove singularities* (**Figure 4c**). As calculated analytically within the tight-binding theory, the electronic band gap of semiconducting SWCNTs scales inversely with the nanotube diameter:

$$E_{\mathrm{g}} = \frac{2\hbar}{m_e e^2}\frac{\gamma}{d} \tag{7}$$

where $\hbar$ is the reduced Plank constant, m_e is the electron mass, e the elemental charge and γ is the interatomic matrix element derived by tight-binding calculations.[88] For commercially available semiconducting SWCNTs, E_{g} usually goes from 0.5 to 1.3 eV.

The absorption spectrum of semiconducting SWCNTs feature sharp peaks corresponding to the dipole-allowed excitonic transitions between the subbands defined by the Van Hove singularities (the E_{11}, $E_{22,}$ …, E_{ii} transitions). By exploiting the correlation between the diameter and the energy of the excitonic transitions, absorption and emission spectra are useful to identify the species composition in networks of SWCNTs.[89,90] To this purpose, Raman spectroscopy represents another valuable technique.[91–93]

Electrochemical or field-induced doping leads to the reduction of the intensity of the excitonic peaks and to the appearance of new absorption peaks, termed X^+ and X^- for p-type and n-type doping, respectively. These peaks are lower in energy with respect to the excitonic peaks and correspond to the appearance of trions, *i.e.* three-body quasi particles equivalent to charged excitons.[94–96] Thus, the doping level in semiconducting SWCNTs can be quantitatively correlated to the appearance of the charge-induced peaks and the bleaching of the excitonic transitions.[97]

Charge transport in individual SWCNT suspended between two contact electrodes is effectively modelled within the Landauer formalism.[88,98] The electron and hole mobility in individual SWCNTs is extraordinarily high and can reach 10^5-10^6 $\mathrm{cm^2\ V^{-1}\ s^{-1}}$.[99] Moreover, they display an extraordinary current carrying capacity of ~10^9 $\mathrm{A\ cm^{-2}}$.[100] These remarkable electronic properties, combined with the excellent air stability, make SWCNTs promising for high-performance digital electronics as well as radio-frequency and sensing applications.[101] Furthermore, the fabrication of SWCNT-based transistors is compatible with conventional manufacturing processes of the semiconductor industry[102] and fulfils the requirements for 3D integration of active devices,[103] such as low device fabrication temperature (< 400 °C) and thin device layer. The use of an individual SWCNT as the channel of a FET has demonstrated ballistic transport and digital circuit operability.[98] However, aligned arrays of SWCNTs with

controlled spacing of ~5 to 10 nm are more suitable for delivering the high current flow necessary for digital and radio-frequency electronics.[104] The demonstration of several electronic components, including a processor with >14000 transistors,[20] has affirmed the potential of SWCNTs to surpass silicon in terms of performance and energy efficiency. Still, it is challenging to produce aligned arrays with regular pitch and to match the stringent requirements for mass production of high-performance nanoscale electronics (semiconducting purity > 99.9999 %).[101]

Remarkably, thin films composed of unaligned (random) networks of SWCNTs (**Figure 4d**) show promise in flexible printed electronics for applications that are alternative to high-performance electronics. For instance, the possibility to deposit large-area thin films of SWCNTs by roll-to-roll[105] and direct-writing[106,107] methods enables the fabrication of cost-effective flexible biosensors[38], display backplanes[108] and disposable circuits for the Internet of Things (IoT)[109]. Compared to conjugated polymers and small molecules, SWCNTs thin film transistors deliver higher charge carriers mobility (10 to 100 $cm^2\ V^{-1}\ s^{-1}$), along with excellent stability in environmental conditions and under bias.[110] Nevertheless, the synthesis and the successive purification of SWCNTs to select a specific (n, m) species represent demanding tasks. Recent developments in purification and sorting techniques, such as aqueous two-phase extraction[111], gel chromatography[112] and selective polymer-wrapping[113,114] permit to avoid the presence of metallic species in the network. SWCNTs thin films typically comprise many semiconducting species, with only few chiralities that can be sorted as a single species (*e.g.*, (6,5) SWCNTs).[113] Since the chirality determines the electronic properties of the nanotubes, further improving the yield of purification is essential to enhance the performance and the reproducibility of SWCNTs-based field-effect transistors. Moreover, SWCNTs inks often suffer from the formation of bundles,[115] which make their deposition generally less facile than for polymeric semiconductors.

At the micrometre scale, charge transport in random networks of semiconducting SWCNTs has been described in terms of variable-range hopping, fluctuation-induced tunneling and percolation theory.[87,116] Multiple factors affect charge transport in SWCNT random networks (**Figure 5**). The network density and the species composition play key roles in determining the performance of field-effect transistors.[117,118] For instance, the network density is crucial to achieve sufficient interconnections among the nanotubes and create percolative paths from the source to the drain electrodes. Accordingly, the carrier mobility of a SWCNT network increases with the network density before it saturates or even deteriorates.[106] The chirality of the carbon nanotubes determines the intra-nanotube mobility, which scales with the diameter as $\sim d^2$.[119]

Moreover, the diameter distribution composing the network has a strong impact on the energetic disorder. Charge hopping between carbon nanotubes having the same chirality is more favourable than between different species[120], and the junction resistance inversely scales with the diameter.[117] By using charge modulation spectroscopy (see **Chapter 3.2**) to study a network composed of five different semiconducting species, Zorn and collaborators have recently demonstrated that small band gap SWCNTs dominate the charge transport especially at low carrier concentrations, while the contribution of large band gap species increases at higher gate voltages.[121]

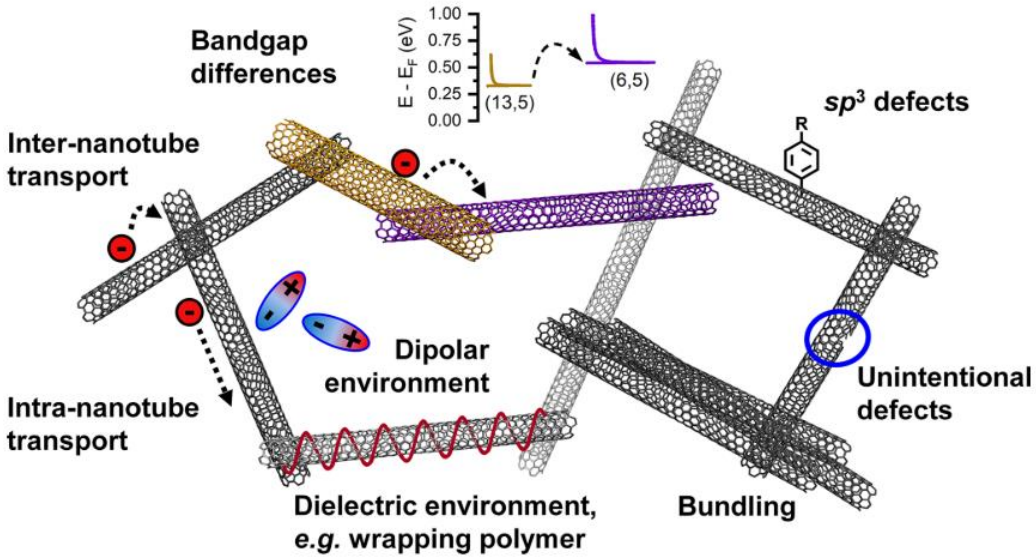

Figure 5. The several factors influencing charge transport in random networks of semiconducting SWCNTs. Reprinted from Zorn N. F. and Zaumseil J., *Applied Physics Reviews*, 2021 (Ref.[87]) with the permission of AIP Publishing.

Chapter 5 of this thesis focuses on the investigation of the charge transport in field effect transistors (FETs) based on both monochiral (6,5) networks and on multichiral networks composed of a mix of five SWCNT species. By using charge modulation microscopy (CMM), which combines the CMS technique with a confocal microscopy setup, local variations of the SWCNT optical absorption are detected upon the sinusoidal modulation of the gate potential. These features are related to the modulation of free carriers under the actual operation conditions of the FET. The presence of preferential charge percolation paths is revealed by mapping with micrometre resolution the charge-modulated signal distribution along the FET channel, demonstrating that the charge distribution does not depend on the polarity of the carriers. A positive correlation between the density of the monochiral (6,5) network and the charge density distribution in the FET subthreshold regime is revealed. Moreover, in the

devices based on the multichiral network, a specific spatial distribution of the free carriers for each species is observed, proving that all of them contribute to some extent to the charge transport. CMM emerges as a valuable technique to estimate the size of preferential percolation domains and to assess the impact of local properties of the network on the charge transport.

Key References

- M. Jiang, S. Pecorario, N. F. Zorn, J. Zaumseil, M. Caironi, Investigating Charge Transport in Semiconducting Single-Walled Carbon Nanotube Networks by Charge Modulation Microscopy, *Adv. Mater. Interfaces* **2023**, *2202454*.
- N. F. Zorn, J. Zaumseil, Charge transport in semiconducting carbon nanotube networks, *Appl. Phys. Rev.* **2021**, *8*, 041318
- D. Franklin, M. C. Hersam, H.-S. P. Wong, Carbon nanotube transistors: Making electronics from molecules, *Science (80-.).* **2022**, *378*, 726.
- N. F. Zorn, F. Scuratti, F. J. Berger, A. Perinot, D. Heimfarth, M. Caironi, J. Zaumseil, Probing Mobile Charge Carriers in Semiconducting Carbon Nanotube Networks by Charge Modulation Spectroscopy, *ACS Nano* **2020**, *14*, 2412.

2.1.3. Cumulenic sp-Carbon Atom Wires

Carbon Atom Wires (CAWs) consist in linear chains of sp-hybridized carbon atoms. This characteristic trait distinguishes them from all the sp^2-carbon-based conductors and semiconductors investigated so far (conjugated polymers and small-molecules, graphene, carbon nanotubes, …). The so-called "carbyne", an infinite linear sp-carbon chain, represents the purely one-dimensional allotropic form of carbon. The chemical community is making several efforts to synthesize and stabilize longer and longer CAWs in order to eventually achieve the carbyne's limit.[23,122] This quest is motivated by the forecasts of several theoretical and computational studies that predicted remarkable properties for the carbyne, such as a Young's modulus up to 32 TPa,[123,124] large specific area,[125] optical absorption,[126] extremely high thermal conductivity (60-200 kW m^{-1} K^{-1}),[127] remarkable nonlinear optical properties,[128–131] and charge mobility even superior to graphene and carbon nanotubes.[132] The electronic properties of CAWs are highly sensitive to the length of the chain and to its structure. The infinite carbyne presents two possible isomeric structures, referred to as polycumulene (or simply cumulene) and polyyne (or oligoyne in the case of short chains). The former consists in an equalized structure of consecutive CC double bonds (=C=C=C=C=), where the p-electrons are delocalized over the chain leading to metallic properties. The latter displays alternating single and triple bonds (−C≡C−C≡C−C≡) and presents semiconducting properties due to the localization of the p-electrons on the triple bonds.[133] The difference in bond lengths for adjacent CC bonds, namely the bond length alternation (BLA), represents a useful parameter to distinguish these two arrangements. The symmetric cumulene structure (BLA ideally equal to zero) is unstable with respect to the alternated polyyne structure (non-zero BLA), because of the onset of Peierls' distorsion in long enough chains (> 52 carbons)[134]. However, it was recently noticed that the zero-point vibrational energy, which is higher for polyyne than for cumulene, partly counteracts the Peierls distorsion and contributes to the stabilization of the cumulene structure.[135,136] The BLA is positevely correlated with the size of the electronic band gap. Hence, the BLA strongly affects the electronic and optical properties of the system. For instance, applying a mechanical strain to linear chains increases the BLA, thus inducing a transition from metallic to semiconducting state deriving from the opening of a band gap.[135,137] Moreover, also the vibrational properties are highly impacted by structural variations of the conjugated backbone, stemming from the strong local electron-phonon coupling typical of π-conjugated systems. As a matter of fact, IR an Raman vibrational spectroscopies are very sensitive techniques to quantify the BLA in π-conjugated systems.[138–

[140] In particular, sp-carbon wires are charachterized by Raman active modes in the 1800-2300 cm^{-1} spectral region, which are assigned to the collective stretching vibrations of CC bonds (*i.e.*, BLA oscillation modes).[22] These modes are well predicted by the "effective conjugation coordinate" (ECC) model for π-conjugated systems proposed by Castiglioni and Zerbi.[141,142] Due to their stiffness, the ECC modes of sp-carbon wires lie at higher frequency when compared to the collective stretching modes of sp^2-based carbon nanostructures and conjugated polymers/molecules. Moreover, the frequency of the ECC mode increases with the BLA, thus with the energy gap.[143]

In real finite CAWs (*i.e.,* "small molecules"), the structure of sp-carbon chains is dictated by the presence of sp^2-endcapping groups, which can induce a more cumulenic or polyyinic arrangement by altering the BLA. Therefore, terminal groups also affect the opto-electronic and vibrational properties of the wires.[22,144–146] In addition, bulky terminal groups are widely employed in the synthesis of sp-carbon wires in order to stabilize the chains, as they prevent cross-linking reactions by offering steric hindrance.[126,147] The synthesis and handling of long cumulenes are more difficult due to a considerably enhanced reactivity with the chain length. The [9]cumulenes (*i.e.*, molecules with an sp-carbon backbone comprising 9 quasi-double bonds) are the longest derivatives reported so far.[147] The alternated structure of polyynes is instead more stable, allowing the recent isolation of a polyyne with record 48 sp-carbons stabilized through pyridyl terminal groups.[148] Anyways, it is worth mentioning that the stability of CAWs often increases in solid state thanks to the reduction of molecular degrees of freedom in the lattice.[144] Encapsulation of the sp-carbon backbone within rotaxanes[149–151] or carbon nanotubes[152] is another effective strategy to achieve long and stable CAWs.

There is a rising number of studies investigating the electronic[24], photophysical[122,131,153–155] and vibrational[130,156,157] properties of isolated CAWs. The single-molecule electrical conductance of functionalized oligoynes was investigated as a function of the chain length and of different endcapping groups using scanning tunneling microscopy break junctions (STM-BJ).[158,159] Recently, it was demonstrated that cumulenes show a conductance increase with growing chain length, paving the way to highly conductive molecular wires.[160–162] This is surprising because the conductivity of molecules typically decreases exponentially with length. Such unusual behaviour can be correlated with the diradical character of cumulenes and of other molecules, such as fused porphyrines and acenes, which were proposed as anti-Ohmic wires.[163] Exploiting their specific vibrational fingerprints, a library of 20 oligoynes was used as Raman probes for optical super-multiplexing apt to to image organelle in individual living cells with high

specificity, sensitivity and photostability.[164] The 20 distinct Raman frequencies were obtained by engineering the conjugation length by varying the chain length, the end-capping groups and by bond-selective isotope doping. The large Raman cross-section of sp-carbon wires and their activity in the cell-silent Raman spectral window resulted as a winning strategy to overcome the fundamental "spectral crowding" limit of traditional fluorescent probes. This enabled multiplexed imaging of a large number of molecular targets.[165] Considering optical properties, CAWs represent ideal candidates as liquid crystalline materials, due to the high birefringence deriving from extended conjugation along the direction of the long molecular axis.[166,167] Despite the great interest in their investigation at the molecular level, the properties of oligoynes and cumulenes in thin-films, as well as applications in printed organic electronics have been essentially unexplored.[24,168–170]

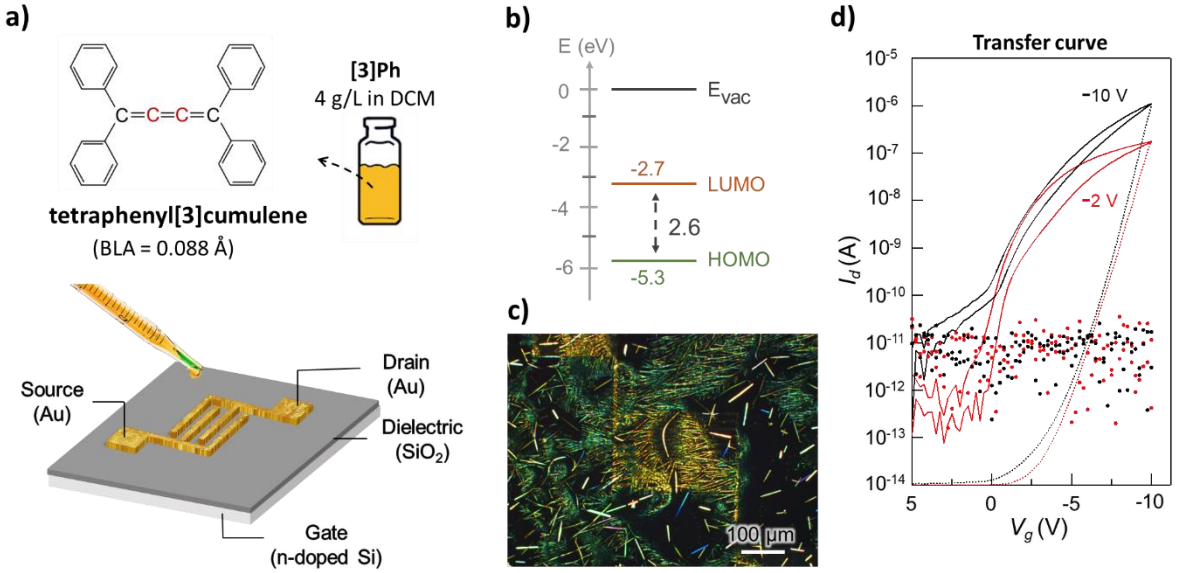

Figure 6. a) Scheme of the deposition of tetraphenyl[3]cumulene ([3]Ph) by drop-casting from a dichloromethane (DCM) solution on a SiO_2 substrate with pre-patterned interdigitated source and drain electrodes. [3]Ph presents a cumulenic backbone with 3 C-C double bonds (bond-length alternation BLA = 0.088 Å) and 2 phenyl terminal groups at each end. The sp-carbons are marked in red. **b)** HOMO-LUMO energy diagram as from UPS measurements on [3]Ph films (courtesy of Dr. Mirko Prato). **c)** Polarized optical microscopy image of a transistor with [3]Ph molecular crystals as semiconducting layer. **d)** Representative transfer characteristic of the device in linear (red, $\boldsymbol{V_{ds} = -2\ V}$) and saturation (black, $\boldsymbol{V_{ds} = -10\ V}$) regimes. d) Reproduced with permission from A. D. Scaccabarozzi, *et al.*, J. Phys. Chem. Lett. 2020, 11, 1970 (Ref.[171]).

Recently, we have demonstrated the fabrication of the first field-effect transistor employing a short cumulenic sp-carbon wire (tetraphenyl[3]cumulene, [3]Ph).[171] In this work, [3]Ph molecular crystals were deposited by solution drop casting and employed as active layer in field-effect transistors (**Figure 6a-c**). The detection of the field-effect behaviour with these proof-of-concept devices demonstrated for the first time the potential of sp-carbon wires as p-type molecular semiconductors for organic electronics. Yet, the devices showed poor field-effect mobility (~10^{-3} cm^2 V^{-1} s^{-1}). Major open issues for the realization of performant devices regarded the FET architecture and the unoptimized morphology of the [3]Ph layer (**Figure 6d**). The efforts to unveil the true potential of cumulene-based molecular crystals for large-area printed electronics are described in the study presented in **Chapter 6**.[3] In this work, a fine control of [3]Ph deposition in thin-film was achieved via wire-bar coating, a scalable printing technique. The microstructure of the semiconducting layer was tuned as a function of the deposition parameters and correlated with the electrical and optical properties of the films. Along with a comprehensive engineering of the transistor architecture, this optimization leaded to OFETs based on sp-carbon wires with highly improved performance, reaching field-effect mobility up to 0.1 cm^2 V^{-1} s^{-1}. Furthermore, the devices showed promising operational stability in environmental conditions, which is a common issue to organic semiconductors. These findings establish a strong foundation for the application in organic electronics of a large class of sp-hybridized molecular semiconductors, introducing a novel paradigm.

Key References

- A. D. Scaccabarozzi, A. Milani, S. Peggiani, S. Pecorario, B. Sun, R. R. Tykwinski, M. Caironi, C. S. Casari, A Field-Effect Transistor Based on Cumulenic sp-Carbon Atomic Wires, *J. Phys. Chem. Lett.* **2020**, *11*, 1970.
- S. Pecorario, A. D. Scaccabarozzi, D. Fazzi, E. Gutiérrez-Fernández, V. Vurro, L. Maserati, M. Jiang, T. Losi, B. Sun, R. R. Tykwinski, C. S. Casari, M. Caironi, Stable and Solution-Processable Cumulenic sp-Carbon Wires: A New Paradigm for Organic Electronics, *Adv. Mater.* **2022**, *34*, 2110468.
- C.S Casari, M. Tommasini, R. R. Tykwinski, A. Milani, Carbon-atom wires: 1-D systems with tunable properties, *Nanoscale*, **2016**, *8*, 4414-4435
- M. R. Bryce, A review of functional linear carbon chains (oligoynes, polyynes, cumulenes) and their applications as molecular wires in molecular electronics and optoelectronics, *J. Mater. Chem. C* **2021**, *9*, 10524.

2.2. Charge Transport Models in Organic Semiconductors

This chapter aims at reviewing the main concepts at the base of charge transport in organic semiconductors. First, key elements ruling charge transport in these systems, such as transfer integrals and reorganization energy, are introduced in the fashion of the well-established polaron hopping theory. A critical discussion of hopping mechanisms highlights the reasons of its inadequacy to explain charge transport in high-mobility organic semiconductors. Hence, the transient localization theory is presented, describing the critical role of dynamic disorder and establishing guidelines to understand and design of novel performant organic semiconductors.

2.2.1. Polaron Hopping

Charge transport in organic semiconductors is strongly dependent on the disordered nature of these materials. Solution processed thin films of conjugated polymers intrinsically present a high degree of structural (*i.e.*, static) disorder that determines the localization of charge carriers on specific segments of the polymer chains. In other words, the absence of a perfect crystalline lattice impedes the description of charge transport as delocalized electrons/holes (*i.e.*, Bloch waves) propagating in a periodic potential. Moreover, charges tend to localize on individual or a few molecular sites even in single crystals of small molecules. This is a consequence of the large thermal molecular motions (*i.e.*, dynamic disorder) due to the weak van der Waals intermolecular interactions. Thus, while in bound inorganic semiconductors the electron-phonon interactions are treated as perturbation of the lattice periodicity and simply account for the scattering of highly delocalized charge carriers, in organic semiconductors the electron-phonon coupling is dominant and leads to the formation of quasi-particles named polarons. In the polaron picture, the transfer of an electron/hole from one molecule to another is intimately coupled with the transfer of a structural deformation associated to the presence of an extra charge.[172,173]

Therefore, charge transport in the great majority of organic semiconductors is well described by thermally activated charge transfer processes that allow polarons to “hop” from one molecule to another. Most of the hopping models employed in the last decades rely on the semiclassical Marcus theory, which was originally developed for redox reactions in solutions and then extended to other systems including organic semiconductors.[174–176]

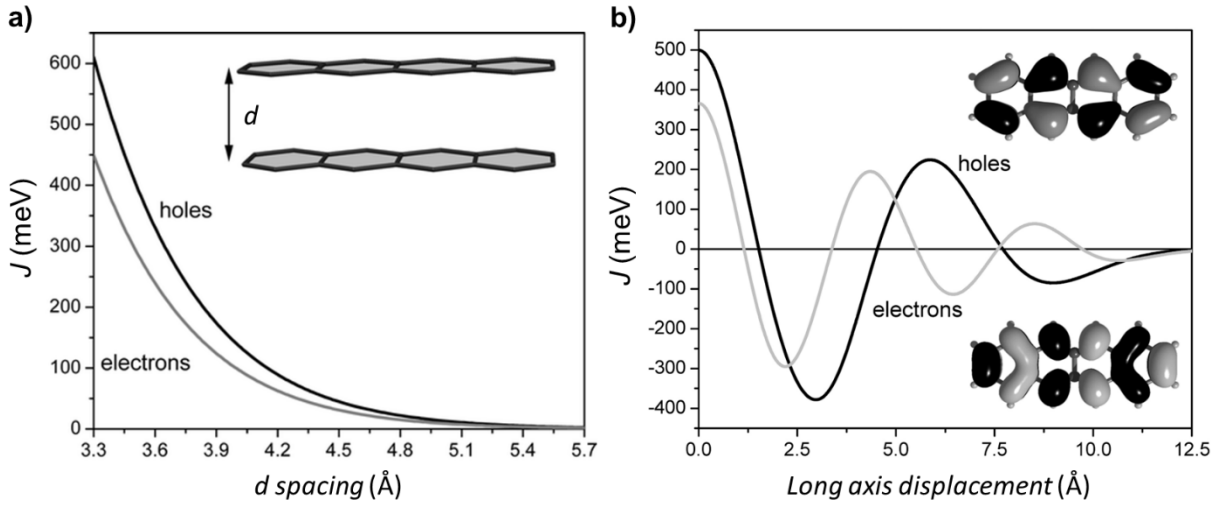

Figure 8. Evolution of the transfer integrals for electron and hole transfer in a tetracene cofacial dimer as a function of **a)** the intermolecular distance *d*, and **b)** the degree of translation of one molecule along its long axis at fixed d = 3.74 Å. Adapted with permission from Coropceanu V., *et al.*, *Chem. Rev.* 2007 (Ref.[177]), Copyright 2007 American Chemical Society.

In this context, the electron-transfer (hopping) rate between two neighbouring molecules *i* and *j* is described by the non-adiabatic Marcus equation:[176,178,179]

$$\kappa_{ij} = \frac{J_{ij}^2}{\hbar}\left(\frac{\pi}{\lambda k_B T}\right)^{1/2} exp\left[-\frac{\left(\Delta E_{ij} - \lambda\right)^2}{4\lambda k_B T}\right], \quad (8)$$

where *h* and k_B are the Planck and Boltzmann constants and *T* the absolute temperature. This model is based on three key parameters, the electronic coupling (J), the reorganization energy (λ) and the site energy difference (ΔE):

- *The electronic coupling* (J), also known as transfer or hopping integral, expresses the strength of the interaction between two neighbouring molecules, being related to the overlap between the frontier molecular orbitals of the charged and neutral molecules. As evident from **Equation 8**, high hopping rates require large charge transfer integrals. Common values of J for state-of-the-art organic semiconductors are in the range from 10 to 100 meV. In molecular crystals as well as in semicrystalline polymers, the charge transfer integrals not only depend on the molecular structure, which determines the frontier molecular orbitals, but also on the molecular packing. Indeed, the electronic couplings are extremely sensitive to the intermolecular distance and to the reciprocal orientation of the donor and acceptor molecules involved in the charge transfer (**Figure 8**).

  In a crystalline lattice, the presence of molecular pairs (*i.e.*, dimers) with diverse reciprocal distance and orientation give rise to different electronic couplings depending on the

direction of charge transport (**Figure 9**). Packing motifs providing isotropic electronic couplings, such as the brick-wall and herringbone packing, usually lead to the highest charge carrier mobility. A way to rationalize this observation is that molecular crystals with isotropic charge transfer integrals are more resilient to both static and dynamic disorder, which strongly hinder transport at the microscopic scale relevant in devices. Instead, the slipped stack and slipped π-stacked packings provide a single preferential transport direction and, despite some notable exceptions like rubrene, they typically give rise to lower charge carrier mobilities.[44]

- The *reorganization energy* (λ) is the sum of all the structural relaxation energies occurring in the system upon the transfer of a charge carrier. It is directly proportional to the energy barrier for a hopping event. Thus, a low reorganization energy (comparable to the magnitude of J) is associated with high charge carrier mobility. λ is composed of two contributions, the inner reorganization energy (λ_{in}) and the outer reorganization energy (λ_{out}). The inner part relates to the relaxation energies of the molecular pair directly involved in the charge transfer upon going from the neutral-state to the charged-state and vice versa. The outer part deals with the medium nuclear polarization, *i.e.*, with the reorganization of the surrounding molecules, which is usually much smaller than the inner part ($\lambda_{in} \gg \lambda_{out}$). Also, the inner reorganization energy is governed by the local electron-phonon coupling, as the structural reorganization of the nuclei is intimately coupled with the molecular vibrations. Indeed, it is possible to distinguish the contribution of each normal mode to the overall reorganization energy by computing the mode-resolved relaxation energy (λ_i):[180]

$$\lambda = \sum_i \lambda_i = \sum_i g_i^2 \hbar\omega_i \tag{9}$$

Here, $\hbar\omega_i$ is the energy of the *i*-th normal mode and g_i are the dimensionless electron-phonon coupling constants, which are formulated from the variation of the site energy ε upon displacement of the normal coordinate X_i:

$$g_i = \frac{\hbar}{\sqrt{2}(\hbar\omega_i)^{3/2}} \frac{\partial \varepsilon}{\partial X_i} \tag{10}$$

- The *site energy difference* (ΔE) is the variation in site energies between the molecules involved in the charge transfer process. In perfectly ordered crystals it would be equal to zero because of translational symmetry. However, its evaluation in real systems represents a very challenging task, as it must account for contributions from the external electric field,

Coulombic effects, structural deformations, defects, and polarization effects (*e.g.*, at the interface with the gate dielectric in OFETs).[179] The degree of energetic disorder (σ) is calculated as the standard deviation of the Gaussian distribution of the site energy differences. This is another key parameter that, along with the reorganization energy, needs to be minimized in order to achieve high mobility.

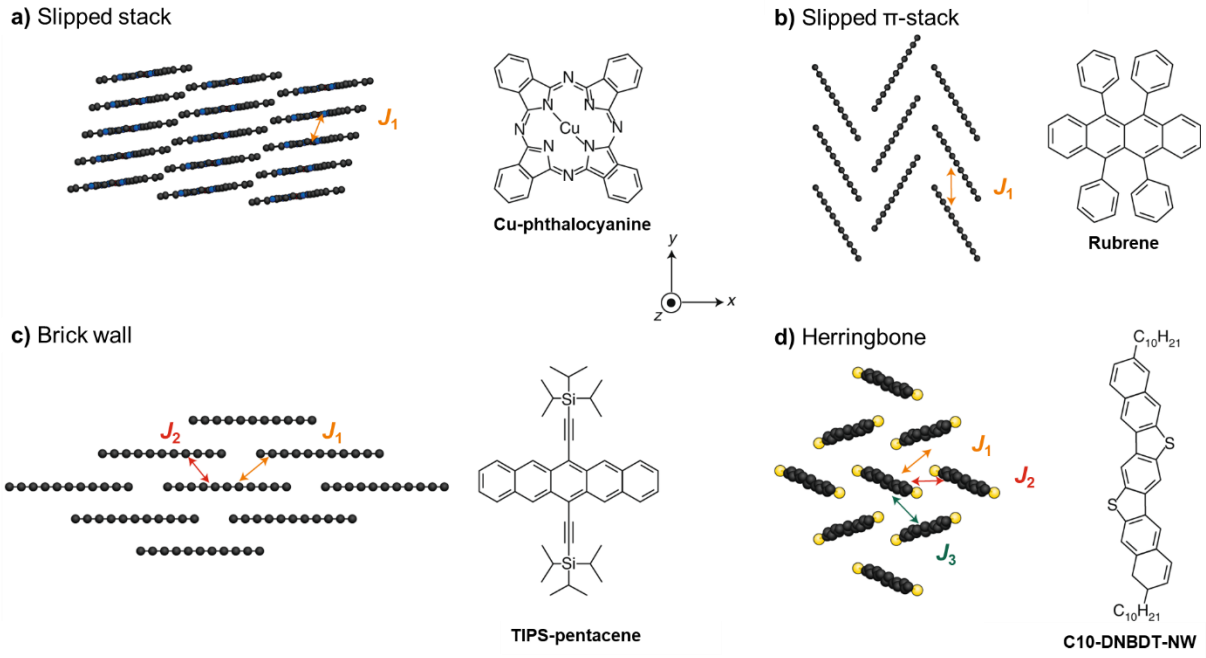

Figure 9. Most common packing motifs in crystals of molecular organic semiconductors with corresponding representative materials. **a, b)** The slipped stack (copper phthalocyanine) and slipped π-stack (rubrene) only present one major transfer integral (J_1). **c)** A second transfer integral (J_2) is accessible within the brick-wall packing (TIPS-pentacene). **d)** The herringbone packing (C10-DNBDT-NW10) allows a more isotropic transport in the x–y plane by providing a third transfer integral (J_3). Reproduced with permission from Fratini S., *et al.*, *Nat. Mater.* 2020 (Ref.[44]), Springer Nature Ltd.

As remarked by Troisi,[176] even if Marcus equation has been extensively employed to compute polaron hopping rates and charge mobility in organic semiconductors, the theory is based on two strong assumptions:

A) It is valid in the non-adiabatic limit, *i.e.*, when the transfer integral J is much smaller than the reorganization energy (λ). In particular, for $|J| \geq \lambda/2$ the electronic wavefunction is delocalized over more than one molecular site, making meaningless the concept of a polaron localized on a single molecule (often referred to as “small polaron”).

B) It assumes a classical treatment of the vibrations that is valid only in the high temperature limit ($k_B T \gg \hbar\omega$). However, this assumption clearly fails for high frequency modes, such as the ring-breathing modes of oligoacenes and of other aromatic organic semiconductors ($\hbar\omega \sim$ 150-200 meV).[180] The same consideration holds true for the ECC mode of cumulenes and oligoynes ($\hbar\omega \sim$ 240-300 meV). In these cases, vibrations must be treated quantum mechanically, by including the effect of the zero-point energy on the potential energy curve of the reaction. In the harmonic approximation, this corresponds to an increase of $\frac{1}{2}\hbar\omega$ of the ground state energy, hence to an equal reduction of the energy barrier for hopping processes.[176] Vandewal *et al.* applied this principle to extract values for the relaxation energy of 20 hole-transporting molecular materials involved in charge transfer (CT) complexes with C_{60} acceptors.[181] By removing the contribution of the high frequency modes (spectral cut-off at 125 meV) to the calculated reorganization energy, they obtained a "reduced relaxation energy" that better agrees with the experimental values derived from numerical fit of the CT absorption tails. Furthermore, the authors highlighted the importance of the quantum mechanical treatment of vibrations especially for small and stiff molecules. In conclusion, the use of the full reorganization energy to estimate the charge carrier mobility is now debated and methods based on the evaluation of mode-resolved electron-phonon couplings should be preferred.[182,183]

2.2.2. Transient Localization

Despite the previously mentioned limitations, models based on polaron hopping have proved successful in predicting the charge carrier mobility of a plethora of organic semiconductors and provided general guidelines for the design of high mobility organic semiconductors. Still, polaron hopping is not able to explain experimental observations of band-like features of transport in high-mobility polymers and in crystals of small molecules displaying room-temperature mobility > 10 $cm^2 V^{-1} s^{-1}$, such as:

- Negative dependence of the mobility with temperature $(d\mu/dT < 0)$ observed in ultrapure crystals of pentacene[184], and rubrene[185] (p-type), as well as of PDIF-CN_2 [186] (n-type). Such a negative trend is typical of inorganic semiconductors where the mobility is limited by phonon scattering at increasing temperature. Diversely, a positive dependence with the temperature would be expected if the transport mechanism was thermal activated hopping, as occurring in most organic semiconductors. Remarkably, band-like temperature dependence of mobility was reported even for solution processed crystals of C8-BTBT[187] and thin films of TIPS-pentacene[188].
- Hall effect measurements on single crystal molecular semiconductors suggest delocalization of the electronic wavefunction over tens of molecules.[189–191]
- The recent observation of metallic behaviour from a two-dimensional hole gas in solution-processed semiconductors clearly demonstrates that charge carriers can fill highly delocalized states at high doping levels.[192] An extremely high charge carrier concentration up to $1 \cdot 10^{14}$ cm^{-2} (approaching 0.25 holes per molecule) was confined two-dimensionally at the interface between a single crystal of the small molecule C8-DNBDT-NW with an electric double layer. Such electric double layer was formed by the insulating alkyl side chains of the C8-DNBDT-NW itself in contact with an ionic gel. The presence of the alkyl side chain layer in between the conducting core of C8-DNBDT-NW and the ionic liquid allows to suppress fluctuations in the electric potential, which are a main cause of carrier localization.

Overall, strong experimental evidence indicates the occurrence of band transport in high-mobility organic semiconductors. From a fundamental viewpoint, organic molecular crystals present an electronic band structure on a par with their inorganic counterpart. Nevertheless, the Van der Walls intermolecular electronic interactions in organic semiconductors are much weaker than in covalent solids, resulting in a nearly flat energy dispersion. The typical

bandwidth in molecular crystals is small, usually in the order of 100-300 meV, as demonstrated for the iconic pentacene crystal by band structure calculations[193] and angle-resolved ultraviolet photoemission spectroscopy (ARPES)[194]. Consequently, the charge carriers effective mass is larger than in inorganic semiconductors, which reflects in lower mobility. Very importantly, the presence of a high degree of static (conformational) and/or dynamic (electron-phonon coupling) disorder impedes observation of band-like transport features in most molecular systems. Even in systems where the temperature dependence of the mobility and the Hall signals would be compatible with band transport, other probes indicate localization of the charges. Several measurements of optical conductivity in rubrene have evidenced a non-Drude behaviour at room temperature, which is ascribed to some form of charge carrier relaxation.[195] Electron spin resonance (ESR) measurements also support the localization of charges over a few molecular units.[191,196] Moreover, charge modulation spectroscopy measurements on pentacene derivatives have testified the coexistence of optical signs of charge localization with a band-like temperature dependence of the mobility.[188,190] Finally, the Bloch-Boltzmann transport model holds only when the charge carrier mean free path between scattering events (from impurities/defects or lattice vibrations) is much larger than the lattice spacing. This condition is only matched with mobility values above 50 $cm^2\,V^{-1}\,s^{-1}$, while organic semiconductors display room temperature mobilities well below this limit.[44]

To explain this paradoxical situation in which both band-like features of transport and signs of polaron localization are observed, it is fundamental to investigate the peculiar role of disorder and electron-phonon coupling in organic semiconductors. In films of conjugated polymers, conformational disorder is typically the limiting factor to efficient charge transport, since the many torsional degrees of freedom of the backbone and of the side chains lead to a wide distribution of site energies and so to high energetic disorder.[59] Because thermal activation is needed to overcome the energetic barriers, the mobility increases with temperature and polaron hopping models are generally effective in describing charge transport in conjugated polymers. Moreover, the vibrational dynamics induces fluctuations of the electronic couplings, which are often of the same order of magnitude of the average value of *J*. In order to achieve as low disorder as possible, a key guideline consists in the design of rigid backbones by locking the torsional degrees of freedom, as it occurs in many donor-acceptor copolymers.[67,197] In small molecules single crystals achieving low degree of static disorder is more feasible. Conversely, the reduction of the dynamic disorder remains very challenging because the soft nature of intermolecular interactions in molecular crystals lead to thermal fluctuations of the nuclei positions. Intermolecular displacements in the order of ~0.1 Å at room temperature have been

revealed in several high-mobility organic semiconductors by electron diffraction measurements.[198,199] In turn, such a structural dynamics leads to very large fluctuations of the transfer integrals.[183] Hence, charge carriers experience a dynamic disordered landscape and the wavefunction tend to localize in different locations at the time scale of the molecular vibrations (< 1 ps). This localization is not permanent but transient: as the molecular energetic landscape changes with molecular vibrations, charges localize and subsequently delocalize in different positions of the lattice (**Figure 10**).[200,201]

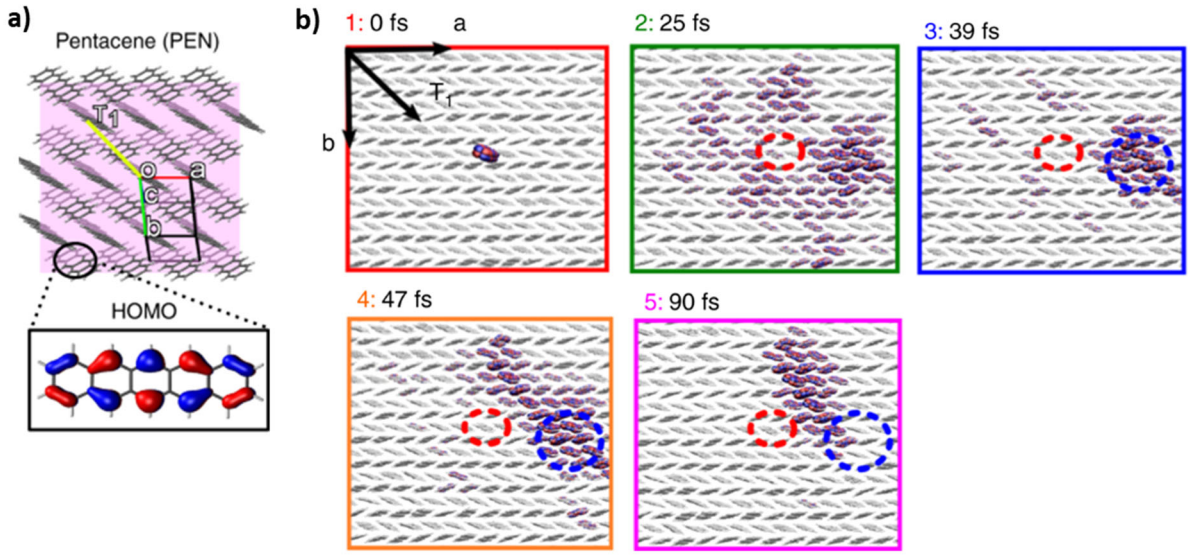

Figure 10. a) the molecular herringbone packing of pentacene and DFT calculated highest occupied molecular orbital (HOMO). **b)** Snapshots capturing the time evolution in the first 100 fs of the hole carrier wavefunction in a simulated pentacene crystal. Depending on the variation of the energy landscape at the fs time scale, the polaron experiences both localization on a few molecular sites, and delocalization over tens of molecules. On average, the polaron is delocalized over 18 molecules. Readapted from Giannini S., *et al.*, *Nat. Commun.* 2019 (Ref.[200]).

This transport regime where charge diffusion is driven by the molecular lattice fluctuations is described by the *transient localization (TL) theory*.[176,202,203]

Within the TL framework, the mobility is expressed as:

$$\mu = \frac{e}{k_B T} \frac{L^2}{2\tau_{vib}}, \tag{11}$$

where e is the elementary charge, $k_B T$ the thermal energy, L is the average transient-localization length of the charge carrier and τ_{vib} the timescale of intermolecular motions. While τ_{vib} does not change much across different molecular crystals, L^2 depends on the electronic

couplings of the specific system and on their fluctuations (see *Supplementary Information* of Ref.[203] for additional details).

The TL regime is able to reconcile band-like features of transport, such as the negative temperature dependence of the mobility and ideal Hall signal, with values of mobility falling below the limit for band transport and with charge localization fingerprints assessed by charge modulation spectroscopy. Moreover, charge localization on a single molecular site is reached at high degree of disorder, determining the breakdown of the TL regime and the transition to a thermally activated hopping regime, which is appropriate when the mobility is approximately lower than 0.5 $cm^2 V^{-1}s^{-1}$.[44]

A fundamental concept of the TL model is that the molecular vibrations not only affect the mobility by determining the τ_{vib} at the denominator in **Equation 11**, but they have a strong impact in modulating the electronic couplings, and so on the transient-localization length *L*.

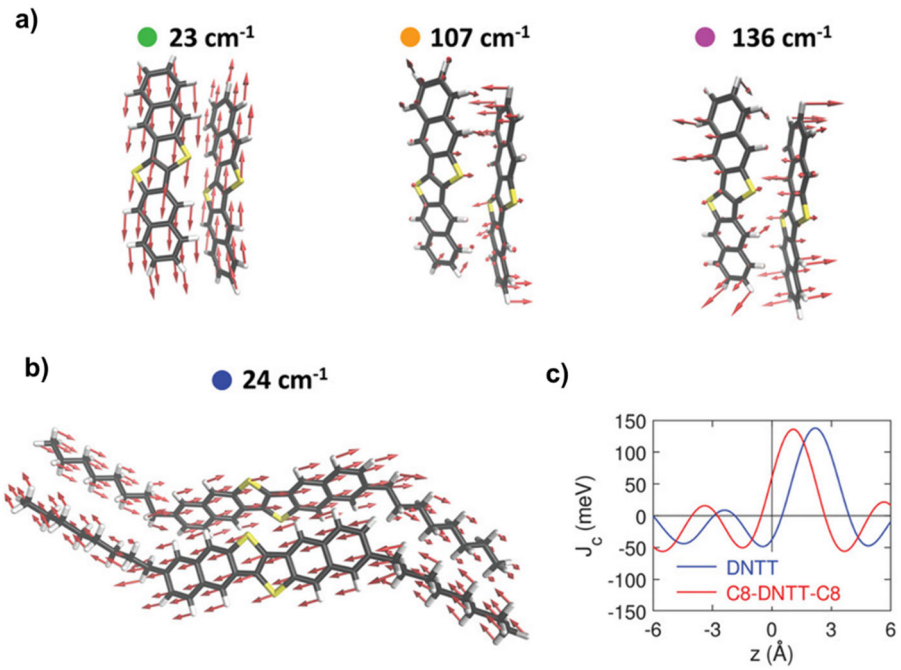

Figure 11. a, b) Illustration of the intermolecular vibrational modes having a strong impact on the energetic disorder in DNTT and in C8-DNTT-C8, respectively. **c)** Fluctuation of the transfer integral of a single molecular pair as a function of the sliding coordinate for DNTT and C8-DNTT-C8. Readapted from Schweicher G., *et al.*, *Adv. Mater.* 2019 (Ref. [204]).

Several studies have investigated the role of intramolecular and intermolecular vibrational modes on charge transport.[138,182,205–210] Remarkably, Schweicher and coauthors have shown that one or a few intermolecular modes, named "killer modes", are responsible for up to 80%

of the total energetic disorder in representative high-mobility molecular crystals. These modes mainly involve sliding of the molecules along their long molecular axis, which causes strong fluctuations of the transfer integrals (**Figure 11**).[198,204] As a matter of fact, not only the magnitude of the transfer integrals is important (*i.e.,* J_1, J_2, J_3) but also the amount of their fluctuation (*i.e.,* $\Delta J_1/J_1, \Delta J_2/J_2, \Delta J_3/J_3$). Designing principles for high-mobility organic semiconductors aim at systems with highly isotropic electronic couplings between nearest neighbors (the overall magnitude of $J = \sqrt{J_1 + J_2 + J_3}$ should be maximized), along with minimal fluctuations of the transfer integrals and of the site energies.[203,211]

Key reviews on charge transport in organic semiconductors:

- Troisi, A. Charge Transport in High Mobility Molecular Semiconductors: Classical Models and New Theories. *Chem. Soc. Rev.* **2011**, *40* (5), 2347–2358.
- Fratini, S.; Nikolka, M.; Salleo, A.; Schweicher, G.; Sirringhaus, H. Charge Transport in High-Mobility Conjugated Polymers and Molecular Semiconductors. *Nat. Mater.* **2020**, *19* (5), 491–502.
- Giannini S., Blumberger, J., Charge Transport in Organic Semiconductors: The Perspective from Nonadiabatic Molecular Dynamics. *Acc. Chem. Res.* **2022**, *55* (6), 819–830.

3. Experimental Methods

This chapter aims to introduce key concepts on organic field-effect transistors, which represent the principal tool used throughout this thesis to investigate charge transport in carbon-based semiconductors. Firstly, the working principles and important design aspects are explained. Then, the focus is set on the two specific deposition processes that have been directly optimized in this work. The first one is the off-centre spin coating deposition of the PNDIT2, polymer and of its encapsulated derivative, which is central to **Chapter 4**. The second one regards the deposition of large-area thin films of cumulenes by wire-bar coating, which are the protagonists of **Chapter 6**.

Finally, Charge Modulation Spectroscopy (CMS) and Charge Modulation Microscopy (CMM) are introduced. These techniques are crucial to the investigation of semiconducting carbon-nanotube networks in **Chapter 5**.

Throughout this chapter, the stress is on the fundamental concepts required to fully understand the results of the thesis, while the details on device fabrication processes, characterization techniques, and data analysis are reported directed in the *Methods* of the attached papers or in the related *Supporting Information*.

3.1. Organic Field-Effect Transistors

Organic field-effect transistors (OFETs) constitute the enabling building block for a plethora of applications such as flexible screens and microchips, stretchable biosensors, electronic skin, and neuromorphic devices. With respect to conventional inorganic semiconductors, a key advantage of organic semiconductors is the possibility to be deposited from solution using large-area scalable processes that are proper of the printing industry (*e.g.*, inkjet, gravure and flexographic printing). Their processing can be carried out at low temperatures (typically < 200 °C) compatible with flexible or biodegradable plastic substrates. Moreover, the manufacturing of OFETs allows to avoid costly high-vacuum processes common to the silicon industry.

Along with their relevance for direct technological applications, OFETs represent an optimal platform for studying the fundamental charge transport properties of organic semiconductors and of semiconducting carbon nanotube networks. Therefore, their impact is broad and extends to other opto-electronic devices and applications like OLEDs, OPV and thermoelectrics.

It is worth mentioning that, even if carbon nanotubes are not regarded as proper "organic semiconductors", they also present the above-mentioned advantages. In addition, the general working principles of OFETs described in this chapter easily lend to FETs based on random networks of semiconducting carbon nanotubes.

3.1.1. Working principles

The OFET is a three-terminal device composed of the organic semiconductor layer, the gate dielectric and three electrodes, namely source (S), drain (D) and gate (G).

The on/off switching and amplification capability of the device is controlled by the combined effect of the potentials applied to the gate (V_{gs}) and to the drain (V_{ds}), while keeping the source grounded. With no V_{gs} applied the channel is highly resistive and only a small off current (I_{off}) can flow under the effect of an applied lateral field (V_{ds}). Upon polarization of the dielectric by a negative gate voltage (V_{gs}), positive charge carriers ("holes") are injected from the contacts and accumulate at the semiconductor/dielectric interface. In analogy, a positive V_{gs} leads to the accumulation of negative carriers ("electrons"). Thus, the charge density in the channel (and so the transconductance) is modulated by the gate voltage, giving rise to the so-called *field-effect*. In real devices, before free charge carriers may build up in the conduction channel, it is first necessary to fill charge traps at the semiconductor-dielectric interface. The value of the gate potential required to fill these traps is termed *threshold voltage* (V_{th}). When the gate voltage exceeds V_{th}, free carriers can move under the action of an applied lateral field provided by the source-drain voltage (V_{ds}) and the transistor switches on.

Field-effect transistors are fully characterized by measuring their two characteristics, namely the output and the transfer curves. **Figure 12** shows an ideal output curve, which is obtained by modulating continuously $|V_{ds}|$ at increasing discrete values of $|V_{gs}|$. Two working regimes can be distinguished by examination of the output curve:

- For $V_{ds} < |V_{gs} - V_{th}|$, the device operates in *linear regime*. The charge density is approximately constant across the whole channel and equal to $\rho = C_{diel}|V_{gs} - V_{th}|$, being C_{diel} the areal capacitance of the dielectric. The transistor behaves like a resistor whose transconductance is modulated by the gate voltage (V_{gs}). Thus, I_{ds} grows linearly with the applied lateral field (V_{ds}) according to Ohm's law.
- When V_{ds} increase up to $V_{ds} = |V_{gs} - V_{th}|$, the charge carrier density at the drain reaches zero (*pinch-off* point). Further increasing V_{ds}, the pinch-off point moves towards

the source and the device enters the so-called *saturation regime*. The excess source-drain potential drops onto the depleted region near the drain electrode, which is highly resistive. Consequently, I_{ds} saturates to a constant value.

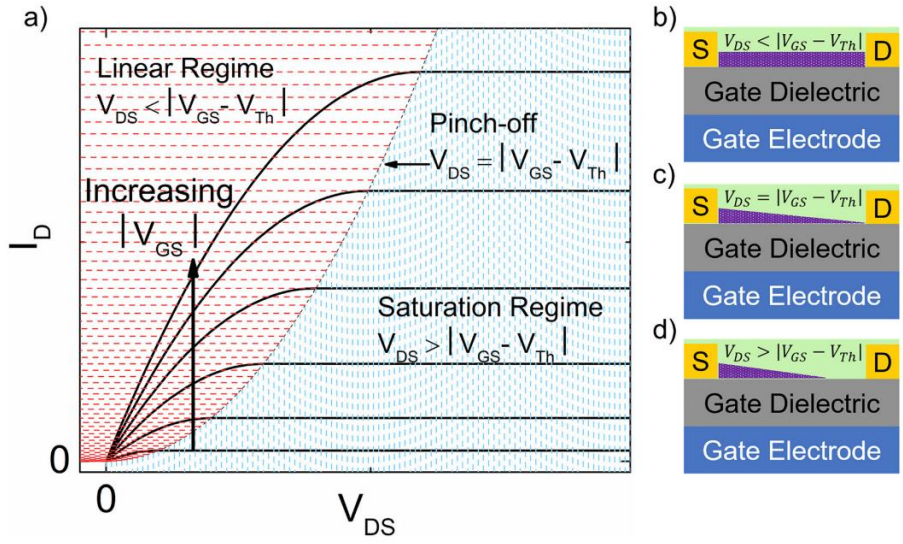

Figure 12. a) "Textbook" output characteristics, **b-d)** sketch of the charge density in the conduction channel (purple), in the linear regime (b), at pinch-off (c), and in the saturation regime (d). Reprinted from Z. A. Lamport, *et al.*, *J. Appl. Phys.* 2018 (Ref.[212]), with the permission of AIP Publishing.

The current-voltage characteristics can be analytically described by the Shockley equations for the linear and the saturation regimes, respectively:

$$I_{ds,lin} = \frac{W}{L}\mu_{lin}C_{diel}\left[(V_{gs} - V_{th})V_{ds} - \frac{1}{2}V_{ds}^2\right], \tag{12}$$

$$I_{ds,sat} = \frac{W}{2L}\mu_{sat}C_{diel}(V_{gs} - V_{th})^2, \tag{13}$$

where W and L the transistor channel width and cannel length.

It is straightforward to obtain the expression for the mobility from (12) and (13) by taking the derivative of I_{ds} with respect to V_{gs}:

$$\mu_{lin} = \frac{L}{C_{diel}WV_{ds}}\frac{\partial I_{ds,lin}}{\partial V_{gs}} \tag{14}$$

$$\mu_{sat} = \frac{2L}{C_{diel}W}\left(\frac{\partial\sqrt{I_{ds,lin}}}{\partial V_{gs}}\right)^2 \tag{15}$$

The Shockley equations are valid within the gradual channel approximation, which holds if:

a) The mobility does not depend on the charge carrier density (hence, it must not vary as a function of V_{gs});
b) The transverse gate electric field is much higher than the lateral source-drain electric field (this condition is usually matched when the channel length is much greater than the dielectric thickness).
c) The contact resistance can be considered negligible compared to the channel resistance.

The other transistor characteristics, namely the transfer curves in linear and saturation regimes, are illustrated in **Figure 13**. In the transfer characteristics the gate voltage is swept continuously, while the source-drain potential is kept constant. Important parameters can be extracted from the transfer curves:

- The *on-current* (I_{on}) and the *off-current* (I_{off}) are defined as the values of the source-drain current when the transistor is in the on- and off-state, respectively. The "on/off ratio", defined as I_{on}/I_{off}, is an important parameter to distinguish whether the transistor can be used as a switch (10^6 is often considered a good target).
- The *field-effect mobility* in linear (μ_{lin}) and saturation (μ_{sat}) regimes are derived according to (14) and (15) by extracting the slope of $I_{ds}\ vs\ V_{gs}$ (linear regime) and of $\sqrt{I_{ds,lin}}\ vs\ V_{gs}$ (saturation regime). In principle, the values of μ_{lin} and μ_{sat} should be identical. Nevertheless, the presence of a non-negligible contact resistance often leads to a lower value of the mobility in linear regime than in saturation regime. Moreover, the dependence of the mobility as a function of V_{gs} should be always reported for a reliable extraction of μ. Indeed, a constant trend should be reached above V_{th} to justify the use of the Shockley formulas. Deviations from this ideal trend are often found in literature, which has caused the so-called "inflation" of the reported mobility values.[49,213]

  A separate discussion is needed for FETs based on carbon nanotube networks. Indeed, the mobility in carbon nanotubes presents an intrinsic dependence on the charge carrier density, which is a direct consequence of the limited quantum capacitance resulting from the one-dimensional DOS of nanotubes.[214] Therefore, a clear maximum is observed in the plot of $\mu\ vs\ V_{gs}$, after which the mobility decreases as the first subband is progressively filled. If the charge carrier concentration is high enough that carriers start occupying the second subband, another increase of mobility can be observed.[215] Due to this intrinsic dependence of the mobility on the applied bias, either the maximum

carrier mobility, either the mobility at a specified charge density should be reported to be able to compare the results from different works.

- The threshold voltage, V_{th}, is calculated by finding the intercept of $I_{ds} = 0$ and the linear fit of I_{ds} *vs* V_{gs} in linear regime and of $\sqrt{I_{ds,lin}}$ *vs* V_{gs} in saturation regime.
- The subthreshold slope (or subthreshold swing), *SS*, is computed as:

$$SS = \frac{\partial V_{gs}}{\partial(\log_{10}(I_{ds}))} \tag{16}$$

It indicates how fast the device switches from the off- to the on-state and is measured in V/decade. A reasonable value for the subthreshold slope is about 1 V/dec. SS depends on the trap density at the semiconductor/dielectric interface, N_{in}, according to:[212]

$$SS = \frac{k_B T \ln(10)}{q}\left(\frac{N_{it} q^2}{C_{diel}} + 1\right) \tag{17}$$

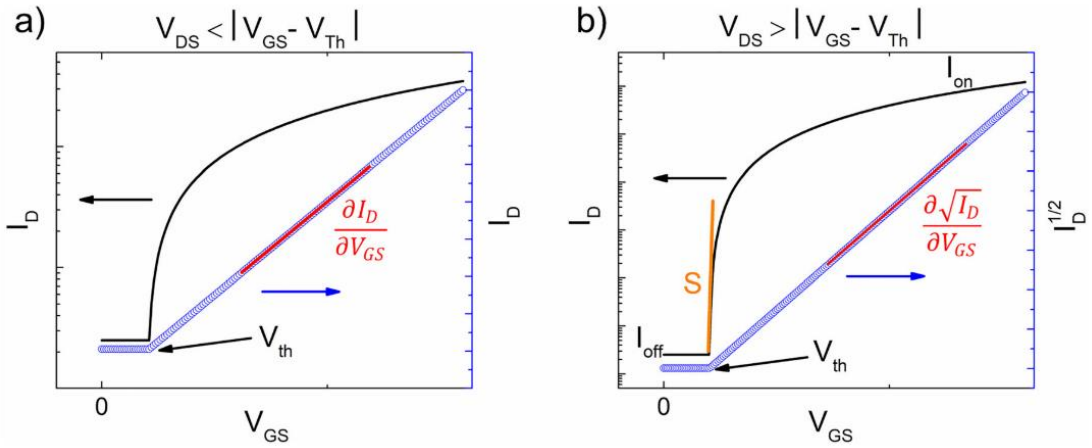

Figure 13. Evolution of I_{ds} at fixed, negative, V_{ds} as a function of increasingly negative V_{gs} in (a) the linear regime and (b) the saturation regime. Reprinted from Z. A. Lamport, *et al.*, *J. Appl. Phys.* 2018 (Ref.[212]), with the permission of AIP Publishing.

3.1.2 Device architecture and semiconductor deposition

The design of the transistor structure as well as the materials choice of every building block play a fundamental role in defining the performance of the device. Several device architectures can be realized depending on requirements on the processing of the materials and on the final application. (**Figure 14**) For instance, staggered configurations like the top-gate bottom-contacts (TGBC, Figure 14a) and the bottom-gate top-contacts (BGTC, Figure 14c) are preferable for charge transport studies, since the large injection area permits to minimize non-ideal effects due to the contact resistance. A comprehensive review of contact energetics and charge injection in solution-processed OFETs can be found in Ref.[216]

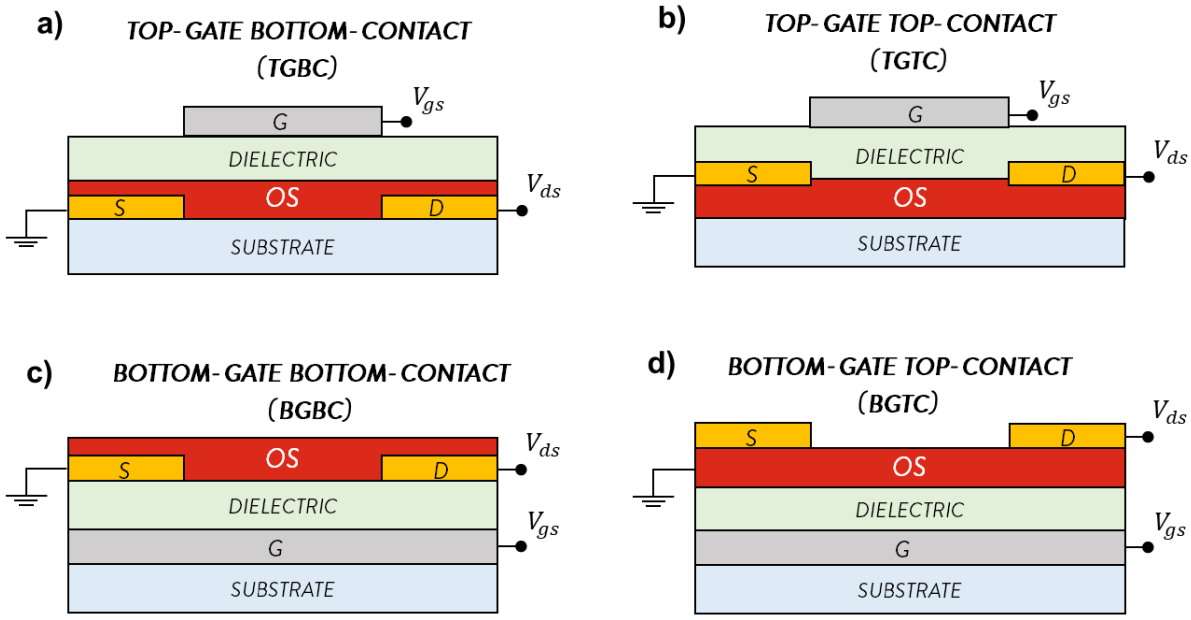

Figure 14. Schemes of the four common OFET architectures (viewed in cross section). **a)** Top-Gate Bottom-Contact (TGBC), **b)** Top-Gate Top-Contact (TGTC), **c)** Bottom-Gate Bottom-Contact (BGBC), **d)** Bottom-Gate Top-Contact (BGTC).

Since free carriers are transported within few molecular layers at the semiconductor-dielectric interface, this region is crucial for charge transport studies and must be carefully optimized.[217] To limit the density of electronic traps at the interface with the semiconductor, an ideal dielectric layer should have a low roughness and low amount of surface states. Silicon oxide (SiO_2) is generally not suitable as gate dielectric in OFETs, because the dangling bonds at the surface act as trapping sites for charge carriers. The use of self-assembled monolayers (SAMs) is a common strategy adopted to passivate the SiO_2 surface.[218] Nevertheless, one must consider

that the change in surface wettability due to the introduction of the SAM strongly affects the final morphology of solution-processed organic semiconductor films. Moreover, the choice of the dielectric is also dictated by the final application. Insulating polymers, which are solution-processable and mechanically flexible, are preferable for the target applications of organic electronics.[219]

The thickness (t) and the relative permittivity (ϵ_r) are other key parameters, since they determine the capacitance per unit area:

$$C_{diel} = \frac{\epsilon_0 \epsilon_r}{t} \tag{18}$$

A thin dielectric layer and the use of high-κ materials (high ϵ_r) allow to reduce the voltages required for device operation. Still, it is generally difficult to reduce the dielectric thickness below ~100 nm without creating pinholes causing high leakage currents. Furthermore, high-κ dielectrics are highly polarizable: the presence of strong dipoles usually raises the energetic disorder at the semiconductor interface, which is detrimental to charge transport.[68] Thus, it is important to achieve high capacitance by reducing the dielectric thickness but without increasing the energetic disorder. A possible strategy consists in using a double-layer dielectric, made of a very thin film of a low-k dielectric (*e.g.*, the fluoropolymer Cytop, PMMA, polystyrene) in direct contact with the organic semiconductor and an outer layer of a higher-κ dielectric.[220]

Lastly, the microstructure of the semiconducting layer is of paramount importance, as it affects the opto-electronic properties of the film. The use of different deposition techniques and processing parameters, such as the solvent properties, the substrate wettability and the annealing temperature, lead to thin films with diverse solid-state packing (*i.e.*, polymorphs), molecular orientation and morphology. Several excellent reviews have covered this wide domain of research, spanning from the growth of large high-purity single crystals to the deposition of polycrystalline thin films of small molecules, and to the alignment of conjugated polymers.[221–226] The following paragraphs will focus on two solution-processing techniques that have been directly optimized in this thesis work.

Deposition of PNDIT2 by off-centre spin coating

The deposition from solution of large-area thin films of conjugated polymers leads to unavoidable structural defects, which can broaden the DOS, thus introducing deep trap states. Indeed, the many degrees of conformational freedom in polymers result in microstructures varying from completely amorphous to crystalline. Semicrystalline conjugated polymers often contain ordered lamellae made of co-facially stacked backbones that present strong π-orbital

overlap. Many experimental observations have reported a strong improvement of charge mobility in films where polymers are aligned in a preferential direction presenting a high degree of microstructural order (*e.g.,* this is the case of the paradigmatic regio-regular P3HT and of PBTTT).[227–229] Conversely, amorphous regions offer lower conductivity and can act as trapping sites. Therefore, there has been a lot of interest in developing techniques for a uniaxial alignment of highly planar conjugated backbones to reduce the conformational disorder by restricting degrees of conformational freedom.[226] Chain planarity can also result in closer intermolecular π-π stacking with increased electronic couplings (**Figure 8**). Moreover, aligning the polymer backbones parallel to the source-drain direction is thought to favour charge transport mainly through extended π-molecular orbitals within the polymer chains, thus reducing the number of slow interchain hopping events. The advent of high-mobility donor-acceptor (D-A) copolymers with very poor long-range crystallinity (*e.g.,* IDT-BT) has posed questions on this belief. In these systems, transport occurs through an interconnected network of ordered domains. Thus, the dominant factor leading to high mobility is more related to the strength of short-range interactions than to crystallinity. For instance, the narrow torsional angle distribution between the D and the A moieties increases the tolerance to the unavoidable presence of disorder by reducing the fluctuations of the transfer integrals and the site energies.[59] Still, it is undoubtedly true that a microstructure with extended ordered domains is beneficial to charge transport. The high-mobility n-type D-A copolymer PNDIT2 offers a paradigmatic example. Matsidik *et al.*[230] have demonstrated the deposition of aligned fibrillar structures of PNDIT2 by using off-centre spin coating. Compared to the standard spin coating process, in the off-centre method the substrate is positioned at a predetermined distance from the spin centre. In this way, the centrifugal force act on every point of the substrate, allowing the unidirectional alignment of the polymer chains in the direction radial to the sample rotation. (**Figure 15a**) as in the standard spin coating process. PNDIT2 films deposited by off-centre spin coating present strong transport anisotropy: when the contacts are oriented perpendicular to the alignment direction the mobility can be up to 5 times higher than with parallel orientation. Importantly, Luzio et al.[86] have shown that the fibrillar structures associated to high degree of orientational order are obtained only when the films are processed from solvents promoting aggregation such as toluene or mesitylene (**Figure 15b-c**). Such behaviour is attributed to the occurrence of self-coiling of the polymer chains in these solvents.[79] Diversely, films processed from solvents that do not promote aggregates, such as chloronaphthalene, do not present the peculiar fibrillar microstructure and lead to lower charge mobility. For these reasons, assessing the occurrence of aggregation in different solvents and optimizing the thin film deposition by

off-centre spin coating played a key role to investigate charge transport in the molecularly encapsulated version of PNDIT2 (**Chapter 4**). The optimized processing variables include the solution concentration, the solvent properties, the spinning speed and acceleration and the postdeposition annealing temperature.

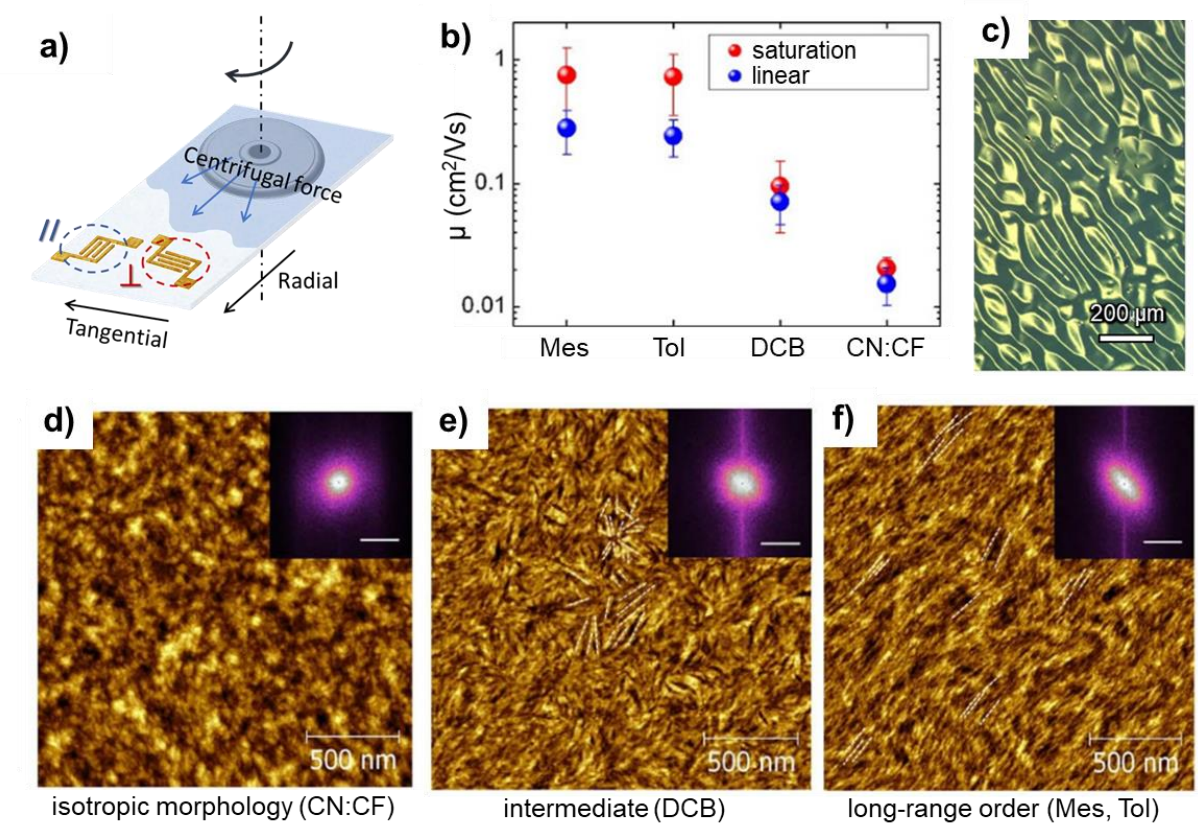

Figure 15. a) Scheme of the off-center spin coating technique. **b)** Mobility of OFETs based on PNDIT2 deposited from various solvents (Mes: mesitylene, Tol: toluene, DCB: 1,2-dichlorobenzene, CN:CF: chloronaphthalene-chloroform mixture). **c)** Cross-polarized optical microscopy image of a PNDIT2 film deposited from toluene. The birefringence originates from the alignment of polymer lamellae in different directions. **d-f)** Atomic force microscopy topographies of PNDIT2 films deposited from CN:CF, DCB and Tol, respectively. The insets show the 2D fast Fourier transform (FFT) of the images. While deposition from CN:CF results in isotropic morphology, fibrils appear in films deposited by DCB and, especially, by Tol (and Mes), which produce a highly aligned fibrillar morphology beneficial for charge transport. Adapted from Luzio A., *et al.*, *Sci. Rep.* 2013 (Ref.[86]).

Wire-bar coating deposition of cumulenic thin films

Wire-bar coating is a scalable printing technique based on meniscus-shearing that allows to deposit large-area thin films (down to few nanometers thickness) and to induce an oriented molecular assembly. The technique has enabled the fabrication of OFETs with record mobility for several organic semiconductor materials, including conjugated polymers like PNDIT2[75], small molecules[231] and binary blends of small molecules and polymers[232]. The working principle is similar to other meniscus-shearing methods like dip-coating, blade coating, zone-casting and slot die coating.[233] It consists in shearing a solution over a substrate using a wire-bar, *i.e.*, a round bar tightly wound with stainless steel spires (**Figure 16a**). When poured near the bar-substrate interface, or directly onto the bar, the solution penetrates within the spires by capillarity and forms a meniscus at the contact line with the substrate. The meniscus is sheared on the sample by the motion of the bar at controlled speed (or vice versa, by moving the substrate while keeping the bar fixed), leading to uniform spreading of the solution over the substrate.

Wire-bar coating provides the advantages of high deposition rate, roll-to-roll compatibility and excellent uniformity over large area.[231] Moreover, it allows to use significantly less solution of precious active materials with respect to spin coating (typically, no more than 5-10 µL are enough for coating a 2 x 2 cm^2 substrate, which is approximately 5 times less than the typical volume used with spin coating). Moreover, it is often challenging to obtain highly crystalline thin films of small molecules by spin coating, while the several processing parameters available in meniscus shearing methods allow to better control the crystallization process. Specifically, attempts of using spin coating to deposit tetraphenyl[3]cumulene ([3]Ph) thin films leaded to small and scattered crystallites, with no improvement of OFETs performance with respect to the drop-cast layers used in our previous work[171]. For these reasons, wire-bar coating was adopted to optimize the deposition of [3]Ph, leading to high-quality polycrystalline thin films, as described in **Chapter 6**.

The mechanism of film formation is very complex, since it depends on the mass flow of the solvated molecules in the meniscus, on the solvent evaporation and on the crystallization kinetics.[225] Thus, several factors need careful optimization, which comprehend physicochemical properties of the solution (solute concentration, solvent boiling point, surface tension, …), solution-substrate interaction (wettability, roughness, patterning, …) and processing parameters (shearing speed, deposition temperature, wire diameter and bar-substrate gap).

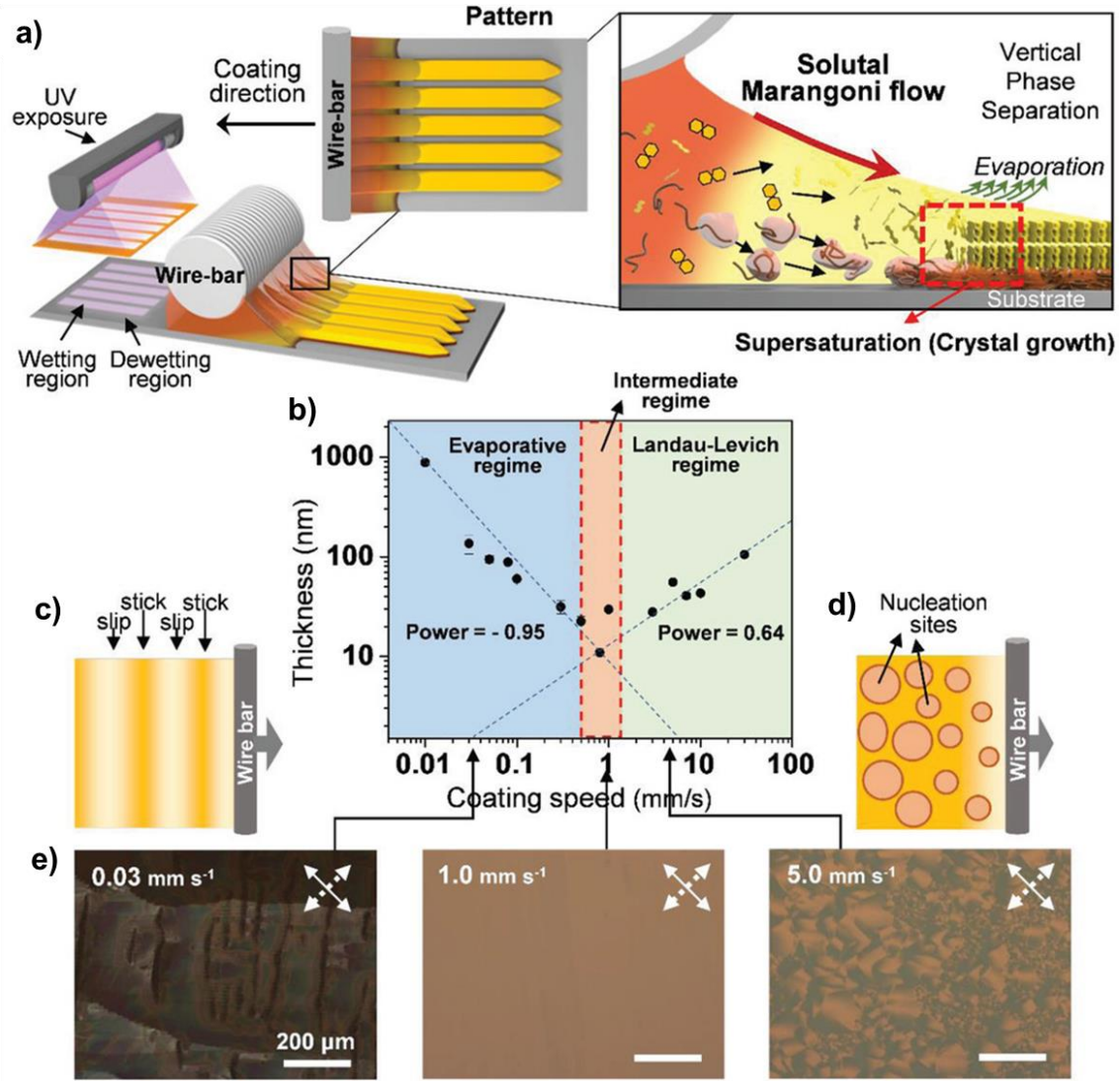

Figure 16. a) Schematic illustration of wire-bar coating technique and of the mass flow and crystallization processes in the meniscus formed between the substrate and the contact line. Substrate patterning with UV-exposure allowed Lee *et al.* to selectively deposit the organic semiconductor (C8-BTBT:PTAA blend) on regions with higher wettability. Moreover, the presence of a solvent additive generates a solutal Marangoni flow with beneficial impact on the vertical phase separation of the blend components. **b)** Film thickness as a function of the coating speed, identifying three different deposition regimes. **c-d)** Schematic illustration of film-formation problems in evaporative regime and Landau–Levich regime, respectively. **e)** Polarized optical microscopy images of films deposited with different shearing speeds. Reproduced with permission from Ref.[234].

Disentangling the separate effects of all these variables and finding a global optimum is a challenging task, which can very much benefit from optimization approaches based on Design of Experiments and Machine Learning (see Ref.[235]). In the following, some general guidelines are ruled based on literature and on the experience developed with the deposition of small molecules (mainly [3]Ph).

1) *Ink formulation*

The concentration of the solution is directly correlated to the thickness of the dried film.[236] Since viscous solutions lead more easily to homogeneous films, increasing the concentration of the organic semiconductor close to the solubility limit (usually about 10-20 g/L in common organic solvents) might be a good starting point for the optimization. One should note that if the solution is too concentrated, the formation of aggregates can act as nucleation seeds for the crystal growth and impact detrimentally on the film homogeneity and on the size of the crystalline domains.

The solvent plays a crucial role because of its direct interaction with the solvated molecules, as already remarked for the case of PNDIT2. Moreover, the boiling point, the vapor pressure and the surface tension directly affect the evaporation rate and the mass flow of the solute in the meniscus. Strategies based on mixing two solvents are often useful to tune these properties. Either high/low boiling solvents or good-solvent/antisolvent mixtures are frequently employed to avoid common drying problems (*e.g.*, the coffee-stain effect) by creating concentration or surface-energy gradients that promote a beneficial solutal Marangoni flow (**Figure 16a**).[222,231,234,237]

Finally, blending the organic semiconductor with insulating polymers is a common approach that often leads to improved processability and enhanced device performance thanks to a vertical phase-separation of the two components (**Figure 16a**). The presence of an insulating polymer can simultaneously improve the crystallinity of the organic semiconductor, provide a low-κ trap-free environment and act as a thin barrier against environmental species contributing to degradation (*e.g.*, moisture, water, oxygen).[46,232,238,239]

2) *Coating speed*

Along with the concentration of the solution, the coating speed is the main factor controlling the thickness of the film.[236] Depending on the balance between the solvent evaporation rate and the shearing speed two deposition regimes can be distinguished (**Figure 16b**):[234,240]

- The *evaporative regime* takes place at slow shearing speed (usually < 1 mm/s, but with a strong dependence on the ink composition and on the other processing parameters). In this

regime most of the solvent evaporation occurs directly in the meniscus while the bar is being sheared. The evaporative regime often allows to obtain large oriented crystalline domains of small molecules, but being slow it is not suitable in view of scaled-up high-throughput technologies. In this regime, the film thickness decreases with the shearing speed.

- The *Landau-Levich regime* occurs at high speeds (usually > 1 mm/s) and the film solidifies after the passage of the bar. In this case, the thickness of the film increases with the shearing speed, due to strong viscous forces that drag out the liquid film from the meniscus.[241]

3) *Deposition temperature*

A heating bed onto which the substrate is placed permits to control the deposition temperature. Heating the substrate accelerates the evaporation of the solvent, promotes convective mass flow of the solvated molecules and can induce the formation of kinetically stable polymorphs.[223,242]

4) *Surface treatments*

The activation of the surface with a mild plasma treatment often helps in avoiding detrimental dewetting effects. Moreover, the use of self-assembled monolayers (SAMs) helps to control the surface wettability. SAMs are also employed to passivate traps at the substrate interface and to modify the electrodes work-function to improve charge injection.[218]

5) *Wire diameter and bar-substrate gap*

The spacing between the spires is directly proportional to the diameter of the wounded wire, ranging from a few to tens of μm. The larger the spacing, the larger the volume of solution that is dispensed onto the substrate while shearing. Thus, bars with small wire diameter (~ 4-10 μm) are preferable to obtain films with a few molecular layers thickness, while larger diameters (~ 20-50 μm) are more suitable for films up to hundreds of nanometers obtained with viscous inks. Another important parameter for the reproducibility of the process is the distance between the wire-bar and the substrate. Since it determines the height of the meniscus, it does affect the whole dynamics of film formation. Thus, this distance should be controlled and kept at a fixed value (usually few μm).[243] For this reason, our bar-coater was customized with two motorized lifters at the two edges of the bar in order to tune the bar-substrate gap with micrometric precision.

6) *Ventilation and humidity*

For the deposition of very thin crystalline films, also the presence of intense ventilation (*e.g.*, the aspiration of the chemical hood) can hinder the formation of homogeneous films. Conversely, a mild and almost laminar flow of nitrogen intentionally blown onto the sample can increase the evaporation rate without heating the substrate at high temperature, which might degrade the film or promote undesired polymorphs. Finally, variations of the environmental humidity can affect the substrate wettability, especially when the deposition occurs at low temperature.

3.2. Charge Modulation Spectroscopy

Charge Modulation Spectroscopy (CMS) is a lock-in based technique able to detect small variations of the optical absorption spectrum of the semiconducting layer upon modulation of the charge density in the operational conditions of an OFET. A schematic diagram of the CMS setup is presented in **Figure 17a.**

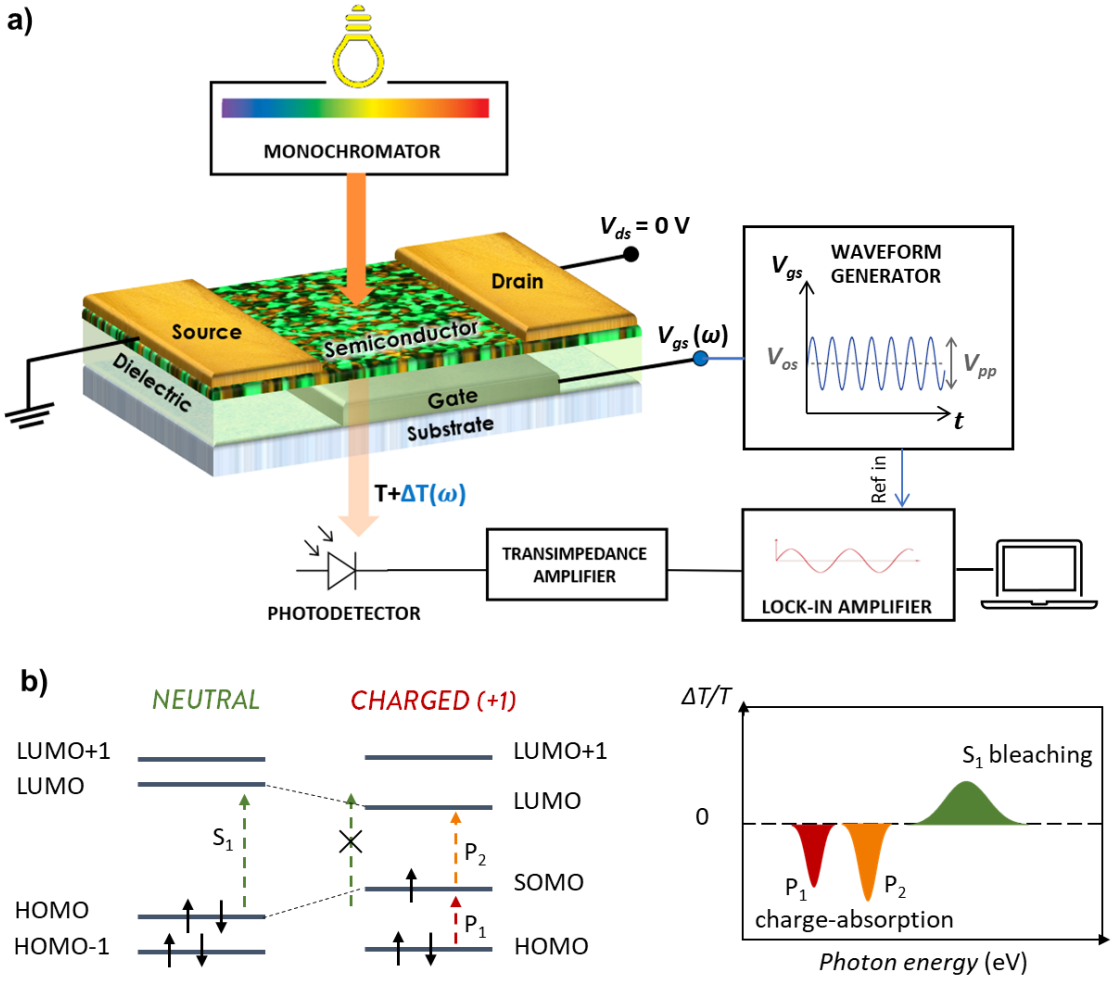

Figure 17. a) Schematic diagram of the Charge Modulation Spectroscopy (CMS) setup. **b)** Variation of the optical transitions of a molecule from the neutral to the charged state (radical cation/localized positive polaron) and sketch of the corresponding CMS spectrum.

In a standard CMS experiment, the source and drain contacts are grounded, while a bias is applied to the gate electrode to induce accumulation of charges within few molecular layers at the semiconductor-dielectric interface. Given the typical areal charge density in OFETs (10^{11}-10^{13} cm^{-2}), about one molecule/polymer segment over 100-1000 neutral molecules becomes charged.[244] Hence, the fractional change in transmission due to the presence of charged

molecules is minimal, usually within 10^{-5} and 10^{-3}. To measure such small variations, in the CMS experiment the charge density is modulated by applying a constant off-set potential, V_{os}, superimposed to a sinusoidal bias $V_{pp}(\omega t)$:

$$V_{gs} = V_{os} + \frac{V_{pp}}{2}\, sin(\omega t), \tag{19}$$

where ω is the modulation frequency and V_{pp} the peak-to-peak amplitude of the sinusoidal bias. The modulation of charge density induces a variation of the transmission (ΔT) of the semiconducting layer with frequency ω, which can be retrieved with a lock-in amplifier "locked" at the modulation frequency. The signal is further normalized by the total transmission (T) when no V_{gs} is applied. Such normalization allows the CMS signal, *i.e.*, $\Delta T/T$, to be insensitive to the spectral dependence of the lamp emission, the detector sensitivity and the absorption of device components other than the semiconductor layer. The CMS spectrum is recorded by selecting the wavelength of the probing beam with a monochromator. A positive CMS signal is associated to increased transmittance ($\Delta T > 0$) due to the bleaching of optical transitions of the neutral molecules. A negative CMS signal relates to decreased transmittance ($\Delta T < 0$) in correspondence to new electronic transitions of the charged molecules linked to the formation of intra-gap polaronic states (**Figure 17b**).

The intensity of the CMS signal can be derived starting from the Lambert-Beer law for the absorption of a material:

$$A = \sigma_c n l, \tag{20}$$

where σ_c is the absorption cross section of the specific transition, l the optical path, and n the density of absorbing units per unit area, which can be considered proportional to the accumulated charges:

$$n \propto \frac{C_{diel} V_{gs}}{e} \tag{21}$$

Thus, combining the **Equations 19-20** and considering that in the CMS experiment the variation in transmission arises due to the difference of carrier density at $V_{gs} = V_{os} \pm V_{pp}/2$, the CMS signal can be written as:

$$\Delta T/T \propto \frac{C_{diel}\sigma_c}{e} |V_{pp}| \tag{22}$$

Hence, the CMS signal is proportional to the peak-to-peak voltage V_{pp} and should not depend on the applied offset potential V_{os}. Still, it is important to remind that **Equation 22** is valid

when the device is in full accumulation and the number of injected free carriers is proportional to the applied gate potential (like in an ideal transfer curve). Indeed, when the device is operated in subthreshold regime and at constant V_{pp}, $\Delta T/T$ might increase with V_{os} up to a certain value close to the V_{th} of the device. Furthermore, when the device is biased into full depletion, the experiment is essentially an electroabsorption measurement due to the modulation of the energy levels of the semiconductor by the external electric field (*i.e.,* Stark effect).

When compared to spectra of charged species measured by photoelectrochemisty, the major advantages of using a modulation technique like CMS are the highly enhanced sensitivity and the ability to detect charged states associated to free carriers only. Indeed, charges filling deep traps cannot follow the frequency modulation of the potential. For these reasons, CMS has proved extremely valuable in numerous works investigating charge transport in organic semiconductors[68,188,245–248] and SWCNT networks[121,249].

3.3. Charge Modulation Microscopy

By combining the CMS technique with a confocal microscope to focus a laser beam on the sample and with a hollow piezoelectric translation stage (**Figure 18a**), it is possible to acquire local CMS spectra with submicrometer resolution. Combining the spectral shape and intensity of local CMS spectra is useful to investigate the impact of local morphological properties of the semiconductor film on charge transport. Moreover, Charge Modulation Microscopy (CMM) maps can be obtained by scanning the active area at fixed wavelength. CMM maps can be correlated directly to the distribution of free charges in the device, as shown in **Figure 18b**, where a direct visualization of the charge density in the channel is demonstrated at varying lateral potential V_{ds}.[250,251] Moreover, the analysis of CMM maps acquired as a function of the polarization of the probing beam enables the identification of structural properties, such as the degree of orientational order and the alignment direction of the polymer backbones (**Figure 18c**), which are peculiar of the active region of the semiconducting layer (independently on the bulk morphological properties).[252]

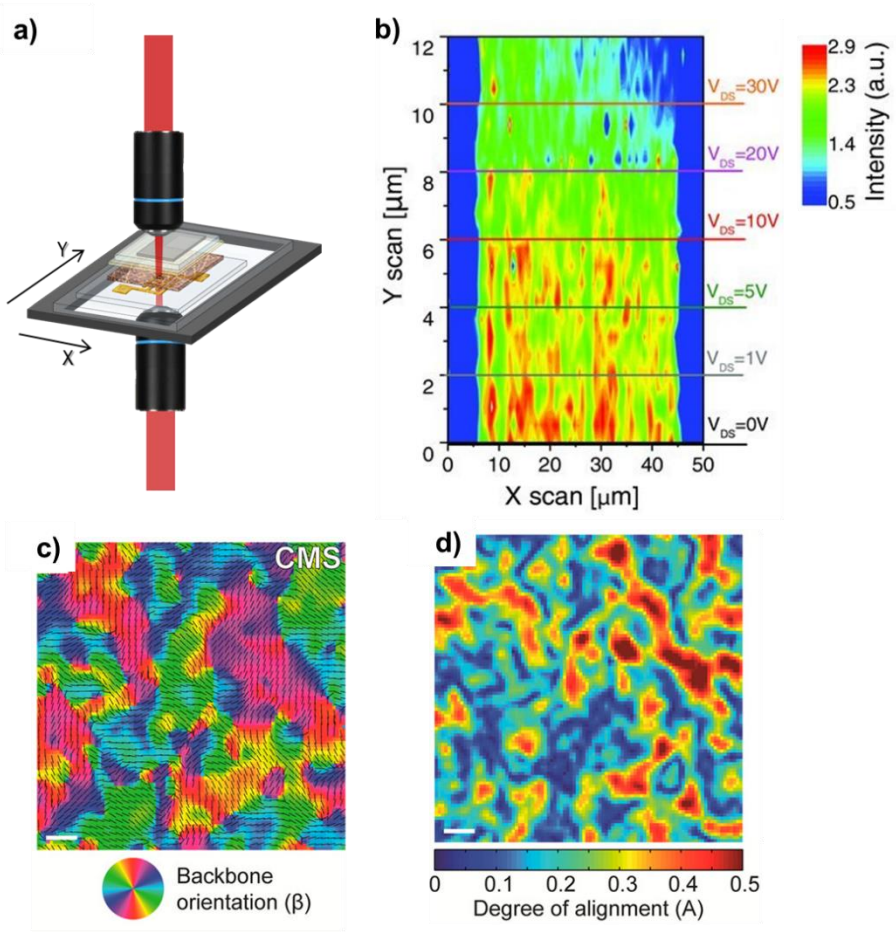

Figure 18. a) Schematic diagram of the confocal microscope and hollow piezoelectric translation stage used to perform Charge Modulation Microscopy (CMM). **b)** ΔT maps with 500 nm resolution on both the X and Y axis recorded across the channel of a PNDIT2-based OFET ($V_{gs} = 20 \pm 15\, sin(2\pi f t)$, $f = 320$ Hz, and V_{ds} is varied from 0 to 30 V). The signal corresponds to the bleaching peak of PNDIT2 at the used wavelength of 690 nm and is directly proportional to the density of charge carriers. Reprinted with permission from Sciascia C., *et al., Adv. Mater.* 2011 (Ref.[250]). **c-d)** Quantitative analysis of the local alignment of PNDIT2 polymeric backbones in a PNDIT2-based OFET performed by polarized CMM. Reprinted with permission from Martino N., *et al., ACS Nano* 2014, Copyright 2014 American Chemical Society (Ref.[252]).

4. Effects of Molecular Encapsulation on the Photophysical and Charge Transport Properties of a Naphthalene Diimide Bithiophene Copolymer

The content of this chapter is published in: [1]

S. Pecorario, J. Royakkers, A. D. Scaccabarozzi, F. Pallini, L. Beverina, H. Bronstein, M. Caironi, Effects of Molecular Encapsulation on the Photophysical and Charge Transport Properties of a Naphthalene Diimide Bithiophene Copolymer, *Chem. Mater.* 2022, *34*, 18, 8324–8335

Authors contributions:

S. Pecorario and J. Royakkers contributed equally to this work.

S. Pecorario developed the deposition of the polymer thin films, fabricated the organic field-effect transistors, performed the investigation of the optical, structural and charge transport properties, analyzed the GIWAXS measurements and leaded the writing of the manuscript.

J. Royakkers synthesized the polymers, performed NMR measurements, DFT calculations, and contributed to write the original manuscript.

Alberto D. Scaccabarozzi conducted the GIWAXS measurements and the related data analysis. F. Pallini and L. Beverina performed DSC and TGA measurements. H. Bronstein and M. Caironi conceived the work and supervised it. All the authors discussed the results and contributed to the revision of the manuscript.

CHEMISTRY OF MATERIALS

pubs.acs.org/cm

Article

Effects of Molecular Encapsulation on the Photophysical and Charge Transport Properties of a Naphthalene Diimide Bithiophene Copolymer

Stefano Pecorario,[▽] Jeroen Royakkers,[▽] Alberto D. Scaccabarozzi, Francesca Pallini, Luca Beverina, Hugo Bronstein,* and Mario Caironi*

Cite This: *Chem. Mater.* 2022, 34, 8324−8335

Read Online

ACCESS | Metrics & More | Article Recommendations | Supporting Information

ABSTRACT: Engineering the molecular structure of conjugated polymers is key to advancing the field of organic electronics. In this work, we synthesized a molecularly encapsulated version of the naphthalene diimide bithiophene copolymer PNDIT2, which is among the most popular high charge mobility organic semiconductors in n-type field-effect transistors and non-fullerene acceptors in organic photovoltaic blends. The encapsulating macrocycles shield the bithiophene units while leaving the naphthalene diimide units available for intermolecular interactions. With respect to PNDIT2, the encapsulated counterpart displays an increased backbone planarity. Molecular encapsulation prevents preaggregation of the polymer chains in common organic solvents, while it permits π-stacking in the solid state and promotes thin film crystallinity through an intermolecular-lock mechanism. Consequently, n-type semiconducting behavior is retained in field-effect transistors, although charge mobility is lower than in PNDIT2 due to the absence of the fibrillar microstructure that originates from preaggregation in solution. Hence, molecularly encapsulating conjugated polymers represent a promising chemical strategy to tune the molecular interaction in solution and the backbone conformation and to consequently control the nanomorphology of casted films without altering the electronic structure of the core polymer.

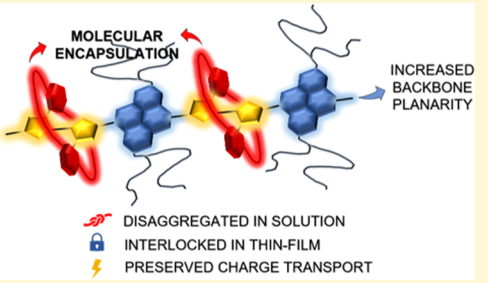

1. INTRODUCTION

Conjugated polymers are an important class of materials that have widespread applications, ranging from organic light-emitting diodes (OLEDs),[1] organic photovoltaics (OPVs),[2−6] and organic field-effect transistors (OFETs),[7,8] to energy storage,[9,10] neuromorphic devices,[11,12] and sensing.[13−15] Their great optoelectronic performance originates from their π-conjugated structure, which enables charge/exciton transport and the absorption or emission of energy. Narrow-band-gap materials are of particular interest given that they can capture a great proportion of incident light (e.g., in OPVs) or emit in biologically relevant optical windows (e.g., for imaging).[16] Owing to their π-conjugated backbone, polymeric chains have a high propensity to aggregate via $\pi-\pi$ stacking. Aggregation can be beneficial for certain thin film devices (by promoting intermolecular charge carrier hopping or charge delocalization),[8,17] while in some cases, it may be unfavorable for the photophysical properties (e.g., photoluminescence (PL)) in condensed phases.[16,18−24] The development of semiconducting polymers that preserve their conjugated backbone from aggregation, while offering more control over intermolecular interactions and processes, remains extremely challenging.

Molecular encapsulation is a powerful, synthetic concept that can be used to study polymer chains (or molecules) in isolation by shielding the conjugated backbone with protective macrocycles and preventing electronic cross-communication between the π-systems.[16,18−21,25−30] Noncovalently threaded polyarylene-based conjugated polymers,[31] along with covalently encapsulated thiophene/phenyl-based[32] and diketopyrrolopyrrole (DPP)-based conjugated polymers,[16] have demonstrated superior photoluminescence and OLED external quantum efficiencies compared to the reference polymers. Thus, even though molecularly encapsulated conjugated polymers display reduced charge transport properties by the suppression of intermolecular hopping, they can afford high-performance optoelectronic devices, an area that has been underexplored.

Naphthalene diimide (NDI)-based π-conjugated polymers have become one of the most heavily studied conjugated polymers for electron transport as they exhibit good electronic properties in relevant optoelectronic devices, such as high charge carrier mobility in n-type OFETs and as non-fullerene

Received: June 24, 2022
Revised: August 22, 2022
Published: September 5, 2022

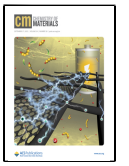

https://doi.org/10.1021/acs.chemmater.2c01894
Chem. Mater. 2022, 34, 8324−8335

Scheme 1. Overall Synthesis of Monomers DMP-BT-SnMe$_3$ and E-BT-SnMe$_3$

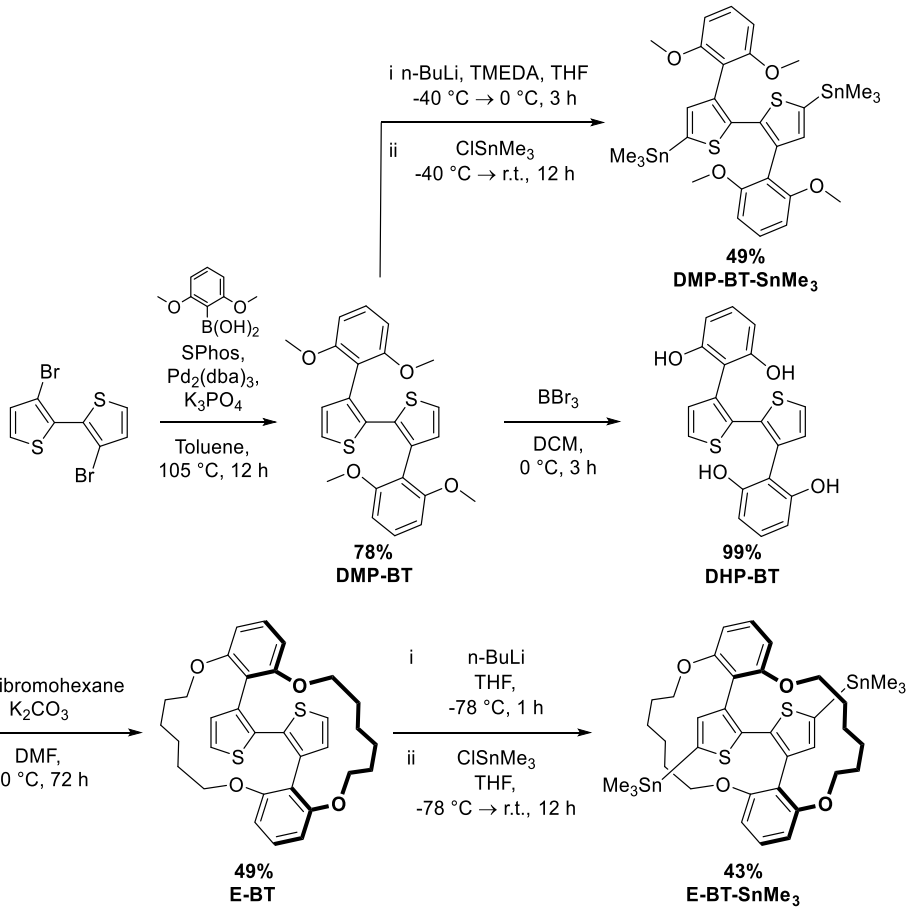

acceptors in OPV blends.[33−35] By preparing a molecularly encapsulated version of the most well-known polymer (i.e., PNDIT2 or otherwise known as P(NDI2OD-T2)) in this study, we can therefore probe the effect of molecular encapsulation on its photophysical and electron transporting properties. We recently reported a molecular encapsulated NDI−thiophene-based conjugated polymer where the naphthalene diimide portion of the molecule was encapsulated, leading to lower photoluminescence quantum yield with respect to the reference polymer.[19] Here, we present the molecular encapsulation of the bithiophene portion of PNDIT2, aiming to control the extent of intermolecular interactions by leaving the naphthalene diimide portion of the conjugated polymer available for intermolecular interactions. A thorough spectroscopic analysis of the absorption and photoluminescence reveals that the molecular encapsulation of PNDIT2 promotes a planarization of the polymer backbone and strongly controls the packing of the polymer both in solution and in thin film. Strikingly, the encapsulating rings covalently bonded to the thiophene units prevent the preaggregation of the polymer chains in common organic solvents. Still, they permit π-stacking between the NDI moieties in solid state, preserving charge transport within the polymer network (field-effect mobility of $\sim 10^{-3}$ cm^2 V^{-1} s^{-1}). Thus, we believe that these new molecularly encapsulated materials may hold the key to advancing optoelectronic devices, allowing control over their intermolecular interactions without compromising other optoelectronic properties.

2. RESULTS AND DISCUSSION

2.1. Synthesis. Molecularly encapsulated bithiophenes have been reported previously by Sugiyasu and coauthors.[30] In our work, we simplified the synthesis of encapsulated bithiophenes by eliminating the need for separate alkylation and metathesis steps. The synthesis of the bithiophene monomers is illustrated in Scheme 1. 3,3-Dibromo-2,2-bithiophene was reacted with 2,6-dimethoxyphenylboronic acid in a Suzuki−Miyaura cross-coupling reaction to afford DMP-BT in a 78% yield. Upon further stannylation (via lithiation), the DMP-BT-SnMe$_3$ monomer was generated in a 49% yield after purification. Next, DMP-BT was demethylated with BBr_3, encapsulated with 1,6-dibromohexane, and stannylated to form the final E-BT-SnMe$_3$ monomer. Lastly, the commercial 5,5′-bis(trimethylstannyl)-2,2′-bithiophene (BT-SnMe$_3$), bulky DMP-BT-SnMe$_3$, and encapsulated E-BT-SnMe$_3$ were each separately copolymerized with Br_2-NDI-2OD (based on previous literature procedures[7,36,37]) to generate PNDIT2, DMP-PNDIT2, and E-PNDIT2, respectively (Scheme 2). By comparing their photophysical, microstructural, and charge transport properties, we aim to elucidate the effect of the encapsulating rings in E-PNDIT2, with respect to both the reference PNDIT2 and the bulky DMP-PNDIT2 analogs.

All polymers were obtained with molecular weights M_n > 19 kDa and dissolved in common organic solvents. The physical properties are summarized in Table 1. The density functional theory (DFT)-optimized structures for the series of polymers are shown in Figure 1a. The calculated dihedral angles, highest

https://doi.org/10.1021/acs.chemmater.2c01894
Chem. Mater. 2022, 34, 8324−8335

Scheme 2. Overall Synthesis of Polymers PNDIT2, DMP-PNDIT2, and E-PNDIT2

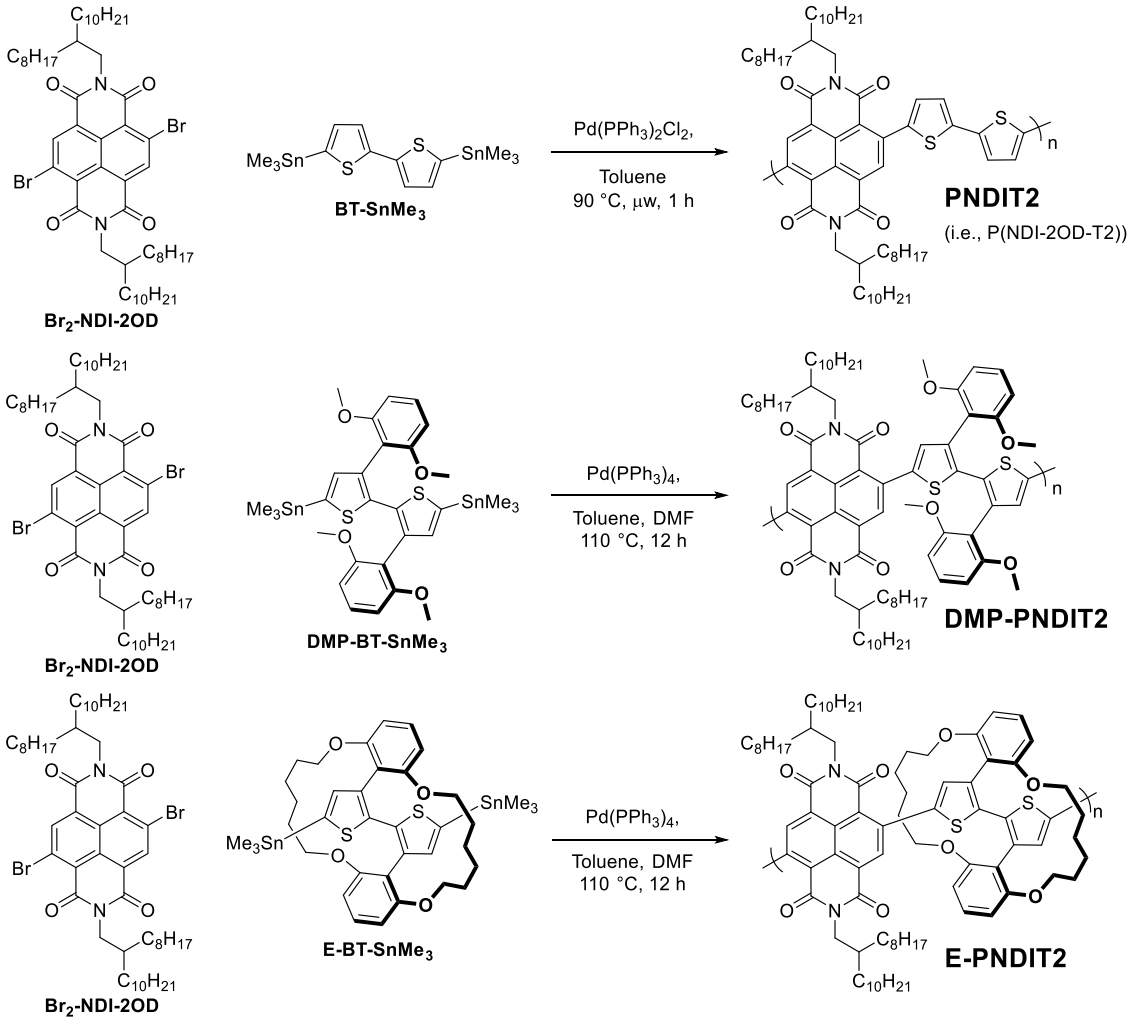

Table 1. Physical Properties of the NDI-Based Conjugated Polymers

polymer	M_n (kDa)[a]	M_w (kDa)[b]	dispersity[c]	$\bar{X}_n$[d]	$\bar{X}_w$[e]	E_g (eV)[f]
PNDIT2 (commercial)	35.3	63.5	1.80	36.8	66.3	1.98
PNDIT2 (synthesized)	45.0	136.1	3.02	47.0	142.1	1.98
DMP-PNDIT2	19.4	37.1	1.91	15.7	30.1	1.85
E-PNDIT2	19.9	46.3	2.33	14.9	34.6	1.80

[a]Number-average molecular weight. [b]Weight-average molecular weight. [c]M_w/M_n. [d]Number-average degree of polymerization (average number of monomer units per polymer chain). [e]Weight-average degree of polymerization. [f]HOMO−LUMO energy gap, calculated by DFT using B3LYP/6-31G*.

occupied molecular orbital (HOMO)/lowest unoccupied molecular orbital (LUMO) energetic levels, and spatial distributions are provided in the Supporting Information (SI).

The thermal properties of the newly synthesized DMP-PNDIT2 and E-PNDIT2 polymers were investigated by thermogravimetric analysis (TGA) and differential scanning calorimetry (DSC), and the results are reported in Figures S1 and S2, respectively. Both polymers are thermally stable up to 400 °C. Interestingly, the DSC measurement of E-PNDIT2 shows a broad exothermic peak between 140 and 250 °C in the first heating cycle. This feature, which is not observed for PNDIT2 and DMP-PNDIT2, is related to a crystallization phenomenon driven by interpenetration of the encapsulating rings, as revealed based on diffraction measurements in the next sections.

2.2. Optical Properties. The UV−vis absorption spectra of PNDIT2, DMP-PNDIT2, and E-PNDIT2 in solution (0.1 g/L in toluene) and in thin film are shown in Figure 1b,c, respectively. As for other donor−acceptor copolymers,[38−42] the absorption spectra are characterized by a high energy band ascribed to the $\pi-\pi^*$ transition and by a low-energy band corresponding to the intramolecular charge-transfer (CT) transition, which reflects a redistribution of the charge density along the polymer chain from the donor moiety (i.e., the T2 unit) to the acceptor one (i.e., the NDI unit). The spectral features of PNDIT2 have been established previously.[38,43,44] It is well known that PNDIT2 forms aggregates when dissolved in toluene and other common organic solvents, except for chloronaphthalene.[38,44,45] Such a preaggregation phenomenon is not due to the interchain stacking but arises from coiling within the single polymer chain, as proven by ultra-centrifugation measurements and by the robustness of the CT spectral features when comparing concentrated and diluted solutions.[38] Hence, the CT band in solution results from the convolution of semicrystalline and amorphous phases and its

https://doi.org/10.1021/acs.chemmater.2c01894
Chem. Mater. 2022, 34, 8324−8335

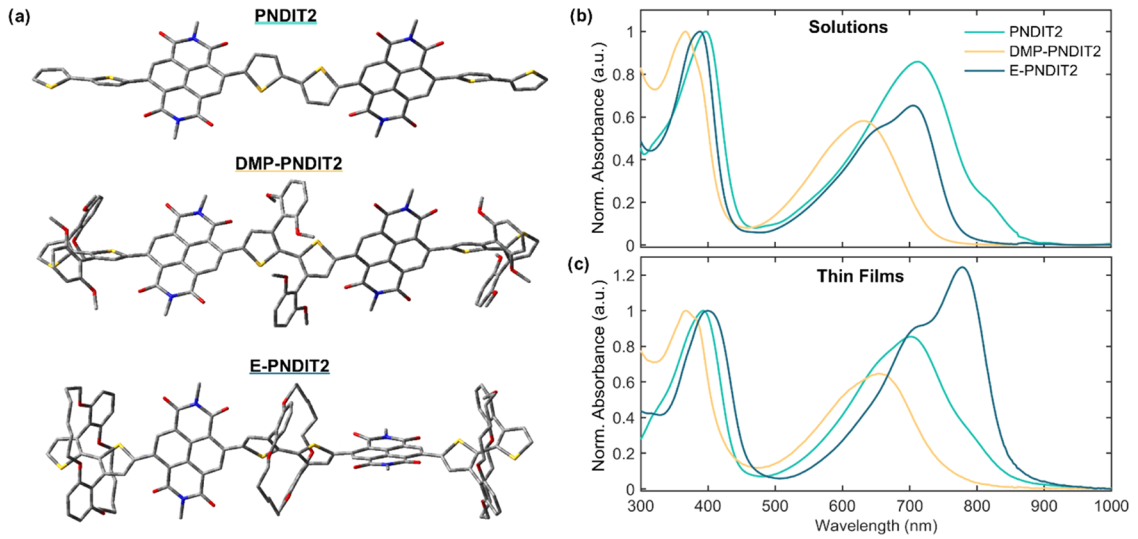

Figure 1. (a) DFT-optimized structures (B3LYP/6-31G*; details in the SI) of PNDIT2, DMP-PNDIT2, and E-PNDIT2 fragments. Side chains are not displayed. (b) UV−vis absorption spectra of PNDIT2, DMP-PNDIT2, and E-PNDIT2 dissolved in toluene at a concentration of 0.1 g/L and (c) in thin film. The spectra are normalized at the $\pi-\pi^*$ transition peaks. The unnormalized and normalized absorption spectra plotted as a function of the photon energy are reported in Figure S3.

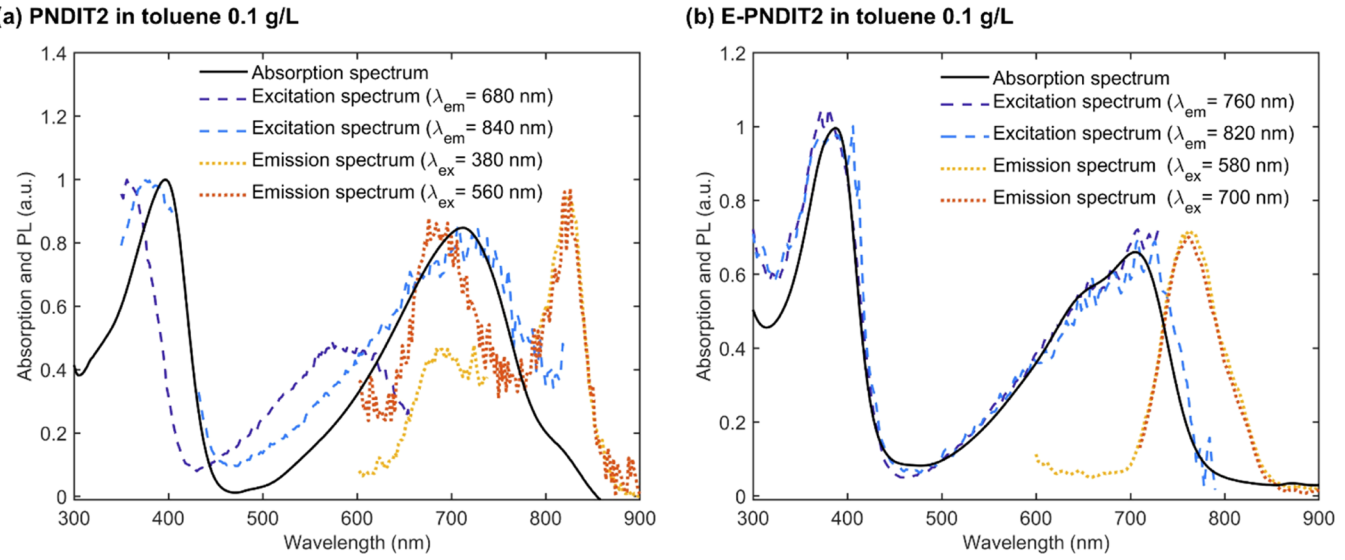

Figure 2. Photoluminescence emission and excitation spectra of (a) PNDIT2 and (b) E-PNDIT2. Both the polymers are dissolved in toluene at a concentration of 0.1 g/L.

fine structure varies depending on the solvent and temperature. More specifically, the peak at 710 nm and the shoulder at ∼800 nm correspond to two distinct aggregation states, while the broad band centered at ∼620 nm originates from unaggregated chains.[38,43] The solid-state spectrum of PNDIT2 resembles the one in solution, with only a slight remodulation of the contributions of the semicrystalline and amorphous phases to the CT band.

The absorption spectra of DMP-PNDIT2, in both solution and thin film, are blue-shifted with respect to PNDIT2 and present a broad CT band centered at 630 nm. Such features resemble the spectrum of unaggregated PNDIT2 in chloronaphthalene solution, in which preaggregation upon coiling of the polymer chain does not occur.[38] Therefore, the absorption features of DMP-PNDIT2 suggest that the dimethoxyphenyl groups likely prevent the preaggregation of the polymer chains in solution. Consequently, unaggregated polymer chains abound in solution and the amorphous phase prevails in solid state. In E-PNDIT2, the encapsulating rings enforce coplanarity within the bithiophene units, hence extending the effective conjugation length of the polymer backbone.[30,46,47] The solution absorption spectrum of E-PNDIT2 is therefore red-shifted with respect to that of DMP-PNDIT2. The $\pi-\pi^*$ transition peak is located at 388 nm with a shoulder at ∼374 nm, while the low-energy band, corresponding to the CT transition, exhibits an evident fine structure with a main peak at 706 nm and a secondary one at ∼650 nm. Similar to PNDIT2, such a structured CT band might suggest the presence of preaggregation in solution as the two peaks represent either an amorphous or aggregated phase. However, this study provides evidence that this is not the case. First, the relative intensity and wavelength of the absorption peaks are not concentration-dependent (Figure S4), meaning that interchain aggregation is not occurring. Second, the absorption spectrum is insensitive

https://doi.org/10.1021/acs.chemmater.2c01894
Chem. Mater. 2022, 34, 8324−8335

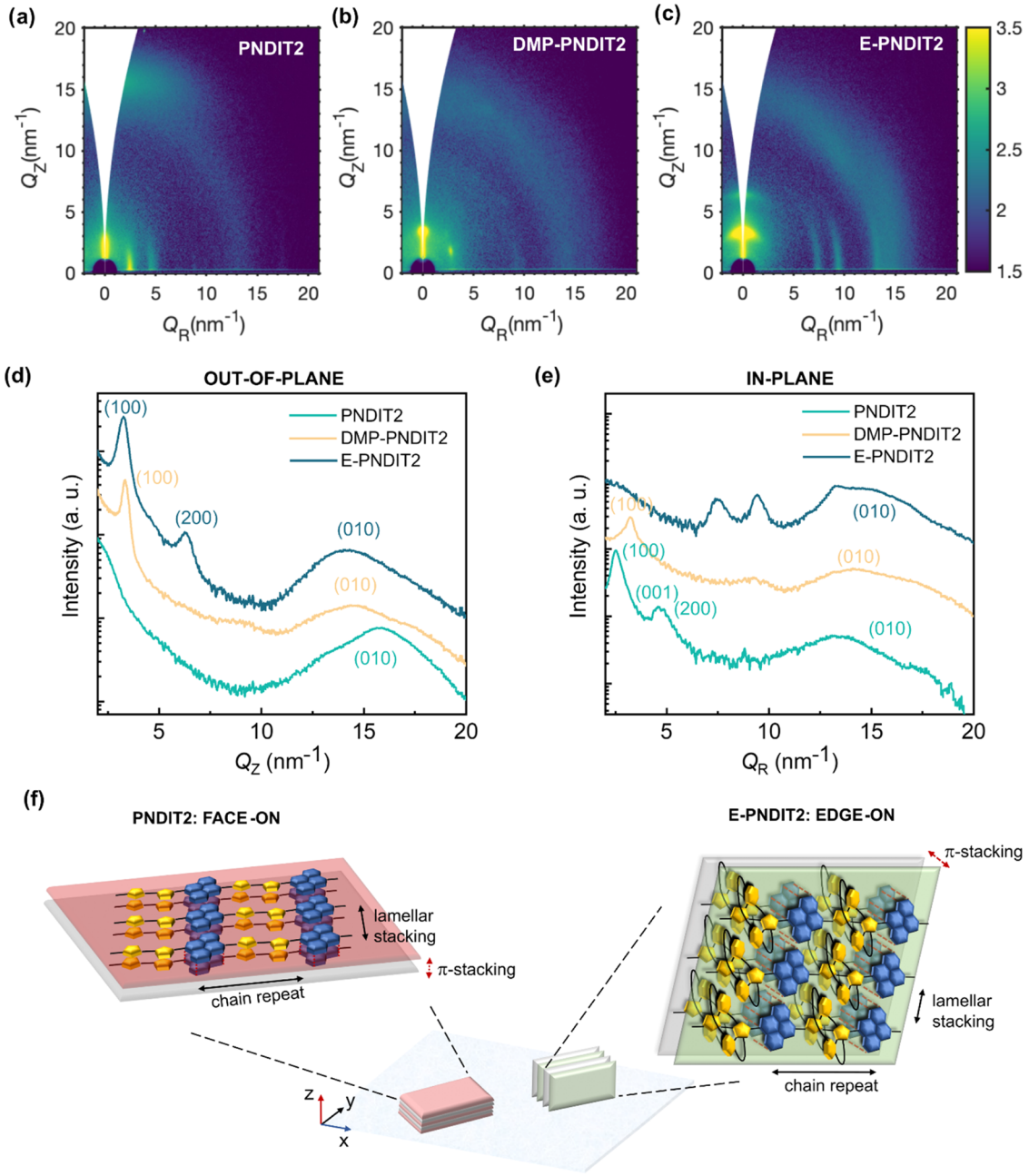

Figure 3. GIWAXS diffraction patterns of thin films of (a) PNDIT2, (b) DMP-PNDIT2, and (c) E-PNDIT2, which were deposited by off-center spin-coating from a toluene solution at a concentration of 5 g/L and annealed for 30 min at 180 °C. Diffractograms of the three polymers integrated along (d) the out-of-plane direction and (e) the in-plane direction. (f) Cartoon depicting the face-on texture characteristic of PNDIT2 films and the edge-on molecular stacking of E-PNDIT2 films.

to the solution temperature, as shown in Figure S5. This provides clear evidence that neither interchain nor intrachain aggregation (coiling) occurs in solution. In fact, the amount of aggregated states would diminish with increasing temperature and result in a change of the absorption spectrum, as observed for PNDIT2.[38]

Figure S6 displays how the absorption of E-PNDIT2 varies when dissolved in a different solvent. The main CT peak and the absorption tail show a clear bathochromic shift with increasing solvent polarity. Except for solvatochromism, there is no neat variation of the absorption features upon solvent change. This contrasts with the behavior of PNDIT2, whose aggregation is strongly affected by the solvent choice. It is worth mentioning that the polymer molecular weight plays an important role in determining the amount of intrachain aggregation at a given concentration, with longer chains (>80 repeating monomer units) being more prone to coiling.[44,45] Based on UV−vis spectroscopy, Nahid and coauthors[48] provided evidence that PNDIT2 with the number-average degree of polymerization $\overline{X}_n$ = 7 is completely unaggregated in dichlorobenzene solution. Instead, starting from $\overline{X}_n$ = 13.6, they observed a systematic increase in the coiling of the polymer chains with the molecular weight. In this work, DMP-PNDIT2 and E-PNDIT2 have respective values of $\overline{X}_n$ = 15.7 and 14.9 (Table 1), which is above the limit for aggregation in the case of PNDIT2.

https://doi.org/10.1021/acs.chemmater.2c01894
Chem. Mater. 2022, 34, 8324−8335

Table 2. Main Diffraction Peaks and Corresponding *d*-Spacing for PNDIT2, DMP-PNDIT2, and E-PNDIT2[a]

	(100) lamellar stacking		(001) backbone chain repeat		(010) π-stacking	
	Q (nm^{-1})	d_{100} (nm)	Q (nm^{-1})	d_{001} (nm)	Q (nm^{-1})	d_{010} (nm)
PNDIT2	2.55 (IP)	2.46 (IP)	4.57 (IP)	1.37 (IP)	15.8 (OOP)	0.39 (OOP)
DMP-PNDIT2	3.22 (IP)	1.95 (IP)	NA	NA	14.1 (IP)	0.45 (IP)
	3.34 (OOP)	1.88 (OOP)			14.6 (OOP)	0.43 (OOP)
E-PNDIT2	3.26 (OOP)	1.92 (OOP)	NA	NA	14.0 (IP)	0.45 (IP)

[a]The diffractions occurring predominantly in the in-plane (IP) and in the out-of-plane (OOP) directions are indicated within parentheses. Since there is not a preferential alignment detected in the DMP-PNDIT2 film, the values for both the in-plane and out-of-plane diffractions are reported.

Further evidence of the different behavior of PNDIT2 and E-PNDIT2 in solution is provided by photoluminescence spectroscopy. The emission and excitation spectra of PNDIT2 and E-PNDIT2 are reported in Figure 2a,b, respectively. In agreement with the findings by Steyrleuthner and coauthors,[38] the emission spectrum of PNDIT2 is characterized by two peaks at ∼680 and ∼825 nm, which are assigned to the emission of the unaggregated and aggregated phases, respectively. Indeed, the relative intensity of these two peaks depends on the excitation wavelength (orange and red curves). In addition, the excitation spectra corresponding to the emission at 680 and 840 nm (dark blue and light blue curves, respectively) do not resemble the absorption spectrum (black curve). In contrast, E-PNDIT2 displays only one emission peak at 760 nm with a shoulder at ∼820 nm, irrespective of the excitation wavelength (Figures 2b and S7). Moreover, the acquired excitation spectra in correspondence with the emission at 760 and 820 nm (dark blue and light blue curves, respectively) are identical and resemble the absorption spectrum (black curve), proving that the fine structure in the absorption and photoluminescence spectra of E-PNDIT2 should not be ascribed to different aggregates but to a vibronic progression of unaggregated polymer chains (further details are provided in Figure S8).[49−52] This has also been shown for other molecularly encapsulated polymers as molecular encapsulation can increase backbone rigidity and suppress rotational and vibrational degrees of freedom.[16] Both the photoluminescence spectra of E-PNDIT2 and PNDIT2 thin films (Figure S9) present a unique peak at ∼820 nm, suggesting that the aggregated phases of PNDIT2 and E-PNDIT2 share a similar electronic structure.

Finally, the absorption spectrum of E-PNDIT2 in thin film displays a rigid red shift with respect to the absorption in solution, which is due to the formation of ordered semicrystalline phases in the solid state. Such a rigid shift would not be possible if the polymer chains were already preaggregated in solution (like for PNDIT2) or if the chains form amorphous domains, as in the case of DMP-PNDIT2. All of these arguments lead to the conclusion that E-PNDIT2 chains are not aggregated in solution. Hence, the bathochromic shift with respect to DMP-PNDIT2 indicates a planarization of the polymer backbone, resulting in a more extended delocalization of the electron density within the polymer chain. In the solid state, ordered semicrystalline phases are forming, as discussed further below. The encapsulating rings of different polymer chains interact with each other, controlling both the intermolecular packing and the intramolecular electronic structure. Indeed, the planarization effect induced by the encapsulating rings becomes even stronger upon aggregation in thin film, likely due to an intermolecular-lock mechanism.[21,53] Thus, a comprehensive rigidification of the backbone occurs as a consequence of the planarization of both the T−T and T−NDI torsional angles. This is testified by the rigid red shift of the absorption spectrum from solution to thin film and by an increase in the intensity of the CT band with reference to the $\pi-\pi^*$ peak.

2.3. Thin Film Microstructure. Several studies highlighted the impact of PNDIT2 preaggregation in solution on the microstructural properties of thin films formed upon solution casting.[43,54−57] On the one hand, preaggregation is a key requirement to achieve thin films with improved energetic order and with a preferential alignment of the polymer chains, resulting in superior charge transport properties.[55,56,58,59] On the other hand, the formation of crystalline clusters can be detrimental for applications requiring an interpenetrating network of different materials, as in the case of donor and acceptor polymers in bulk heterojunction solar cells[44,60,61] or of doped blends based on organic semiconductors for thermoelectric applications.[62,63]

To investigate the effect of molecular encapsulation on the microstructure, we performed grazing-incidence wide-angle X-ray scattering (GIWAXS) on films of PNDIT2, DMP-PNDIT2, and E-PNDIT2. All of the films were spin-casted from a toluene solution at a concentration of 5 g/L and then annealed at 180 °C for 30 min. The bidimensional diffraction patterns of the three polymers are displayed in Figure 3a−c. The one-dimensional profiles along the out-of-plane (OOP) and in-plane (IP) scattering directions are reported in Figure 3d,e, respectively. The diffraction pattern of PNDIT2 (Figure 3a) is in very good agreement with previous reports.[48,64] The film presents a preferential face-on packing, as schematically depicted in the cartoon in Figure 3f. Indeed, the (100) and (001) peaks, corresponding to the lamellar stacking and to the chain backbone repeat, are oriented in the in-plane direction, while the broad (010) peak associated with the π-stacking of the NDI moieties is oriented in the out-of-plane direction. The diffraction pattern of DMP-PNDIT2 indicates a semicrystalline microstructure (Figure 3b). However, compared to PNDIT2, the scattering features are less sharp, meaning that the degree of crystallinity of the film is lower. Strikingly, the pattern of E-PNDIT2 presents sharp and oriented diffractions, implying higher semicrystallinity with respect to DMP-PNDIT2 and revealing a preferential edge-on orientation, as illustrated in the cartoon in Figure 3f.

A complete assignment of the diffraction features of DMP-PNDIT2 and E-PNDIT2 would require resolving their single-crystal structure. However, a close comparison with PNDIT2 offers the possibility to assign most of the diffraction peaks (Figure S10). The Q vectors and interplanar spacings corresponding to the (100), (001), and (010) diffraction peaks of the thin films of the three polymers are listed in Table 2. DMP-PNDIT2 and E-PNDIT2 display a similar lamellar stacking distance (d_{100} ∼ 1.92 nm), which is shorter than for PNDIT2 (d_{100} ∼ 2.5 nm): we propose an explanation later on

https://doi.org/10.1021/acs.chemmater.2c01894
Chem. Mater. 2022, 34, 8324−8335

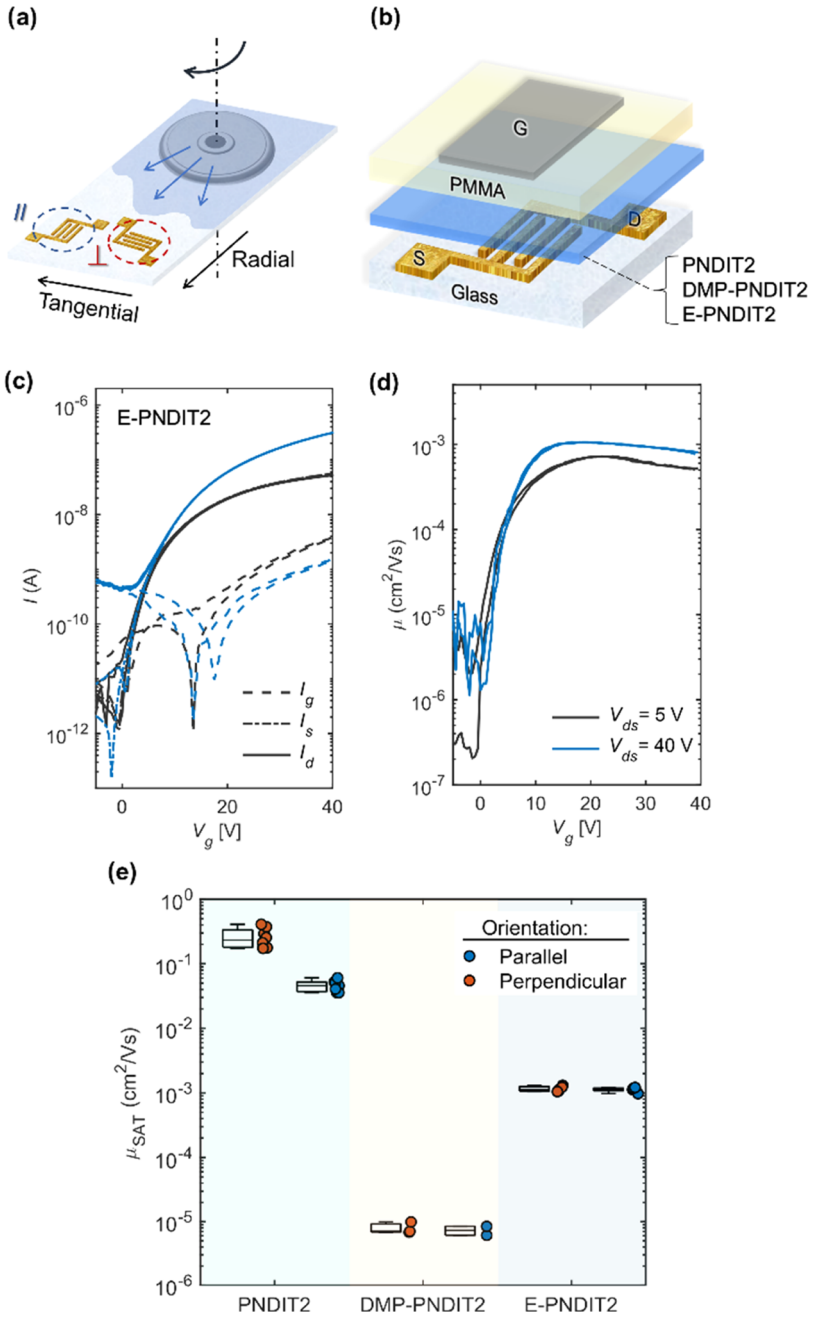

Figure 4. (a) Scheme of the deposition of the semiconductor layer (PNDIT2, DMP-PNDIT2, and E-PNDIT2) by off-center spin-coating. Glass substrates are prepatterned with gold interdigitated source and drain contacts, oriented both perpendicularly (⊥) and parallelly (∥) to the alignment direction. (b) TGBC transistor structure composed of a glass substrate, a gold source, drain contacts, a semiconducting film, a PMMA dielectric layer, and an aluminum gate electrode. (c) Transfer curves of an optimized device with the E-PNDIT2 active layer in linear and saturation regimes (in black and blue, respectively) and (d) plot of the related gate voltage-dependent mobility. The device has a channel length L = 10 μm and a channel width W = 2 mm. (e) Box-plot comparing the mobility values in the saturation regime (extracted from the linear fit of $I_{ds}^{0.5}$ in the range V_g = 20−30 V; details are provided in Figure S19) of transistors based on PNDIT2, DMP-PNDIT2, and E-PNDIT2. The values are grouped accordingly to the parallel/perpendicular orientation of the contacts.

in the paragraph. Furthermore, the presence of a second-order diffraction of the lamellar stacking in the E-PNDIT2 pattern ($Q \sim 6.50$ nm^{-1}) implies a high crystallinity. The (001) scattering peak, which corresponds to the chain backbone repeat length, is not detectable in the DMP-PNDIT2 and E-PNDIT2 diffractograms. However, the chain backbone repeat length is not expected to vary with the addition of the dimethoxyphenyl groups, or of the encapsulating rings, and can be assumed equal to 1.37 nm as for PNDIT2. The π-stacking distance has a large variability, hence disorder, for all polymers, as indicated by the wide diffraction at high Q-values. For E-PNDIT2 and DMP-PNDIT2, the average d-spacing corresponding to the π-stacking distance ($d_{010} \sim 0.45$ nm) is longer than for PNDIT2 ($d_{010} \sim 0.39$ nm). This is a clear consequence of the steric hindrance provided by the dimethoxyphenyl groups in DMP-PNDIT2 and by the encapsulating rings in E-PNDIT2. Remarkably, considering the axial symmetry of the encapsulating ring with a diameter of

https://doi.org/10.1021/acs.chemmater.2c01894
Chem. Mater. 2022, 34, 8324−8335

about 1 nm, it follows from simple geometrical considerations that a π-stacking distance of about 0.45 nm between the NDI moieties implies a close interpenetration of the encapsulating rings, as schematized in Figure 3f. This is further corroborated by the appearance of three sharp in-plane diffractions (Q = 7.46, 9.22, 13.30 nm^{-1}), which do not find correspondence in the PNDIT2 diffractogram, and are tentatively assigned to interlocking of the encapsulating rings of adjacent polymer chains. Overall, molecular encapsulation promotes a significant thin film crystallinity, induces a preferential edge-on orientation, and controls the packing of the E-PNDIT2 chains. On the one hand, it regulates the interchain distances in the polymer aggregates, making the lamellar stacking distance shorter and the π-stacking distance longer than in PNDIT2. On the other hand, the interlocking rings support a planarization of the polymer backbones with respect to unaggregated chains, which is also confirmed by the rigid red shift of the absorption spectrum in thin film with respect to solution. Interestingly, an increased structural order of E-PNDIT2 is achieved upon thermal annealing. Indeed, nonannealed films show GIWAXS patterns exhibiting a few, low-intensity, and diffuse diffractions, suggesting a low degree of structural order, in contrast with the sharper diffraction of samples annealed at 180 °C that we described in Figure 3. GIWAXS measurements performed in situ during annealing of the E-PNDIT2 film provide insights into the development of such a microstructure (Figures S11 and S12). The low ordered microstructure is kinetically quenched during spin-casting. Upon heating the as-cast film at temperatures >150 °C, its microstructure undergoes a crystallization, achieving a higher degree of structural order. Further annealing at higher temperatures (up to 300 °C) does not lead to other structural changes.

2.4. Charge Transport. To investigate the effect of molecular encapsulation on charge transport, we fabricated organic field-effect transistors (OFETs) in a top-gate bottom-contact (TGBC) architecture, employing PNDIT2, DMP-PNDIT2, and E-PNDIT2 as the active layer. Source and drain interdigitated contacts were defined by photolithography on glass substrates, followed by a thermal evaporation of 30 nm of gold with a 2 nm chromium adhesion layer. The semiconducting layers, either PNDIT2, DMP-PNDIT2, or E-PNDIT2, were deposited by off-center spin-coating with the same conditions adopted for the preparation of the films investigated by GIWAXS. As a result of the applied centrifugal force, this deposition technique induces a preferential alignment of PNDIT2 microfibrils and a corresponding charge transport anisotropy.[56,65] It is therefore interesting to evaluate if any transport anisotropy can derive from aligned structures also for DMP-PNDIT2 and E-PNDIT2. To this extent, contacts with both parallel and perpendicular orientations with respect to the radial spinning direction were employed to assess the eventual charge transport anisotropy typical of aligned textures (Figure 4a). A 500 nm film of poly(methyl methacrylate) (PMMA) was spin-coated to obtain a dielectric layer, which notoriously provides an interface with PNDIT2 suitable for charge transport.[66,67] Finally, aluminum gate electrodes were thermally evaporated to complete the TGBC transistor structure (Figure 4b).

To compare the electrical transport properties of the three polymers in films with optimized morphology, we performed preliminary tests using different solvents and deposition parameters. The UV−vis absorption spectra of films of E-PNDIT2 deposited from various organic solvents at a concentration of 5 g/L are shown in Figure S13. No differences are observed in the normalized absorption spectra, implying identical electronic transitions in thin film and thus a common intramolecular structure and intermolecular arrangement of the polymer chains. Instead, the variation of the absolute absorbance is ascribed to a different thickness and coverage of the films over the 2 × 2 cm^2 substrate. The films deposited from toluene displayed the best uniformity. Moreover, toluene is one of the most employed solvents to deposit films of PNDIT2 with high charge transport performance due to the property of promoting a high level of preaggregation in solution.[55,57] Hence, we compare here transistors with the three polymers deposited by off-center spin-coating from a 5 g/L toluene solution. The films were annealed for 30 min at 180 °C immediately after the deposition, which has a significant impact on the microstructure of E-PNDIT2, as confirmed by in situ GIWAXS measurements (Figures S11 and S12), UV−vis spectroscopy (Figure S14), and field-effect mobility evaluation (Figure S15). Figure 4c displays the transfer curves in the linear (V_{ds} = 5 V, in black) and saturation regimes (V_{ds} = 40 V, in blue) of a representative device based on E-PNDIT2. The encapsulated polymer shows a clear n-type field-effect behavior, with an $I_{on}/I_{off} \sim 10^4$ and a field-effect mobility $\mu \sim 10^{-3}$ cm^2 V^{-1} s^{-1}, which is weakly dependent on the gate voltage above threshold (Figure 4d). No differences in charge transport performance were observed in transistors with contacts oriented parallel or perpendicularly to the centrifugal force induced by off-center spin-coating. As opposed to PNDIT2 (Figure S16), the films do not show anisotropic charge transport. Such evidence suggests the absence of oriented supramolecular assemblies for E-PNDIT2. The surface of E-PNDIT2, imaged by atomic force microscopy (AFM) (Figure S17), consistently presents a subnanometric roughness, and no structuration of the polymer fibrils typically observed in PNDIT2 films can be detected within the resolution of the instrument. The transfer characteristics for representative devices of PNDIT2, DMP-PNDIT2, and E-PNDIT2 are shown in Figure S18, along with the plots of the mobility as a function of the gate voltage.

Figure 4e collects the distribution of field-effect mobility in the saturation regime from devices based on the three polymers grouped depending on the orientation of the contacts. The three polymers present significantly different field-effect mobilities. DMP-PNDIT2 provides the worst charge transport performance, with isotropic and very poor field-effect mobility on the order of 10^{-5} cm^2 V^{-1} s^{-1}. According to the previous literature, PNDIT2 shows the highest field-effect mobility and a clear charge transport anisotropy due to the fibrillar alignment induced by off-center spin-coating, which is fundamental to form effective charge percolation paths.[55,59] Transistors with contacts oriented perpendicularly to the alignment direction offer charge mobility values >10^{-1} cm^2 V^{-1} s^{-1}. The performance of the transistors based on E-PNDIT2 stands halfway between those of PNDIT2 and DMP-PNDIT2, with an isotropic mobility of about 10^{-3} cm^2 V^{-1} s^{-1}. Importantly, molecular encapsulation still allows π-stacking between different polymer backbones but with a longer d-spacing than in PNDIT2, which is likely associated with a reduced charge-transfer rate. Together with the absence of a directional supramolecular order, as found by AFM, such structural considerations explain the reduced charge carrier mobility in E-PNDIT2 with respect to PNDIT2.

https://doi.org/10.1021/acs.chemmater.2c01894
Chem. Mater. 2022, 34, 8324−8335

3. CONCLUSIONS

This article reports the synthesis of naphthalene diimide bithiophene-based conjugated polymers and studies the effect of molecular encapsulation (around the bithiophene unit) on the photophysical and charge transport properties of the polymer. The molecular encapsulation prevents preaggregation of the polymer chains in all employed organic solvents (effect on the intrachain packing, i.e., coiling). The electronic structure of the core polymer is mostly preserved, with a positive effect on the backbone conjugation ascribed to increased planarization of the polymer backbone. The encapsulating rings influence the solid-state packing, changing the interchain distances and the molecular orientation in thin films. Semicrystalline order is likely achieved through interdigitating macrocycles. Remarkably, even though the associated *d*-spacing for E-PNDIT2 is longer than for PNDIT2, the π-stacking between NDI moieties is preserved, affording a decent field-effect mobility of $\sim 10^{-3}$ cm^2 V^{-1} s^{-1}. Therefore, molecular encapsulation emerges as a general approach to tune the nanomorphology of casted films, without altering the electronic structure of the core polymer and still allowing charge transport properties in thin films. Supramolecular fibrillary microstructures, which are essential to form effective percolative paths for charge transport, are not formed in the absence of aggregated chains in solution. Still, avoiding preaggregation in solution holds promise for improving the intermixing of multiple components in a common solvent. This feature is strongly desirable in blends of donor and acceptor organic semiconductors for bulk heterojunction solar cells and to reach effective intercalation of molecular dopants within a polymeric matrix for organic thermoelectrics.

4. EXPERIMENTAL SECTION

4.1. Synthesis. A detailed description of the synthetic process of the naphthalene diimide bithiophene copolymers, and of their characterization, is reported in the Supporting Information.

4.2. Thin Film Deposition. PNDIT2, DMP-PNDIT2, and E-PNDIT2 were dissolved in toluene (Sigma-Aldrich) at a concentration of 5 g/L unless stated otherwise in the text. The thin films of the three polymers were deposited in a nitrogen glovebox by off-center spin-coating onto glass substrates (low alkali 1737F Corning glasses, purchased from Präzisions Glas & Optik GmbH). A double-step process was adopted (first step: 500 rpm/s for 10 s with acceleration 50 rpm/s; second step: 1000 rpm/s for 60 s with acceleration 2000 rpm/s). The deposition was followed by annealing at 180 °C for 30 min. The obtained films had a thickness of 40 ± 10 nm.

4.3. Optical Measurements. The absorption spectra were measured with a PerkinElmer Lambda 1050 UV/vis/near-infrared (NIR) spectrometer. The photoluminescence (PL) spectra and the excitation profiles were collected with a iHR320Horiba NanoLog Fluorometer. All absorption and PL spectra were collected in air and at room temperature unless stated otherwise.

4.4. Film Topography and Thickness. The film thickness was measured with a KLA Tencor P-17 Surface Profiler. The surface topography of the E-PNDIT2 thin film was imaged with an Agilent 5500 atomic force microscope operating in a tapping mode.

4.5. Grazing-Incidence Wide-Angle X-ray Scattering (GIWAXS). GIWAXS measurements were performed at the noncrystalline diffraction beamline (BL11-NCD-Sweet) at ALBA Synchrotron Radiation Facility in Barcelona (Spain). A detector (Rayonix, WAXS LX255-HS) with a resolution of 1920 × 5760 pixels was used to collect the scattering signals. The sample holder position was calibrated with the chromium oxide (Cr_2O_3) standard. The incident energy was 12.4 eV, and the sample-to-detector distance was set at 216.5 mm. The angle of incidence α_i was 0.12°, and the exposure time was 1 s. 2D-GIWAXS patterns were corrected as a function of the components of the scattering vector with a MATLAB script developed by Aurora Nogales and Edgar Gutiérrez.[68] Thin films were cast onto highly doped silicon substrates following the same processing route used for the device fabrication.

4.6. OFET Fabrication and Electrical Characterization. The OFETs were fabricated with a bottom-contact top-gate architecture onto glass substrates (low alkali 1737F Corning glasses). Bottom source and drain interdigitated electrodes were defined by standard photolithography and deposited by thermal evaporation of a 30 nm thick Au layer with a 3 nm thick Cr adhesion layer. The semiconducting layer (either PNDIT2, DMP-PNDIT2, or E-PNDIT2) was deposited by off-center spin-coating in a nitrogen glovebox according to the procedure described above. Successively, a 500 nm thick dielectric layer of PMMA (M_w = 120 000, purchased from Sigma-Aldrich, dissolved in *n*-butyl acetate at a concentration of 80 g/L) was deposited by on-center spin-coating (1300 rpm for 60 s with 1000 rpm/s acceleration) and then baked at 80 °C for ∼1 h. Finally, the top-gate electrode was obtained by thermal evaporation of a 40 nm Al layer patterned using a shadow mask. OFET transfer and output electrical characteristics were measured with a semiconductor parameter analyzer (Agilent B1500A) in a nitrogen glovebox on a Wentworth Laboratories probe station. The samples were further annealed at 120 °C overnight before measuring the electrical characteristics. The mobility was extracted from the linear fit of $I_{ds}^{0.5}$ from the transfer curves in the saturation regime (in the range V_g = 20−30 V; details are provided in Figure S19).

■ ASSOCIATED CONTENT

Supporting Information

The Supporting Information is available free of charge at https://pubs.acs.org/doi/10.1021/acs.chemmater.2c01894.

Detailed information on the synthesis of all compounds, NMR spectra, DFT-computed dihedral angles and HOMO/LUMO levels, and additional experimental details (PDF)

■ AUTHOR INFORMATION

Corresponding Authors

Hugo Bronstein − *Department of Chemistry, University of Cambridge, Cambridge CB2 1EW, U.K.; Cavendish Laboratory, University of Cambridge, Cambridge CB3 0HE, U.K.;* orcid.org/0000-0003-0293-8775; Email: hab60@cam.ac.uk

Mario Caironi − *Center for Nano Science and Technology@PoliMi, Istituto Italiano di Tecnologia, Milan 20133, Italy;* orcid.org/0000-0002-0442-4439; Email: mario.caironi@iit.it

Authors

Stefano Pecorario − *Center for Nano Science and Technology@PoliMi, Istituto Italiano di Tecnologia, Milan 20133, Italy; Department of Energy, Micro and Nanostructured Materials Laboratory—NanoLab, Politecnico di Milano, Milano 20133, Italy;* orcid.org/0000-0001-9217-550X

Jeroen Royakkers − *Sensor Engineering Department, Faculty of Science and Engineering, Maastricht University, 6200 MD Maastricht, The Netherlands; Department of Chemistry, University of Cambridge, Cambridge CB2 1EW, U.K.; Cavendish Laboratory, University of Cambridge, Cambridge CB3 0HE, U.K.;* orcid.org/0000-0002-6827-0969

Alberto D. Scaccabarozzi − *Center for Nano Science and Technology@PoliMi, Istituto Italiano di Tecnologia, Milan 20133, Italy*

Francesca Pallini − *Department of Materials Science, Università di Milano-Bicocca, 20125 Milan, Italy*
Luca Beverina − *Department of Materials Science, Università di Milano-Bicocca, 20125 Milan, Italy;* orcid.org/0000-0002-6450-545X

Complete contact information is available at: https://pubs.acs.org/10.1021/acs.chemmater.2c01894

Author Contributions

[▽]S.P. and J.R. contributed equally to this work. H.B. and M.C. planned the study and supervised it. J.R. synthesized the polymers and performed NMR measurements and DFT calculations. S.P. fabricated the polymer thin films and devices and performed the investigation of the optical, structural, and charge transport properties. A.D.S. conducted the GIWAXS measurements and data analysis. F.P. and L.B. performed DSC and TGA measurements. The manuscript was written through contributions of all authors. All authors have given approval to the final version of the manuscript.

Funding

M.C. and A.D.S. acknowledge the European Research Council (ERC) project funded under the European Union's Horizon 2020 research and innovation programme "ELFO", Grant Agreement no. 864299. J.R. and H.B. gratefully acknowledge the Winton Programme for the Physics of Sustainability and EPSRC grant: EP/S003126/1.

Notes

The authors declare no competing financial interest.

■ ACKNOWLEDGMENTS

GIWAXS experiments were performed at BL11-NCD-SWEET beamline at ALBA Synchrotron (Spain) with the collaboration of ALBA staff. Photolithography for the fabrication of the OFET contacts was carried out at Polifab, the Micro- and Nanotechnology Center of the Politecnico di Milano. The authors acknowledge Edgar Gutiérrez-Fernández for his help with GIWAXS measurements. S.P. wishes to thank Alessandro Luzio for insightful discussion and Arianna Magni for advice on the photoluminescence measurements.

■ REFERENCES

(1) Burroughes, J. H.; Bradley, D. D. C.; Brown, A. R.; Marks, R. N.; Mackay, K.; Friend, R. H.; Burns, P. L.; Holmes, A. B. Light-Emitting Diodes Based on Conjugated Polymers. *Nature* **1990**, *347*, 539−541.
(2) Günes, S.; Neugebauer, H.; Sariciftci, N. S. Conjugated Polymer-Based Organic Solar Cells. *Chem. Rev.* **2007**, *107*, 1324−1338.
(3) Facchetti, A. π-Conjugated Polymers for Organic Electronics and Photovoltaic Cell Applications. *Chem. Mater.* **2011**, *23*, 733−758.
(4) Liu, C.; Wang, K.; Gong, X.; Heeger, A. J. Low Bandgap Semiconducting Polymers for Polymeric Photovoltaics. *Chem. Soc. Rev.* **2016**, 4825−4846.
(5) Guo, X.; Baumgarten, M.; Müllen, K. Designing π-Conjugated Polymers for Organic Electronics. *Prog. Polym. Sci.* **2013**, 1832−1908.
(6) Xu, X.; Li, Z.; Zhang, W.; Meng, X.; Zou, X.; Di Carlo Rasi, D.; Ma, W.; Yartsev, A.; Andersson, M. R.; Janssen, R. A. J.; Wang, E. 8.0% Efficient All-Polymer Solar Cells with High Photovoltage of 1.1 V and Internal Quantum Efficiency near Unity. *Adv. Energy Mater.* **2018**, *8*, No. 1700908.
(7) Yan, H.; Chen, Z.; Zheng, Y.; Newman, C.; Quinn, J. R.; Dötz, F.; Kastler, M.; Facchetti, A. A High-Mobility Electron-Transporting Polymer for Printed Transistors. *Nature* **2009**, *457*, 679−686.
(8) Sirringhaus, H.; Brown, P. J.; Friend, R. H.; Nielsen, M. M.; Bechgaard, K.; Langeveld-Voss, B. M. W.; Spiering, A. J. H.; Janssen, R. A. J.; Meijer, E. W.; Herwig, P.; De Leeuw, D. M. Two-Dimensional Charge Transport in Self-Organized, High-Mobility Conjugated Polymers. *Nature* **1999**, *401*, 685−688.
(9) Novák, P.; Müller, K.; Santhanam, K. S. V.; Haas, O. Electrochemically Active Polymers for Rechargeable Batteries. *Chem. Rev.* **1997**, *97*, 207−281.
(10) Mike, J. F.; Lutkenhaus, J. L. Recent Advances in Conjugated Polymer Energy Storage. *J. Polym. Sci., Part B: Polym. Phys.* **2013**, 468−480.
(11) Van De Burgt, Y.; Melianas, A.; Keene, S. T.; Malliaras, G.; Salleo, A. Organic Electronics for Neuromorphic Computing. *Nat. Electron.* **2018**, *1*, 386−397.
(12) Yu, Y.; Ma, Q.; Ling, H.; Li, W.; Ju, R.; Bian, L.; Shi, N.; Qian, Y.; Yi, M.; Xie, L.; Huang, W. Small-Molecule-Based Organic Field-Effect Transistor for Nonvolatile Memory and Artificial Synapse. *Adv. Funct. Mater.* **2019**, *29*, No. 1904602.
(13) Ohayon, D.; Nikiforidis, G.; Savva, A.; Giugni, A.; Wustoni, S.; Palanisamy, T.; Chen, X.; Maria, I. P.; Di Fabrizio, E.; Costa, P. M. F. J.; McCulloch, I.; Inal, S. Biofuel Powered Glucose Detection in Bodily Fluids with an N-Type Conjugated Polymer. *Nat. Mater.* **2020**, *19*, 456−463.
(14) Inal, S.; Rivnay, J.; Suiu, A. O.; Malliaras, G. G.; McCulloch, I. Conjugated Polymers in Bioelectronics. *Acc. Chem. Res.* **2018**, *51*, 1368−1376.
(15) McQuade, D. T.; Pullen, A. E.; Swager, T. M. Conjugated Polymer-Based Chemical Sensors. *Chem. Rev.* **2000**, *100*, 2537−2574.
(16) Leventis, A.; Royakkers, J.; Rapidis, A. G.; Goodeal, N.; Corpinot, M. K.; Frost, J. M.; Bučar, D.-K. K.; Blunt, M. O.; Cacialli, F.; Bronstein, H. Highly Luminescent Encapsulated Narrow Bandgap Polymers Based on Diketopyrrolopyrrole. *J. Am. Chem. Soc.* **2018**, *140*, 1622−1626.
(17) Fratini, S.; Nikolka, M.; Salleo, A.; Schweicher, G.; Sirringhaus, H. Charge Transport in High-Mobility Conjugated Polymers and Molecular Semiconductors. *Nat. Mater.* **2020**, *19*, 491−502.
(18) Royakkers, J.; Bronstein, H. Macrocyclic Encapsulated Conjugated Polymers. *Macromolecules* **2021**, 1083−1094.
(19) Royakkers, J.; Guo, K.; Toolan, D. T. W.; Feng, L. W.; Minotto, A.; Congrave, D. G.; Danowska, M.; Zeng, W.; Bond, A. D.; Al-Hashimi, M.; Marks, T. J.; Facchetti, A.; Cacialli, F.; Bronstein, H. Molecular Encapsulation of Naphthalene Diimide (NDI) Based π-Conjugated Polymers: A Tool for Understanding Photoluminescence. *Angew. Chem., Int. Ed.* **2021**, *60*, 25005−25012.
(20) Royakkers, J.; Minotto, A.; Congrave, D. G.; Zeng, W.; Hassan, A.; Leventis, A.; Cacialli, F.; Bronstein, H. Suppressing Solid-State Quenching in Red-Emitting Conjugated Polymers. *Chem. Mater.* **2020**, *32*, 10140−10145.
(21) Royakkers, J.; Minotto, A.; Congrave, D. G.; Zeng, W.; Patel, A.; Bond, A. D.; Bučar, D. K.; Cacialli, F.; Bronstein, H. Doubly Encapsulated Perylene Diimides: Effect of Molecular Encapsulation on Photophysical Properties. *J. Org. Chem.* **2020**, *85*, 207−214.
(22) Pan, C.; Sugiyasu, K.; Wakayama, Y.; Sato, A.; Takeuchi, M. Thermoplastic Fluorescent Conjugated Polymers: Benefits of Preventing π-π Stacking. *Angew. Chem., Int. Ed.* **2013**, *52*, 10775−10779.
(23) Harkin, D. J.; Broch, K.; Schreck, M.; Ceymann, H.; Stoy, A.; Yong, C. K.; Nikolka, M.; McCulloch, I.; Stingelin, N.; Lambert, C.; Sirringhaus, H. Decoupling Charge Transport and Electroluminescence in a High Mobility Polymer Semiconductor. *Adv. Mater.* **2016**, *28*, 6378−6385.
(24) Wu, Y.; Schneider, S.; Walter, C.; Chowdhury, A. H.; Bahrami, B.; Wu, H. C.; Qiao, Q.; Toney, M. F.; Bao, Z. Fine-Tuning Semiconducting Polymer Self-Aggregation and Crystallinity Enables Optimal Morphology and High-Performance Printed All-Polymer Solar Cells. *J. Am. Chem. Soc.* **2020**, *142*, 392−406.
(25) Frampton, M. J.; Anderson, H. L. Insulated Molecular Wires. *Angew. Chem., Int. Ed.* **2007**, 1028−1064.
(26) Congrave, D. G.; Drummond, B. H.; Gray, V.; Bond, A. D.; Rao, A.; Friend, R. H.; Bronstein, H. Suppressing Aggregation Induced Quenching in Anthracene Based Conjugated Polymers. *Polym. Chem.* **2021**, *12*, 1830−1836.

(27) Lillis, R.; Thomas, M. R.; Mohanan, M.; Gavvalapalli, N. Enhancing Insulated Conjugated Polymer Fluorescence Quenching by Incorporating Dithia[3.3]Paracyclophanes. *Macromolecules* **2021**, *54*, 3112−3119.
(28) Ahrens, L.; Tverskoy, O.; Weigold, S.; Ganschow, M.; Rominger, F.; Freudenberg, J.; Bunz, U. H. F. (Aza)Pentacenes Clipped into a Ring: Stabilization of Large (Aza)Acenes. *Angew. Chem., Int. Ed.* **2021**, *60*, 9270−9273.
(29) Fujiwara, Y.; Ozawa, R.; Onuma, D.; Suzuki, K.; Yoza, K.; Kobayashi, K. Double Alkylene-Strapped Diphenylanthracene as a Photostable and Intense Solid-State Blue-Emitting Material. *J. Org. Chem.* **2013**, *78*, 2206−2212.
(30) Sugiyasu, K.; Honsho, Y.; Harrison, R. M.; Sato, A.; Yasuda, T.; Seki, S.; Takeuchi, M. A Self-Threading Polythiophene: Defect-Free Insulated Molecular Wires Endowed with Long Effective Conjugation Length. *J. Am. Chem. Soc.* **2010**, *132*, 14754−14756.
(31) Cacialli, F.; Wilson, J. S.; Michels, J. J.; Daniel, C.; Silva, C.; Friend, R. H.; Severin, N.; Samori, P.; Rabe, J. P.; O'connell, M. J.; Taylor, P. N.; Anderson, H. L. Cyclodextrin-Threaded Conjugated Polyrotaxanes as Insulated Molecular Wires with Reduced Interstrand Interactions. *Nat. Mater.* **2002**, *1*, 160−164.
(32) Méhes, G.; Pan, C.; Bencheikh, F.; Zhao, L.; Sugiyasu, K.; Takeuchi, M.; Ribierre, J. C.; Adachi, C. Enhanced Electroluminescence from a Thiophene-Based Insulated Molecular Wire. *ACS Macro Lett.* **2016**, *5*, 781−785.
(33) Sommer, M. Conjugated Polymers Based on Naphthalene Diimide for Organic Electronics. *J. Mater. Chem. C* **2014**, *2*, 3088−3098.
(34) Zhou, N.; Facchetti, A. Naphthalenediimide (NDI) Polymers for All-Polymer Photovoltaics. *Mater. Today* **2018**, 377−390.
(35) Guo, X.; Facchetti, A.; Marks, T. J. Imide-and Amide-Functionalized Polymer Semiconductors. *Chem. Rev.* **2014**, *114*, 8943−9021.
(36) Chen, Z.; Zheng, Y.; Yan, H.; Facchetti, A. Naphthalenedicarboximide- vs Perylenedicarboximide-Based Copolymers. Synthesis and Semiconducting Properties in Bottom-Gate N-Channel Organic Transistors. *J. Am. Chem. Soc.* **2009**, *131*, 8−9.
(37) Heuvel, R.; Colberts, F. J. M.; Li, J.; Wienk, M. M.; Janssen, R. A. J. The Effect of Side-Chain Substitution on the Aggregation and Photovoltaic Performance of Diketopyrrolopyrrole-Alt-Dicarboxylic Ester Bithiophene Polymers. *J. Mater. Chem. A* **2018**, *6*, 20904−20915.
(38) Steyrleuthner, R.; Schubert, M.; Howard, I.; Klaumünzer, B.; Schilling, K.; Chen, Z.; Saalfrank, P.; Laquai, F.; Facchetti, A.; Neher, D. Aggregation in a High-Mobility n-Type Low-Bandgap Copolymer with Implications on Semicrystalline Morphology. *J. Am. Chem. Soc.* **2012**, *134*, 18303−18317.
(39) Rodrigues, P. C.; Berlim, L. S.; Azevedo, D.; Saavedra, N. C.; Prasad, P. N.; Schreiner, W. H.; Atvars, T. D. Z.; Akcelrud, L. Electronic Structure and Optical Properties of an Alternated Fluorene-Benzothiadiazole Copolymer: Interplay between Experimental and Theoretical Data. *J. Phys. Chem. A* **2012**, *116*, 3681−3690.
(40) Bronstein, H.; Frost, J. M.; Hadipour, A.; Kim, Y.; Nielsen, C. B.; Ashraf, R. S.; Rand, B. P.; Watkins, S.; McCulloch, I. Effect of Fluorination on the Properties of a Donor-Acceptor Copolymer for Use in Photovoltaic Cells and Transistors. *Chem. Mater.* **2013**, *25*, 277−285.
(41) Jenekhe, S. A.; Lu, L.; Alam, M. M. New Conjugated Polymers with Donor-Acceptor Architectures: Synthesis and Photophysics of Carbazole-Quinoline and Phenothiazine-Quinoline Copolymers and Oligomers Exhibiting Large Intramolecular Charge Transfer. *Macromolecules* **2001**, *34*, 7315−7324.
(42) Beaujuge, P. M.; Amb, C. M.; Reynolds, J. R. Spectral Engineering in π-Conjugated Polymers with Intramolecular Donor-Acceptor Interactions. *Acc. Chem. Res.* **2010**, *43*, 1396−1407.
(43) Steyrleuthner, R.; Di Pietro, R.; Collins, B. A.; Polzer, F.; Himmelberger, S.; Schubert, M.; Chen, Z.; Zhang, S.; Salleo, A.; Ade, H.; Facchetti, A.; Neher, D. The Role of Regioregularity, Crystallinity, and Chain Orientation on Electron Transport in a High-Mobility n-Type Copolymer. *J. Am. Chem. Soc.* **2014**, *136*, 4245−4256.
(44) Schubert, M.; Dolfen, D.; Frisch, J.; Roland, S.; Steyrleuthner, R.; Stiller, B.; Chen, Z.; Scherf, U.; Koch, N.; Facchetti, A.; Neher, D. Influence of Aggregation on the Performance of All-Polymer Solar Cells Containing Low-Bandgap Naphthalenediimide Copolymers. *Adv. Energy Mater.* **2012**, *2*, 369−380.
(45) Caddeo, C.; Fazzi, D.; Caironi, M.; Mattoni, A. Atomistic Simulations of P(NDI2OD-T2) Morphologies: From Single Chain to Condensed Phases. *J. Phys. Chem. B* **2014**, *118*, 12556−12565.
(46) Brédas, J. L.; Street, G. B.; Thémans, B.; André, J. M. Organic Polymers Based on Aromatic Rings (Polyparaphenylene, Polypyrrole, Polythiophene): Evolution of the Electronic Properties as a Function of the Torsion Angle between Adjacent Rings. *J. Chem. Phys.* **1985**, *83*, 1323−1329.
(47) Che, Y.; Perepichka, D. F. Quantifying Planarity in the Design of Organic Electronic Materials. *Angew. Chem., Int. Ed.* **2021**, *60*, 1364−1373.
(48) Nahid, M. M.; Matsidik, R.; Welford, A.; Gann, E.; Thomsen, L.; Sommer, M.; McNeill, C. R. Unconventional Molecular Weight Dependence of Charge Transport in the High Mobility N-Type Semiconducting Polymer P(NDI2OD-T2). *Adv. Funct. Mater.* **2017**, *27*, No. 1604744.
(49) Chang, X.; Balooch Qarai, M.; Spano, F. C. HJ-Aggregates of Donor-Acceptor-Donor Oligomers and Polymers. *J. Chem. Phys.* **2021**, *155*, No. 034905.
(50) Hestand, N. J.; Spano, F. C. Expanded Theory of H- and J-Molecular Aggregates: The Effects of Vibronic Coupling and Intermolecular Charge Transfer. *Chem. Rev.* **2018**, *118*, 7069−7163.
(51) Qarai, M. B.; Chang, X.; Spano, F. C. Vibronic Exciton Model for Low Bandgap Donor-Acceptor Polymers. *J. Chem. Phys.* **2020**, *153*, No. 244901.
(52) Denti, I.; Cimò, S.; Brambilla, L.; Milani, A.; Bertarelli, C.; Tommasini, M.; Castiglioni, C. Polaron Confinement in N-Doped P(NDI2OD-T2) Unveiled by Vibrational Spectroscopy. *Chem. Mater.* **2019**, *31*, 6726−6739.
(53) Jin, J.; Wang, W.; Xue, P.; Yang, Q.; Jiang, H.; Tao, Y.; Zheng, C.; Xie, G.; Huang, W.; Chen, R. Intermolecular Locking Design of Red Thermally Activated Delayed Fluorescence Molecules for High-Performance Solution-Processed Organic Light-Emitting Diodes. *J. Mater. Chem. C* **2021**, *9*, 2291−2297.
(54) Rivnay, J.; Steyrleuthner, R.; Jimison, L. H.; Casadei, A.; Chen, Z.; Toney, M. F.; Facchetti, A.; Neher, D.; Salleo, A. Drastic Control of Texture in a High Performance N-Type Polymeric Semiconductor and Implications for Charge Transport. *Macromolecules* **2011**, *44*, 5246−5255.
(55) Luzio, A.; Criante, L.; D'Innocenzo, V.; Caironi, M. Control of Charge Transport in a Semiconducting Copolymer by Solvent-Induced Long-Range Order. *Sci. Rep.* **2013**, *3*, No. 3425.
(56) Matsidik, R.; Luzio, A.; Hameury, S.; Komber, H.; McNeill, C. R.; Caironi, M.; Sommer, M. Effects of PNDIT2 End Groups on Aggregation, Thin Film Structure, Alignment and Electron Transport in Field-Effect Transistors. *J. Mater. Chem. C* **2016**, *4*, 10371−10380.
(57) Kim, Y. J.; Kim, N. K.; Park, W. T.; Liu, C.; Noh, Y. Y.; Kim, D. Y. Kinetically Controlled Crystallization in Conjugated Polymer Films for High-Performance Organic Field-Effect Transistors. *Adv. Funct. Mater.* **2019**, *29*, No. 1807786.
(58) Bucella, S. G.; Luzio, A.; Gann, E.; Thomsen, L.; McNeill, C. R.; Pace, G.; Perinot, A.; Chen, Z.; Facchetti, A.; Caironi, M. Macroscopic and High-Throughput Printing of Aligned Nanostructured Polymer Semiconductors for MHz Large-Area Electronics. *Nat. Commun.* **2015**, *6*, No. 8394.
(59) Martino, N.; Fazzi, D.; Sciascia, C.; Luzio, A.; Antognazza, M. R.; Caironi, M. Mapping Orientational Order of Charge-Probed Domains in a Semiconducting Polymer. *ACS Nano* **2014**, *8*, 5968−5978.
(60) Fabiano, S.; Himmelberger, S.; Drees, M.; Chen, Z.; Altamimi, R. M.; Salleo, A.; Loi, M. A.; Facchetti, A. Charge Transport

Orthogonality in All-Polymer Blend Transistors, Diodes, and Solar Cells. *Adv. Energy Mater.* **2014**, *4*, No. 1301409.
(61) Alqahtani, O.; Babics, M.; Gorenflot, J.; Savikhin, V.; Ferron, T.; Balawi, A. H.; Paulke, A.; Kan, Z.; Pope, M.; Clulow, A. J.; Wolf, J.; Burn, P. L.; Gentle, I. R.; Neher, D.; Toney, M. F.; Laquai, F.; Beaujuge, P. M.; Collins, B. A. Mixed Domains Enhance Charge Generation and Extraction in Bulk-Heterojunction Solar Cells with Small-Molecule Donors. *Adv. Energy Mater.* **2018**, *8*, No. 1702941.
(62) Zuo, G.; Abdalla, H.; Kemerink, M. Conjugated Polymer Blends for Organic Thermoelectrics. *Adv. Electron. Mater.* **2019**, *5*, No. 1800821.
(63) Abtahi, A.; Johnson, S.; Park, S. M.; Luo, X.; Liang, Z.; Mei, J.; Graham, K. R. Designing π-Conjugated Polymer Blends with Improved Thermoelectric Power Factors. *J. Mater. Chem. A* **2019**, *7*, 19774−19785.
(64) Rivnay, J.; Toney, M. F.; Zheng, Y.; Kauvar, I. V.; Chen, Z.; Wagner, V.; Facchetti, A.; Salleo, A. Unconventional Face-on Texture and Exceptional in-Plane Order of a High Mobility n-Type Polymer. *Adv. Mater.* **2010**, *22*, 4359−4363.
(65) Sun, H.; Wang, Q.; Qian, J.; Yin, Y.; Shi, Y.; Li, Y. Unidirectional Coating Technology for Organic Field-Effect Transistors: Materials and Methods. *Semicond. Sci. Technol.* **2015**, *30*, No. 054001.
(66) Caironi, M.; Bird, M.; Fazzi, D.; Chen, Z.; Di Pietro, R.; Newman, C.; Facchetti, A.; Sirringhaus, H. Very Low Degree of Energetic Disorder as the Origin of High Mobility in an N-Channel Polymer Semiconductor. *Adv. Funct. Mater.* **2011**, *21*, 3371−3381.
(67) Li, J.; Du, J.; Xu, J.; Chan, H. L. W.; Yan, F. The Influence of Gate Dielectrics on a High-Mobility n-Type Conjugated Polymer in Organic Thin-Film Transistors. *Appl. Phys. Lett.* **2012**, *100*, No. 033301.
(68) Nogales, A.; Gutiérrez, E.*2D Representation of a Wide Angle X-ray Scattering Pattern as a Function of Q Vector Components*; MathWorks, Inc., 2019.

https://doi.org/10.1021/acs.chemmater.2c01894
Chem. Mater. 2022, 34, 8324−8335

5. Investigating Charge Transport in Semiconducting Single-Walled Carbon Nanotube Networks by Charge Modulation Microscopy

The content of this chapter is published in: [2]

M. Jiang, S. Pecorario, N. F. Zorn, J. Zaumseil, M. Caironi, Investigating Charge Transport in Semiconducting Single-Walled Carbon Nanotube Networks by Charge Modulation Microscopy, *Adv. Mater. Interfaces* **2023**, *2202454*.

Authors contributions:

M. Jiang and S. Pecorario contributed equally to this work.

S. Pecorario performed the analysis of the data, interpreted the CMS and CMM results, contributed to the design of the experiments and to their supervision, and leaded the writing of the manuscript.

M.J. performed the electrical, CMS and CMM measurements and contributed to their analysis and description.

N.F. Zorn fabricated the field-effect transistors and performed AFM. J. Zaumseil and M. Caironi conceived the work and supervised it. All the authors revised the manuscript and contributed to its discussion.

ADVANCED MATERIALS INTERFACES
Open Access
www.advmatinterfaces.de

Investigating Charge Transport in Semiconducting Single-Walled Carbon Nanotube Networks by Charge Modulation Microscopy

Mengting Jiang, Stefano Pecorario, Nicolas F. Zorn, Jana Zaumseil, and Mario Caironi**

Solution-processed networks of semiconducting single-walled carbon nanotubes (SWCNTs) hold promise as active layers for large-scale digital circuits, thermoelectric devices, and healthcare applications. Yet, the combined effects of local network properties and (*n*,*m*) species composition need to be addressed to improve the performance and reproducibility of state-of-the-art devices. Charge modulation microscopy (CMM) is used to investigate charge transport in field-effect transistors (FETs) based on monochiral (6,5) SWCNT networks and multichiral networks containing five semiconducting SWCNT species with different band gaps. By mapping the charge-modulated signal within the FET channel with sub-micrometer resolution, the spatial distribution of free carriers and its evolution during the switching of the FET are revealed. The CMM maps provide direct evidence that holes and electrons are transported preferentially through the same percolation paths. A moderate positive correlation between the SWCNT density in the monochiral (6,5) network and the charge density in subthreshold regime is demonstrated. In multichiral networks, the charge transport paths are on average less fragmented when involving low band gap species. CMM emerges as a valuable technique to estimate the size of preferential percolation domains associated with the average distance traversed by charge carriers on SWCNTs of the same chirality before tunneling onto other species.

1. Introduction

Networks of semiconducting single-walled carbon nanotubes (SWCNTs) have great potential for applications in electronic circuits due to their outstanding electrical properties, such as high hole and electron mobilities combined with mechanical flexibility, environmental stability, solution processability, and biocompatibility.[1–4] These features make them particularly appealing as active layers in field-effect transistors (FETs) and biosensors on large-area flexible substrates.[5–7] Still, a deep understanding and engineering of SWCNT network properties, along with scaling up of the manufacturing processes, is needed to fulfill the stringent technological and cost requirements for large-scale digital circuits and healthcare applications. The ability to accurately select the diameter and type of the SWCNTs composing the network is particularly challenging. It is especially important to avoid the presence of any metallic SWCNTs. Recent advances in purification and sorting techniques, such as aqueous two-phase extraction[8,9] and selective polymer-wrapping,[10–14] have enabled electronic devices based on networks of purely semiconducting SWCNTs. Nowadays, solution-processed randomly oriented networks of highly purified SWCNTs have established carrier mobilities above 10 $cm^2 V^{-1} s^{-1}$ in FETs.[15–17] SWCNT networks usually contain several semiconducting species. While various effective separation approaches have been developed[18,19] especially for aqueous dispersions, only a few highly scalable methods exist that provide large amounts of monochiral dispersions

M. Jiang,[+] S. Pecorario, M. Caironi
Center for Nano Science and Technology@PoliMi
Istituto Italiano di Tecnologia
via Raffaele Rubattino 81, 20134 Milan, Italy
E-mail: mario.caironi@iit.it

The ORCID identification number(s) for the author(s) of this article can be found under https://doi.org/10.1002/admi.202202454.

[+]Present address: Institute of Materials Research and Engineering (IMRE), Agency for Science, Technology and Research (A*STAR) , 2 Fusionopolis Way, Innovis #08-03, Singapore 138634, Republic of Singapore

S. Pecorario
Department of Energy
Micro and Nanostructured Materials Laboratory – NanoLab
Politecnico di Milano
Via Ponzio 34/3, 20133 Milan, Italy

N. F. Zorn, J. Zaumseil
Institute for Physical Chemistry
Universität Heidelberg
D-69120 Heidelberg, Germany
E-mail: zaumseil@uni-heidelberg.de

DOI: 10.1002/admi.202202454

in suitable solvents for devices fabrication. One example is polymer-sorted (6,5) SWCNTs, which can be produced and processed into networks from toluene dispersion.[11] Thus, even though charge transport is more effective in networks with only a single nanotube species (i.e., monochiral networks), polydisperse samples of semiconducting nanotubes with different species (i.e., multichiral networks) are still commonly employed.

The effects of the network composition and density on the charge transport have been investigated in several studies by temperature-dependent measurements of conductivity and field-effect mobility,[20–22] along with thermoelectric parameters.[23] Moreover, spectroscopic techniques such as photoluminescence (PL),[24] electroluminescence (EL),[25,26] and Raman[27] are valuable methods to study the charge transport in multichiral networks by exploiting characteristic optical transitions and monitoring the spectral evolution in the presence of charge carriers. The significant energetic disorder due to the presence of multiple species represents the main obstacle for achieving efficient charge transport in multichiral networks.[22,28] Semiconducting SWCNTs with large diameter, hence with small electronic band gap, provide higher intrinsic charge carrier mobility, lower junction resistance,[29] and smaller injection barriers when compared to small-diameter nanotubes.[30] The SWCNT density,[16,31] the degree of alignment,[32] and the presence of bundles[33] are additional network parameters that must be carefully optimized to improve charge transport. Recently, Zorn et al. employed charge modulation spectroscopy (CMS) and charge-modulated PL to study charge transport in FETs based on random networks of monochiral (6,5) SWCNTs and of a mixture of five chiralities.[34] CMS is a lock-in-based technique that has been widely employed to study charge transport in organic semiconductors.[35–39] In the CMS experiment, the charge density at the interface between the semiconducting and the dielectric layer is modulated by applying a gate potential composed of a constant offset potential, V_{os}, and of a sinusoidal waveform with peak-to-peak intensity V_{pp} and modulation frequency ω. By correlating the mobile carriers with the ground-state bleaching and charge-induced absorption of the different SWCNT chiralities, it has been shown that small band gap SWCNTs dominate the charge transport especially at low carrier concentrations, while the contribution of large band gap species increases at higher gate voltages.[34]

In this work, we deepen the investigation of charge transport in monochiral and multichiral random networks of SWCNTs by charge modulation microscopy (CMM), which allows us to image CMS features with a sub-micrometer spatial resolution using a confocal microscopy setup. A schematic layout of the CMM system is presented in **Figure 1**a, while a detailed description of the setup is provided in Figure S1, Supporting Information. CMM mapping of the FET channel area has already enabled direct visualizations of the charge density distribution in films of organic semiconductors, allowing to analyze the impact of local film properties (e.g., morphology, density, and degree of alignment) on charge transport.[40–44] By tracking the evolution of the charge carrier distribution in a monochiral (6,5) SWCNT network as a function of the applied gate voltage in the subthreshold regime, that is, when the conductive channel is being formed, we are able to detect a progressive activation of percolation paths and highlight the impact of the network density. In networks composed of five different semiconducting SWCNT species, our CMM analysis shows that all of them clearly take an active role in charge transport. Being able to directly visualize charge transport paths, we show that charges distribute more homogeneously on the species with larger diameters (i.e., smaller band gap). Furthermore, we provide a method to estimate in a comparative way relevant length scales related to the size of percolation domains in the different species, thus providing insights for the design and dimensionality of electronic devices based on random SWCNT networks.

2. Results

2.1. Monochiral (6,5) SWCNT Networks

Using selective polymer-wrapping[11] we prepared a nearly monochiral dispersion of (6,5) SWCNTs in toluene from CoMoCAT SWCNT raw material with the wrapping polymer poly[(9,9-dioctylfluorenyl-2,7-diyl)-*alt*-(6,6′-(2,2′-bipyridine))] (PFO-BPy; details provided in the Experimental Section). We fabricated FETs in bottom-contact, top-gate configuration (scheme displayed in Figure 1a) by depositing the SWCNTs dispersion via spin-coating onto pre-patterned gold electrodes. As confirmed by atomic force microscopy (AFM) (Figure 1b), this leads to dense networks of randomly distributed (6,5) SWCNTs. Due to a thin silver top gate, the FETs are semi-transparent, thus enabling optical measurements in transmission mode. The characteristic transfer and output curves of a representative device are shown in Figure 1c and in Figure S2, Supporting Information, respectively. The transfer curve exhibits a nearly ideal ambipolar behavior, high on/off current ratio above 10^6, and negligible hysteresis. The field-effect mobility of the monochiral network, as extracted from the slope of the linear fit of $I_{ds}(V_g)$, reaches about 6.6 $cm^2\ V^{-1}\ s^{-1}$ for holes and 9.8 $cm^2\ V^{-1}\ s^{-1}$ for electrons. The threshold voltages in hole and electron accumulation regimes amount to −5.3 and 4.1 V, respectively (Figure S4, Supporting Information).

By using CMS, Zorn et al.[34] previously analyzed the differential changes in the optical absorption of the SWCNT network upon modulation of the gate potential in FETs that were identical to those fabricated for this study. The CMS signal originates from the differential transmittance, namely $\Delta T/T$, induced by the mobile charges upon the sinusoidal modulation. A positive CMS signal corresponds to an increased transmittance ($\Delta T > 0$) due to the bleaching of the absorption of neutral SWCNTs. A negative CMS signal is observed when there is a decreased transmittance ($\Delta T < 0$) because of charge-induced absorption. The modulated spectra presented very high signal intensities and signal-to-noise ratios, enabling clear observation of charge-induced exciton bleaching of the E_{11} transition and charge-induced absorption features (related to a polaron or trion) caused by mobile carrier modulation. In this study, we perform CMM to record local charge-modulation spectra with sub-micrometer resolution and acquire microscopy images of the CMS signal by fixing the incident wavelength and scanning a large area of the sample.

Figure 1d shows the local charge-modulation spectrum (V_{os} = −1 V, V_{pp} = 0.2 V) acquired in the middle of the transistor

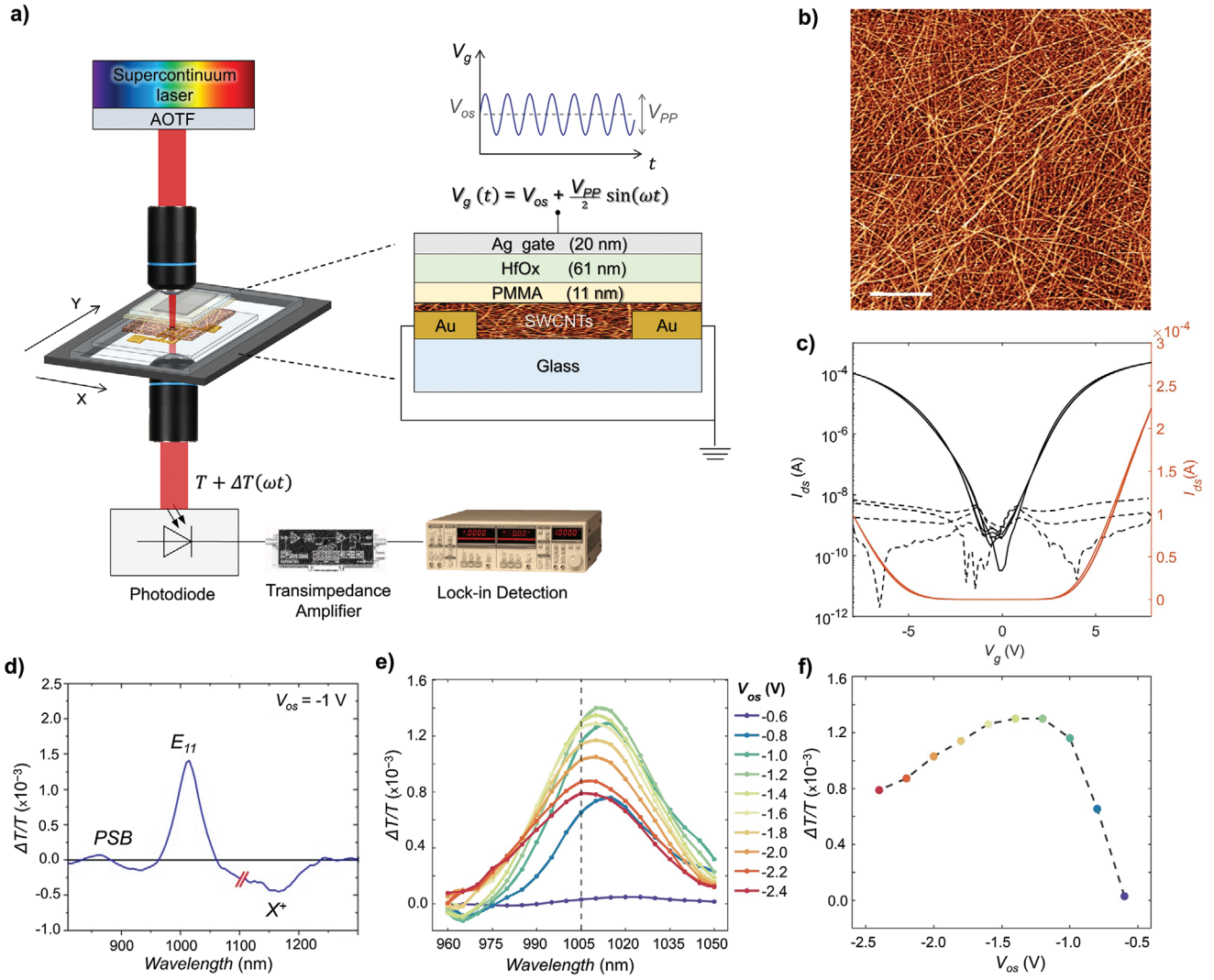

Figure 1. a) Schematic diagram of the charge modulation microscopy (CMM) setup. The inset shows a scheme of a SWCNT-based field-effect transistor architecture. b) AFM topography of a monochiral (6,5) SWCNT network. The scale bar is 500 nm. c) Transfer curve (V_{ds} = –0.1 V) for the monochiral (6,5) SWCNT-based FET plotted on logarithmic (black) and on linear (red) scales. The device has channel length L = 20 µm and channel width W = 1 cm. d) Local charge modulation spectrum of monochiral (6,5) SWCNTs (V_{os} = –1 V, V_{pp} = 0.2 V). The focal spot is ≈0.8 µm wide. The x-axis is interrupted at 1100 nm because the spectrum before and after this wavelength is acquired with different optical fibers and acousto-optic tunable filter (AOTF). e) Trend of the local E_{11} bleaching signal at different V_{os} and fixed V_{pp} = 0.2 V. f) Evolution of the CMS signal at 1005 nm (E_{11} bleaching peak) as a function of the applied offset potential V_{os}.

channel by means of the confocal microscope setup with a focal spot of ≈0.8 µm (Figure S1b, Supporting Information). Two positive peaks are present: a pronounced and sharp peak at around 1010 nm, which is assigned to the bleaching of the E_{11} absorption peak (Figure S3, Supporting Information), and a phonon side band (PSB) at around 860 nm.[34] The negative band in the NIR is due to the absorption of positively charged nanotubes (polarons or trions, X^+). Trions are three-body particles (i.e., charged excitons) that eventually form upon optical excitation of doped carbon nanotubes.[45,46] The local spectrum is in very good agreement with the macroscopic CMS spectrum measured from the entire device (Figure S5a,b, Supporting Information) and with the CMS spectra previously reported for monochiral (6,5) networks.[34] Furthermore, local spectra acquired from different positions of the sample exhibit the same CMS features, with only slight variations in the peak intensities, which is a consequence of the differences in the local distribution of free charges throughout the active area (Figure S5c, Supporting Information). Importantly, the local CMS spectra measured in the center of the FET channel and close to the electrodes are virtually identical (Figure S5d, Supporting Information), thus excluding the presence of any spurious electro-absorption effect that would be more pronounced at the electrode edges.[39,42]

The CMS signal intensity shows a characteristic trend as a function of the applied offset potential V_{os}, which is found also for local CMS spectra (Figure 1e,f). The maximum of the E_{11} bleaching peak is associated to a critical value of the charge carrier density, d^*, which is reached at $V_{os}^* \approx -1.2$ V for the FET based on the (6,5) network (Figure 1f). For $|V_{os}| < |V_{os}^*|$,

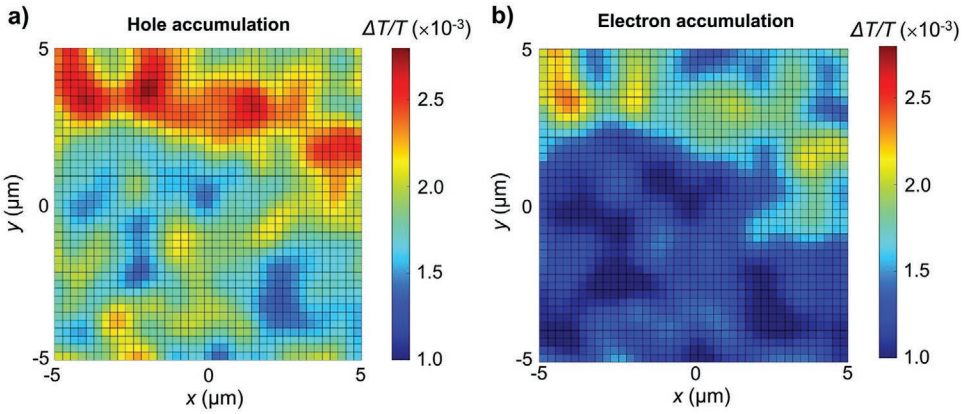

Figure 2. CMM maps monitoring the E_{11} bleaching peak intensity at 1005 nm on a 10 × 10 μm^2 area with spatial resolution of ≈0.8 μm (Figure S1b, Supporting Information) in a) hole accumulation regime (V_{os} = –2.0 V) and b) in electron accumulation regime (V_{os} = 2.2 V).

the E_{11} bleaching peak grows with the offset potential because the quantum capacitance of the carbon nanotubes increases, thus resulting in higher modulated charge density. Instead, for $|V_{os}| > |V_{os}^*|$, the CMS signal drops due to the reduction of the oscillator strength of the E_{11} transition when the charge carrier density is greater than d^*.[47,48]

Keeping the wavelength of the incident laser beam fixed at 1005 nm, we scan a 10 × 10 μm^2 area within the FET channel to obtain CMM maps of the E_{11} bleaching peak as a function of V_{os}, which provide information on the local density distribution of free carriers when varying the offset potential (Figure S6, Supporting Information). Importantly, by applying a positive/negative offset voltage we can visualize the CMM maps that correspond selectively to hole/electron accumulation regimes, as shown in **Figure 2**a,b. The difference of the average intensity of the CMS signal in the two CMM maps is consistent with the general trend of the signal for $|V_{os}| > |V_{os}^*|$. Indeed, the average signal in the map recorded for V_{os} = –2.0 V (hole accumulation regime) is higher than in the one measured for V_{os} = 2.2 V (electron accumulation regime). Remarkably, the two CMM maps present the same local features. Hence, both holes and electrons accumulate preferentially in the same regions (those with higher CMS signal), meaning that there are favorable percolation paths in the network regardless of the polarity of the charge carriers. This is consistent with the nearly ideal ambipolar characteristics of the device and with previous observations of electron-hole recombination paths by electroluminescence experiments.[25,49] A convenient way to quantify the similarity in spatial distribution of the signal in two different CMM maps consists in computing the zero-mean normalized cross-correlation (ZNCC) coefficient. With this approach, the two maps are first standardized by subtracting the mean and dividing by the standard deviation of the signal, and then they are cross-correlated (details in the Experimental Section). This method is frequently used in image-processing and template-matching applications to recognize common patterns in images where the brightness and contrast vary because of different lighting conditions. The ZNCC coefficient ranges from –1 to 1 and represents the 2D version of the Pearson correlation coefficient, which is a measure of the linear correlation between two signals or datasets. Therefore, when the ZNCC coefficient is close to 1, the two images are positively correlated, when it approaches –1 they are inversely correlated, while when it is close to 0 the two images are uncorrelated. Intermediate values (about ±0.5) indicate a moderate correlation. In the case of the CMM maps in hole and electron accumulation regimes (Figure 2a,b), the ZNCC coefficient is 0.93, thus confirming the high level of positive correlation (i.e., similarity of the charge density distribution).

As a next step toward understanding the impact of local network properties on the charge transport, we assess whether the non-uniform carrier distribution in the channel can be correlated with the presence of local orientational order at the micrometer scale within the random network, or with the local density of the SWCNT network. Hence, we performed polarized CMM measurements, and quantified the local degree of orientational order of the SWCNT active layer as previously shown by Martino et al.[41] This analysis is detailed in the Figure S7 (and discussion therein), Supporting Information, and clearly indicates that there is no sufficient local alignment of the SWCNTs network to support a positive correlation with the signal intensity. In addition, we carefully measured the local optical density (OD) of the film to reveal any possible correlation with the network density. In fact, previous studies have demonstrated that the density of SWCNTs has a strong impact on the charge carrier percolation.[24,50] Since the examined SWCNT networks are only few nanometers thin, the film is highly transparent. Hence, we averaged 20 OD maps acquired by scanning the same area to obtain reliable values (details in Figure S8, Supporting Information). It is important to highlight that the contrast of signal intensity in the CMM maps is more difficult to be rationalized when $|V_{os}| > |V_{os}^*|$, since the signal starts to drop because of high electrostatic doping (Figure S6 and discussion therein, Supporting Information). However, it is fairly straightforward for $|V_{os}| < |V_{os}^*|$, where the E_{11} bleaching peak increases monotonously with the offset potential, that is, with the carrier density. For this reason, we analyze in **Figure 3**a–c how the CMM map in hole accumulation regime evolves by subsequently tuning V_{os} from –0.6 to –0.8 and to –1.0 V. Here, we report the standardized OD on the *z*-axis, which is identical for all the panels since the mapped area is the same. Thus, the structuration on the *z*-axis allows

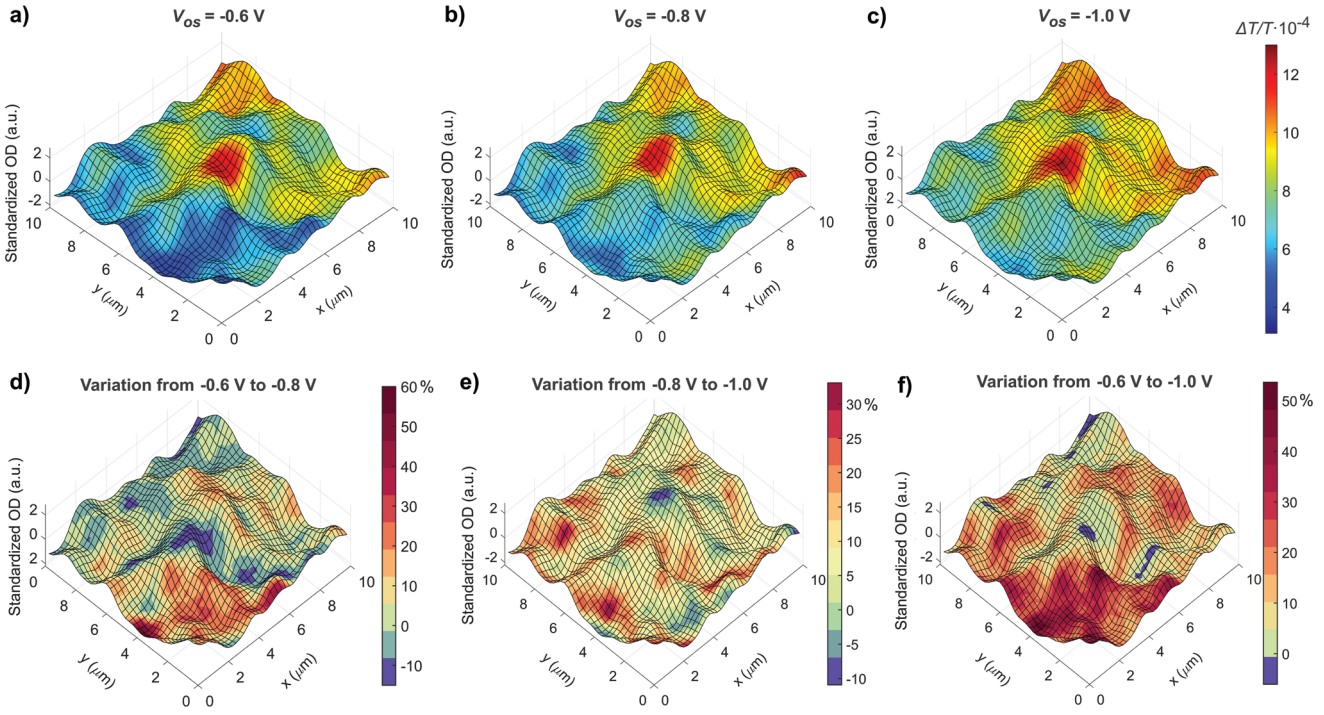

Figure 3. a–c) CMM maps on a monochiral (6,5) SWCNT network, corresponding to the E_{11} bleaching peak at 1005 nm, acquired in hole accumulation at increasing V_{os} (in subthreshold regime and with the condition $|V_{os}| < |V_{os}^*| \approx 1.2$ V). The scanned area is 10×10 μm^2 large (40×40 pixels), the *z*-axis corresponds to the standardized optical density (OD) of the network, and the colormap indicates the intensity of the local CMS signal ($\Delta T/T$). Percentage variation of the local E_{11} bleaching when passing d) from $V_{os} = -0.6$ to -0.8 V, e) from $V_{os} = -0.8$ to -1.0 V, and f) from $V_{os} = -0.8$ to -1.0 V.

to visually compare pixel-by-pixel the SWCNT network density with the local CMS signal (colormap). It is possible to detect a good correlation between those regions of the maps where the CMS signal is high and peaks in OD (e.g., at the center of the scan and at the top corner), and between regions with low CMS signal and valleys of SWCNT density (e.g., the bottom corner).

This trend is further corroborated by plotting the distribution of $\Delta T/T$ versus the standardized OD for all the pixels (Figure S9, Supporting Information). Such a correlation suggests that regions with higher network density present more connections among the carbon nanotubes, favoring the formation of percolative pathways and therefore preferential transport of charges. Still, there are some locations such as the top-right corner where $\Delta T/T$ is high, but OD is average. To quantify the degree of correlation between the charge density distribution and the SWCNT density, we computed the ZNCC coefficients of the CMM maps at $V_{os} = -0.6$, -0.8, -1.0 V with the OD map. In agreement with previous visual observations, the obtained ZNCC coefficients are 0.39, 0.41, and 0.37, respectively, which indicate a moderate positive correlation of the charge carrier density with the SWCNT network density. Thus, SWCNT density alone cannot explain the distribution of free carriers in the channel, which must be influenced by other local properties such as bundles, or residues of wrapping polymer, or screening from the gate field.

Moreover, it is interesting to investigate how the charge distribution evolves by progressively increasing the offset potential. This information is valuable to understand the early stages of device switching and possibly relate it to parameters like subthreshold swing and threshold voltage. Although the CMM maps in Figure 3a–c generally present a similar signal distribution, the increase of the CMS signal with $|V_{os}|$ is not uniform. Hence, we analyze the variation of the CMS signal as a function of V_{os} in Figure 3d–f, showing that the charge density varies locally in different ways.

From –0.6 to –1.0 V (Figure 3f), there is an increase of charge density nearly everywhere in the mapped area. Remarkably, the increase of the CMS signal is higher in the regions with the lowest SWCNT density (see for instance the map at $x,y < 5$ μm). In contrast, a negative variation of the CMS signal when increasing $|V_{os}|$ (blue regions in Figure 3d–f) can indicate two opposite phenomena: 1) the charge density locally decreases even if $|V_{os}|$ is raised because of the activation of different percolation paths at higher $|V_{os}|$, or 2) the charge density increases with $|V_{os}|$ in agreement with the average trend for the entire active area, and locally reaches values greater than d^*.

The former mechanism is at the origin of the few blue spots in Figure 3f, where the CMS signal variation is tracked from –0.6 to –1.0 V. The reduction of the local CMS signal in these areas is likely due to a drop of the local charge density from –0.6 to –0.8 V (Figure 3d), followed by a partial recovery from –0.8 to –1.0 V (Figure 3e). The decrease of the local charge density from –0.6 to –0.8 V can be rationalized considering that the percolation paths at –0.6 V become less effective once other pathways are being activated at –0.8 V. This effect might be attributed to a non-linear activation of tunneling processes among the SWCNTs that depends on the specific bias point (V_{os}) and on the local morphological properties of the network.

The latter mechanism can explain the blue spots in Figure 3e (negative signal variation from –0.8 to –1.0 V). In these regions, the local charge density likely reaches values greater than d^* already at –1.0 V. Indeed, the CMS signal grows in these regions from –0.6 to –0.8 V (Figure 3d), locally reaching an absolute intensity higher than average at –0.8 V (red spots in Figure 3b). Hence, it is plausible that the charge density keeps on increasing in these zones as $|V_{os}|$ is progressively raised from 0.6 to 0.8 and then to 1.0 V.

As a matter of fact, these CMM maps capture an evolution of the quasi-static charge density distribution as the transistor is gradually switching to its on-state. By increasing $|V_{os}|$, the charge density does not rise homogeneously, but a redistribution of the most favorable percolation paths occurs likely because of a nonlinear activation of tunneling processes among the SWCNTs. Overall, the areas with the lowest OD (i.e., the lowest density of SWCNTs) are those experiencing the highest increase in CMS signal as $|V_{os}|$ raises, with up to 60 % positive variation (see also Figure S9, Supporting Information). These variations indicate that even in a monochiral nanotube network charge transport paths are complex and vary with the applied gate voltage.

2.2. Multichiral SWCNT Networks

Starting from the knowledge acquired from monochiral SWCNT networks, in the following we will analyze CMM measurements on FETs based on a multichiral network composed of a mix of five different SWCNT species (Table S1, Supporting Information). The aim is to unveil the role of the network composition on the charge transport. The dispersion was obtained by selective polymer-wrapping from HiPco SWCNT raw material (details in the Experimental Section), which produces a mix of only five semiconducting species, namely (7,5), (7,6), (8,6), (8,7), and (9,7) SWCNTs, which are identified from their characteristic E_{11} transition at 1045, 1135, 1200, 1285, and 1350 nm, respectively (Figure S3, Supporting Information).[10]

We fabricated FETs based on the multichiral network using the same architecture as for the devices with monochiral (6,5) nanotubes. A transfer curve is shown in **Figure 4**a, and a representative AFM image of the active layer is displayed in Figure 4b. The mix of different SWCNTs species introduces some non-idealities, such as a marked hysteresis and a threshold voltage shift. Also, the field-effect mobility is lower than in the previous case (about 0.5 $cm^2\ V^{-1}\ s^{-1}$ for both electrons and holes, with a strong dependence on the gate potential as already seen for the monochiral network, see Figure S4, Supporting Information).

A typical local CMS spectrum of the multichiral network (Figure 4c) presents five positive peaks, which correspond to the bleaching of the E_{11} transitions of each SWCNT species (absorption spectrum provided in Figure S3, Supporting Information). The trend of each E_{11} bleaching peak as a function of V_{os} is analogous to that analyzed for the monochiral network (Figure S10, Supporting Information). The negative band above 1350 nm is assigned to charge-induced absorption (see Table S1, Supporting Information). The (9,7) bleaching peak overlaps with the (8,6) trion peak, complicating the correct quantification of its intensity. In agreement with reports by Zorn et al.,[34] the relative intensity ratio between the CMS bleaching peaks of the five SWCNT species varies as a function of the applied V_{os} (Figure S10a, Supporting Information). When normalizing the spectra at the bleaching peak of the (8,7) species (Figure S10b, Supporting Information), the (7,6) and (8,6) bleaching peaks grow with respect to the (8,7) peak when $|V_{os}|$ is increased, while the (9,7) bleaching peak decreases.

These observations confirm at the micrometer scale that SWCNT species with a low band gap dominate the charge transport at low gate voltage, while the contribution of larger band gap species becomes more relevant as the potential increases and the applied bias favors tunneling between nanotubes of different chirality. Yet, at the micrometer scale the intensity ratios among the peaks associated to the E_{11} bleaching of the various chiralities depend on the probing position. The latter can be observed by comparing local CMS spectra measured in different locations of the same device in Figure 4d. CMS spectra measured on the entire device area result from a statistical average of the local spectra, highlighting the significant role of the local composition of the networks on charge transport (Figure S11 and discussion therein, Supporting Information). Note that within one measurement spot of ≈0.8 µm width, ≈25–35 nanotubes are located and contribute to the signal.

Figures 4e and 4f depict the CMM maps corresponding to E_{11} bleaching of the (7,6) species (1135 nm) in hole and electron accumulation regimes, respectively. The two maps are very well correlated (ZNCC coefficient is equal to 0.80), which means that holes and electrons share the same percolation paths as in the case of the monochiral network. The CMS spectra reported in Figure S12, Supporting Information, acquired from the entire device also support this conclusion, as the ratios among the characteristic E_{11} peaks of the five chiralities are the same in hole and electron accumulation regimes.

We map the E_{11} bleaching peak in hole accumulation regime for all the five species in a $10 \times 10\ \mu m^2$ area (**Figure 5**a–e). All the maps present characteristic patterns that indicate the presence of different percolative pathways involving all the chiralities. Importantly, we perform the CMM measurements at $V_{os} = -0.5$ V ($|V_{os}^*| > 0.6$ V for all the species), so to correlate the intensity of the CMS signal with the density of charge carriers accumulated on the specific SWCNT chirality in the FET subthreshold regime. In addition, at such low potential the intensity of the polaron/trion peak could be considered much lower than the (9,7) bleaching peak, allowing us to include all the chiralities in the analysis. We further investigate the complex charge carrier distribution originating from the presence of energy barriers by comparing the CMM maps and the OD maps corresponding to the E_{11} peak of the five SWCNT species (Figure 5f–j).

The OD maps display similarities in the distribution of SWCNT between species with close values of the band gap, while they seem uncorrelated for those with large band gap difference (e.g., (7,5) and (9,7) SWCNTs). Such a distribution can be rationalized based on previous literature suggesting that aggregation is favorable among species having similar band gap.[51] The cross-correlation analysis among the five OD maps corroborates this observation (Figure S13a, Supporting Information). We note that for some spots, the OD of a certain chirality is close to zero. While the absorption spectrum (Figure S3,

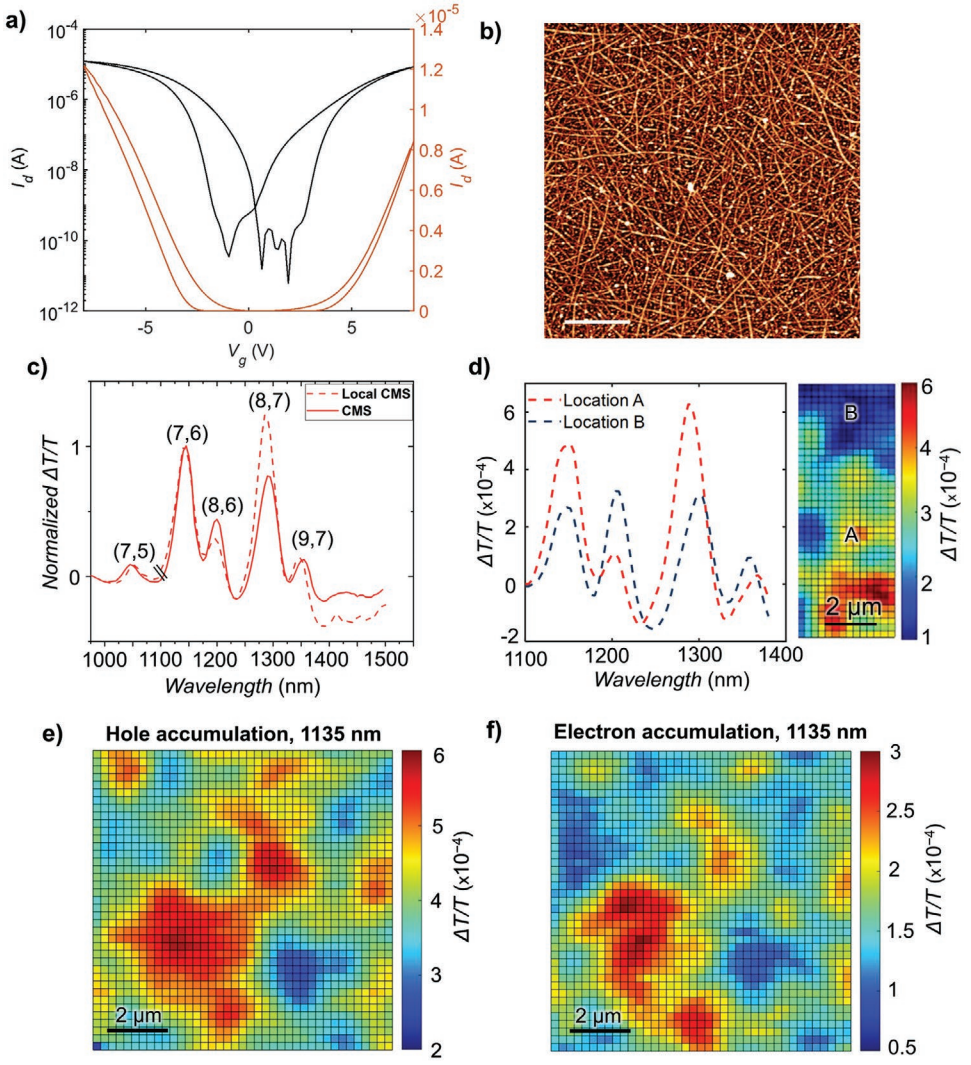

Figure 4. a) Transfer curve (V_{ds} = –0.1 V) for the multichiral SWCNT-based FET plotted on a logarithmic (black) and on a linear (red) scale, respectively. The device has a channel length L = 20 µm and channel width W = 1 cm. b) AFM topography of a representative multichiral SWCNT network. The scale bar is 500 nm. c) Local CMS spectrum for the multichiral SWCNT network inside the FET channel versus CMS spectrum from the entire device (V_{os} = –0.5 V, V_{pp} = 0.2 V). d) Local CMS spectra (V_{os} = –0.6 V, V_{pp} = 0.2 V) at the two different positions within the FET channel. The A and B locations are marked in the CMM map on the right side of the panel, which was acquired at 1135 nm with V_{os} = –0.5 V and V_{pp} = 0.2 V. e,f) CMM maps in hole accumulation regime (V_{os} = –0.6 V) and electrons accumulation (V_{os} = 0.6 V) recorded at 1135 nm (i.e., the (7,6) SWCNT E_{11} bleaching peak). Map dimensions: 10 × 10 µm² (40 × 40 pixels).

Supporting Information) already shows a low abundance of (7,5) SWCNTs and some local inhomogeneities are expected, it seems unlikely that species with a higher abundance (such as (8,7) and (9,7) SWCNTs) are not present in extended regions of the dense networks. Some fluctuations might arise during the transmission measurements of the highly transparent films or due to minor shifts of the E_{11} absorption peaks for different dielectric environments. By selecting the probing wavelength corresponding to the E_{11} peak of each of the species, we could map the local CMS signal arising from the modulation of the charge density of each chirality independently (Figure 5a–e). Although the local CMS features in these maps appear generally more fragmented than for the (6,5) monochiral network, it is remarkable that charge carriers distribute on all the species and throughout the 10 × 10 µm² mapped area. Thus, all five SWCNT species clearly take an active role in charge transport. Effective percolation pathways across the FET channel likely involve hopping of charge carriers among regions where the transport proceeds preferentially on different chiral species. In contrast to the monochiral (6,5) SWCNT network, there is no clear correlation between the SWCNT density (proportional to the OD maps of Figure 5f–j) and the accumulated free carrier density (proportional to the CMS signal in Figure 5a–e). Consistently, the ZNCC coefficients of each CMM map with the corresponding OD map range from 0.09 to –0.20 for all the species (Figure S13b, Supporting Information), thus indicating extremely low linear correlation as opposed to the ZNCC coefficient of ≈0.40 obtained for the monochiral network. Such evidence suggests that the bottleneck to the charge transport in the multichiral network is not represented by the number of

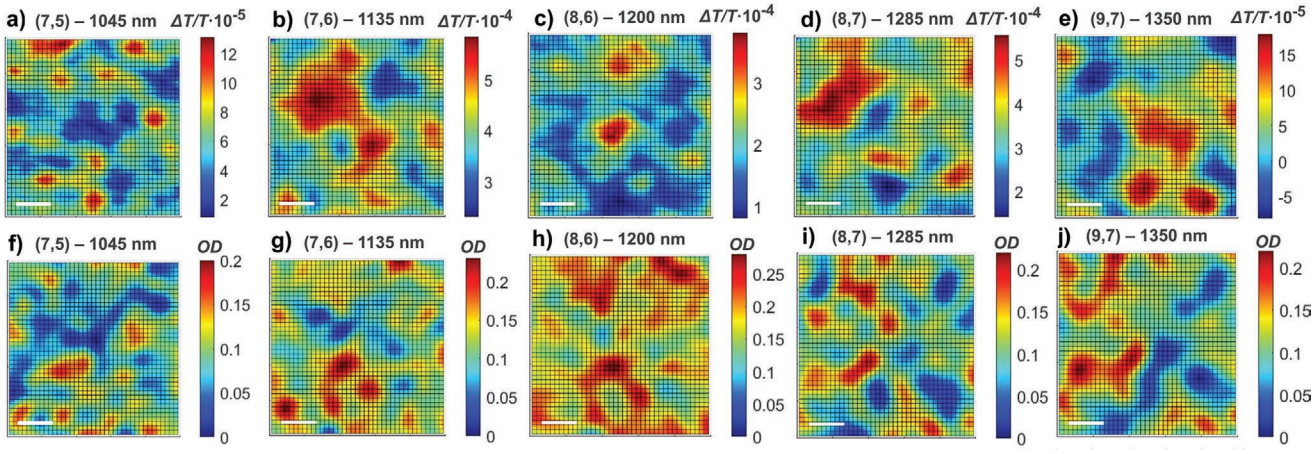

Figure 5. a–e) CMM maps (V_{os} = –0.5 V) and f–j) optical density maps for a multichiral SWCNT network (scale bars are 2 µm). From left to right the maps show the E_{11} peak for (7,5), (7,6), (8,6), (8,7), and (9,7) species, respectively.

tunneling junctions among SWCNTs, but by the energy barriers arising between nanotubes with different diameters and band gaps.[52]

2.3. Average Size of Percolation Pathways

To corroborate this hypothesis, we compare the average dimension of percolation pathways in the monochiral and multichiral networks. We aim to identify a characteristic length scale of regions of the CMM maps displaying similar signal intensity, as this corresponds to areas with uniform charge carrier density. The rationale is that a homogeneous charge carrier distribution arises in presence of extended effective percolation pathways, while a heterogenous charge density is associated to inefficient fragmented percolation pathways. To this purpose, we compute the 2D autocorrelation function (ACF) of the CMM maps and derive the autocorrelation length. The autocorrelation length of an image, ξ, represents the average distance at which a pattern is repeated, and so it refers to the typical size of domains on an image. The procedure is illustrated in **Figure 6**a for the CMM map of the (6,5) monochiral network measured at V_{os} = –0.6 V (Figure 3a). First, we calculated the 2D ACF of the CMM map, which is equivalent to the ZNCC of the CMM map with itself shifted along the x- and y-axis of d_x and d_y, respectively. Thus, the colormap represents the ZNCC as a function of the spatial shift (d_x, d_y), that is, the relative distance between the two CMM maps that are being cross-correlated (computational details reported in the Experimental Section). Then, we calculate the ACFs related to the magnitude of the spatial shift ($R = \sqrt{d_x^2 + d_y^2}$), by averaging in all directions the points of the 2D autocorrelation map as a function of R. The ACF is identically equal to 1 at zero shift (R = 0), being the correlation of the map with itself, and then it drops exponentially with R. Hence, we interpolate the ACF with an exponential function, $f(R) = k \cdot \exp(-R/\xi)$, where $k \approx 1$, and ξ denotes the correlation length. The value of the correlation length for the CMM map of the (6,5) monochiral network is ξ = 0.89 µm. As defined, ξ corresponds to the shift R at which the ACF decays in value to $1/e$. Importantly, ξ is not to be considered as a characteristic transport length (e.g., it is not a mean free path between two tunneling events). It represents the average distance between two pixels of the CMM map at which the local CMS signal preserves a high correlation. Hence, ξ is correlated to the size of areas of the semiconducting film displaying very similar conductivity and it can be used to compare the extension of percolation paths in networks with different composition. Therefore, in Figure 6b we adopt the same procedure to compute the 2D ACFs of the CMM maps for the multichiral network (Figure 5a–e) and we derive the correlation lengths associated to percolation domains of all the five (n,m) species composing the network. The values of the correlation lengths are reported in Figure 6b and range from 0.52 to 0.83 µm. Except for the (7,6) species, ξ grows from (7,5) to (9,7) SWCNTs: small band gap species are those contributing the most to charge transport, hence the extent of the percolation domains is larger than for large band gap species, whose percolation paths are more fragmented as evident for the CMM map of the (7,5) species (Figure 5a). Consistently, the largest ξ is obtained for the monochiral (6,5) SWCNT network (Figure 6a), for which no energy barriers due to a mixed composition are present. The large value of ξ for the (7,6) species is difficult to be rationalized and it might originate from the complex dependence of the charge transport on the specific local composition of the network and on the correlation with the applied gate potential.

3. Conclusions

We studied the charge transport in FETs based on nearly monochiral (6,5) SWCNT networks and on a multichiral network with five different chiralities on a microscopic scale using CMM. By measuring local charge modulation spectra and mapping the signal distribution within the FET channel, we could visualize how free carriers are spatially distributed in the device under operating conditions. In particular, we provide direct evidence that both holes and electrons are preferentially moving along the same percolation paths. For the case of the monochiral network, we highlight non-linear local changes of

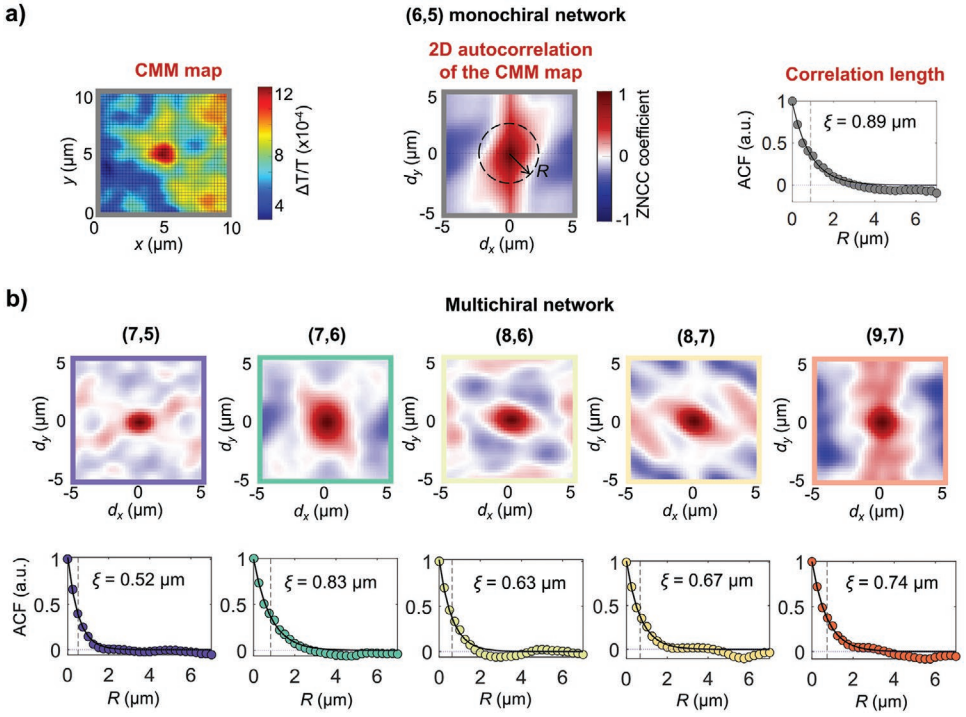

Figure 6. a) Procedure to extract the correlation length from the CMM map of the (6,5) monochiral network (V_{os} = –0.6 V, corresponding to Figure 3a). First, the 2D autocorrelation function is obtained by computing the zero-mean normalized cross-correlation of the CMM map with itself as a function of the spatial shift (d_x, d_y). Hence, the autocorrelation as a function of the distance from the origin, $R = \sqrt{d_x^2 + d_y^2}$, is computed by averaging the points of the 2D autocorrelation map at the same R. The data are fitted with an exponential function, $f = k \cdot \exp(-R/\xi)$, where $k \approx 1$ and ξ is the correlation length. b) The same procedure is applied to the CMM maps of the five species composing the multichiral network (Figure 5a–e), deriving the corresponding 2D autocorrelation functions and correlation lengths.

charge density distribution in the subthreshold regime when the gating potential is progressively increased. While in monochiral networks we observed a moderate dependence of the charge distribution on the network density, in multichiral networks the charge transport is influenced more by the energy barriers between SWCNTs with different band gaps. We analyzed the 2D ACFs of the CMM maps for the (6,5) monochiral network and for all the five nanotube chiralities present in the mixed network. This allowed us to estimate a correlation length, ξ, associated with the average extent of charge percolation paths. The value of ξ for the CMM map of the monochiral network is larger than for the maps of the five species in the multichiral network, which is consistent with the presence of more extended percolation pathways beneficial to charge transport. The correlation length derived from the CMM maps of each species present in the multichiral network can be related to the average distance traversed by a charge carrier on nanotubes of the same chirality before it eventually tunnels onto another species. Such a distance is on average longer for SWCNTs with large diameters (hence, narrow band gap), while the most fragmented percolation paths are observed for species with the smallest diameter (larger band gap). Overall, CMM emerges as a valuable technique to investigate the local charge transport properties of random SWCNT networks and to identify critical length scales in solution-processed thin film devices.

4. Experimental Section

Monochiral (6,5) SWCNT Dispersion: Essentially monochiral dispersions of (6,5) SWCNTs in toluene were obtained from CoMoCAT SWCNT raw material (CHASM Advanced Materials Inc., SG65i-L58) via selective polymer-wrapping with PFO-BPy (American Dye Source, M_w = 34 kg mol^{-1}) under shear force mixing as described previously.[11] Shear force mixing (Silverson L2/Air mixer) was applied at 10 230 rpm for 72 h at a constant temperature of 20 °C. Then, the dispersion was centrifuged twice for 45 min at 60 000 *g* (Beckman Coulter Avanti J26XP centrifuge), and the supernatant was filtered with a polytetrafluoroethylene (PTFE) syringe filter (pore size 5 µm) to remove the undispersed material and aggregates. SWCNTs were collected by filtration through a PTFE filter (Millipore JVWP, pore size 0.1 µm) and the filter cake was washed with hot toluene to remove excess unwrapped polymer. Ultimately, the filter cake was immersed in 1 mL of toluene and bath sonicated for 30 min to obtain the ink, which appears of purple color with OD of 10 cm^{-1} at the E_{11} transition.

Multichiral SWCNT Dispersion: Multichiral SWCNT dispersions in toluene were obtained by polymer-wrapping with poly(9,9-dioctylfluorene) (PFO, Sigma Aldrich, M_w > 20 kg mol^{-1}) from HiPco SWCNT raw material (Unidym Inc., batch no. 2172) using bath sonication (45 min) as exfoliation method. The resulting suspension was centrifuged for 45 min at 60 000 × *g* (Beckman Coulter Avanti J26XP centrifuge), and the supernatant was collected. The pellet was recycled twice, and the supernatants were combined to increase the overall yield. The PFO-wrapped SWCNTs were sedimented by ultracentrifugation for 20 h at 284 600 × *g* (Beckman Coulter Optima XPN-80 centrifuge), and the obtained SWCNT pellet was washed with tetrahydrofuran (THF) and re-dispersed in 1 mL of toluene via bath sonication for 30 min to obtain a greenish dispersion.

Device Fabrication: SWCNT FETs were fabricated in a bottom-contact top-gate configuration. Source and drain interdigitated contacts (L = 20 µm, W = 10 mm) were patterned on glass substrates (Schott AG, AF32eco, 300 µm) using standard photolithography (LOR5B/S1813 double-layer resist), electron-beam evaporation of chromium (2 nm) and gold (30 nm), and lift-off in *N*-methyl pyrrolidone. Before depositing the SWCNT films, samples were cleaned by ultrasonication in acetone and 2-propanol (10 min each), followed by UV ozone treatment (Ossila E511, 10 min). Dense, monochiral (6,5) and multichiral SWCNT networks were deposited from the dispersions via a spin-coating process (2000 rpm, 30 s) that was repeated for three times with brief annealing steps (100 °C, 2 min) in between. The SWCNT films were rinsed with THF and 2-propanol to remove excess polymer. The SWCNTs outside of the channel area were removed using photolithography as detailed above and oxygen plasma treatment (Nordson MARCH AP-600/30, 100 W, 2 min). Samples were annealed at 300 °C for 1 h in inert atmosphere before deposition of the double-layer gate dielectric. First, a thin PMMA layer (≈11 nm) was spin-coated (4000 rpm, 1 min) on the SWCNTs film from a solution in *n*-butyl acetate (6 g L^{-1}). Then, atomic layer deposition (Ultratech Savanna S100) at 100 °C was used to deposit a hafnium oxide (HfO_x) layer (≈61 nm) which simultaneously served as encapsulant for the devices. The measured total capacitance of the dielectric layer was C = 120 nF cm^{-2} for the (6,5) SWCNT-based FET and C = 98 nF cm^{-2} for the multichiral SWCNT-based device. Finally, silver top gates (20 nm) were thermally evaporated through a shadow mask.

Characterization: AFM images were acquired on a Bruker Dimension Icon in ScanAsyst mode under ambient conditions. Baseline-corrected absorption spectra of SWCNT dispersions were measured on a Varian Cary 6000i UV–vis–NIR spectrometer. The transfer and output electrical characteristics of the FETs were measured with a semiconductor parameter analyzer (Agilent B1500A) in a nitrogen glove box on a Wentworth Laboratories probe station.

Charge Modulation Spectroscopy and Charge Modulation Microscopy: CMS measurements on the entire active area of the FETs were performed in vacuum (≈10^{-6} mbar) by modulating the gate voltage with a waveform generator (3390, Keithley), while both the source and drain electrode were grounded. A tungsten lamp was used as light source in combination with a monochromator to select the wavelength during the measurement, and the light transmission was measured with an InGaAs photodiode. The electrical signal was amplified through a trans-impedance amplifier (Femto DHPCA-100) and read with a DSP Lock-in amplifier (Stanford Research Systems SR830), synchronized to the wave generator.

CMM measurements were performed with a home-made setup, whose details are provided in the Figure S1, Supporting Information.

Zero-Mean Normalized Cross-Correlation Calculation: The signal in every pixel i of the A and B maps was previously standardized according to:

$$A_i = \frac{A_i - \mu_A}{\sigma_A}, \quad B_i = \frac{B_i - \mu_B}{\sigma_B} \tag{1}$$

where μ corresponded to the mean signal of the map, and σ to its standard deviation.

The ZNCC map C of the CMM/OD map A with the map B was calculated as:

$$C = A \times B = \mathcal{F}^{-1}\left\{\overline{\mathcal{F}\{A\}} \times \mathcal{F}\{B\}\right\} \tag{2}$$

where $\mathcal{F}$ denoted the Fourier transform.

The 2D cross-correlation maps were plotted as a function of the spatial shift (often called "lag") along the x- and y-axis (d_x and d_y, respectively), so that the origin corresponds to the zero-lag cross-correlation maps. The Matlab code that was implemented for this calculation is reported in the Supporting Information. Note that for $A = B$, the cross-correlation coincided with the 2D ACF of the map. From the 2D autocorrelation maps (2D-ACF), the radial average of the 2D-ACF was obtained by calculating the mean value of the ACF as a function of the distance R from the origin ($R = \sqrt{d_x^2 + d_y^2}$).

Supporting Information

Supporting Information is available from the Wiley Online Library or from the author.

Acknowledgements

This work was partially supported by the European Union's H2020-EU.4.b. – Twinning of research institutions "GREENELIT," grant agreement number 951747. The authors are thankful to Francesca Scuratti for preliminary CMM studies. S.P and M.J. thank Alessandro Luzio for fruitful discussions.

Conflict of Interest

The authors declare no conflict of interest.

Author Contributions

M.J. and S.P. contributed equally to this work. M.J. performed the electrical, CMS, and CMM measurements. S.P. and M.J. analyzed the data. N.F.Z. fabricated the field-effect transistors and performed AFM. S.P, M.J., and M.C designed the experiments. M.C and J.Z conceived the work. S.P. and M.J. wrote the manuscript. All the authors revised the manuscript and contributed to its discussion.

Data Availability Statement

The data that support the findings of this study are available from the corresponding author upon reasonable request.

Keywords

charge modulation microscopy, charge modulation spectroscopy, percolating networks, semiconducting carbon nanotubes, single-walled carbon nanotubes

Received: December 9, 2022
Revised: February 8, 2023
Published online:

[1] N. F. Zorn, J. Zaumseil, *Appl. Phys. Rev.* **2021**, *8*, 041318.
[2] G. Hills, C. Lau, A. Wright, S. Fuller, M. D. Bishop, T. Srimani, P. Kanhaiya, R. Ho, A. Amer, Y. Stein, D. Murphy, A. C. Arvind, M. M. Shulaker, *Nature* **2019**, *572*, 595.
[3] B. Shkodra, M. Petrelli, M. A. C. Angeli, D. Garoli, N. Nakatsuka, P. Lugli, L. Petti, *Appl. Phys. Rev.* **2021**, *8*, 041325.
[4] A. D. Franklin, M. C. Hersam, H.-S. P. Wong, *Science* **2022**, *378*, 726.
[5] J. Pan, F. Li, J. H. Choi, *J. Mater. Chem. B* **2017**, *5*, 6511.
[6] S. Lu, A. D. Franklin, *Nanoscale* **2020**, *12*, 23371.
[7] Y. Hu, L. M. Peng, L. Xiang, H. Zhang, *Acc. Mater. Res.* **2020**, *1*, 88.
[8] J. A. Fagan, C. Y. Khripin, C. A. S. Batista, J. R. Simpson, E. H. Hároz, A. R. H. Walker, M. Zheng, *Adv. Mater.* **2014**, *26*, 2800.
[9] J. A. Fagan, E. H. Hároz, R. Ihly, H. Gui, J. L. Blackburn, J. R. Simpson, S. Lam, A. R. H. Walker, S. K. Doorn, M. Zheng, *ACS Nano* **2015**, *9*, 5377.

[10] A. Nish, J.-Y. Hwang, J. Doig, R. J. Nicholas, *Nat. Nanotechnol.* **2007**, *2*, 640.
[11] A. Graf, Y. Zakharko, S. P. Schießl, C. Backes, M. Pfohl, B. S. Flavel, J. Zaumseil, *Carbon* **2016**, *105*, 593.
[12] J. Ding, Z. Li, J. Lefebvre, F. Cheng, G. Dubey, S. Zou, P. Finnie, A. Hrdina, L. Scoles, G. P. Lopinski, C. T. Kingston, B. Simard, P. R. L. Malenfant, *Nanoscale* **2014**, *6*, 2328.
[13] W. Talsma, A. A. Sengrian, J. M. Salazar-Rios, H. Duim, M. Abdu-Aguye, S. Jung, S. Allard, U. Scherf, M. A. Loi, *Adv. Electron. Mater.* **2019**, *5*, 1900288.
[14] T. Lei, I. Pochorovski, Z. Bao, *Acc. Chem. Res.* **2017**, *50*, 1096.
[15] F. Scuratti, J. M. Salazar-Rios, A. Luzio, S. Kowalski, S. Allard, S. Jung, U. Scherf, M. A. Loi, M. Caironi, *Adv. Funct. Mater.* **2021**, *31*, 2006895.
[16] S. P. Schießl, M. Rother, J. Lüttgens, J. Zaumseil, *Appl. Phys. Lett.* **2017**, *111*, 193301.
[17] L. Ding, Z. Zhang, S. Liang, T. Pei, S. Wang, Y. Li, W. Zhou, J. Liu, L. M. Peng, *Nat. Commun.* **2012**, *3*, 677.
[18] D. Yang, L. Li, X. Wei, Y. Wang, W. Zhou, H. Kataura, S. Xie, H. Liu, *Sci. Adv.* **2021**, *7*, eabe0084.
[19] X. Wei, S. Li, W. Wang, X. Zhang, W. Zhou, S. Xie, H. Liu, *Adv. Sci.* **2022**, *9*, 2200054.
[20] Q. Cao, M. Xia, C. Kocabas, M. Shim, J. A. Rogers, S. V. Rotkin, *Appl. Phys. Lett.* **2007**, *90*, 2005.
[21] J. Yoon, D. Lee, C. Kim, J. Lee, B. Choi, D. M. Kim, D. H. Kim, M. Lee, Y. K. Choi, S. J. Choi, *Appl. Phys. Lett.* **2014**, *105*, 212103.
[22] M. Brohmann, M. Rother, S. P. Schießl, E. Preis, S. Allard, U. Scherf, J. Zaumseil, *J. Phys. Chem. C* **2018**, *122*, 19886.
[23] M. Statz, S. Schneider, F. J. Berger, L. Lai, W. A. Wood, M. Abdi-Jalebi, S. Leingang, H.-J. Himmel, J. Zaumseil, H. Sirringhaus, *ACS Nano* **2020**, *14*, 15552.
[24] M. Rother, S. P. Schießl, Y. Zakharko, F. Gannott, J. Zaumseil, *ACS Appl. Mater. Interfaces* **2016**, *8*, 5571.
[25] A. Malhofer, M. Rother, Y. Zakharko, A. Graf, S. P. Schießl, J. Zaumseil, *Org. Electron.* **2017**, *45*, 151.
[26] F. Jakubka, S. B. Grimm, Y. Zakharko, F. Gannott, J. Zaumseil, *ACS Nano* **2014**, *8*, 8477.
[27] J. Zaumseil, F. Jakubka, M. Wang, F. Gannott, *J. Phys. Chem. C* **2013**, *117*, 26361.
[28] M. Brohmann, F. J. Berger, M. Matthiesen, S. P. Schießl, S. Schneider, J. Zaumseil, *ACS Nano* **2019**, *13*, 7323.
[29] Z. Li, J. Ouyang, J. Ding, *ACS Appl. Electron. Mater.* **2022**, *4*, 6335.
[30] V. Perebeinos, J. Tersoff, P. Avouris, *Phys. Rev. Lett.* **2005**, *94*, 027402.
[31] S. P. Schießl, X. De Vries, M. Rother, A. Massé, M. Brohmann, P. A. Bobbert, J. Zaumseil, *Phys. Rev. Mater.* **2017**, *1*, 046003.
[32] V. Derenskyi, W. Gomulya, W. Talsma, J. M. Salazar-Rios, M. Fritsch, P. Nirmalraj, H. Riel, S. Allard, U. Scherf, M. A. Loi, *Adv. Mater.* **2017**, *29*, 1606757.
[33] S. Schneider, J. Lefebvre, N. J. Diercks, F. J. Berger, F. Lapointe, J. Schleicher, P. R. L. Malenfant, J. Zaumseil, *ACS Appl. Nano Mater.* **2020**, *3*, 12314.
[34] N. F. Zorn, F. Scuratti, F. J. Berger, A. Perinot, D. Heimfarth, M. Caironi, J. Zaumseil, *ACS Nano* **2020**, *14*, 2412.
[35] D. Beljonne, J. Cornil, H. Sirringhaus, P. J. Brown, M. Shkunov, R. H. Friend, J. L. Brédas, *Adv. Funct. Mater.* **2001**, *11*, 229.
[36] G. Pace, I. Bargigia, Y. Y. Noh, C. Silva, M. Caironi, *Nat. Commun.* **2019**, *10*, 5226.
[37] T. Sakanoue, H. Sirringhaus, *Nat. Mater.* **2010**, *9*, 736.
[38] A. D. Scaccabarozzi, F. Scuratti, A. J. Barker, A. Basu, A. F. Paterson, Z. Fei, O. Solomeshch, A. Petrozza, N. Tessler, M. Heeney, T. D. Anthopoulos, M. Caironi, *Adv. Electron. Mater.* **2020**, *6*, 2000539.
[39] X. Y. Chin, G. Pace, C. Soci, M. Caironi, *J. Mater. Chem. C* **2017**, *5*, 754.
[40] C. Sciascia, N. Martino, T. Schuettfort, B. Watts, G. Grancini, M. R. Antognazza, M. Zavelani-Rossi, C. R. McNeill, M. Caironi, *Adv. Mater.* **2011**, *23*, 5086.
[41] N. Martino, D. Fazzi, C. Sciascia, A. Luzio, M. R. Antognazza, M. Caironi, *ACS Nano* **2014**, *8*, 5968.
[42] X. Y. Chin, J. Yin, Z. Wang, M. Caironi, C. Soci, *Sci. Rep.* **2014**, *4*, 3626.
[43] D. Fazzi, M. Caironi, *Phys. Chem. Chem. Phys.* **2015**, *17*, 8573.
[44] S. G. Bucella, A. Luzio, E. Gann, L. Thomsen, C. R. McNeill, G. Pace, A. Perinot, Z. Chen, A. Facchetti, M. Caironi, *Nat. Commun.* **2015**, *6*, 8394.
[45] J. S. Park, Y. Hirana, S. Mouri, Y. Miyauchi, N. Nakashima, K. Matsuda, *J. Am. Chem. Soc.* **2012**, *134*, 14461.
[46] R. Matsunaga, K. Matsuda, Y. Kanemitsu, *Phys. Rev. Lett.* **2011**, *106*, 037404.
[47] C. D. Spataru, F. Léonard, *Phys. Rev. Lett.* **2010**, *104*, 177402.
[48] K. H. Eckstein, F. Oberndorfer, M. M. Achsnich, F. Schöppler, T. Hertel, *J. Phys. Chem. C* **2019**, *123*, 30001.
[49] M. Brohmann, S. Wieland, S. Angstenberger, N. J. Herrmann, J. Lüttgens, D. Fazzi, J. Zaumseil, *ACS Appl. Mater. Interfaces* **2020**, *12*, 28392.
[50] F. Scuratti, J. M. Salazar-Rios, A. Luzio, S. Kowalski, S. Allard, S. Jung, U. Scherf, M. A. Loi, M. Caironi, *Adv. Funct. Mater.* **2021**, *31*, 2006895.
[51] I. A. Khan, A. R. M. N. Afrooz, J. R. V. Flora, P. A. Schierz, P. L. Ferguson, T. Sabo-Attwood, N. B. Saleh, *Environ. Sci. Technol.* **2013**, *47*, 1844.
[52] E. Sano, T. Tanaka, *J. Appl. Phys.* **2014**, *115*, 154507.

6. Stable and Solution-Processable Cumulenic sp-Carbon Wires: A New Paradigm for Organic Electronics

The content of this chapter is published in: [3]

S. Pecorario, A. D. Scaccabarozzi, D. Fazzi, E. Gutiérrez-Fernández, V. Vurro, L. Maserati, M. Jiang, T. Losi, B. Sun, R. R. Tykwinski, C. S. Casari, M. Caironi, Stable and Solution-Processable Cumulenic sp-Carbon Wires: A New Paradigm for Organic Electronics, *Adv. Mater*. 2022, *34*, 2110468.

Authors contributions:

S. Pecorario designed the experiments, optimized the thin film deposition of tetraphenyl[3]cumulene ([3]Ph), fabricated the field-effect transistors, performed the electrical characterization, AFM, absorption spectroscopy, polarized optical microscopy, contributed to the GIWAXS discussion, and wrote the manuscript.

A. D. Scaccabarozzi supervised the work and contributed to the analysis of the GIWAXS experiments. D. Fazzi performed the DFT calculations. E. Gutiérrez-Fernández performed the GIWAXS measurements and analysed the related data. V. Vurro contributed to the photodegradation experiments. L. Maserati and M. Jiang contributed to the design of the setup and to the measurement of local polarized absorption spectra. T. Losi contributed to the fabrication of preliminary [3]Ph-based field effect transistors, B. Sun and R. R. Tykwinski synthesized [3]Ph, C. S. Casari and M. Caironi conceived the work and supervised it. All the authors revised the manuscript and contributed to its discussion.

Stable and Solution-Processable Cumulenic sp-Carbon Wires: A New Paradigm for Organic Electronics

*Stefano Pecorario, Alberto D. Scaccabarozzi, Daniele Fazzi, Edgar Gutiérrez-Fernández, Vito Vurro, Lorenzo Maserati, Mengting Jiang, Tommaso Losi, Bozheng Sun, Rik R. Tykwinski, Carlo S. Casari, and Mario Caironi**

Solution-processed, large-area, and flexible electronics largely relies on the excellent electronic properties of sp^2-hybridized carbon molecules, either in the form of π-conjugated small molecules and polymers or graphene and carbon nanotubes. Carbon with sp-hybridization, the foundation of the elusive allotrope carbyne, offers vast opportunities for functionalized molecules in the form of linear carbon atomic wires (CAWs), with intriguing and even superior predicted electronic properties. While CAWs represent a vibrant field of research, to date, they have only been applied sparingly to molecular devices. The recent observation of the field-effect in microcrystalline cumulenes suggests their potential applications in solution-processed thin-film transistors but concerns surrounding the stability and electronic performance have precluded developments in this direction. In the present study, ideal field-effect characteristics are demonstrated for solution-processed thin films of tetraphenyl[3]cumulene, the shortest semiconducting CAW. Films are deposited through a scalable, large-area, meniscus-coating technique, providing transistors with hole mobilities in excess of 0.1 $cm^2 V^{-1} s^{-1}$, as well as promising operational stability under dark conditions. These results offer a solid foundation for the exploitation of a vast class of molecular semiconductors for organic electronics based on sp-hybridized carbon systems and create a previously unexplored paradigm.

1. Introduction

The synthesis of novel organic semiconductors, along with advances in processing techniques and device engineering, has boosted the field of large-area flexible and printed electronics. These advances have enabled a plethora of applications such as organic light-emitting diodes,[1,2] organic photovoltaics,[3,4] organic thermoelectrics,[5,6] organic field-effect transistors (OFETs),[7–10] organic (bio)sensors,[11–13] and neuromorphic devices.[14,15] In this context, organic field-effect transistors (OFETs) are not only relevant for their direct technological application, but they also represent an ideal test-bed to investigate thin-film electrical properties. Organic semiconductors are typically classified in two main families, namely conjugated polymers and small molecules. The former, polymers, are particularly appealing as a result of their solution processability, and OFETs with charge mobility above the standard for hydrogenated amorphous silicon (0.5–1 $cm^2 V^{-1} s^{-1}$) have been extensively reported.[16] The latter, small molecules, are prone to arrange in ordered molecular crystals, and through several years of chemical tailoring and fine tuning of the films processing, small-molecule OFETs with field-effect mobility >10 $cm^2 V^{-1} s^{-1}$ have been achieved.[17–19] The chemical root of the π-conjugation of these materials is associated with the sp^2-hybridization of carbon atoms in their backbone. This peculiar trait is also common to

S. Pecorario, A. D. Scaccabarozzi, V. Vurro, L. Maserati, M. Jiang, T. Losi, M. Caironi
Center for Nano Science and Technology@PoliMi
Istituto Italiano di Tecnologia
via Giovanni Pascoli 70/3, Milano 20133, Italy
E-mail: mario.caironi@iit.it

The ORCID identification number(s) for the author(s) of this article can be found under https://doi.org/10.1002/adma.202110468.

DOI: 10.1002/adma.202110468

S. Pecorario, C. S. Casari
Department of Energy
Micro and Nanostructured Materials Laboratory – NanoLab
Politecnico di Milano
Via Ponzio 34/3, Milano 20133, Italy

D. Fazzi
Department of Chemistry "Giacomo Ciamician"
Università di Bologna
Via F. Selmi, 2, Bologna 40126, Italy

E. Gutiérrez-Fernández
POLYMAT
University of the Basque Country
UPV/EHU, Av. de Tolosa 72, San Sebastián 20018, Spain

B. Sun, R. R. Tykwinski
Department of Chemistry
University of Alberta
Edmonton, AB T6G 2G2, Canada

low-dimensional carbon nanostructures that show exceptional (opto-)electronic properties, such as graphene, fullerenes, and carbon nanotubes.[20–23]

There exists an alternative class of π-conjugated molecules with backbones formed from sp-hybridized carbon atoms. Known as carbon atom wires (CAWs) or linear carbon chains, these molecules are regarded as an oligomeric form of the so-called "carbyne," a purely one-dimensional carbon allotrope made of an infinite chain of sp-carbons.[24] Several theoretical and computational studies have predicted remarkable properties for carbyne, such as an exceptional Young's modulus[25] and a high surface area,[26] as well as significant optical absorption,[27] thermal conductivity,[28] nonlinear optical properties,[29–32] and charge mobilities, which might rival those of graphene and carbon nanotubes.[33] For decades, chemists have been attempting to overcome the chemical reactivity of molecules composed of sp-carbon, developing syntheses to provide longer and longer CAWs in the ultimate pursuit of the "carbyne" limit.[34–37] A successful approach to stable CAWs in powder form consists of endcapping the sp-carbon chain with bulky terminal groups that prevent chain cross-linking through steric hindrance. Endgroups are also exploited to control the bond-length alternation (BLA) of the CAWs that, in turn, affects the vibrational, optical, and electronic properties.[24,38–42] Indeed, two isomeric structures of CAWs are possible based on BLA: cumulenes, displaying a sequence of quasi-double bonds (BLA < 0.1 Å) and oligoynes with a sequence of alternated single and triple bonds (BLA > 0.1 Å). The structure of cumulenes enables extensive π-electron delocalization along the backbone, resulting in a lowering of the HOMO-LUMO gap. On the contrary, the bond alternated structure of oligoynes is characterized by localization of π-electrons on the triple bonds, which accounts for a larger HOMO-LUMO gap. While recently long oligoynes with a record length of 48 sp-carbons have been successfully isolated,[37] the synthesis and handling of long cumulenes is more problematic due to a drastically increased reactivity with the chain length, and [9]cumulenes (i.e., CAWs with 9 consecutive double bonds) are the longest derivatives reported so far.[43] Despite challenges posed by chemical instability, there is a growing interest in exploiting CAWs in molecular electronics and optoelectronics,[44] justified by intriguing evidence such as increased conductance with longer cumulene length.[45–48]

Surprisingly, the properties of oligoynes and cumulenes in thin films toward large-area electronics remain almost completely unknown.[44,49,50] Recently, the first OFETs based on tetraphenyl[3]cumulene (also known as tetraphenylbutatriene and with the abbreviated form [3]Ph, which will be used hereafter) have been demonstrated. A simple drop-casting procedure gave micrometers-long, needle-like molecular crystals of [3]Ph.[51] Being the shortest of the cumulenes series, [3]Ph is constructed of three cumulated carbon-carbon double bonds (BLA = 0.088 Å) and it is terminated at each end by two phenyl groups (**Figure 1**a). This short cumulene was selected as a model material because it can be synthesized on a gram scale, it is soluble in organic solvents, thermally stable up to 250 °C, and characterized by an optical gap in the visible range (properties are summarized in Table S1 in the Supporting Information). A random network of [3]Ph microcrystals shows clear p-type semiconducting behavior, with a field effect mobility conservatively estimated to be $\approx 2 \times 10^{-3}$ cm^2 V^{-1} s^{-1}.[51] The needle-like texture, despite exhibiting a remarkable crystallinity, presents intrinsic limits associated with poor coverage of the active area, inadequate carrier injection, and the presence of hysteresis in the transfer curve characteristics. Furthermore, the stability of [3]Ph-based OFETs in operational conditions represents a natural challenge that needs to be addressed. Therefore, serious questions and concerns remain for the credible adoption of sp-hybridized molecules for solution-processed thin-film electronics.

Herein, we provide proof that transistors can be based on solution-processed polycrystalline cumulenic thin films, with charge carrier mobilities close to that of a:Si and promising stability in dark-conditions. In particular, we present OFETs based on thin films of [3]Ph deposited from solution via a scalable, large-area wire-bar coating technique, and we analyze the impact of the deposition temperature on morphological, optical, structural and electrical properties of the films by means of extensive structural and electrical characterization. The optimized deposition temperature for [3]Ph (i.e., 80 °C) provides a higher degree of crystallinity, as well as fewer defects. The resulting devices show field-effect mobility values exceeding 0.1 cm^2 V^{-1} s^{-1}, in both the linear and saturation regime, marking an improvement of two orders of magnitude relatively to previous studies on sparse microcrystalline networks.[51] Supported by density functional theory (DFT)/time-dependent DFT (TD-DFT) calculations, we emphasize that the measured mobilities represent a lower bound to the intrinsic mobility of [3]Ph as the result of marked charge transport anisotropy, the lack of preferential orientation in the plane of the films, and the presence of grain boundaries in polycrystalline films. Finally, transistors based on [3]Ph show promising ambient stability under dark conditions, therefore addressing a major concern for the effective application of sp-based semiconducting molecules in electronic devices. These findings establish cumulenic sp-carbon atom wires as promising class of organic semiconductors for large-area, printed electronics.

2. Results

2.1. Deposition and Characterization of Thin Films

To investigate the potential of cumulenes toward large-area printed electronics, we began by optimizing the deposition of thin films of [3]Ph from solution (10 g L^{-1} in 1,2-dichlorobenzene) employing wire-bar coating, which is a scalable bar-assisted meniscus-shearing technique (Figure 1b).[52–54] The deposition temperature has a strong impact on the crystallization of solution-processed small-molecule organic semiconductors, which in turn defines the charge transport characteristics in the solid state.[55,56] Accordingly, we systematically varied the deposition temperature using a heating bed and examined the impact on the optical, morphological, structural, and electrical properties of the thin films. The choice of a high-boiling-point solvent such as 1,2-dichlorobenzene led to homogeneous thin films with excellent coverage over an area of 2 cm^2 and a wide range of deposition temperatures, spanning from 50 to 110 °C.

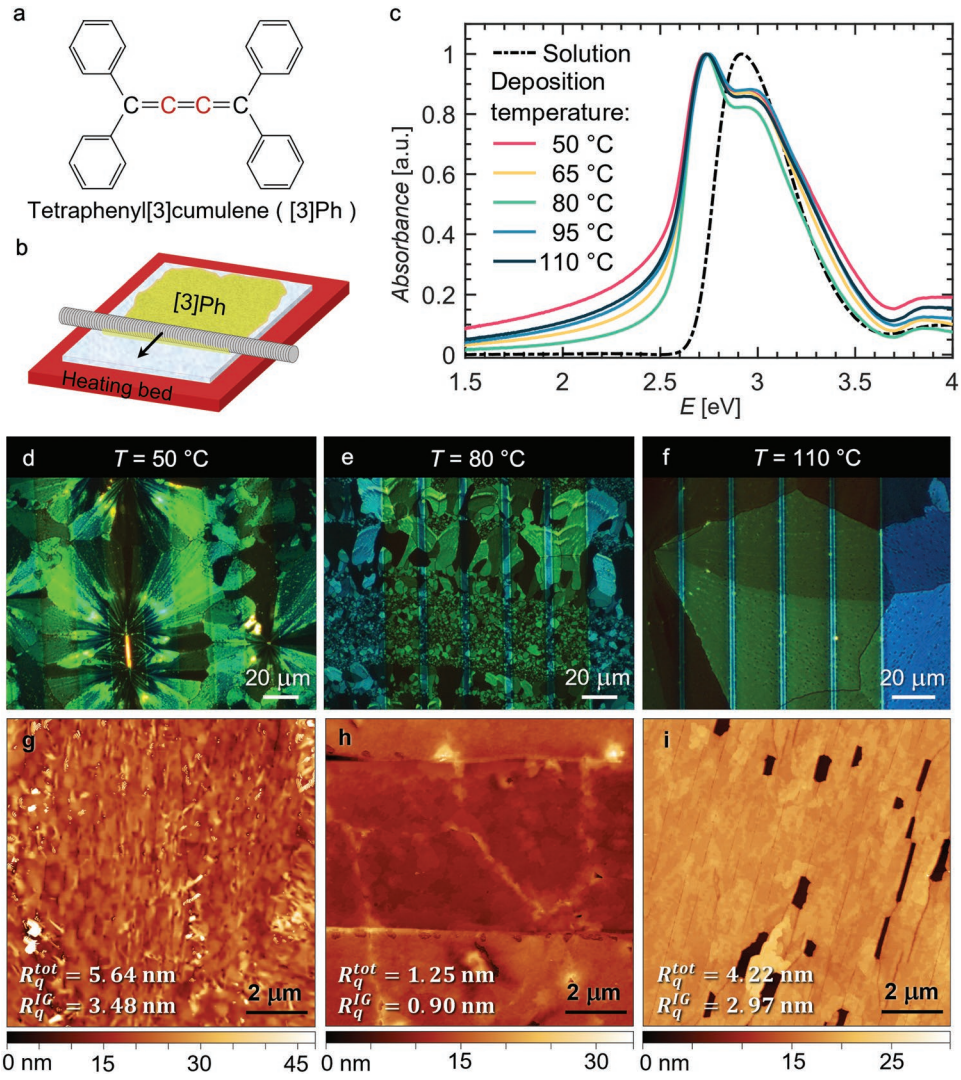

Figure 1. a) Molecular structure of [3]Ph. The sp-hybridized carbons constituting the cumulenic backbone are indicated in red. b) Scheme of the deposition of large-area [3]Ph thin films from solution (10 g L^{-1} in 1,2-dichlorobenzene) on a glass substrate via wire-bar coating. c) Normalized absorption spectra of [3]Ph in solution (10^{-4} M in 1,2-dichlorobenzene, dashed black line) and of thin films deposited at different temperatures (full colored lines). d–f) POM images of films of [3]Ph bar coated on top of gold interdigitated source and drain electrodes at 50, 80, and 110 °C, respectively. g–i) AFM topographies of films of [3]Ph deposited at 50, 80, and 110 °C, respectively. The derived root-mean-square roughness values are reported, distinguished in intragrain roughness (R_q^{IG}) and total roughness (R_q^{tot}).

To assess aggregation in thin films, we compared the UV–vis absorption spectra of [3]Ph in a dilute solution (Figure 1c, black dotted line) and in films deposited at different temperatures (Figure 1c, colored solid lines). In solution, only one intense absorption peak at 2.92 eV characterizes the low energy region of the spectrum. For thin films, on the other hand, two absorption bands are observed at 2.73 eV and 2.97 eV, with the former significantly red-shifted and the latter slightly blue-shifted with respect to the absorption band in solution (Figure S1, Supporting Information). The intense peak at 2.73 eV has been attributed to the occurrence of intermolecular interactions of [3]Ph in the solid state.[51,57] All of the absorption spectra of thin films have bands located at the analogous energies, suggesting a common intermolecular arrangement independent of the deposition temperature.

From a morphological point of view, the films of [3]Ph are polycrystalline and display a clear variation in the crystalline grain dimensions depending on the deposition temperature, which can be appreciated by the polarized optical microscopy (POM) images of films deposited at 50, 80, and 110 °C (Figure 1d–f and Figure S2, Supporting Information). Based on mechanical profilometry and atomic force microscopy (AFM) analyses (Figure 1g–i), we determined that the film thickness varies, on average, between 15 and 30 nm, with a slight thinning of films deposited at higher temperatures. The films deposited at 50 °C present spherulitic-like structures, measuring tens of micrometers, which grow radially from a central nucleation site and produce the characteristic Maltese crosses (Figure 1d). In addition, needle-like crystals are visible on the surface, resembling on a smaller scale the long crystals formed by drop-casting (Figure S3, Supporting Information).

The films deposited at 80 °C appear more homogeneous and feature few micrometer-scale 2D crystalline grains and no needle-like crystals (Figure 1e). The increased homogeneity and

smaller grain size can be rationalized in terms of faster solvent evaporation and reduced time for nucleation and crystal growth.[58–60] Further increasing the temperature to 110 °C leads to films with qualitatively similar 2D grains, although the grain size is increased up to several tens of micrometers (Figure 1f). The latter is likely associated with the higher deposition temperature, which can lead to an increased rate of crystallization, according to the bell-shaped nature of the crystallization rate as a function of temperature.[61,62]

The surface morphology of the films was further investigated by AFM. The spherulitic structures, typical of films deposited at 50 °C, present a rough surface, predominantly due to the small needle-like crystals that abound close to the grain boundaries (Figure 1g and Figure S4, Supporting Information). The 2D crystalline grains obtained at 80 °C have a much smoother surface, and it is even possible to identify terraces with regular steps with a height of about 1 nm (Figure S5, Supporting Information), which is compatible with the thickness of a single monolayer of [3]Ph molecules stacked with the sp-chain parallel to the substrate (further details provided with crystalline structure analysis, vide infra). Finally, the larger grains of the films deposited at 110 °C include lines of defects and pits, as evident in Figure 1i, which relates to a topographic image acquired within the same grain (see also Figure S6a,b, Supporting Information). These defects might originate from the cracking of the films due to the rapid cooling from 110 °C to ambient temperature. We derived the root-mean-square roughness values of the films (R_q) and distinguished between the intragrain roughness (R_q^{IG}), considering only the portion inside a single-crystalline grain, and the total one (R_q^{tot}), which includes more crystalline domains and the grain boundaries. A detailed illustration of the roughness extraction procedure is provided in Figures S4–S6 in the Supporting Information. Importantly, the small 2D grains distinctive of the deposition at 80 °C have a total roughness that is even lower than the intragrain roughness of the films deposited at 50 and 110 °C.

To investigate the structural arrangement of the [3]Ph molecules in thin films, we performed grazing-incidence wide-angle X-ray scattering (GIWAXS) measurements on films obtained at the various deposition temperatures (**Figure 2**a–c, Supporting Information). The presence of bright, point-like diffraction peaks corroborates crystallinity and anisotropy of the films with respect to the substrate. The assignment of Miller indices is provided in Figure S7 in the Supporting Information. The unit cell is reported to be triclinic and formed by a basis of two [3]Ph molecules closely packed as illustrated in the 2 × 2 supercell representation of Figure 2d,e.[63] Regardless of deposition temperature, the diffraction patterns of the films fit well with the single-crystal structural analysis,[51,63] meaning that the crystal structure of the single crystal is retained in the polycrystalline thin films. From the angular position of the peaks in the diffractograms (in-plane/out-of-plane diffractions reported in Figure S8 in the Supporting Information), it is possible to determine the orientation of the lattice axis. In this regard, the location of the (001) reflection in the out-of-plane direction (Q_Z = 6.22 nm^{-1}) are associated with a *d*-spacing of 1.01 nm and indicates that the molecules are stacked along the normal direction of the substrate plane and separated by the phenyl groups. At the same time, the reflections (200) at Q = 12.8 nm^{-1} and (120) at Q = 16 nm^{-1}, are associated with shorter packing

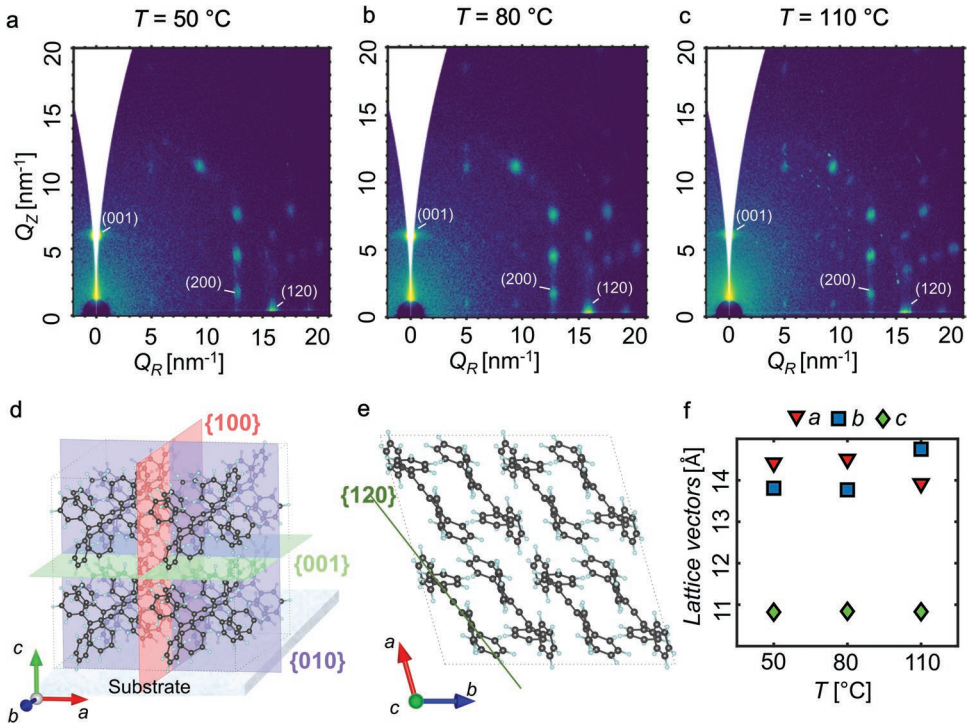

Figure 2. a–c) GIWAXS patterns of thin films of [3]Ph deposited at 50, 80, and 110 °C, respectively. d) Graphical representation of the crystal orientation of [3]Ph (2 × 2 supercell) with respect to the substrate; molecules are aligned with the cumulenic backbone quasi-parallel to the substrate. e) Portrayal of the in-plane lamellar molecular stacking of [3]Ph. f) Length of the lattice vectors as a function of the deposition temperature.

distances located near the Q_R axis. These reflections correspond to the diffraction along the sp-chains π-stacking and indicate that the cumulene π-stacking occurs parallel to the substrate (Figure 2d,e). Furthermore, the presence of Bragg rods confirms that the *a* and *b* vectors of all grains lie in the substrate plane, while the azimuthal orientation is random.[64] This arrangement is consistent with the polycrystalline nature of the films, as previously observed based on the POM images. Interestingly, the computed unit cell based on the GIWAXS pattern of thin films deposited at 110 °C shows a contraction along the *a*-axis and an elongation along the *b*-axis, with respect to films cast at lower temperatures (Figure 2f, details in Figure S9 and Table S2 in the Supporting Information). Instead, the molecular distance along the *c*-axis is not affected by the deposition temperature.

2.2. Excitonic and Electronic Molecular Couplings

DFT/TD-DFT calculations on a single molecule and on molecular dimers were performed to correlate the excited-state properties with the molecular packing and to provide insight into the optical absorption changes upon film deposition (Figure 1c). The low-energy computed dipole active excited state for a single molecule of [3]Ph is 3.13 eV. Exciton splitting occurs upon aggregation (i.e., passing from the single molecule to the dimer model), thus resulting in a higher and a lower energy state.[65] In the dimer-based analysis, we considered all nearest neighbor molecules that could be extracted from the crystalline structure (**Figure 3**a,b) and computed the low-energy excited states for each of them (Table S3, Supporting Information). Three molecular dimers, designated dimer 1 (D1), dimer 3 (D3), and dimer 4 (D4) mainly contribute to the excitonic properties in crystals of [3]Ph. Dimer D1 is representative of the π–π face-to-face interaction between cumulenic chains, and it lies along the *b*-axis of the crystal. Dimers D3 and D4 show a head-to-tail interaction between the chains and are oriented in the *ab*-plane of the crystal. Accordingly, D1 shows very different excitonic properties in comparison to D3 and D4, as revealed by TD-DFT calculations. For D1 the computed high- and low-energy states are at 3.17 and 2.99 eV, for D3 and D4 they are at 3.17 and 3.07 eV (Table S3, Supporting Information). Due to the molecular packing, D1 represents the prototypical H-type aggregate, with the high-energy state (3.17 eV) that is dipole active, while D3 and D4 represent J-type aggregates, with a bright, low-energy state at 3.07 eV (Figure S10, Supporting Information). Figure 3c reports the computed active electronic transition energies for the single molecule (S, black), D1 (yellow), D3 (orange) and D4 (green). Dimers D3 and D4 show a higher oscillator strength than D1, both being more intense than the single molecule case.

The low-energy absorption band observed for [3]Ph in dilute solution (2.92 eV) is thus assigned to the single molecule transition. On the other hand, the low-energy band observed in solid-state thin films (2.73 eV) corresponds to the D3- and D4-like dimers (i.e., J-type) and the high- energy band (2.97 eV) to D1-like dimers (i.e., H-type). With two types of aggregates oriented in different crystallographic directions, the low-energy band is polarized along D3 and D4, i.e., in the *ab*-plane, while the high-energy band is polarized along D1, i.e., the *b*-axis (Figure S11, Supporting Information).

Based on a molecular dimer approach, we computed the charge transfer integrals (V_{ij}) at the DFT level for a hole transport mechanism, and this correlates well with experimentally observed results for OFETs of [3]Ph (see Section 2.3; details in the Experimental Section). V_{ij} is a measure of the electronic

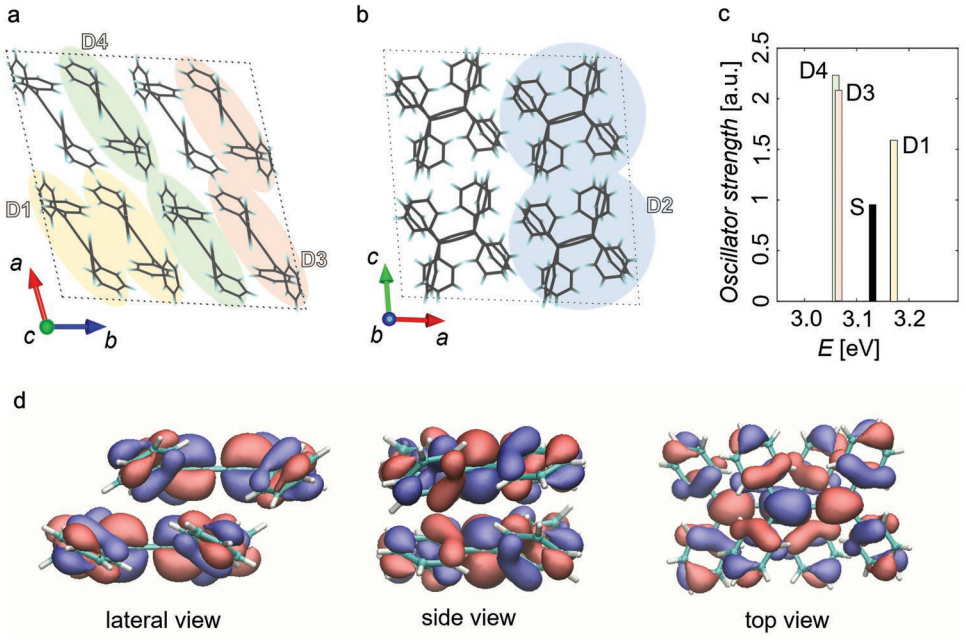

Figure 3. a,b) Schematic views of the molecular dimers extrapolated from the crystal structure by considering the nearest neighbor molecules in the *ab*-plane (a) and in the *ac*-plane (b). c) TD-DFT-computed allowed electronic transitions for the single molecule (S, black), dimer D1 (yellow), dimer D3 (orange) and dimer D4 (green). d) DFT-computed highest occupied molecular orbital (HOMO, isosurface 0.01 a.u.) for dimer D1.

coupling (e.g., overlap) between the charge-carrier wavefunction of nearest neighbor sites (i and j).[66,67] Within the hopping regime, higher values of V_{ij} designate higher transfer rates between hopping sites. For [3]Ph, the highest hole V_{ij} is computed for D1, being 46 meV, followed by D2 and D3, both at 13 meV, while V_{ij} for D4 is negligible (Table S4, Supporting Information). Such electronic couplings suggest anisotropic charge transport within the crystal, with hole percolation occurring mainly along the direction of D1 (b-axis) and corresponding to the π-stacking direction of the sp-chain (Figure 3a). Notably, the increased spacing along the b-axis, as observed from GIWAXS measurements for films deposited at 110 °C (Figure 2f and Figure S9, Supporting Information) suggests a lower electronic coupling for D1, thus indicating a less favorable platform for the charge transport under these deposition conditions. Charge transfer is also possible along the D2 (c-axis) and the D3 directions (a-axis), but with a lower probability than along D1.

To elucidate the importance of the sp-conjugated backbone in contributing to charge transport, the HOMO and LUMO isosurfaces for [3]Ph are reported in Figure S12a in the Supporting Information. The molecular orbitals are delocalized over the carbon chain. Furthermore, the conjugation of the sp-chain extends to the phenyl groups, which is consistent with previous evidence for cumulenic chains with varied chain lengths and end-groups.[39] The computed hole reorganization energy for [3]Ph is equal to 0.366 eV and is comparable to common organic semiconductors based on sp^2-hybridized carbon scaffolds in organic electronics, such as oligothiophenes and acenes.[68,69] The major structural reorganization process occurring upon charging (i.e., adding a hole) involves the carbon chain, namely a variation of the bond length alternation (Figure S12b, Supporting Information). Additionally, Figure 3d depicts the HOMO orbital of dimer D1, which shows the highest hole transfer integral. The overlap between the orbitals of the two carbon chains can be easily observed, thus confirming the importance of the carbon backbone in determining and tuning the overall magnitude of the transfer integral for sp-systems.

2.3. [3]Ph-Based OFETs

Top-gate bottom-contact FETs were fabricated to investigate the electrical transport properties and ultimately evaluate the charge mobility in solution-processed [3]Ph polycrystalline thin films (**Figure 4**a). A solution of [3]Ph was deposited onto a glass substrate patterned with gold interdigitated source and drain electrodes using bar-coating at deposition temperatures ranging from 50 to 110 °C. For each deposition temperature, at least 14 devices were fabricated, with channel lengths (L) ranging from 2.5 to 40 µm and channel widths (W) from 0.2 to 2 mm. Parylene-C was selected for the dielectric layer. Finally, PEDOT:PSS gate contacts were inkjet-printed on top of the dielectric as the last step.

The characteristic transfer curves in the linear (V_{ds} = −5 V, black curve) and saturation (V_{ds} = −40 V, blue curve) regimes of a representative, optimized device measured in nitrogen atmosphere are shown in Figure 4b (films deposited at 80 °C). The

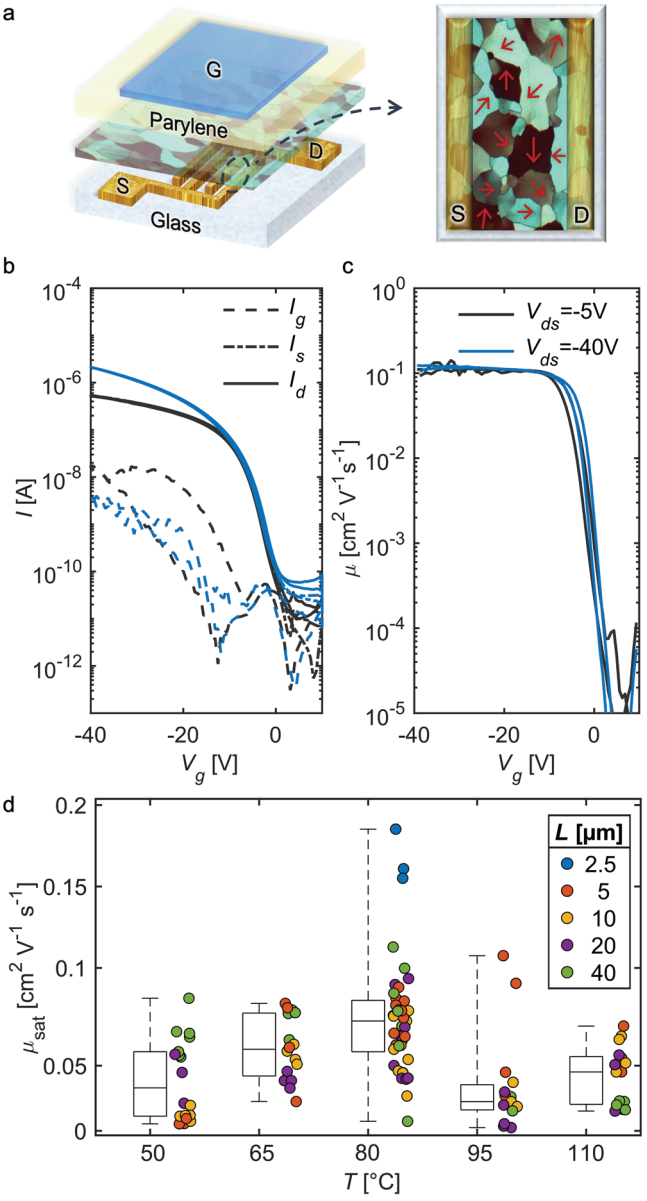

Figure 4. a) Structure of the OFETs fabricated with thin films of [3]Ph: source and drain electrodes are constructed from photolithographically patterned gold; a 450 nm-thick layer of Parylene-C serves as the dielectric layer (C_{diel} = 5.7 nF cm^{-2}) and the PEDOT:PSS gate electrode was inkjet printed. The inset represents the random azimuthal orientation of the crystalline grains within the channel area, with the red arrows oriented along the preferential transport direction in the respective domain. b) Transfer characteristic curves in the linear (V_{ds} = −5 V, in black) and saturation regimes (V_{ds} = −40 V, in blue) representative of optimized OFETs, with a channel width W = 200 µm and channel length L = 40 µm, based on a film of [3]Ph deposited at T = 80 °C. c) Corresponding charge mobilities as a function of the gating potential V_g. d) Charge mobilities extracted in saturation regime (V_{ds} = −40 V) as a function of the deposition temperature. At least 14 devices were tested for each deposition temperature. Each boxplot in this figure extends from the 25th to the 75th percentile of the distribution of measured mobilities, with the central bar indicating the median and the whiskers spanning from the minimum to the maximum values. The mobility values of all the transistors are reported next to each box-plot.

curves show unipolar p-type behavior, negligible hysteresis, and ideal linear (square root) behavior of current as a function of the gate voltage in the linear (saturation) regime (Figure S13, Supporting Information). The ideality of the characteristic curves confirms robust hole mobility extraction, which is identical in the linear and saturation regime, almost independent of the gate potential (V_g) above threshold, and values as high as 0.11 $cm^2 V^{-1} s^{-1}$ (Figure 4c). The mobility values extracted in the saturation regime as a function of the deposition temperature are shown in Figure 4d. The highest-performing films are those deposited at 80 °C, with an average saturation mobility of 0.08 $cm^2 V^{-1} s^{-1}$ and a maximum value of 0.19 $cm^2 V^{-1} s^{-1}$. This superior performance can be rationalized by considering that the 2D crystalline grains obtained from deposition at 80 °C show the lowest surface roughness and the lowest defectivity. The trend of the absorption tail of thin films as a function of the deposition temperature, as well as of the relative intensity of the absorption peaks assigned to the single-molecule and to the molecular aggregates, also support this hypothesis (Figure S1, Supporting Information). It is noteworthy that even though deposition at 110 °C leads to larger crystalline grains and fewer grain boundaries, the elongation of the crystalline structure along the *b*-axis decreases the electronic coupling, thus reducing the charge-carrier mobility. The mobility values obtained in this study represent a remarkable improvement of two orders of magnitude with respect to previous field-effect transistors based on [3]Ph.[51]

Given the ideality of the devices, mobility values have a reliability factor (*r*) close to 1.[70] The I_{on}/I_{off}, computed as the ratio between the highest and the lowest drain current values in the transfer characteristic curve, spans from 5×10^4 to 10^6; this variability is a direct consequence of the wide range of channel lengths (*L*) that have been tested (Figure S14, Supporting Information). The complete set of parameters derived from the electrical characterization of the optimized devices deposited at 80 °C are listed in Table S5 in the Supporting Information.

We evaluated the contact resistance per unit width ($R_c W$) by the transmission-line method (TLM),[71,72] resulting in $R_c W$ = 41 kΩ cm with V_g = –40 V (Figure S15 and Table S6, Supporting Information). The contact resistance comprises two contributions: the Schottky barrier at the metal-semiconductor interface and the access resistance.[73,74] The former originates from the energy mismatch between the HOMO level of [3]Ph (≈–5.48 eV as estimated by cyclic voltammetry, Table S1, Supporting Information) and the work function of the gold contacts (nominally at around 5.1 eV[75]). The latter is due to the vertical transport between the contacts and the active channel at the semiconductor–dielectric interface, which occurs along the *c*-axis; as previously discussed, charge transport in this crystallographic direction is less effective than in the *ab*-plane. The impact of the contact resistance on the electrical characteristics of the devices is discussed quantitatively in Figure S15b,c in the Supporting Information. The effect of contact resistance on device performance is minimized with sufficiently long channel lengths ($L > 10$ μm), at which point the channel resistance R_{ch} is dominating (Figures S15 and S16, Supporting Information). Non-ideal behavior, e.g., a discrepancy in the mobility extracted in linear and saturation regimes, begins to appear in devices with L = 2.5 μm (Figure S14, Supporting Information). High contact resistance may explain the high threshold voltage values (on average, –8.6 V and –6.1 V in linear and saturation regime, respectively).

2.4. OFET Operational Stability

Since the reactivity of the sp-carbon chain represents a major concern for the application of cumulenes in electronic devices, we addressed the shelf-life stability of the [3]Ph-based OFETs. Previous differential scanning calorimetry analysis demonstrated that [3]Ph crystals are stable up to about 250 °C.[51] Therefore, the material does not thermally degrade during the deposition within the applied range of temperatures. Moreover, [3]Ph can be stored and processed in air without decomposition, when not exposed to direct sunlight. Under intense irradiation, [3]Ph is known to dimerize in the solid state.[43,76]

The decreased absorbance for films of [3]Ph during irradiation at 405 nm with a light-emitting diode (Figure S17, Supporting Information) suggests degradation, likely through a photochemical cross-linking process. Photodegradation would produce defects that are highly detrimental for charge transport, as suggested by the deteriorating transfer characteristics upon irradiation to white light (Figure S18, Supporting Information). Conversely, [3]Ph-based devices show promising operational stability when measured under dark conditions. The transfer curves in linear regime of devices measured every 10 minutes for a total time of 10 hours in nitrogen atmosphere (**Figure 5**a) and 12 hours in air (Figure 5b) have been examined. Over this timeframe, the transfer characteristics of the OFET do not degrade, and only a slight decrease in the field-effect mobilities (–2% in nitrogen atmosphere and –1% in air, Figure 5c) is observed, together with a substantial improvement of the I_{on}/I_{off} ratio (+400% in nitrogen atmosphere and +3200% in air, Figure 5d).

3. Conclusion

This work clearly demonstrates that solution-processed thin films formed from molecules based on sp-hybridized carbon atoms can be adopted for large-area electronics. In particular, field-effect transistors based on polycrystalline thin films of a short cumulene, [3]Ph, show ideal p-type field-effect behavior and reliable hole mobility exceeding 0.1 $cm^2 V^{-1} s^{-1}$ for optimized conditions. Furthermore, the active layer of these FETs is deposited via a simple large-area coating technique. Remarkably, non-encapsulated transistors display promising stability under dark conditions, suggesting the potential for other future applications of these molecules. We expect that the mobility values achieved in this study could be further improved. On the one hand, enhanced performance using [3]Ph is expected by considering the large anisotropy of the electronic couplings within crystals as computed by DFT/TD-DFT, the random azimuthal orientation of the crystalline grains, and the presence of grain boundaries. Enlarged crystalline grains would be beneficial due to the concurrent reduction of grain boundaries, while directional control of the crystal growth would remedy the anisotropic charge transport. On the other hand, we open

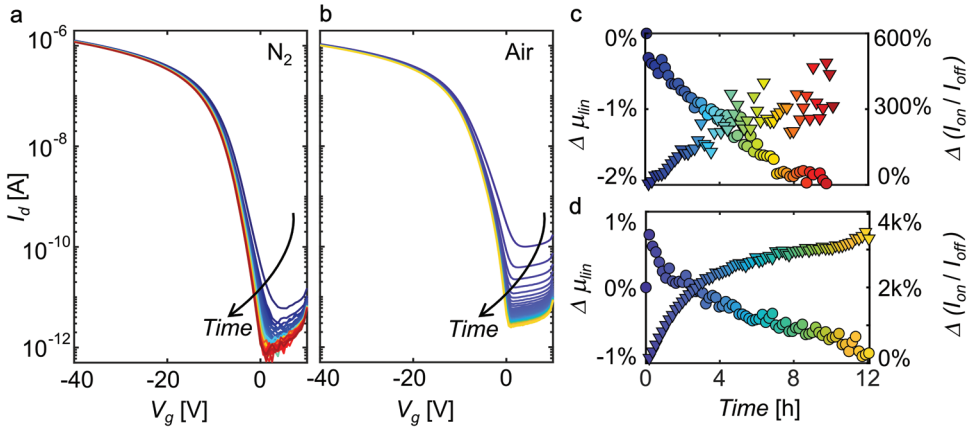

Figure 5. a,b) Assessment of operational stability under a nitrogen atmosphere (a) and in air (b) for OFETs with [3]Ph deposited at 80 °C (L = 5 µm, W = 200 µm). The time evolution of the transfer curves is depicted using a graded color scale (one measurement every 10 min for 1 h, V_{ds} = −5 V). c,d) The percentage time variations of the linear field-effect mobility, $\Delta\mu_{lin}$, and on–off current ratio, $\Delta(I_{on}/I_{off})$, related to the transfer curves measured under a nitrogen atmosphere (c) and in air (d).

the path to exploiting a vast library of cumulenic molecules, characterized by, for example, a longer conjugated backbone and tunable molecular bandgap. As well, synthetic modulation of the endcapping groups presents an exquisite opportunity to optimize crystalline packing and, thus, opto-electronic properties. The exploration of carbon atom wires in large-area organic electronics has just begun.

4. Experimental Section

[3]Ph: Tetraphenylbutatriene ([3]Ph) has been synthesized as previously reported[77] and stored in air at about 5 °C. Single-crystal diffraction data for [3]Ph (CCDC-1817320, 1 275 120, or 1 275 121) can be obtained free of charge from The Cambridge Crystallographic Data Centre via www.ccdc.cam.ac.uk/data_request/cif.

Deposition of Thin Films of [3]Ph: Pure [3]Ph in powder form was dissolved in 1,2-dichlorobenzene (Sigma Aldrich) at a concentration of 10 g L^{-1}, stirred at 50 °C for at least 1 h, and this solution used for deposition of [3]Ph by wire-bar coating in air.

Glass substrates (low alkali 1737F Corning glasses, purchased from Präzisions Glas & Optik GmbH) were cut to a size of 2 × 2 cm, cleaned by sonication with fresh acetone and isopropyl alcohol (both purchased from Sigma Aldrich) for 10 min, and then dried under a flow of nitrogen. Subsequently, the substrates surface was cleaned and activated by an oxygen-plasma treatment for 5 min (Diener Electronic Femto Plasma, chamber pressure 40 mbar, power 100 W).

The thin films of [3]Ph were deposited under a chemical fume hood by wire-bar coating using a TQC Sheen Automatic Film Applicator AB4400, which has been equipped with a homemade system to control the gap between the substrate and the wire-bar and with a nitrogen blow system to reduce the film drying time. The employed wire-bar applicator had a wire-wound rod diameter of 6 µm. The coating speed was set to 30 mm s^{-1}, and the deposition temperature was controlled in the range 50–110 °C with the integrated heated bed.

Optical Characterization: Polarized optical microscopy images were recorded in reflection mode with a Zeiss Axio Scope A1 equipped with a single polarizer (EpiPol mode).

Absorption spectra were obtained by measuring transmission spectra on a PerkinElmer Lambda 1050 UV/Vis/NIR spectrometer.

Local Polarized Absorption Spectra: The UV–vis spectra in Figure S11 in the Supporting Information were recorded with a homemade confocal microscope. The incident white light firstly passed through a linear polarizer, and then it was focused on the sample through an objective with numerical apertute (NA) of 0.7 (S Plan Fluor 60×, Nikon). Successively, the beam was collected through a 0.75 NA objective (CFI Plan Apochromat VC 20×, Nikon), and finally detected by a fiber-coupled spectrometer (Avantes, AvaSpec-HS2048XL-EVO).

Light-Induced UV–vis Evolution: UV–vis spectra in Figure S17 in the Supporting Information were acquired by a fiber-fed spectrometer (Avantes, AvaSpec-HS2048XL-EVO) coupled with a deuterium-halogen lamp (AvaLight-D(H)-S). The photodegradation process was induced using a LED lamp (Thorlabs, M405LP1-C5) centered at 405 nm at a power of 60 mW cm^{-2}. This source was placed on top of the sample illuminating it uniformly.

Films Topography and Thickness: The surface topography of the films was imaged with a Keysight 5600LS atomic force microscope operated in tapping mode. Gwyddion software[78] was used for image processing and surface roughness calculation (details in the Supporting Information). The film thickness was measured with a KLA Tencor P-17 Surface Profiler.

Grazing-Incidence Wide-Angle Scattering (GIWAXS): GIWAXS measurements were performed at the non-crystalline diffraction beamline (BL11-NCD-Sweet) at ALBA Synchrotron Radiation Facility in Barcelona (Spain). A detector (Rayonix, WAXS LX255-HS) with a resolution of 1920 × 5760 pixels was used to collect the scattering signals. Sample holder position was calibrated with chromium oxide (Cr_2O_3) standard. The incident energy was 12.4 eV, and the sample-to-detector distance was set at 216.5 mm. The angle of incidence α_i was 0.11° and the exposure time was 1 s. 2D-GIWAXS patterns were corrected as a function of the components of the scattering vector with a MATLAB script developed by Aurora Nogales and Edgar Gutiérrez.[79] Thin films were cast onto highly doped silicon substrates following same processing route used for the device fabrication.

Miller indexing and simulation of the lattice unit were performed with the MATLAB-SIIRkit package, designed and coded by Savikhin et al.;[80] using the diffraction peaks localized in the experimental GIWAXS maps as input data. The patterns were previously transformed into q-space and corrected by taking into account the curvature of the Ewald sphere (missing wedge). The presented results are the best fittings that adjust to all the experimental diffraction peaks.

OFETs Fabrication: [3]Ph-based OFETs were fabricated with a bottom-contact top-gate architecture. Bottom source and drain interdigitated electrodes were defined by standard photolithography onto the glass substrates and deposited by thermal evaporation of 30 nm-thick Au with a 3 nm-thick Cr adhesion layer. The [3]Ph active layer was deposited by wire-bar coating according to the procedure described above. About 500 nm-thick dielectric layer of poly(chloro-p-xylene)-C (Parylene-C, dimer purchased from Specialty Coating Systems) was deposited by CVD with a SCS Labcoater 2—PDS2010 system. PEDOT:PSS (Clevios PJ700 formulation, purchased from Heraeus) gate contacts were inkjet-

printed on top of the dielectric layer by means of a Fujifilm Dimatix DMP2831.

Electrical Characterization: OFETs transfer and output electrical characteristics were measured with a semiconductor parameter analyzer (Agilent B1500A) in a nitrogen glove box on a Wentworth Laboratories probe station. The transfer curves for the stability test in Figure 5b were measured in air with the same setup.

DFT/TD-DFT Calculations on Single Molecule and Dimers: Single-molecule and dimer DFT/TDDFT calculations were performed by using the ωB97X-D3 range-separated functional and the double (triple) split valence basis set with 6–31G* (6-311G*) polarization function. Calculations were carried out with the Gaussian16/C.01 code.[81] Electronic transfer integrals were computed using the symmetry projection dimer methods as reported in ref. [82]. Exciton couplings were evaluated by performing TD-DFT calculation on the dimers and by using the dimer-splitting method. The computed hole reorganization energy of [3]Ph was evaluated via the adiabatic potential energy method at the DFT level (ωB97X-D3/cc-pVTZ).

Supporting Information

Supporting Information is available from the Wiley Online Library or from the author.

Acknowledgements

E.G.F. acknowledges the support through the EU Horizon 2020 research and innovation program, H2020-FETOPEN-01-2018-2020 (FET-Open Challenging Current Thinking), "LION-HEARTED", grant agreement no. 828984. C.S.C. acknowledges funding from the European Research Council (ERC) under the European Union's Horizon 2020 research and innovation program ERC-Consolidator Grant (ERC CoG 2016 EspLORE grant agreement no. 724610, website: www.esplore.polimi.it). R.R.T. acknowledges funding from the Natural Sciences and Engineering Research Council of Canada (NSERC) and the Canada Foundation for Innovation (CFI). This work was partially supported by the European Union's H2020-EU.4.b. – Twinning of research institutions "GREENELIT", grant agreement number 951747. GIWAXS experiments were performed at BL11 NCD-SWEET beamline at ALBA Synchrotron (Spain) with the collaboration of ALBA staff. This work was in part carried out at Polifab, the micro- and nanotechnology centre of the Politecnico di Milano.

Open access funding provided by Istituto Italiano di Tecnologia within the CRUI-CARE Agreement.

Conflict of Interest

The authors declare no conflict of interest.

Data Availability Statement

The data that support the findings of this study are available from the corresponding author upon reasonable request.

Keywords

carbyne, cumulenes, organic semiconductors, organic transistors, printed electronics, sp-carbon wires

Received: December 23, 2021
Revised: February 7, 2022
Published online: March 3, 2022

[1] C. Keum, C. Murawski, E. Archer, S. Kwon, A. Mischok, M. C. Gather, *Nat. Commun.* **2020**, *11*, 6250.
[2] Y. Liu, C. Li, Z. Ren, S. Yan, M. R. Bryce, *Nat. Rev. Mater.* **2018**, *3*, 18020.
[3] V. V. Brus, J. Lee, B. R. Luginbuhl, S. J. Ko, G. C. Bazan, T. Q. Nguyen, *Adv. Mater.* **2019**, *31*, 1900904.
[4] L. Zhan, S. Li, X. Xia, Y. Li, X. Lu, L. Zuo, M. Shi, H. Chen, *Adv. Mater.* **2021**, *33*, 2007231.
[5] G. Prunet, F. Pawula, G. Fleury, E. Cloutet, A. J. Robinson, G. Hadziioannou, A. Pakdel, *Mater. Today Phys.* **2021**, *18*, 100402.
[6] J. Ding, W. Zhao, W. Jin, C. an Di, D. Zhu, *Adv. Funct. Mater.* **2021**, *31*, 2010695.
[7] C. Wang, H. Dong, W. Hu, Y. Liu, D. Zhu, *Chem. Rev.* **2012**, *112*, 2208.
[8] X. Guo, Y. Xu, S. Ogier, T. N. Ng, M. Caironi, A. Perinot, L. Li, J. Zhao, W. Tang, R. A. Sporea, A. Nejim, J. Carrabina, P. Cain, F. Yan, *IEEE Trans. Electron Devices* **2017**, *64*, 1906.
[9] A. Perinot, M. Giorgio, V. Mattoli, D. Natali, M. Caironi, *Adv. Sci.* **2021**, *8*, 2001098.
[10] Z. Qin, H. Gao, H. Dong, W. Hu, *Adv. Mater.* **2021**, *33*, 2007149.
[11] R. A. Picca, K. Manoli, E. Macchia, L. Sarcina, C. Di Franco, N. Cioffi, D. Blasi, R. Österbacka, F. Torricelli, G. Scamarcio, L. Torsi, *Adv. Funct. Mater.* **2020**, *30*, 1904513.
[12] E. Macchia, L. Sarcina, C. Driescher, Z. Gounani, A. Tewari, R. Osterbacka, G. Palazzo, A. Tricase, Z. M. Kovacs Vajna, F. Viola, F. Modena, M. Caironi, F. Torricelli, I. Esposito, L. Torsi, *Adv. Electron. Mater.* **2021**, *7*, 2100304.
[13] J. C. Yang, J. Mun, S. Y. Kwon, S. Park, Z. Bao, S. Park, *Adv. Mater.* **2019**, *31*, 1904765.
[14] Y. Van De Burgt, A. Melianas, S. T. Keene, G. Malliaras, A. Salleo, *Nat. Electron.* **2018**, *1*, 386.
[15] Y. Yu, Q. Ma, H. Ling, W. Li, R. Ju, L. Bian, N. Shi, Y. Qian, M. Yi, L. Xie, W. Huang, *Adv. Funct. Mater.* **2019**, *29*, 1904602.
[16] H. Sirringhaus, *Adv. Mater.* **2014**, *26*, 1319.
[17] H. Bronstein, C. B. Nielsen, B. C. Schroeder, I. McCulloch, *Nat. Rev. Chem.* **2020**, *4*, 66.
[18] A. F. Paterson, S. Singh, K. J. Fallon, T. Hodsden, Y. Han, B. C. Schroeder, H. Bronstein, M. Heeney, I. McCulloch, T. D. Anthopoulos, *Adv. Mater.* **2018**, *30*, 1801079.
[19] S. Riera-Galindo, F. Leonardi, R. Pfattner, M. Mas-Torrent, *Adv. Mater. Technol.* **2019**, *4*, 1900104.
[20] S. Pang, Y. Hernandez, X. Feng, K. Müllen, *Adv. Mater.* **2011**, *23*, 2779.
[21] H. Jang, Y. J. Park, X. Chen, T. Das, M. S. Kim, J. H. Ahn, *Adv. Mater.* **2016**, *28*, 4184.
[22] J. Zaumseil, *Adv. Electron. Mater.* **2019**, *5*, 1800514.
[23] E. Grądzka, M. Wysocka-Żołopa, K. Winkler, *Adv. Energy Mater.* **2020**, *10*, 2001443.
[24] C. S. Casari, M. Tommasini, R. R. Tykwinski, A. Milani, *Nanoscale* **2016**, *8*, 4414.
[25] M. Liu, V. I. Artyukhov, H. Lee, F. Xu, B. I. Yakobson, *ACS Nano* **2013**, *7*, 10075.
[26] P. B. Sorokin, H. Lee, L. Y. Antipina, A. K. Singh, B. I. Yakobson, *Nano Lett.* **2011**, *11*, 2660.
[27] R. R. Tykwinski, W. Chalifoux, S. Eisler, A. Lucotti, M. Tommasini, D. Fazzi, M. Del Zoppo, G. Zerbi, *Pure Appl. Chem.* **2010**, *82*, 891.
[28] M. Wang, S. Lin, *Sci. Rep.* **2015**, *5*, 18122.
[29] A. D. Slepkov, F. A. Hegmann, S. Eisler, E. Elliott, R. R. Tykwinski, *J. Chem. Phys.* **2004**, *120*, 6807.
[30] S. Eisler, A. D. Slepkov, E. Elliott, T. Luu, R. McDonald, F. A. Hegmann, R. R. Tykwinski, *J. Am. Chem. Soc.* **2005**, *127*, 2666.
[31] P. Marabotti, A. Milani, A. Lucotti, L. Brambilla, M. Tommasini, C. Castiglioni, P. Męcik, B. Pigulski, S. Szafert, C. S. Casari, *Carbon Trends* **2021**, *5*, 100115.

[32] N. R. Agarwal, A. Lucotti, M. Tommasini, W. A. Chalifoux, R. R. Tykwinski, *J. Phys. Chem. C* **2016**, *120*, 11131.
[33] Y. Zhu, H. Bai, Y. Huang, *ChemistryOpen* **2016**, *5*, 78.
[34] W. A. Chalifoux, R. R. Tykwinski, *Nat. Chem.* **2010**, *2*, 967.
[35] L. Shi, P. Rohringer, K. Suenaga, Y. Niimi, J. Kotakoski, J. C. Meyer, H. Peterlik, M. Wanko, S. Cahangirov, A. Rubio, Z. J. Lapin, L. Novotny, P. Ayala, T. Pichler, *Nat. Mater.* **2016**, *15*, 634.
[36] J. Zirzlmeier, S. Schrettl, J. C. Brauer, E. Contal, L. Vannay, É. Brémond, E. Jahnke, D. M. Guldi, C. Corminboeuf, R. R. Tykwinski, H. Frauenrath, *Nat. Commun.* **2020**, *11*, 4797.
[37] Y. Gao, Y. Hou, F. Gordillo Gámez, M. J. Ferguson, J. Casado, R. R. Tykwinski, *Nat. Chem.* **2020**, *12*, 1143.
[38] F. Banhart, *ChemTexts* **2020**, *6*, 3.
[39] M. Tommasini, A. Milani, D. Fazzi, A. Lucotti, C. Castiglioni, J. A. Januszewski, D. Wendinger, R. R. Tykwinski, *J. Phys. Chem. C* **2014**, *118*, 26415.
[40] A. La Torre, A. Botello-Mendez, W. Baaziz, J. C. Charlier, F. Banhart, *Nat. Commun.* **2015**, *6*, 2.
[41] A. Milani, M. Tommasini, V. Barbieri, A. Lucotti, V. Russo, F. Cataldo, C. S. Casari, *J. Phys. Chem. C* **2017**, *121*, 10562.
[42] A. Milani, V. Barbieri, A. Facibeni, V. Russo, A. Li Bassi, A. Lucotti, M. Tommasini, M. D. Tzirakis, F. Diederich, C. S. Casari, *Sci. Rep.* **2019**, *9*, 1648.
[43] D. Wendinger, R. R. Tykwinski, *Acc. Chem. Res.* **2017**, *50*, 1468.
[44] M. R. Bryce, *J. Mater. Chem. C* **2021**, *9*, 10524.
[45] W. Xu, E. Leary, S. Hou, S. Sangtarash, M. T. González, G. Rubio-Bollinger, Q. Wu, H. Sadeghi, L. Tejerina, K. E. Christensen, N. Agraït, S. J. Higgins, C. J. Lambert, R. J. Nichols, H. L. Anderson, *Angew. Chem., Int. Ed.* **2019**, *58*, 8378.
[46] Y. Zang, T. Fu, Q. Zou, F. Ng, H. Li, M. L. Steigerwald, C. Nuckolls, L. Venkataraman, *Nano Lett.* **2020**, *20*, 8415.
[47] O. Cretu, A. R. Botello-Mendez, I. Janowska, C. Pham-Huu, J. C. Charlier, F. Banhart, *Nano Lett.* **2013**, *13*, 3487.
[48] M. H. Garner, W. Bro-Jørgensen, P. D. Pedersen, G. C. Solomon, *J. Phys. Chem. C* **2018**, *122*, 26777.
[49] B. J. Eckstein, F. S. Melkonyan, N. Zhou, E. F. Manley, J. Smith, A. Timalsina, R. P. H. Chang, L. X. Chen, A. Facchetti, T. J. Marks, *Macromolecules* **2017**, *50*, 1430.
[50] R. He, Z. Xu, S. Valandro, H. D. Arman, J. Xue, K. S. Schanze, *ACS Appl. Mater. Interfaces* **2021**, *13*, 5327.
[51] A. D. Scaccabarozzi, A. Milani, S. Peggiani, S. Pecorario, B. Sun, R. R. Tykwinski, M. Caironi, C. S. Casari, *J. Phys. Chem. Lett.* **2020**, *11*, 1970.
[52] I. Temiño, F. G. Del Pozo, M. R. Ajayakumar, S. Galindo, J. Puigdollers, M. Mas-Torrent, *Adv. Mater. Technol.* **2016**, *1*, 1600090.
[53] D. Khim, H. Han, K. J. Baeg, J. Kim, S. W. Kwak, D. Y. Kim, Y. Y. Noh, *Adv. Mater.* **2013**, *25*, 4302.
[54] S. B. Lee, B. Kang, D. Kim, C. Park, S. Kim, M. Lee, W. B. Lee, K. Cho, *ACS Appl. Mater. Interfaces* **2019**, *11*, 47153.
[55] S. Galindo, A. Tamayo, F. Leonardi, M. Mas-Torrent, *Adv. Funct. Mater.* **2017**, *27*, 1700526.
[56] M. Chen, B. Peng, S. Huang, P. K. L. Chan, *Adv. Funct. Mater.* **2020**, *30*, 1905963.
[57] V. Chynwat, T. L. Coffin, H. Wang, R. E. Connors, *J. Phys. Chem.* **1996**, *100*, 5217.
[58] X. Zhang, W. Deng, B. Lu, X. Fang, X. Zhang, J. Jie, *Nanoscale Horiz.* **2020**, *5*, 1096.
[59] L. Yu, G. Portale, N. Stingelin, *J. Mater. Chem. C* **2021**, *9*, 10547.
[60] A. A. Virkar, S. Mannsfeld, Z. Bao, N. Stingelin, *Adv. Mater.* **2010**, *22*, 3857.
[61] F. P. V. Koch, M. Heeney, P. Smith, *J. Am. Chem. Soc.* **2013**, *135*, 13699.
[62] N. D. Treat, P. Westacott, N. Stingelin, *Annu. Rev. Mater. Res.* **2015**, *45*, 459.
[63] Z. Berkovitch-Yellin, L. Leiserowitz, *Acta Crystallogr., Sect. B Struct: Crystallogr. Cryst. Chem.* **1977**, *33*, 3657.
[64] S. C. B. Mannsfeld, M. L. Tang, Z. Bao, *Adv. Mater.* **2011**, *23*, 127.
[65] N. J. Hestand, F. C. Spano, *Chem. Rev.* **2018**, *118*, 7069.
[66] F. Gajdos, S. Valner, F. Hoffmann, J. Spencer, M. Breuer, A. Kubas, M. Dupuis, J. Blumberger, *J. Chem. Theory Comput.* **2014**, *10*, 4653.
[67] V. Coropceanu, J. Cornil, D. A. da Silva Filho, Y. Olivier, R. Silbey, J. L. Brédas, *Chem. Rev.* **2007**, *107*, 926.
[68] W. Huang, W. Xie, H. Huang, H. Zhang, H. Liu, *J. Phys. Chem. Lett.* **2020**, *11*, 4548.
[69] Z. Shuai, H. Geng, W. Xu, Y. Liao, J. M. André, *Chem. Soc. Rev.* **2014**, *43*, 2662.
[70] H. H. Choi, K. Cho, C. D. Frisbie, H. Sirringhaus, V. Podzorov, *Nat. Mater.* **2017**, *17*, 2.
[71] D. Natali, M. Caironi, *Adv. Mater.* **2012**, *24*, 1357.
[72] C. Liu, Y. Xu, Y. Y. Noh, *Mater. Today* **2015**, *18*, 79.
[73] T. Hamai, S. Arai, H. Minemawari, S. Inoue, R. Kumai, T. Hasegawa, *Phys. Rev. Appl.* **2017**, *8*, 054011.
[74] Q. Wang, S. Jiang, B. Zhang, E. Y. Shin, Y. Y. Noh, Y. Xu, Y. Shi, Y. Li, *J. Phys. Chem. Lett.* **2020**, *11*, 1466.
[75] H. B. Michaelson, *J. Appl. Phys.* **1977**, *48*, 4729.
[76] Z. Berkovitch-Yellin, M. Lahav, L. Leiserowitz, *J. Am. Chem. Soc.* **1974**, *96*, 918.
[77] P. Gawel, C. Dengiz, A. D. Finke, N. Trapp, C. Boudon, J. P. Gisselbrecht, F. Diederich, *Angew. Chem., Int. Ed.* **2014**, *53*, 4341.
[78] D. Nečas, P. Klapetek, *Cent. Eur. J. Phys.* **2012**, *10*, 181.
[79] A. Nogales, E. Gutiérrez, *2D Representation of a Wide Angle X Ray Scattering Pattern as a Function of Q Vector Components*, MathWorks File Exchange **2019**, https://it.mathworks.com/matlabcentral/fileexchange/71958-grazing-incidence-wide-angle-X-ray-scattering-representation.
[80] V. Savikhin, H. G. Steinru ck, R. Z. Liang, B. A. Collins, S. D. Oosterhout, P. M. Beaujuge, M. F. Toney, *J. Appl. Crystallogr.* **2020**, *53*, 1108.
[81] M. J. Frisch, G. W. Trucks, H. B. Schlegel, G. E. Scuseria, M. A. Robb, J. R. Cheeseman, G. Scalmani, V. Barone, G. A. Petersson, H. Nakatsuji, X. Li, M. Caricato, A. V. Marenich, J. Bloino, B. G. Janesko, R. Gomperts, B. Mennucci, H. P. Hratchian, J. V. Ortiz, A. F. Izmaylov, J. L. Sonnenberg, F. D. Williams, F. Lipparini, F. Egidi, J. Goings, B. Peng, A. Petrone, T. Henderson, D. Ranasinghe, V. G. Zakrzewski, et al., *Gaussian 16*, Gaussian, Inc., Wallingford CT, USA **2016**.
[82] B. Baumeier, J. Kirkpatrick, D. Andrienko, *Phys. Chem. Chem. Phys.* **2010**, *12*, 11103.

7. Final Remarks and Future Perspectives

This dissertation reports about the study of the charge transport properties in three classes of solution processable carbon-based materials.

The first part discusses about the effects of molecular encapsulation on the photophysical and charge transport properties of PNDIT2, a high-mobility n-type polymer and non-fullerene acceptor. A throughout study of absorption and fluorescence spectra reveals that molecular encapsulation avoids preaggregation of the polymer chains in common organic solvents. Preventing preaggregation in solution is desirable to enhance the intermixing of several components in a common solvent. For instance, this is appealing for bulk heterojunction solar cells, and to intercalate molecular dopants inside a polymeric matrix for thermoelectric applications. An enhancement of the backbone conjugation is observed in the encapsulated polymer, *i.e.*, E-PNDIT2, which is ascribed to increased backbone planarity and rigidity. The solid-state packing is strongly affected by the encapsulating rings, altering the molecules orientation and the intermolecular packing distances. Remarkably, interpenetration of the macrocycles promotes semicrystalline order thanks to an intermolecular-lock mechanism. Due to the absence of coiling of the polymer chains in solution, the typical fibrillar microstructure of PNDIT2 is lost in E-PNDIT2. Since this microstructure is necessary to provide long-range percolative pathways, OFETs based on E-PNDIT2 preserve ideal n-type characteristics but afford charge carriers mobility of 10^{-3} cm^2 V^{-1} s^{-1}, which is about two orders of magnitude lower than in PNDIT2. Overall, this work demonstrates the potential of molecular encapsulation as a general strategy to tune the nanomorphology of the cast films without significant alteration of the electronic structure of the core polymer. The possibility to shield segments of the polymer backbone while allowing π-stacking between specific moieties offer an ideal platform to investigate the relative impact of inter- and intra-molecular interactions on optoelectronic properties. Future investigations might exploit these systems to study the interactions between the semiconducting polymers and intercalated molecular dopants. Positioning the macrocycles in controlled locations along the polymer chain seems promising to promote selective interactions between the dopant and desired parts of the backbone, while protecting other segments from undesired interactions with the counterions. Finally, the possibility to tune the intermolecular distance and, at the same time, to increase the film crystallinity thanks to backbone rigidification and intermolecular-locking look appealing for organic electrochemical transistors (OECTs).

The second part of the thesis deals with the charge modulation microscopy (CMM) investigation of the impact of the network composition in determining efficient charge percolation pathways in FETs based on solution processed SWCNTs networks. In this study, FETs based on a monochiral (6,5) SWCNT network and on a multichiral network with five different (n,m) species are compared. By measuring charge-induced optical features with micrometric resolution, CMM allows to map the free carriers distribution along the device channel and to visualize its evolution in subthreshold regime as a function of the gate potential. Clear evidence show that holes and electrons are transported along the same preferential percolation paths. For the monochiral network, which is characterized by low energetic disorder, the CMM maps demonstrate a correlation between network density and percolation pathways. This effect is not detected in multichiral networks, which are impacted by a higher energetic disorder because of the presence of five (n,m) species with diverse electronic structure. The presence of energy barriers between different species hinders hopping of charge carriers, as testified by the more fragmented percolation pathways when compared to the monochiral network. Finally, a method based on the analysis of the 2d spatial autocorrelation and cross-correlation functions of the CMM maps is established. This approach allows to identify a critical length scale, namely the correlation length, that is associated to the average size of percolation paths with the same charge transport efficiency. High values of the correlation length are associated with extended percolation paths where the local resistivity of the film is homogeneous (like in monochiral networks). Instead, low values of the correlation length correspond to more fragmented pathways (like in multichiral networks), due to mixing of high and low resistive percolation pathways at a shorter length scale. Thus, this methodology looks promising to identify at which scale length the overall performance of the device becomes insensitive to local properties of the network, providing guidelines for scaling-down the device dimensions without increasing the performance variability. Indeed, if the active area of the FET is larger than the average size of the percolation pathways, a scattered distribution of the device performance is expected, since some devices will contain only high-conductive paths, and other more resistive paths. Diversely, if the active area is larger than the correlation length, the performance of the device is averaged over high- and low-resistivity domains, resulting in homogenous performance among different FETs. In future works, this approach can be extended to other systems, including aligned conjugated polymers and small molecules thin films.

Finally, solution processed thin films of tetraphenyl[3]cumulene ([3]Ph) are introduced as first example of a new class of performant conjugated molecules based on sp-hybridized carbon atom wires. [3]Ph thin films are employed as active layer to fabricate field effect transistors. Performant devices were achieved through a comprehensive optimization of the deposition of polycrystalline thin films by wire-bar coating, which is a scalable meniscus-shearing technique. [3]Ph films demonstrates ideal p-type characteristics with reliable hole mobility exceeding 0.1 $cm^2\ V^{-1}\ s^{-1}$ in best devices. Moreover, the transistors display promising operational stability in environmental conditions without any specific encapsulation, thus affirming the potential to employ sp-carbon wires in real applications despite being often considered highly reactive. Also, an in-depth study of the thin film properties as a function of the deposition temperature is presented, which allows to establish relations between the morphology and crystalline structure of the thin films and their electrical performance. The combination of polarized optical microscopy, absorption spectroscopy and GIWAXS unveils the nature of crystalline packing and molecular orientation of [3]Ph molecules in the thin films. Furthermore, DFT calculations lead to identify a highly preferential charge transfer direction in correspondence to the π-π stacking between parallel sp-chains. In perspective, increasing the average grain size of the polycrystalline films and achieving directional control of the crystal growth would remedy the anisotropic charge transport and result in enhanced field-effect mobility. Blending [3]Ph with either insulating or semiconducting polymers could also be an effective strategy to improve the crystallinity of the films and the devices performance. Overall, these findings on the shortest of the cumulenes series open the way to a whole new series of conjugated molecules containing linear sp-carbon chains, which can be exploited in large-area printed electronics. The expected impact regards both technological and fundamental points of view. First, tuning the sp-chain length and the end-capping groups would allow to control the optoelectronic properties and the molecular packing of these highly conjugated systems. For instance, functionalizing cumulenes with halogenated terminal groups might result in performant n-type semiconductors. Another fascinating way to exploit the unique properties of sp-carbon chains (*e.g.*, their stiffness) might involve their use in donor-acceptor copolymers. On the fundamental side, sp-carbon wires offer the intriguing possibility to investigate the impact of intra- and inter-molecular vibrations on charge transport. Indeed, they are characterized by a linear and extremely rigid backbone which result in peculiar high-frequency vibrational modes. This unique trait distinguishes sp-carbon wires from all the other sp^2-hybridized molecular semiconductors, which traditionally present planar backbones.

Bibliography

(1) Pecorario, S.; Royakkers, J.; Scaccabarozzi, A. D.; Pallini, F.; Beverina, L.; Bronstein, H.; Caironi, M. Effects of Molecular Encapsulation on the Photophysical and Charge Transport Properties of a Naphthalene Diimide Bithiophene Copolymer. *Chem. Mater.* **2022**, *34* (18), 8324–8335. https://doi.org/10.1021/acs.chemmater.2c01894.

(2) Jiang, M.; Pecorario, S.; Zorn, N. F.; Zaumseil, J.; Caironi, M. Investigating Charge Transport in Semiconducting Single-Walled Carbon Nanotube Networks by Charge Modulation Microscopy. *Adv. Mater. Interfaces* **2023**, *2202454*. https://doi.org/10.1002/admi.202202454.

(3) Pecorario, S.; Scaccabarozzi, A. D.; Fazzi, D.; Gutiérrez-Fernández, E.; Vurro, V.; Maserati, L.; Jiang, M.; Losi, T.; Sun, B.; Tykwinski, R. R.; Casari, C. S.; Caironi, M. Stable and Solution-Processable Cumulenic Sp-Carbon Wires: A New Paradigm for Organic Electronics. *Adv. Mater.* **2022**, *34* (15), 2110468. https://doi.org/10.1002/adma.202110468.

(4) Tsumura, A.; Koezuka, H.; Ando, T. Macromolecular Electronic Device: Field-effect Transistor with a Polythiophene Thin Film. *Appl. Phys. Lett.* **1986**, *49* (18), 1210–1212. https://doi.org/10.1063/1.97417.

(5) Sirringhaus, H.; Brown, P. J.; Friend, R. H.; Nielsen, M. M.; Bechgaard, K.; Langeveld-Voss, B. M. W.; Spiering, A. J. H.; Janssen, R. A. J.; Meijer, E. W.; Herwig, P.; De Leeuw, D. M. Two-Dimensional Charge Transport in Self-Organized, High-Mobility Conjugated Polymers. *Nature* **1999**, *401* (6754), 685–688. https://doi.org/10.1038/44359.

(6) Hall, N. Twenty-Five Years of Conducting Polymers. *Chemical Communications*. 2003. https://doi.org/10.1039/b210718j.

(7) Shirakawa, H.; Louis, E. J.; MacDiarmid, A. G.; Chiang, C. K.; Heeger, A. J. Synthesis of Electrically Conducting Organic Polymers: Halogen Derivatives of Polyacetylene, (CH)X. *J. Chem. Soc. Chem. Commun.* **1977**, No. 16. https://doi.org/10.1039/C39770000578.

(8) Tyagi, A.; Mišeikis, V.; Martini, L.; Forti, S.; Mishra, N.; Gebeyehu, Z. M.; Giambra, M. A.; Zribi, J.; Frégnaux, M.; Aureau, D.; Romagnoli, M.; Beltram, F.; Coletti, C. Ultra-Clean High-Mobility Graphene on Technologically Relevant Substrates. *Nanoscale* **2022**, *14* (6), 2167–2176. https://doi.org/10.1039/d1nr05904a.

(9) 15 Years of Graphene Electronics. *Nat. Electron.* **2019**, *2* (9), 369. https://doi.org/10.1038/s41928-019-0312-4.

(10) Bennett, P. B.; Pedramrazi, Z.; Madani, A.; Chen, Y.-C.; de Oteyza, D. G.; Chen, C.; Fischer, F. R.; Crommie, M. F.; Bokor, J. Bottom-up Graphene Nanoribbon Field-Effect Transistors. *Appl. Phys. Lett.* **2013**, *103* (25), 253114. https://doi.org/10.1063/1.4855116.

(11) Moreno, C.; Vilas-Varela, M.; Kretz, B.; Garcia-Lekue, A.; Costache, M. V.; Paradinas, M.; Panighel, M.; Ceballos, G.; Valenzuela, S. O.; Peña, D.; Mugarza, A. Bottom-up Synthesis of Multifunctional Nanoporous Graphene. *Science (80-.).* **2018**, *360* (6385), 199–203. https://doi.org/10.1126/science.aar2009.

(12) Wang, S.; Kailian Ang, P.; Wang, Z.; Ling Lena Tang, A.; T. L. Thong, J.; Ping Loh, K. High Mobility, Printable, and Solution-Processed Graphene Electronics. *Nano Lett.*

2009, *10* (1), 92–98. https://doi.org/10.1021/nl9028736.

(13) Liu, Z.; Qiu, H.; Fu, S.; Wang, C.; Yao, X.; G. Dixon, A.; Campidelli, S.; Pavlica, E.; Bratina, G.; Zhao, S.; Rondin, L.; Lauret, J.-S.; Narita, A.; Bonn, M.; Müllen, K.; Ciesielski, A.; I. Wang, H.; Samorì, P. Solution-Processed Graphene–Nanographene van Der Waals Heterostructures for Photodetectors with Efficient and Ultralong Charge Separation. *J. Am. Chem. Soc.* **2021**, *143* (41), 17109–17116. https://doi.org/10.1021/jacs.1c07615.

(14) Lin, Z.; Huang, Y.; Duan, X. Van Der Waals Thin-Film Electronics. *Nat. Electron.* **2019**, *2* (9), 378–388. https://doi.org/10.1038/s41928-019-0301-7.

(15) Anthopoulos, T. D.; Singh, B.; Marjanovic, N.; Sariciftci, N. S.; Montaigne Ramil, A.; Sitter, H.; Cölle, M.; de Leeuw, D. M. High Performance N-Channel Organic Field-Effect Transistors and Ring Oscillators Based on C60 Fullerene Films. *Appl. Phys. Lett.* **2006**, *89* (21), 213504. https://doi.org/10.1063/1.2387892.

(16) Grądzka, E.; Wysocka-Żołopa, M.; Winkler, K. Fullerene-Based Conducting Polymers: N-Dopable Materials for Charge Storage Application. *Adv. Energy Mater.* **2020**, *10* (40), 2001443. https://doi.org/10.1002/aenm.202001443.

(17) Thompson, B. C.; Fréchet, J. M. J. Polymer–Fullerene Composite Solar Cells. *Angew. Chemie Int. Ed.* **2008**, *47* (1), 58–77. https://doi.org/https://doi.org/10.1002/anie.200702506.

(18) Yan, C.; Barlow, S.; Wang, Z.; Yan, H.; Jen, A. K. Y.; Marder, S. R.; Zhan, X. Non-Fullerene Acceptors for Organic Solar Cells. *Nature Reviews Materials*. 2018. https://doi.org/10.1038/natrevmats.2018.3.

(19) Armin, A.; Li, W.; Sandberg, O. J.; Xiao, Z.; Ding, L.; Nelson, J.; Neher, D.; Vandewal, K.; Shoaee, S.; Wang, T.; Ade, H.; Heumüller, T.; Brabec, C.; Meredith, P. A History and Perspective of Non-Fullerene Electron Acceptors for Organic Solar Cells. *Advanced Energy Materials*. 2021. https://doi.org/10.1002/aenm.202003570.

(20) Hills, G.; Lau, C.; Wright, A.; Fuller, S.; Bishop, M. D.; Srimani, T.; Kanhaiya, P.; Ho, R.; Amer, A.; Stein, Y.; Murphy, D.; Arvind; Chandrakasan, A.; Shulaker, M. M. Modern Microprocessor Built from Complementary Carbon Nanotube Transistors. *Nature* **2019**, *572* (7771). https://doi.org/10.1038/s41586-019-1493-8.

(21) Zaumseil, J. Single-Walled Carbon Nanotube Networks for Flexible and Printed Electronics. *Semicond. Sci. Technol.* **2015**, *30* (7). https://doi.org/10.1088/0268-1242/30/7/074001.

(22) Casari, C. S.; Tommasini, M.; Tykwinski, R. R.; Milani, A. Carbon-Atom Wires: 1-D Systems with Tunable Properties. *Nanoscale* **2016**, *8* (8), 4414–4435. https://doi.org/10.1039/c5nr06175j.

(23) Chalifoux, W. A.; Tykwinski, R. R. Synthesis of Polyynes to Model the Sp-Carbon Allotrope Carbyne. *Nat. Chem.* **2010**, *2* (11), 967–971. https://doi.org/10.1038/nchem.828.

(24) Bryce, M. R. A Review of Functional Linear Carbon Chains (Oligoynes, Polyynes, Cumulenes) and Their Applications as Molecular Wires in Molecular Electronics and Optoelectronics. *J. Mater. Chem. C* **2021**, *9* (33), 10524–10546. https://doi.org/10.1039/D1TC01406D.

(25) Schweicher, G.; Garbay, G.; Jouclas, R.; Vibert, F.; Devaux, F.; Geerts, Y. H. Molecular

Semiconductors for Logic Operations: Dead-End or Bright Future? *Adv. Mater.* **2020**, *32* (10). https://doi.org/10.1002/adma.201905909.

(26) Zschieschang, U.; Waizmann, U.; Weis, J.; Borchert, J. W.; Klauk, H. Nanoscale Flexible Organic Thin-Film Transistors. *Sci. Adv.* **2022**, *8* (13), 1–11. https://doi.org/10.1126/sciadv.abm9845.

(27) Perinot, A.; Giorgio, M.; Mattoli, V.; Natali, D.; Caironi, M. Organic Electronics Picks Up the Pace: Mask-Less, Solution Processed Organic Transistors Operating at 160 MHz. *Adv. Sci.* **2021**, *8* (4), 2001098. https://doi.org/10.1002/advs.202001098.

(28) Yang, J. C.; Mun, J.; Kwon, S. Y.; Park, S.; Bao, Z.; Park, S. Electronic Skin: Recent Progress and Future Prospects for Skin-Attachable Devices for Health Monitoring, Robotics, and Prosthetics. *Adv. Mater.* **2019**, *31* (48), 1904765. https://doi.org/10.1002/adma.201904765.

(29) Pataki, N.; Rossi, P.; Caironi, M. Solution Processed Organic Thermoelectric Generators as Energy Harvesters for the Internet of Things. *Appl. Phys. Lett.* **2022**, *121* (23), 230501. https://doi.org/10.1063/5.0129861.

(30) Mytafides, C. K.; Tzounis, L.; Karalis, G.; Formanek, P.; Paipetis, A. S. High-Power All-Carbon Fully Printed and Wearable SWCNT-Based Organic Thermoelectric Generator. *ACS Appl. Mater. Interfaces* **2021**, *13* (9), 11151–11165. https://doi.org/10.1021/acsami.1c00414.

(31) Fukuda, K.; Yu, K.; Someya, T. The Future of Flexible Organic Solar Cells. *Adv. Energy Mater.* **2020**, *10* (25), 2000765. https://doi.org/https://doi.org/10.1002/aenm.202000765.

(32) Jing, J.; Dong, S.; Zhang, K.; Zhou, Z.; Xue, Q.; Song, Y.; Du, Z.; Ren, M.; Huang, F. Semitransparent Organic Solar Cells with Efficiency Surpassing 15%. *Adv. Energy Mater.* **2022**, *12* (20), 2200453. https://doi.org/https://doi.org/10.1002/aenm.202200453.

(33) Irimia-Vladu, M.; Głowacki, E. D.; Voss, G.; Bauer, S.; Sariciftci, N. S. Green and Biodegradable Electronics. *Mater. Today* **2012**, *15* (7), 340–346. https://doi.org/https://doi.org/10.1016/S1369-7021(12)70139-6.

(34) Sharova, A. S.; Melloni, F.; Lanzani, G.; Bettinger, C. J.; Caironi, M. Edible Electronics: The Vision and the Challenge. *Adv. Mater. Technol.* **2021**, *6* (2). https://doi.org/10.1002/admt.202000757.

(35) Van De Burgt, Y.; Melianas, A.; Keene, S. T.; Malliaras, G.; Salleo, A. Organic Electronics for Neuromorphic Computing. *Nat. Electron.* **2018**, *1* (7), 386–397. https://doi.org/10.1038/s41928-018-0103-3.

(36) Torricelli, F.; Adrahtas, D. Z.; Bao, Z.; Berggren, M.; Biscarini, F.; Bonfiglio, A.; Bortolotti, C. A.; Frisbie, C. D.; Macchia, E.; Malliaras, G. G.; McCulloch, I.; Moser, M.; Nguyen, T.-Q.; Owens, R. M.; Salleo, A.; Spanu, A.; Torsi, L. Electrolyte-Gated Transistors for Enhanced Performance Bioelectronics. *Nat. Rev. Methods Prim.* **2021**, *1* (1), 66. https://doi.org/10.1038/s43586-021-00065-8.

(37) Campana, A.; Cramer, T.; Simon, D. T.; Berggren, M.; Biscarini, F. Electrocardiographic Recording with Conformable Organic Electrochemical Transistor Fabricated on Resorbable Bioscaffold. *Adv. Mater.* **2014**, *26* (23), 3874–3878. https://doi.org/https://doi.org/10.1002/adma.201400263.

(38) Shkodra, B.; Petrelli, M.; Costa Angeli, M. A.; Garoli, D.; Nakatsuka, N.; Lugli, P.; Petti, L. Electrolyte-Gated Carbon Nanotube Field-Effect Transistor-Based Biosensors: Principles and Applications. *Applied Physics Reviews*. 2021. https://doi.org/10.1063/5.0058591.

(39) Bronstein, H.; Nielsen, C. B.; Schroeder, B. C.; McCulloch, I. The Role of Chemical Design in the Performance of Organic Semiconductors. *Nat. Rev. Chem.* **2020**, *4* (2), 66–77. https://doi.org/10.1038/s41570-019-0152-9.

(40) de Leeuw, D. M.; Simenon, M. M. J.; Brown, A. R.; Einerhand, R. E. F. Stability of N-Type Doped Conducting Polymers and Consequences for Polymeric Microelectronic Devices. *Synth. Met.* **1997**, *87* (1), 53–59. https://doi.org/https://doi.org/10.1016/S0379-6779(97)80097-5.

(41) Griggs, S.; Marks, A.; Bristow, H.; McCulloch, I. N-Type Organic Semiconducting Polymers: Stability Limitations, Design Considerations and Applications. *J. Mater. Chem. C* **2021**, *9* (26), 8099–8128. https://doi.org/10.1039/d1tc02048j.

(42) Yang, Y.; Liu, Z.; Zhang, G.; Zhang, X.; Zhang, D. The Effects of Side Chains on the Charge Mobilities and Functionalities of Semiconducting Conjugated Polymers beyond Solubilities. *Adv. Mater.* **2019**, *31* (46), 1903104. https://doi.org/https://doi.org/10.1002/adma.201903104.

(43) Flagg, L. Q.; Bischak, C. G.; Onorato, J. W.; Rashid, R. B.; Luscombe, C. K.; Ginger, D. S. Polymer Crystallinity Controls Water Uptake in Glycol Side-Chain Polymer Organic Electrochemical Transistors. *J. Am. Chem. Soc.* **2019**, *141* (10). https://doi.org/10.1021/jacs.8b12640.

(44) Fratini, S.; Nikolka, M.; Salleo, A.; Schweicher, G.; Sirringhaus, H. Charge Transport in High-Mobility Conjugated Polymers and Molecular Semiconductors. *Nat. Mater.* **2020**, *19* (5), 491–502. https://doi.org/10.1038/s41563-020-0647-2.

(45) Wang, C.; Dong, H.; Jiang, L.; Hu, W. Organic Semiconductor Crystals. *Chem. Soc. Rev.* **2018**, *47* (2), 422–500. https://doi.org/10.1039/c7cs00490g.

(46) Galindo, S.; Tamayo, A.; Leonardi, F.; Mas-Torrent, M. Control of Polymorphism and Morphology in Solution Sheared Organic Field-Effect Transistors. *Adv. Funct. Mater.* **2017**, *27* (25), 1–9. https://doi.org/10.1002/adfm.201700526.

(47) Jurchescu, O. D.; Mourey, D. A.; Subramanian, S.; Parkin, S. R.; Vogel, B. M.; Anthony, J. E.; Jackson, T. N.; Gundlach, D. J. Effects of Polymorphism on Charge Transport in Organic Semiconductors. *Phys. Rev. B - Condens. Matter Mater. Phys.* **2009**, *80* (8), 21–23. https://doi.org/10.1103/PhysRevB.80.085201.

(48) Bergantin, S.; Moret, M. Rubrene Polymorphs and Derivatives: The Effect of Chemical Modification on the Crystal Structure. *Cryst. Growth & Des.* **2012**, *12* (12), 6035–6041. https://doi.org/10.1021/cg301130n.

(49) Paterson, A. F.; Singh, S.; Fallon, K. J.; Hodsden, T.; Han, Y.; Schroeder, B. C.; Bronstein, H.; Heeney, M.; McCulloch, I.; Anthopoulos, T. D. Recent Progress in High-Mobility Organic Transistors: A Reality Check. *Adv. Mater.* **2018**, *30* (36), 1–33. https://doi.org/10.1002/adma.201801079.

(50) Gundlach, D. J.; Lin, Y. Y.; Jackson, T. N.; Nelson, S. F.; Schlom, D. G. Pentacene Organic Thin-Film Transistors-Molecular Ordering and Mobility. *IEEE Electron Device Lett.* **1997**, *18* (3), 87–89. https://doi.org/10.1109/55.556089.

(51) Podzorov, V.; Pudalov, V. M.; Gershenson, M. E. Field-Effect Transistors on Rubrene Single Crystals with Parylene Gate Insulator. *Appl. Phys. Lett.* **2003**, *82* (11), 1739–1741. https://doi.org/10.1063/1.1560869.

(52) Anthony, J. E.; Brooks, J. S.; Eaton, D. L.; Parkin, S. R. Functionalized Pentacene: Improved Electronic Properties from Control of Solid-State Order [20]. *Journal of the American Chemical Society*. August 30, 2001, pp 9482–9483. https://doi.org/10.1021/ja0162459.

(53) Subramanian, S.; Kyu Park, S.; R. Parkin, S.; Podzorov, V.; N. Jackson, T.; E. Anthony, J. Chromophore Fluorination Enhances Crystallization and Stability of Soluble Anthradithiophene Semiconductors. *J. Am. Chem. Soc.* **2008**, *130* (9), 2706–2707. https://doi.org/10.1021/ja073235k.

(54) Ebata, H.; Izawa, T.; Miyazaki, E.; Takimiya, K.; Ikeda, M.; Kuwabara, H.; Yui, T. Highly Soluble [1]Benzothieno[3,2-b]Benzothiophene (BTBT) Derivatives for High-Performance, Solution-Processed Organic Field-Effect Transistors. *J. Am. Chem. Soc.* **2007**, *129* (51), 15732–15733. https://doi.org/10.1021/ja074841i.

(55) Yamamoto, T.; Takimiya, K. Facile Synthesis of Highly π-Extended Heteroarenes, Dinaphtho[2,3-b:2‘,3‘-f]Chalcogenopheno[3,2-b]Chalcogenophenes, and Their Application to Field-Effect Transistors. *J. Am. Chem. Soc.* **2007**, *129* (8), 2224–2225. https://doi.org/10.1021/ja068429z.

(56) Li, H.; Tee, B. C. K.; Cha, J. J.; Cui, Y.; Chung, J. W.; Lee, S. Y.; Bao, Z. High-Mobility Field-Effect Transistors from Large-Area Solution-Grown Aligned C 60 Single Crystals. *J. Am. Chem. Soc.* **2012**, *134* (5), 2760–2765. https://doi.org/10.1021/ja210430b.

(57) Liang, Z.; Tang, Q.; Xu, J.; Miao, Q. Soluble and Stable N-Heteropentacenes with High Field-Effect Mobility. *Adv. Mater.* **2011**, *23* (13), 1535–1539. https://doi.org/https://doi.org/10.1002/adma.201004325.

(58) Würthner, F.; Stolte, M. Naphthalene and Perylene Diimides for Organic Transistors. *Chem. Commun.* **2011**, *47* (18), 5109–5115. https://doi.org/10.1039/c1cc10321k.

(59) Noriega, R.; Rivnay, J.; Vandewal, K.; Koch, F. P. V.; Stingelin, N.; Smith, P.; Toney, M. F.; Salleo, A. A General Relationship between Disorder, Aggregation and Charge Transport in Conjugated Polymers. *Nat. Mater.* **2013**, *12* (11), 1038–1044. https://doi.org/10.1038/nmat3722.

(60) Janasz, L.; Borkowski, M.; Blom, P. W. M.; Marszalek, T.; Pisula, W. Organic Semiconductor/Insulator Blends for Elastic Field-Effect Transistors and Sensors. *Adv. Funct. Mater.* **2022**, *32* (7). https://doi.org/10.1002/adfm.202105456.

(61) Chen, J.; Huang, W.; Zheng, D.; Xie, Z.; Zhuang, X.; Zhao, D.; Chen, Y.; Su, N.; Chen, H.; Pankow, R. M.; Gao, Z.; Yu, J.; Guo, X.; Cheng, Y.; Strzalka, J.; Yu, X.; Marks, T. J.; Facchetti, A. Highly Stretchable Organic Electrochemical Transistors with Strain-Resistant Performance. *Nat. Mater.* **2022**, *21* (5), 564–571. https://doi.org/10.1038/s41563-022-01239-9.

(62) Keene, S. T.; van der Pol, T. P. A.; Zakhidov, D.; Weijtens, C. H. L.; Janssen, R. A. J.; Salleo, A.; van de Burgt, Y. Enhancement-Mode PEDOT:PSS Organic Electrochemical Transistors Using Molecular De-Doping. *Adv. Mater.* **2020**, *32* (19). https://doi.org/10.1002/adma.202000270.

(63) Giovannitti, A.; Sbircea, D. T.; Inal, S.; Nielsen, C. B.; Bandiello, E.; Hanifi, D. A.;

Sessolo, M.; Malliaras, G. G.; McCulloch, I.; Rivnay, J. Controlling the Mode of Operation of Organic Transistors through Side-Chain Engineering. *Proc. Natl. Acad. Sci. U. S. A.* **2016**, *113* (43), 12017–12022. https://doi.org/10.1073/pnas.1608780113.

(64) Paulsen, B. D.; Tybrandt, K.; Stavrinidou, E.; Rivnay, J. Organic Mixed Ionic–Electronic Conductors. *Nat. Mater.* **2020**, *19* (1), 13–26. https://doi.org/10.1038/s41563-019-0435-z.

(65) Inal, S.; Rivnay, J.; Suiu, A. O.; Malliaras, G. G.; McCulloch, I. Conjugated Polymers in Bioelectronics. *Acc. Chem. Res.* **2018**, *51* (6), 1368–1376. https://doi.org/10.1021/acs.accounts.7b00624.

(66) Kim, M.; Ryu, S. U.; Park, S. A.; Choi, K.; Kim, T.; Chung, D.; Park, T. Donor–Acceptor-Conjugated Polymer for High-Performance Organic Field-Effect Transistors: A Progress Report. *Advanced Functional Materials*. 2020. https://doi.org/10.1002/adfm.201904545.

(67) Venkateshvaran, D.; Nikolka, M.; Sadhanala, A.; Lemaur, V.; Zelazny, M.; Kepa, M.; Hurhangee, M.; Kronemeijer, A. J.; Pecunia, V.; Nasrallah, I.; Romanov, I.; Broch, K.; McCulloch, I.; Emin, D.; Olivier, Y.; Cornil, J.; Beljonne, D.; Sirringhaus, H. Approaching Disorder-Free Transport in High-Mobility Conjugated Polymers. *Nature* **2014**, *515* (7527), 384–388. https://doi.org/10.1038/nature13854.

(68) Caironi, M.; Bird, M.; Fazzi, D.; Chen, Z.; Di Pietro, R.; Newman, C.; Facchetti, A.; Sirringhaus, H. Very Low Degree of Energetic Disorder as the Origin of High Mobility in an N-Channel Polymer Semiconductor. *Adv. Funct. Mater.* **2011**, *21* (17), 3371–3381. https://doi.org/10.1002/adfm.201100592.

(69) Sommer, M.; Huettner, S.; Thelakkat, M. Donor-Acceptor Block Copolymers for Photovoltaic Applications. *J. Mater. Chem.* **2010**, *20* (48), 10788–10797. https://doi.org/10.1039/c0jm00665c.

(70) Zhang, M.; Tsao, H. N.; Pisula, W.; Yang, C.; Mishra, A. K.; Müllen, K. Field-Effect Transistors Based on a Benzothiadiazole−Cyclopentadithiophene Copolymer. *J. Am. Chem. Soc.* **2007**, *129* (12), 3472–3473. https://doi.org/10.1021/ja0683537.

(71) Bronstein, H.; Frost, J. M.; Hadipour, A.; Kim, Y.; Nielsen, C. B.; Ashraf, R. S.; Rand, B. P.; Watkins, S.; McCulloch, I. Effect of Fluorination on the Properties of a Donor-Acceptor Copolymer for Use in Photovoltaic Cells and Transistors. *Chem. Mater.* **2013**, *25* (3), 277–285. https://doi.org/10.1021/cm301910t.

(72) Guo, X.; Facchetti, A.; Marks, T. J. Imide- and Amide-Functionalized Polymer Semiconductors. *Chemical Reviews*. American Chemical Society September 2, 2014, pp 8943–9012. https://doi.org/10.1021/cr500225d.

(73) Guo, X.; Baumgarten, M.; Müllen, K. Designing π-Conjugated Polymers for Organic Electronics. *Progress in Polymer Science*. Elsevier 2013, pp 1832–1908. https://doi.org/10.1016/j.progpolymsci.2013.09.005.

(74) Yan, H.; Chen, Z.; Zheng, Y.; Newman, C.; Quinn, J. R.; Dötz, F.; Kastler, M.; Facchetti, A. A High-Mobility Electron-Transporting Polymer for Printed Transistors. *Nature* **2009**, *457* (7230), 679–686. https://doi.org/10.1038/nature07727.

(75) Bucella, S. G.; Luzio, A.; Gann, E.; Thomsen, L.; McNeill, C. R.; Pace, G.; Perinot, A.; Chen, Z.; Facchetti, A.; Caironi, M. Macroscopic and High-Throughput Printing of Aligned Nanostructured Polymer Semiconductors for MHz Large-Area Electronics. *Nat. Commun.* **2015**, *6*, 8394. https://doi.org/10.1038/ncomms9394.

(76) Sommer, M. Conjugated Polymers Based on Naphthalene Diimide for Organic Electronics. *J. Mater. Chem. C* **2014**, *2* (17), 3088–3098. https://doi.org/10.1039/c3tc31755b.

(77) Zhou, N.; Facchetti, A. Naphthalenediimide (NDI) Polymers for All-Polymer Photovoltaics. *Materials Today*. Elsevier May 1, 2018, pp 377–390. https://doi.org/10.1016/j.mattod.2018.02.003.

(78) Liu, J.; Ye, G.; van der Zee, B.; Dong, J.; Qiu, X.; Liu, Y.; Portale, G.; Chiechi, R. C.; Koster, L. J. A. N-Type Organic Thermoelectrics of Donor–Acceptor Copolymers: Improved Power Factor by Molecular Tailoring of the Density of States. *Adv. Mater.* **2018**, *30* (44). https://doi.org/10.1002/adma.201804290.

(79) Steyrleuthner, R.; Schubert, M.; Howard, I.; Klaumünzer, B.; Schilling, K.; Chen, Z.; Saalfrank, P.; Laquai, F.; Facchetti, A.; Neher, D. Aggregation in a High-Mobility n-Type Low-Bandgap Copolymer with Implications on Semicrystalline Morphology. *J. Am. Chem. Soc.* **2012**, *134* (44), 18303–18317. https://doi.org/10.1021/ja306844f.

(80) Leventis, A.; Royakkers, J.; Rapidis, A. G.; Goodeal, N.; Corpinot, M. K.; Frost, J. M.; Bučar, D.-K. K.; Blunt, M. O.; Cacialli, F.; Bronstein, H. Highly Luminescent Encapsulated Narrow Bandgap Polymers Based on Diketopyrrolopyrrole. *J. Am. Chem. Soc.* **2018**, *140* (5), 1622–1626. https://doi.org/10.1021/jacs.7b13447.

(81) Royakkers, J.; Minotto, A.; Congrave, D. G.; Zeng, W.; Hassan, A.; Leventis, A.; Cacialli, F.; Bronstein, H. Suppressing Solid-State Quenching in Red-Emitting Conjugated Polymers. *Chem. Mater.* **2020**, *32* (23), 10140–10145. https://doi.org/10.1021/acs.chemmater.0c03604.

(82) Royakkers, J.; Minotto, A.; Congrave, D. G.; Zeng, W.; Patel, A.; Bond, A. D.; Bučar, D. K.; Cacialli, F.; Bronstein, H. Doubly Encapsulated Perylene Diimides: Effect of Molecular Encapsulation on Photophysical Properties. *J. Org. Chem.* **2020**, *85* (1), 207–214. https://doi.org/10.1021/acs.joc.9b02597.

(83) Royakkers, J.; Bronstein, H. Macrocyclic Encapsulated Conjugated Polymers. *Macromolecules*. ACS Publications 2021, pp 1083–1094. https://doi.org/10.1021/acs.macromol.0c01916.

(84) Cacialli, F.; Wilson, J. S.; Michels, J. J.; Daniel, C.; Silva, C.; Friend, R. H.; Severin, N.; Samori, P.; Rabe, J. P.; O'connell, M. J.; Taylor, P. N.; Anderson, H. L. Cyclodextrin-Threaded Conjugated Polyrotaxanes as Insulated Molecular Wires with Reduced Interstrand Interactions. *Nat. Mater.* **2002**, *1* (3), 160–164. https://doi.org/10.1038/nmat750.

(85) Schubert, M.; Dolfen, D.; Frisch, J.; Roland, S.; Steyrleuthner, R.; Stiller, B.; Chen, Z.; Scherf, U.; Koch, N.; Facchetti, A.; Neher, D. Influence of Aggregation on the Performance of All-Polymer Solar Cells Containing Low-Bandgap Naphthalenediimide Copolymers. *Adv. Energy Mater.* **2012**, *2* (3), 369–380. https://doi.org/10.1002/aenm.201100601.

(86) Luzio, A.; Criante, L.; D'Innocenzo, V.; Caironi, M. Control of Charge Transport in a Semiconducting Copolymer by Solvent-Induced Long-Range Order. *Sci. Rep.* **2013**, *3*, 1–6. https://doi.org/10.1038/srep03425.

(87) Zorn, N. F.; Zaumseil, J. Charge Transport in Semiconducting Carbon Nanotube Networks. *Appl. Phys. Rev.* **2021**, *8* (4). https://doi.org/10.1063/5.0065730.

(88) Wong, H.-S. P.; Akinwande, D. *Carbon Nanotube and Graphene Device Physics*;

Cambridge University Press: Cambridge, 2010. https://doi.org/DOI: 10.1017/CBO9780511778124.

(89) Bachilo, S. M.; Strano, M. S.; Kittrell, C.; Hauge, R. H.; Smalley, R. E.; Weisman, R. B. Structure-Assigned Optical Spectra of Single-Walled Carbon Nanotubes. *Science (80-.).* **2002**, *298* (5602), 2361–2366. https://doi.org/10.1126/science.1078727.

(90) O'Connell, M. J.; Bachilo, S. M.; Huffman, C. B.; Moore, V. C.; Strano, M. S.; Haroz, E. H.; Rialon, K. L.; Boul, P. J.; Noon, W. H.; Kittrell, C.; Ma, J.; Hauge, R. H.; Weisman, R. B.; Smalley, R. E. Band Gap Fluorescence from Individual Single-Walled Carbon Nanotubes. *Science (80-.).* **2002**, *297* (5581), 593–596. https://doi.org/10.1126/science.1072631.

(91) Di Donato, E.; Tommasini, M.; Castiglioni, C.; Zerbi, G. Assignment of the G+ and G- Raman Bands of Metallic and Semiconducting Carbon Nanotubes Based on a Common Valence Force Field. *Phys. Rev. B - Condens. Matter Mater. Phys.* **2006**, *74* (18), 1–12. https://doi.org/10.1103/PhysRevB.74.184306.

(92) Grimm, S.; Schießl, S. P.; Zakharko, Y.; Rother, M.; Brohmann, M.; Zaumseil, J. Doping-Dependent G-Mode Shifts of Small Diameter Semiconducting Single-Walled Carbon Nanotubes. *Carbon N. Y.* **2017**, *118*, 261–267. https://doi.org/10.1016/j.carbon.2017.03.040.

(93) Zaumseil, J.; Jakubka, F.; Wang, M.; Gannott, F. In Situ Raman Mapping of Charge Carrier Distribution in Electrolyte-Gated Carbon Nanotube Network Field-Effect Transistors. *J. Phys. Chem. C* **2013**, *117* (49), 26361–26370. https://doi.org/10.1021/jp409849w.

(94) Matsunaga, R.; Matsuda, K.; Kanemitsu, Y. Observation of Charged Excitons in Hole-Doped Carbon Nanotubes Using Photoluminescence and Absorption Spectroscopy. *Phys. Rev. Lett.* **2011**, *106* (3), 1–4. https://doi.org/10.1103/PhysRevLett.106.037404.

(95) Park, J. S.; Hirana, Y.; Mouri, S.; Miyauchi, Y.; Nakashima, N.; Matsuda, K. Observation of Negative and Positive Trions in the Electrochemically Carrier-Doped Single-Walled Carbon Nanotubes. *J. Am. Chem. Soc.* **2012**, *134* (35). https://doi.org/10.1021/ja304282j.

(96) Eckstein, K. H.; Hartleb, H.; Achsnich, M. M.; Schöppler, F.; Hertel, T. Localized Charges Control Exciton Energetics and Energy Dissipation in Doped Carbon Nanotubes. *ACS Nano* **2017**, *11* (10), 10401–10408. https://doi.org/10.1021/acsnano.7b05543.

(97) Eckstein, K. H.; Oberndorfer, F.; Achsnich, M. M.; Schöppler, F.; Hertel, T. Quantifying Doping Levels in Carbon Nanotubes by Optical Spectroscopy. *J. Phys. Chem. C* **2019**, *123* (49), 30001–30006. https://doi.org/10.1021/acs.jpcc.9b08663.

(98) Zhang, Z.; Liang, X.; Wang, S.; Yao, K.; Hu, Y.; Zhu, Y.; Chen, Q.; Zhou, W.; Li, Y.; Yao, Y.; Zhang, J.; Peng, L.-M. Doping-Free Fabrication of Carbon Nanotube Based Ballistic CMOS Devices and Circuits. *Nano Lett.* **2007**, *7* (12), 3603–3607. https://doi.org/10.1021/nl0717107.

(99) Dürkop, T.; A. Getty, S.; Cobas, E.; S. Fuhrer, M. Extraordinary Mobility in Semiconducting Carbon Nanotubes. *Nano Lett.* **2003**, *4* (1), 35–39. https://doi.org/10.1021/nl034841q.

(100) Wei, B. Q.; Vajtai, R.; Ajayan, P. M. Reliability and Current Carrying Capacity of Carbon Nanotubes. *Appl. Phys. Lett.* **2001**, *79* (8), 1172–1174.

https://doi.org/10.1063/1.1396632.

(101) Franklin, A. D.; Hersam, M. C.; Wong, H.-S. P. Carbon Nanotube Transistors: Making Electronics from Molecules. *Science (80-.).* **2022**, *378* (6621), 726–732. https://doi.org/10.1126/science.abp8278.

(102) Bishop, M. D.; Hills, G.; Srimani, T.; Lau, C.; Murphy, D.; Fuller, S.; Humes, J.; Ratkovich, A.; Nelson, M.; Shulaker, M. M. Fabrication of Carbon Nanotube Field-Effect Transistors in Commercial Silicon Manufacturing Facilities. *Nat. Electron.* **2020**, *3* (8), 492–501. https://doi.org/10.1038/s41928-020-0419-7.

(103) Shulaker, M. M.; Hills, G.; Park, R. S.; Howe, R. T.; Saraswat, K.; Wong, H.-S. P.; Mitra, S. Three-Dimensional Integration of Nanotechnologies for Computing and Data Storage on a Single Chip. *Nature* **2017**, *547* (7661), 74–78. https://doi.org/10.1038/nature22994.

(104) Liu, L.; Han, J.; Xu, L.; Zhou, J.; Zhao, C.; Ding, S.; Shi, H.; Xiao, M.; Ding, L.; Ma, Z.; Jin, C.; Zhang, Z.; Peng, L.-M. Aligned, High-Density Semiconducting Carbon Nanotube Arrays for High-Performance Electronics. *Science (80-.).* **2020**, *368* (6493), 850–856. https://doi.org/10.1126/science.aba5980.

(105) Heng Lau, P.; Takei, K.; Wang, C.; Ju, Y.; Kim, J.; Yu, Z.; Takahashi, T.; Cho, G.; Javey, A. Fully Printed, High Performance Carbon Nanotube Thin-Film Transistors on Flexible Substrates. *Nano Lett.* **2013**, *13* (8), 3864–3869. https://doi.org/10.1021/nl401934a.

(106) Scuratti, F.; Salazar-Rios, J. M.; Luzio, A.; Kowalski, S.; Allard, S.; Jung, S.; Scherf, U.; Loi, M. A.; Caironi, M. Charge Transport in High-Mobility Field-Effect Transistors Based on Inkjet Printed Random Networks of Polymer Wrapped Single-Walled Carbon Nanotubes. *Adv. Funct. Mater.* **2021**, *31* (5). https://doi.org/10.1002/adfm.202006895.

(107) Chen, P.; Fu, Y.; Aminirad, R.; Wang, C.; Zhang, J.; Wang, K.; Galatsis, K.; Zhou, C. Fully Printed Separated Carbon Nanotube Thin Film Transistor Circuits and Its Application in Organic Light Emitting Diode Control. *Nano Lett.* **2011**, *11* (12), 5301–5308. https://doi.org/10.1021/nl202765b.

(108) Schnittker, K.; Tursunniyaz, M.; Andrews, J. B. Recent Advances in Printable Carbon Nanotube Transistors for Large-Area Active Matrices. *J. Inf. Disp.* **2021**, *22* (4), 193–209. https://doi.org/10.1080/15980316.2021.1957032.

(109) Wang, S.; Zhao, J.; Wang, Q.; Zhang, D. Preparation and Recycling of High-Performance Carbon Nanotube Films. *ACS Sustain. Chem. Eng.* **2022**, *10* (12), 3851–3861. https://doi.org/10.1021/acssuschemeng.1c07089.

(110) Franklin, A. D.; Hersam, M. C. Making Electronics from Molecules. **2022**, *732* (November), 726–732.

(111) Fagan, J. A.; Hároz, E. H.; Ihly, R.; Gui, H.; Blackburn, J. L.; Simpson, J. R.; Lam, S.; Hight Walker, A. R.; Doorn, S. K.; Zheng, M. Isolation of >1 Nm Diameter Single-Wall Carbon Nanotube Species Using Aqueous Two-Phase Extraction. *ACS Nano* **2015**, *9* (5). https://doi.org/10.1021/acsnano.5b01123.

(112) Liu, H.; Nishide, D.; Tanaka, T.; Kataura, H. Large-Scale Single-Chirality Separation of Single-Wall Carbon Nanotubes by Simple Gel Chromatography. *Nat. Commun.* **2011**, *2* (1), 309. https://doi.org/10.1038/ncomms1313.

(113) Graf, A.; Zakharko, Y.; Schießl, S. P.; Backes, C.; Pfohl, M.; Flavel, B. S.; Zaumseil, J.

Large Scale, Selective Dispersion of Long Single-Walled Carbon Nanotubes with High Photoluminescence Quantum Yield by Shear Force Mixing. *Carbon N. Y.* **2016**, *105*. https://doi.org/10.1016/j.carbon.2016.05.002.

(114) Lei, T.; Pochorovski, I.; Bao, Z. Separation of Semiconducting Carbon Nanotubes for Flexible and Stretchable Electronics Using Polymer Removable Method. *Acc. Chem. Res.* **2017**, *50* (4), 1096–1104. https://doi.org/10.1021/acs.accounts.7b00062.

(115) Tortorich, R. P.; Choi, J.-W. Inkjet Printing of Carbon Nanotubes. *Nanomaterials*. 2013, pp 453–468. https://doi.org/10.3390/nano3030453.

(116) Statz, M.; Schneider, S.; J. Berger, F.; Lai, L.; A. Wood, W.; Abdi-Jalebi, M.; Leingang, S.; Himmel, H.-J.; Zaumseil, J.; Sirringhaus, H. Charge and Thermoelectric Transport in Polymer-Sorted Semiconducting Single-Walled Carbon Nanotube Networks. *ACS Nano* **2020**, *14* (11), 15552–15565. https://doi.org/10.1021/acsnano.0c06181.

(117) Li, Z.; Ouyang, J.; Ding, J. Diameter-Dependent Semiconducting Carbon Nanotube Network Transistor Performance. *ACS Appl. Electron. Mater.* **2022**, *0* (0). https://doi.org/10.1021/acsaelm.2c01469.

(118) Schießl, S. P.; De Vries, X.; Rother, M.; Massé, A.; Brohmann, M.; Bobbert, P. A.; Zaumseil, J. Modeling Carrier Density Dependent Charge Transport in Semiconducting Carbon Nanotube Networks. *Phys. Rev. Mater.* **2017**, *1* (4). https://doi.org/10.1103/PhysRevMaterials.1.046003.

(119) Perebeinos, V.; Tersoff, J.; Avouris, P. Electron-Phonon Interaction and Transport in Semiconducting Carbon Nanotubes. *Phys. Rev. Lett.* **2005**, *94* (8), 2–5. https://doi.org/10.1103/PhysRevLett.94.086802.

(120) Sano, E.; Tanaka, T. A Simple Drain Current Model for Single-Walled Carbon Nanotube Network Thin-Film Transistors. *J. Appl. Phys.* **2014**, *115* (15). https://doi.org/10.1063/1.4871775.

(121) Zorn, N. F.; Scuratti, F.; Berger, F. J.; Perinot, A.; Heimfarth, D.; Caironi, M.; Zaumseil, J. Probing Mobile Charge Carriers in Semiconducting Carbon Nanotube Networks by Charge Modulation Spectroscopy. *ACS Nano* **2020**, *14* (2), 2412–2423. https://doi.org/10.1021/acsnano.9b09761.

(122) Zirzlmeier, J.; Schrettl, S.; Brauer, J. C.; Contal, E.; Vannay, L.; Brémond, É.; Jahnke, E.; Guldi, D. M.; Corminboeuf, C.; Tykwinski, R. R.; Frauenrath, H. Optical Gap and Fundamental Gap of Oligoynes and Carbyne. *Nat. Commun.* **2020**, *11* (1), 1–10. https://doi.org/10.1038/s41467-020-18496-4.

(123) Liu, M.; Artyukhov, V. I.; Lee, H.; Xu, F.; Yakobson, B. I. Carbyne from First Principles: Chain of c Atoms, a Nanorod or a Nanorope. *ACS Nano* **2013**, *7* (11), 10075–10082. https://doi.org/10.1021/nn404177r.

(124) Itzhaki, L.; Altus, E.; Basch, H.; Hoz, S. Harder than Diamond: Determining the Cross-Sectional Area and Young's Modulus of Molecular Rods. *Angew. Chemie Int. Ed.* **2005**, *44* (45), 7432–7435. https://doi.org/https://doi.org/10.1002/anie.200502448.

(125) Sorokin, P. B.; Lee, H.; Antipina, L. Y.; Singh, A. K.; Yakobson, B. I. Calcium-Decorated Carbyne Networks as Hydrogen Storage Media. *Nano Lett.* **2011**, *11* (7), 2660–2665. https://doi.org/10.1021/nl200721v.

(126) Tykwinski, R. R.; Chalifoux, W.; Eisler, S.; Lucotti, A.; Tommasini, M.; Fazzi, D.; Del Zoppo, M.; Zerbi, G. Toward Carbyne: Synthesis and Stability of Really Long Polyynes.

Pure Appl. Chem. **2010**, *82* (4), 891–904. https://doi.org/10.1351/PAC-CON-09-09-04.

(127) Wang, M.; Lin, S. Ballistic Thermal Transport in Carbyne and Cumulene with Micron-Scale Spectral Acoustic Phonon Mean Free Path. *Sci. Rep.* **2015**, *5*, 18122. https://doi.org/10.1038/srep18122.

(128) Slepkov, A. D.; Hegmann, F. A.; Eisler, S.; Elliott, E.; Tykwinski, R. R. The Surprising Nonlinear Optical Properties of Conjugated Polyyne Oligomers. *J. Chem. Phys.* **2004**, *120* (15), 6807–6810. https://doi.org/10.1063/1.1707011.

(129) Eisler, S.; Slepkov, A. D.; Elliott, E.; Luu, T.; McDonald, R.; Hegmann, F. A.; Tykwinski, R. R. Polyynes as a Model for Carbyne: Synthesis, Physical Properties, and Nonlinear Optical Response. *J. Am. Chem. Soc.* **2005**, *127* (8), 2666–2676. https://doi.org/10.1021/ja044526l.

(130) Marabotti, P.; Milani, A.; Lucotti, A.; Brambilla, L.; Tommasini, M.; Castiglioni, C.; Męcik, P.; Pigulski, B.; Szafert, S.; Casari, C. S. Vibrational and Nonlinear Optical Properties of Amine-Capped Push-Pull Polyynes by Infrared and Raman Spectroscopy. *Carbon Trends* **2021**, *5*, 100115. https://doi.org/10.1016/j.cartre.2021.100115.

(131) Agarwal, N. R.; Lucotti, A.; Tommasini, M.; Chalifoux, W. A.; Tykwinski, R. R. Nonlinear Optical Properties of Polyynes: An Experimental Prediction for Carbyne. *J. Phys. Chem. C* **2016**, *120* (20), 11131–11139. https://doi.org/10.1021/acs.jpcc.6b03071.

(132) Zhu, Y.; Bai, H.; Huang, Y. Electronic Property Modulation of One-Dimensional Extended Graphdiyne Nanowires from a First-Principle Crystal Orbital View. *ChemistryOpen* **2016**, *5* (1), 78–87. https://doi.org/10.1002/open.201500154.

(133) Banhart, F. Elemental Carbon in the Sp 1 Hybridization. *ChemTexts* **2020**, *6* (1), 1–10. https://doi.org/10.1007/s40828-019-0098-z.

(134) Yang, S.; Kertesz, M. Bond Length Alternation and Energy Band Gap of Polyyne. *J. Phys. Chem. A* **2006**, *110* (31), 9771–9774. https://doi.org/10.1021/jp062701+.

(135) Artyukhov, V. I.; Liu, M.; Yakobson, B. I. Mechanically Induced Metal-Insulator Transition in Carbyne. *Nano Lett.* **2014**, *14* (8), 4224–4229. https://doi.org/10.1021/nl5017317.

(136) Kartoon, D.; Argaman, U.; Makov, G. Driving Forces behind the Distortion of One-Dimensional Monatomic Chains: Peierls Theorem Revisited. *Phys. Rev. B* **2018**, *94* (16), 1–5. https://doi.org/10.1103/PhysRevB.98.165429.

(137) Milani, A.; Tommasini, M.; Barbieri, V.; Lucotti, A.; Russo, V.; Cataldo, F.; Casari, C. S. Semiconductor-to-Metal Transition in Carbon-Atom Wires Driven by Sp2 Conjugated End Groups. *J. Phys. Chem. C* **2017**, *121* (19), 10562–10570. https://doi.org/10.1021/acs.jpcc.7b02246.

(138) Nuraliev, M. K.; Parashchuk, O. D.; Tukachev, N. V.; Repeev, Y. A.; Maslennikov, D. R.; Borshchev, O. V.; Vainer, Y. G.; Paraschuk, D. Y.; Sosorev, A. Y. Toward Probing of the Local Electron-Phonon Interaction in Small-Molecule Organic Semiconductors with Raman Spectroscopy. *J. Chem. Phys.* **2020**, *153* (17). https://doi.org/10.1063/5.0023754.

(139) Giussani, E.; Fazzi, D.; Brambilla, L.; Caironi, M.; Castiglioni, C. Molecular Level Investigation of the Film Structure of a High Electron Mobility Copolymer via Vibrational Spectroscopy. *Macromolecules* **2013**, *46* (7), 2658–2670. https://doi.org/10.1021/ma302664s.

(140) Milani, A.; Tommasini, M.; Russo, V.; Li Bassi, A.; Lucotti, A.; Cataldo, F.; Casari, C. S. Raman Spectroscopy as a Tool to Investigate the Structure and Electronic Properties of Carbon-Atom Wires. *Beilstein J. Nanotechnol.* **2015**, *6*, 480–491.

(141) Castiglioni, C.; Lopez Navarrete, J. T.; Zerbi, G.; Gussoni, M. A Simple Interpretation of the Vibrational Spectra of Undoped, Doped and Photoexcited Polyacetylene: Amplitude Mode Theory in the GF Formalism. *Solid State Commun.* **1988**, *65* (7), 625–630. https://doi.org/https://doi.org/10.1016/0038-1098(88)90352-3.

(142) Zerbi, G.; Castiglioni, C.; Lopez Navarrete, J. T.; Bogang, T.; Gussoni, M. A Molecular Viewpoint of Lattice Dynamics and Spectra of Conducting Polymers. *Synth. Met.* **1989**, *28* (3), D359–D368. https://doi.org/https://doi.org/10.1016/0379-6779(89)90715-7.

(143) Milani, A.; Tommasini, M.; Del Zoppo, M.; Castiglioni, C.; Zerbi, G. Carbon Nanowires: Phonon and π -Electron Confinement. *Phys. Rev. B - Condens. Matter Mater. Phys.* **2006**, *74* (15), 1–4. https://doi.org/10.1103/PhysRevB.74.153418.

(144) Januszewski, J. A.; Wendinger, D.; Methfessel, C. D.; Hampel, F.; Tykwinski, R. R. Synthesis and Structure of Tetraarylcumulenes: Characterization of Bond-Length Alternation versus Molecule Length. *Angew. Chemie Int. Ed.* **2013**, *52* (6), 1817–1821. https://doi.org/https://doi.org/10.1002/anie.201208058.

(145) Tommasini, M.; Milani, A.; Fazzi, D.; Lucotti, A.; Castiglioni, C.; Januszewski, J. A.; Wendinger, D.; Tykwinski, R. R. π-Conjugation and End Group Effects in Long Cumulenes: Raman Spectroscopy and DFT Calculations. *J. Phys. Chem. C* **2014**, *118* (45), 26415–26425. https://doi.org/10.1021/jp509724d.

(146) Peggiani, S.; Marabotti, P.; Lotti, R. A.; Facibeni, A.; Serafini, P.; Milani, A.; Russo, V.; Li Bassi, A.; Casari, C. S. Solvent-Dependent Termination, Size and Stability in Polyynes Synthesized: Via Laser Ablation in Liquids. *Phys. Chem. Chem. Phys.* **2020**, *22* (45), 26312–26321. https://doi.org/10.1039/d0cp04132g.

(147) Wendinger, D.; Tykwinski, R. R. Odd [n]Cumulenes (n = 3, 5, 7, 9): Synthesis, Characterization, and Reactivity. *Acc. Chem. Res.* **2017**, *50* (6), 1468–1479. https://doi.org/10.1021/acs.accounts.7b00164.

(148) Gao, Y.; Hou, Y.; Gordillo Gámez, F.; Ferguson, M. J.; Casado, J.; Tykwinski, R. R. The Loss of Endgroup Effects in Long Pyridyl-Endcapped Oligoynes on the Way to Carbyne. *Nat. Chem.* **2020**, *12* (12), 1143–1149. https://doi.org/10.1038/s41557-020-0550-0.

(149) Franz, M.; Januszewski, J. A.; Wendinger, D.; Neiss, C.; Movsisyan, L. D.; Hampel, F.; Anderson, H. L.; Görling, A.; Tykwinski, R. R. Cumulene Rotaxanes: Stabilization and Study of [9]Cumulenes. *Angew. Chemie Int. Ed.* **2015**, *54* (22), 6645–6649. https://doi.org/https://doi.org/10.1002/anie.201501810.

(150) Milan, D. C.; Krempe, M.; Ismael, A. K.; Movsisyan, L. D.; Franz, M.; Grace, I.; Brooke, R. J.; Schwarzacher, W.; Higgins, S. J.; Anderson, H. L.; Lambert, C. J.; Tykwinski, R. R.; Nichols, R. J. The Single-Molecule Electrical Conductance of a Rotaxane-Hexayne Supramolecular Assembly. *Nanoscale* **2017**, *9* (1), 355–361. https://doi.org/10.1039/C6NR06355A.

(151) Gawel, P.; Woltering, S. L.; Xiong, Y.; Christensen, K. E.; Anderson, H. L. Masked Alkyne Equivalents for the Synthesis of Mechanically Interlocked Polyynes**. *Angew. Chemie Int. Ed.* **2021**, *60* (11), 5941–5947. https://doi.org/https://doi.org/10.1002/anie.202013623.

(152) Shi, L.; Rohringer, P.; Suenaga, K.; Niimi, Y.; Kotakoski, J.; Meyer, J. C.; Peterlik, H.; Wanko, M.; Cahangirov, S.; Rubio, A.; Lapin, Z. J.; Novotny, L.; Ayala, P.; Pichler, T. Confined Linear Carbon Chains as a Route to Bulk Carbyne. *Nat. Mater.* **2016**, *15* (6), 634–639. https://doi.org/10.1038/nmat4617.

(153) Pinter, P.; Munz, D. Controlling Möbius-Type Helicity and the Excited-State Properties of Cumulenes with Carbenes. *J. Phys. Chem. A* **2020**, *124* (49), 10100–10110. https://doi.org/10.1021/acs.jpca.0c07940.

(154) Ahmed, M. K.; Rahman, M. M.; Naher, M.; Mehdi, S. S.; Khan, A. R.; Khan, M. M. R.; Islam, S. M. S.; Younus, M.; Wedler, S.; Bagnich, S.; Hofmann, A.-L.; Rudnick, A.; Köhler, A. A New Series of Conjugated Platinum-Co-Poly(p-Phenylenebutadiynylene)s Polymers: Syntheses and Photophysical Properties. *Macromol. Chem. Phys.* **2019**, *220* (8), 1800494. https://doi.org/https://doi.org/10.1002/macp.201800494.

(155) D. Movsisyan, L.; D. Peeks, M.; M. Greetham, G.; Towrie, M.; L. Thompson, A.; W. Parker, A.; L. Anderson, H. Photophysics of Threaded Sp-Carbon Chains: The Polyyne Is a Sink for Singlet and Triplet Excitation. *J. Am. Chem. Soc.* **2014**, *136* (52), 17996–18008. https://doi.org/10.1021/ja510663z.

(156) Marabotti, P.; Tommasini, M.; Castiglioni, C.; Serafini, P.; Peggiani, S.; Tortora, M.; Rossi, B.; Li Bassi, A.; Russo, V.; Casari, C. S. Electron-Phonon Coupling and Vibrational Properties of Size-Selected Linear Carbon Chains by Resonance Raman Scattering. *Nat. Commun.* **2022**, *13* (1), 1–9. https://doi.org/10.1038/s41467-022-32801-3.

(157) Milani, A.; Barbieri, V.; Facibeni, A.; Russo, V.; Li Bassi, A.; Lucotti, A.; Tommasini, M.; Tzirakis, M. D.; Diederich, F.; Casari, C. S. Structure Modulated Charge Transfer in Carbon Atomic Wires. *Sci. Rep.* **2019**, *9* (1), 1–11. https://doi.org/10.1038/s41598-018-38367-9.

(158) Wang, C.; Batsanov, A. S.; Bryce, M. R.; Martín, S.; Nichols, R. J.; Higgins, S. J.; García-Suárez, V. M.; Lambert, C. J. Oligoyne Single Molecule Wires. *J. Am. Chem. Soc.* **2009**, *131* (43), 15647–15654. https://doi.org/10.1021/ja9061129.

(159) Moreno-García, P.; Gulcur, M.; Zsolt Manrique, D.; Pope, T.; Hong, W.; Kaliginedi, V.; Huang, C.; S. Batsanov, A.; R. Bryce, M.; Lambert, C.; Wandlowski, T. Single-Molecule Conductance of Functionalized Oligoynes: Length Dependence and Junction Evolution. *J. Am. Chem. Soc.* **2013**, *135* (33), 12228–12240. https://doi.org/10.1021/ja4015293.

(160) Zang, Y.; Fu, T.; Zou, Q.; Ng, F.; Li, H.; Steigerwald, M. L.; Nuckolls, C.; Venkataraman, L. Cumulene Wires Display Increasing Conductance with Increasing Length. *Nano Lett.* **2020**, *20* (11), 8415–8419. https://doi.org/10.1021/acs.nanolett.0c03794.

(161) Xu, W.; Leary, E.; Hou, S.; Sangtarash, S.; González, M. T.; Rubio-Bollinger, G.; Wu, Q.; Sadeghi, H.; Tejerina, L.; Christensen, K. E.; Agraït, N.; Higgins, S. J.; Lambert, C. J.; Nichols, R. J.; Anderson, H. L. Unusual Length Dependence of the Conductance in Cumulene Molecular Wires. *Angew. Chemie - Int. Ed.* **2019**, *58* (25), 8378–8382. https://doi.org/10.1002/anie.201901228.

(162) Garner, M. H.; Bro-Jørgensen, W.; Pedersen, P. D.; Solomon, G. C. Reverse Bond-Length Alternation in Cumulenes: Candidates for Increasing Electronic Transmission with Length. *J. Phys. Chem. C* **2018**, *122* (47), 26777–26789. https://doi.org/10.1021/acs.jpcc.8b05661.

(163) Stuyver, T.; Zeng, T.; Tsuji, Y.; Geerlings, P.; De Proft, F. Diradical Character as a Guiding Principle for the Insightful Design of Molecular Nanowires with an Increasing Conductance with Length. *Nano Lett.* **2018**, *18* (11), 7298–7304. https://doi.org/10.1021/acs.nanolett.8b03503.

(164) Hu, F.; Zeng, C.; Long, R.; Miao, Y.; Wei, L.; Xu, Q.; Min, W. Supermultiplexed Optical Imaging and Barcoding with Engineered Polyynes. *Nat. Methods* **2018**, *15* (3), 194–200. https://doi.org/10.1038/nmeth.4578.

(165) Zhao, Z.; Chen, C.; Wei, S.; Xiong, H.; Hu, F.; Miao, Y.; Jin, T.; Min, W. Ultra-Bright Raman Dots for Multiplexed Optical Imaging. *Nat. Commun.* **2021**, *12* (1), 1305. https://doi.org/10.1038/s41467-021-21570-0.

(166) Arakawa, Y.; Kang, S.; Nakajima, S.; Sakajiri, K.; Cho, Y.; Kawauchi, S.; Watanabe, J.; Konishi, G. Diphenyltriacetylenes: Novel Nematic Liquid Crystal Materials and Analysis of Their Nematic Phase-Transition and Birefringence Behaviours. *J. Mater. Chem. C* **2013**, *1* (48), 8094–8102. https://doi.org/10.1039/C3TC31658K.

(167) Grant, B. Diacetylenic Liquid Crystals: Synthesis and Preliminary Characterization of 4,4′-Dialkyl and 4,4′-Dialkoxy Derivatives of Diphenyldiacetylene. *Mol. Cryst. Liq. Cryst.* **1978**, *48* (3–4), 175–182. https://doi.org/10.1080/00268947808083757.

(168) Jiang, G.; Michinobu, T.; Yuan, W.; Feng, M.; Wen, Y.; Du, S.; Gao, H.; Jiang, L.; Song, Y.; Diederich, F.; Zhu, D. Crystalline Thin Film of a Donor- Substituted Cyanoethynylethene for Nanoscale Data Recording Through Intermolecular Charge-Transfer Interactions. *Adv. Mater.* **2005**, *17* (18), 2170–2173. https://doi.org/https://doi.org/10.1002/adma.200500559.

(169) Eckstein, B. J.; Melkonyan, F. S.; Zhou, N.; Manley, E. F.; Smith, J.; Timalsina, A.; Chang, R. P. H.; Chen, L. X.; Facchetti, A.; Marks, T. J. Buta-1,3-Diyne-Based π-Conjugated Polymers for Organic Transistors and Solar Cells. *Macromolecules* **2017**, *50* (4), 1430–1441. https://doi.org/10.1021/acs.macromol.6b02702.

(170) He, R.; Xu, Z.; Valandro, S.; Arman, H. D.; Xue, J.; Schanze, K. S. High-Purity and Saturated Deep-Blue Luminescence from Trans-NHC Platinum(II) Butadiyne Complexes: Properties and Organic Light Emitting Diode Application. *ACS Appl. Mater. Interfaces* **2021**, *13* (4), 5327–5337. https://doi.org/10.1021/acsami.0c21193.

(171) Scaccabarozzi, A. D.; Milani, A.; Peggiani, S.; Pecorario, S.; Sun, B.; Tykwinski, R. R.; Caironi, M.; Casari, C. S. A Field-Effect Transistor Based on Cumulenic Sp-Carbon Atomic Wires. *J. Phys. Chem. Lett.* **2020**, *11* (5), 1970–1974. https://doi.org/10.1021/acs.jpclett.0c00141.

(172) Holstein, T. Studies of Polaron Motion. Part I. The Molecular-Crystal Model. *Ann. Phys. (N. Y).* **1959**, *8* (3), 325–342. https://doi.org/10.1016/0003-4916(59)90002-8.

(173) Holstein, T. Studies of Polaron Motion: Part II. The "Small" Polaron. *Ann. Phys. (N. Y).* **1959**, *8* (3), 343–389. https://doi.org/https://doi.org/10.1016/0003-4916(59)90003-X.

(174) Marcus, R. A. Exchange Reactions and Electron Transfer Reactions Including Isotopic Exchange. Theory of Oxidation-Reduction Reactions Involving Electron Transfer. Part 4.—A Statistical-Mechanical Basis for Treating Contributions from Solvent, Ligands, and Inert Salt. *Discuss. Faraday Soc.* **1960**, *29* (0), 21–31. https://doi.org/10.1039/DF9602900021.

(175) Jortner, J. Temperature Dependent Activation Energy for Electron Transfer between Biological Molecules. *J. Chem. Phys.* **1976**, *64* (12), 4860–4867.

https://doi.org/10.1063/1.432142.

(176) Troisi, A. Charge Transport in High Mobility Molecular Semiconductors: Classical Models and New Theories. *Chem. Soc. Rev.* **2011**, *40* (5), 2347–2358. https://doi.org/10.1039/c0cs00198h.

(177) Coropceanu, V.; Cornil, J.; da Silva Filho, D. A.; Olivier, Y.; Silbey, R.; Brédas, J. L. Charge Transport in Organic Semiconductors. *Chem. Rev.* **2007**, *107* (4), 926–952. https://doi.org/10.1021/cr050140x.

(178) Brédas, J. L.; Calbert, J. P.; Da Silva Filho, D. A.; Cornil, J. Organic Semiconductors: A Theoretical Characterization of the Basic Parameters Governing Charge Transport. *Proc. Natl. Acad. Sci. U. S. A.* **2002**, *99* (9), 5804–5809. https://doi.org/10.1073/pnas.092143399.

(179) Yavuz, I.; Martin, B. N.; Park, J.; Houk, K. N. Theoretical Study of the Molecular Ordering, Paracrystallinity, and Charge Mobilities of Oligomers in Different Crystalline Phases. *J. Am. Chem. Soc.* **2015**, *137* (8), 2856–2866. https://doi.org/10.1021/ja5076376.

(180) Ortmann, F.; Radke, K. S.; Günther, A.; Kasemann, D.; Leo, K.; Cuniberti, G. Materials Meets Concepts in Molecule-Based Electronics. *Adv. Funct. Mater.* **2015**, *25* (13), 1933–1954. https://doi.org/10.1002/adfm.201402334.

(181) Vandewal, K.; Benduhn, J.; Schellhammer, K. S.; Vangerven, T.; Rückert, J. E.; Piersimoni, F.; Scholz, R.; Zeika, O.; Fan, Y.; Barlow, S.; Neher, D.; Marder, S. R.; Manca, J.; Spoltore, D.; Cuniberti, G.; Ortmann, F. Absorption Tails of Donor:C60 Blends Provide Insight into Thermally Activated Charge-Transfer Processes and Polaron Relaxation. *J. Am. Chem. Soc.* **2017**, *139* (4), 1699–1704. https://doi.org/10.1021/jacs.6b12857.

(182) Hutsch, S.; Panhans, M.; Ortmann, F. Time-Consistent Hopping Transport with Vibration-Mode-Resolved Electron-Phonon Couplings. *Phys. Rev. B* **2021**, *104* (5), 1–14. https://doi.org/10.1103/PhysRevB.104.054306.

(183) Brédas, J. L.; Beljonne, D.; Coropceanu, V.; Cornil, J. Charge-Transfer and Energy-Transfer Processes in π-Conjugated Oligomers and Polymers: A Molecular Picture. *Chem. Rev.* **2004**, *104* (11), 4971–5003. https://doi.org/10.1021/cr040084k.

(184) Jurchescu, O. D.; Baas, J.; Palstra, T. T. M. Effect of Impurities on the Mobility of Single Crystal Pentacene. *Appl. Phys. Lett.* **2004**, *84* (16), 3061–3063. https://doi.org/10.1063/1.1704874.

(185) Podzorov, V.; Menard, E.; Borissov, A.; Kiryukhin, V.; Rogers, J. A.; Gershenson, M. E. Intrinsic Charge Transport on the Surface of Organic Semiconductors. *Phys. Rev. Lett.* **2004**, *93* (8), 1–4. https://doi.org/10.1103/PhysRevLett.93.086602.

(186) Minder, N. A.; Ono, S.; Chen, Z.; Facchetti, A.; Morpurgo, A. F. Band-like Electron Transport in Organic Transistors and Implication of the Molecular Structure for Performance Optimization. *Adv. Mater.* **2012**, *24* (4), 503–508. https://doi.org/10.1002/adma.201103960.

(187) Liu, C.; Minari, T.; Lu, X.; Kumatani, A.; Takimiya, K.; Tsukagoshi, K. Solution-Processable Organic Single Crystals with Bandlike Transport in Field-Effect Transistors. *Adv. Mater.* **2011**, *23* (4), 523–526. https://doi.org/10.1002/adma.201002682.

(188) Sakanoue, T.; Sirringhaus, H. Band-like Temperature Dependence of Mobility in a Solution-Processed Organic Semiconductor. *Nat. Mater.* **2010**, *9* (9), 736–740. https://doi.org/10.1038/nmat2825.

(189) Podzorov, V.; Menard, E.; Rogers, J. A.; Gershenson, M. E. Hall Effect in the Accumulation Layers on the Surface of Organic Semiconductors. *Phys. Rev. Lett.* **2005**, *95* (22), 1–4. https://doi.org/10.1103/PhysRevLett.95.226601.

(190) Chang, J. F.; Sakanoue, T.; Olivier, Y.; Uemura, T.; Dufourg-Madec, M. B.; Yeates, S. G.; Cornil, J.; Takeya, J.; Troisi, A.; Sirringhaus, H. Hall-Effect Measurements Probing the Degree of Charge-Carrier Delocalization in Solution-Processed Crystalline Molecular Semiconductors. *Phys. Rev. Lett.* **2011**, *107* (6), 1–4. https://doi.org/10.1103/PhysRevLett.107.066601.

(191) Tsurumi, J.; Matsui, H.; Kubo, T.; Häusermann, R.; Mitsui, C.; Okamoto, T.; Watanabe, S.; Takeya, J. Coexistence of Ultra-Long Spin Relaxation Time and Coherent Charge Transport in Organic Single-Crystal Semiconductors. *Nat. Phys.* **2017**, *13* (10), 994–998. https://doi.org/10.1038/nphys4217.

(192) Kasuya, N.; Tsurumi, J.; Okamoto, T.; Watanabe, S.; Takeya, J. Two-Dimensional Hole Gas in Organic Semiconductors. *Nat. Mater.* **2021**, *20* (10), 1401–1406. https://doi.org/10.1038/s41563-021-01074-4.

(193) Tiago, M. L.; Louie, S. G.; Tiago, M. L.; Louie, S. G.; Northrup, J. E. Ab Initio Calculation of the Electronic and Optical Properties of Solid Pentacene. *Phys. Rev. B - Condens. Matter Mater. Phys.* **2003**, *67* (11), 6. https://doi.org/10.1103/PhysRevB.67.115212.

(194) Kakuta, H.; Hirahara, T.; Matsuda, I.; Nagao, T.; Hasegawa, S.; Ueno, N.; Sakamoto, K. Electronic Structures of the Highest Occupied Molecular Orbital Bands of a Pentacene Ultrathin Film. *Phys. Rev. Lett.* **2007**, *98* (24), 1–4. https://doi.org/10.1103/PhysRevLett.98.247601.

(195) Uchida, R.; Yada, H.; Makino, M.; Matsui, Y.; Miwa, K.; Uemura, T.; Takeya, J.; Okamoto, H. Charge Modulation Infrared Spectroscopy of Rubrene Single-Crystal Field-Effect Transistors. *Appl. Phys. Lett.* **2013**, *102* (9). https://doi.org/10.1063/1.4794055.

(196) Matsui, H.; Mishchenko, A. S.; Hasegawa, T. Distribution of Localized States from Fine Analysis of Electron Spin Resonance Spectra in Organic Transistors. *Phys. Rev. Lett.* **2010**, *104* (5), 1–4. https://doi.org/10.1103/PhysRevLett.104.056602.

(197) Xiao, M.; Carey, R. L.; Chen, H.; Jiao, X.; Lemaur, V.; Schott, S.; Nikolka, M.; Jellett, C.; Sadhanala, A.; Rogers, S.; Senanayak, S. P.; Onwubiko, A.; Han, S.; Zhang, Z.; Abdi-Jalebi, M.; Zhang, Y.; Thomas, T. H.; Mahmoudi, N.; Lai, L.; Selezneva, E.; Ren, X.; Nguyen, M.; Wang, Q.; Jacobs, I.; Yue, W.; McNeill, C. R.; Liu, G.; Beljonne, D.; McCulloch, I.; Sirringhaus, H. Charge Transport Physics of a Unique Class of Rigid-Rod Conjugated Polymers with Fused-Ring Conjugated Units Linked by Double Carbon-Carbon Bonds. *Sci. Adv.* **2021**, *7* (18), 1–14. https://doi.org/10.1126/sciadv.abe5280.

(198) Illig, S.; Eggeman, A. S.; Troisi, A.; Jiang, L.; Warwick, C.; Nikolka, M.; Schweicher, G.; Yeates, S. G.; Henri Geerts, Y.; Anthony, J. E.; Sirringhaus, H. Reducing Dynamic Disorder in Small-Molecule Organic Semiconductors by Suppressing Large-Amplitude Thermal Motions. *Nat. Commun.* **2016**, *7*, 1–10. https://doi.org/10.1038/ncomms10736.

(199) Eggeman, A. S.; Illig, S.; Troisi, A.; Sirringhaus, H.; Midgley, P. A. Measurement of Molecular Motion in Organic Semiconductors by Thermal Diffuse Electron Scattering. *Nat. Mater.* **2013**, *12* (11), 1045–1049. https://doi.org/10.1038/nmat3710.

(200) Giannini, S.; Carof, A.; Ellis, M.; Yang, H.; Ziogos, O. G.; Ghosh, S.; Blumberger, J. Quantum Localization and Delocalization of Charge Carriers in Organic Semiconducting Crystals. *Nat. Commun.* **2019**, *10* (1), 1–12. https://doi.org/10.1038/s41467-019-11775-9.

(201) Giannini, S.; Ziogos, O. G.; Carof, A.; Ellis, M.; Blumberger, J. Flickering Polarons Extending over Ten Nanometres Mediate Charge Transport in High-Mobility Organic Crystals. *Adv. Theory Simulations* **2020**, *3* (9), 1–11. https://doi.org/10.1002/adts.202000093.

(202) Fratini, S.; Mayou, D.; Ciuchi, S. The Transient Localization Scenario for Charge Transport in Crystalline Organic Materials. *Adv. Funct. Mater.* **2016**, *26* (14), 2292–2315. https://doi.org/10.1002/adfm.201502386.

(203) Fratini, S.; Ciuchi, S.; Mayou, D.; De Laissardière, G. T.; Troisi, A. A Map of High-Mobility Molecular Semiconductors. *Nat. Mater.* **2017**, *16* (10), 998–1002. https://doi.org/10.1038/nmat4970.

(204) Schweicher, G.; D'Avino, G.; Ruggiero, M. T.; Harkin, D. J.; Broch, K.; Venkateshvaran, D.; Liu, G.; Richard, A.; Ruzié, C.; Armstrong, J.; Kennedy, A. R.; Shankland, K.; Takimiya, K.; Geerts, Y. H.; Zeitler, J. A.; Fratini, S.; Sirringhaus, H. Chasing the "Killer" Phonon Mode for the Rational Design of Low-Disorder, High-Mobility Molecular Semiconductors. *Adv. Mater.* **2019**, *31* (43), 1902407. https://doi.org/10.1002/adma.201902407.

(205) Bakulin, A. A.; Lovrincic, R.; Yu, X.; Selig, O.; Bakker, H. J.; Rezus, Y. L. A.; Nayak, P. K.; Fonari, A.; Coropceanu, V.; Brédas, J. L.; Cahen, D. Mode-Selective Vibrational Modulation of Charge Transport in Organic Electronic Devices. *Nat. Commun.* **2015**, *6* (May). https://doi.org/10.1038/ncomms8880.

(206) Selezneva, E.; Vercouter, A.; Schweicher, G.; Lemaur, V.; Broch, K.; Antidormi, A.; Takimiya, K.; Coropceanu, V.; Brédas, J.; Melis, C.; Cornil, J.; Sirringhaus, H. Strong Suppression of Thermal Conductivity in the Presence of Long Terminal Alkyl Chains in Low-Disorder Molecular Semiconductors. *Adv. Mater.* **2021**, *33* (37), 2008708. https://doi.org/10.1002/adma.202008708.

(207) Kharlanov, O. G.; Maslennikov, D. R.; Feldman, E. V.; Abashev, G. G.; Borshchev, O. V.; Ponomarenko, S. A.; Vener, M. V.; Paraschuk, D. Y.; Sosorev, A. Y. Spectroscopic Assessment of Charge-Carrier Mobility in Crystalline Organic Semiconductors. *Adv. Electron. Mater.* **2021**, *2100579*, 2100579. https://doi.org/10.1002/aelm.202100579.

(208) Harrelson, T. F.; Dantanarayana, V.; Xie, X.; Koshnick, C.; Nai, D.; Fair, R.; Nuñez, S. A.; Thomas, A. K.; Murrey, T. L.; Hickner, M. A.; Grey, J. K.; Anthony, J. E.; Gomez, E. D.; Troisi, A.; Faller, R.; Moulé, A. J. Direct Probe of the Nuclear Modes Limiting Charge Mobility in Molecular Semiconductors. *Mater. Horizons* **2019**, *6* (1), 182–191. https://doi.org/10.1039/c8mh01069b.

(209) Bittle, E. G.; Biacchi, A. J.; Fredin, L. A.; Herzing, A. A.; Allison, T. C.; Hight Walker, A. R.; Gundlach, D. J. Correlating Anisotropic Mobility and Intermolecular Phonons in Organic Semiconductors to Investigate Transient Localization. *Commun. Phys.* **2019**, *2* (1). https://doi.org/10.1038/s42005-019-0129-5.

(210) Stoeckel, M. A.; Olivier, Y.; Gobbi, M.; Dudenko, D.; Lemaur, V.; Zbiri, M.; Guilbert, A. A. Y.; D'Avino, G.; Liscio, F.; Migliori, A.; Ortolani, L.; Demitri, N.; Jin, X.; Jeong, Y. G.; Liscio, A.; Nardi, M. V.; Pasquali, L.; Razzari, L.; Beljonne, D.; Samorì, P.; Orgiu, E. Analysis of External and Internal Disorder to Understand Band-Like Transport in n-Type Organic Semiconductors. *Adv. Mater.* **2021**, *33* (13), 1–10. https://doi.org/10.1002/adma.202007870.

(211) Giannini, S.; Blumberger, J. Charge Transport in Organic Semiconductors: The Perspective from Nonadiabatic Molecular Dynamics. *Acc. Chem. Res.* **2022**, *55* (6), 819–830. https://doi.org/10.1021/acs.accounts.1c00675.

(212) Lamport, Z. A.; Haneef, H. F.; Anand, S.; Waldrip, M.; Jurchescu, O. D. Tutorial: Organic Field-Effect Transistors: Materials, Structure and Operation. *J. Appl. Phys.* **2018**, *124* (7), 071101. https://doi.org/10.1063/1.5042255.

(213) Choi, H. H.; Cho, K.; Frisbie, C. D.; Sirringhaus, H.; Podzorov, V. Critical Assessment of Charge Mobility Extraction in FETs. *Nat. Mater.* **2017**, *17* (1), 2–7. https://doi.org/10.1038/nmat5035.

(214) Ilani, S.; Donev, L. A. K.; Kindermann, M.; McEuen, P. L. Measurement of the Quantum Capacitance of Interacting Electrons in Carbon Nanotubes. *Nat. Phys.* **2006**, *2* (10), 687–691. https://doi.org/10.1038/nphys412.

(215) Shimotani, H.; Tsuda, S.; Yuan, H.; Yomogida, Y.; Moriya, R.; Takenobu, T.; Yanagi, K.; Iwasa, Y. Continuous Band-Filling Control and One-Dimensional Transport in Metallic and Semiconducting Carbon Nanotube Tangled Films. *Adv. Funct. Mater.* **2014**, *24* (22), 3305–3311. https://doi.org/10.1002/adfm.201303566.

(216) Natali, D.; Caironi, M. Charge Injection in Solution-Processed Organic Field-Effect Transistors: Physics, Models and Characterization Methods. *Adv. Mater.* **2012**, *24* (11), 1357–1387. https://doi.org/10.1002/adma.201104206.

(217) Ponce Ortiz, R.; Facchetti, A.; J. Marks, T. High-k Organic, Inorganic, and Hybrid Dielectrics for Low-Voltage Organic Field-Effect Transistors. *Chem. Rev.* **2009**, *110* (1), 205–239. https://doi.org/10.1021/cr9001275.

(218) Casalini, S.; Bortolotti, C. A.; Leonardi, F.; Biscarini, F. Self-Assembled Monolayers in Organic Electronics. *Chem. Soc. Rev.* **2017**, *46* (1), 40–71. https://doi.org/10.1039/c6cs00509h.

(219) Stucchi, E.; Scaccabarozzi, A. D.; Viola, F. A.; Caironi, M. Ultraflexible All-Organic Complementary Transistors and Inverters Based on Printed Polymers. *J. Mater. Chem. C* **2020**, *8* (43), 15331–15338. https://doi.org/10.1039/d0tc03064c.

(220) Stucchi, E.; Dell'Erba, G.; Colpani, P.; Kim, Y. H.; Caironi, M. Low-Voltage, Printed, All-Polymer Integrated Circuits Employing a Low-Leakage and High-Yield Polymer Dielectric. *Adv. Electron. Mater.* **2018**, *4* (12). https://doi.org/10.1002/aelm.201800340.

(221) Wang, C.; Dong, H.; Jiang, L.; Hu, W. Organic Semiconductor Crystals. *Chem. Soc. Rev.* **2018**, *47* (2), 422–500. https://doi.org/10.1039/c7cs00490g.

(222) Diao, Y.; Shaw, L.; Bao, Z.; Mannsfeld, S. C. B. Morphology Control Strategies for Solution-Processed Organic Semiconductor Thin Films. *Energy Environ. Sci.* **2014**, *7* (7), 2145–2159. https://doi.org/10.1039/C4EE00688G.

(223) Riera-Galindo, S.; Tamayo, A.; Mas-Torrent, M. Role of Polymorphism and Thin-Film Morphology in Organic Semiconductors Processed by Solution Shearing. *ACS Omega*

2018, *3* (2), 2329–2339. https://doi.org/10.1021/acsomega.8b00043.

(224) Virkar, A. A.; Mannsfeld, S.; Bao, Z.; Stingelin, N. Organic Semiconductor Growth and Morphology Considerations for Organic Thin-Film Transistors. *Adv. Mater.* **2010**, *22* (34), 3857–3875. https://doi.org/10.1002/adma.200903193.

(225) Patel, B. B.; Diao, Y. Multiscale Assembly of Solution-Processed Organic Electronics: The Critical Roles of Confinement, Fluid Flow, and Interfaces. *Nanotechnology* **2018**, *29* (4). https://doi.org/10.1088/1361-6528/aa9d7c.

(226) Khim, D.; Luzio, A.; Bonacchini, G. E.; Pace, G.; Lee, M. J.; Noh, Y. Y.; Caironi, M. Uniaxial Alignment of Conjugated Polymer Films for High-Performance Organic Field-Effect Transistors. *Adv. Mater.* **2018**, *30* (20), 1–34. https://doi.org/10.1002/adma.201705463.

(227) Wang, G.; Swensen, J.; Moses, D.; Heeger, A. J. Increased Mobility from Regioregular Poly(3-Hexylthiophene) Field-Effect Transistors. *J. Appl. Phys.* **2003**, *93* (10), 6137–6141. https://doi.org/10.1063/1.1568526.

(228) McCulloch, I.; Heeney, M.; Bailey, C.; Genevicius, K.; MacDonald, I.; Shkunov, M.; Sparrowe, D.; Tierney, S.; Wagner, R.; Zhang, W.; Chabinyc, M. L.; Kline, R. J.; McGehee, M. D.; Toney, M. F. Liquid-Crystalline Semiconducting Polymers with High Charge-Carrier Mobility. *Nat. Mater.* **2006**, *5* (4), 328–333. https://doi.org/10.1038/nmat1612.

(229) Lee, M. J.; Chen, Z.; Pietro, R. Di; Heeney, M.; Sirringhaus, H. Electrooptical Spectroscopy of Uniaxially Aligned Polythiophene Films in Field-Effect Transistors. *Chem. Mater.* **2013**, *25* (10), 2075–2082. https://doi.org/10.1021/cm400266h.

(230) Matsidik, R.; Luzio, A.; Hameury, S.; Komber, H.; McNeill, C. R.; Caironi, M.; Sommer, M. Effects of PNDIT2 End Groups on Aggregation, Thin Film Structure, Alignment and Electron Transport in Field-Effect Transistors. *J. Mater. Chem. C* **2016**, *4* (43), 10371–10380. https://doi.org/10.1039/c6tc03804b.

(231) Zhang, Z.; Peng, B.; Ji, X.; Pei, K.; Chan, P. K. L. Marangoni-Effect-Assisted Bar-Coating Method for High-Quality Organic Crystals with Compressive and Tensile Strains. *Adv. Funct. Mater.* **2017**, *27* (37), 1703443. https://doi.org/10.1002/adfm.201703443.

(232) Riera-Galindo, S.; Leonardi, F.; Pfattner, R.; Mas-Torrent, M. Organic Semiconductor/Polymer Blend Films for Organic Field-Effect Transistors. *Adv. Mater. Technol.* **2019**, *4* (9), 1–20. https://doi.org/10.1002/admt.201900104.

(233) Lu, Z.; Wang, C.; Deng, W.; Achille, M. T.; Jie, J.; Zhang, X. Meniscus-Guided Coating of Organic Crystalline Thin Films for High-Performance Organic Field-Effect Transistors. *J. Mater. Chem. C* **2020**, *8* (27), 9133–9146. https://doi.org/10.1039/d0tc01887b.

(234) Lee, S. B.; Lee, S.; Kim, D. G.; Kim, S. H.; Kang, B.; Cho, K. Solutal-Marangoni-Flow-Mediated Growth of Patterned Highly Crystalline Organic Semiconductor Thin Film Via Gap-Controlled Bar Coating. *Adv. Funct. Mater.* **2021**, *31* (28), 2100196. https://doi.org/10.1002/adfm.202100196.

(235) Reale, S. Mobility Maximization in Organic Field-Effect Transistors via Machine Learning and Design of Experiments, Politecnico di Milano, 2020.

(236) Chen, M.; Peng, B.; Huang, S.; Chan, P. K. L. Understanding the Meniscus-Guided

Coating Parameters in Organic Field-Effect-Transistor Fabrications. *Adv. Funct. Mater.* **2020**, *30* (1), 1905963. https://doi.org/10.1002/adfm.201905963.

(237) Zhao, H.; Wang, Z.; Dong, G.; Duan, L. Fabrication of Highly Oriented Large-Scale TIPS Pentacene Crystals and Transistors by the Marangoni Effect-Controlled Growth Method. *Phys. Chem. Chem. Phys.* **2015**, *17* (9), 6274–6279. https://doi.org/10.1039/c4cp05378h.

(238) Scaccabarozzi, A. D.; Basham, J. I.; Yu, L.; Westacott, P.; Zhang, W.; Amassian, A.; McCulloch, I.; Caironi, M.; Gundlach, D. J.; Stingelin, N. High-Density Polyethylene - An Inert Additive with Stabilizing Effects on Organic Field-Effect Transistors. *J. Mater. Chem. C* **2020**, *8* (43), 15406–15415. https://doi.org/10.1039/d0tc03173a.

(239) Temiño, I.; Del Pozo, F. G.; Ajayakumar, M. R.; Galindo, S.; Puigdollers, J.; Mas-Torrent, M. A Rapid, Low-Cost, and Scalable Technique for Printing State-of-the-Art Organic Field-Effect Transistors. *Adv. Mater. Technol.* **2016**, *1* (5), 1600090. https://doi.org/10.1002/admt.201600090.

(240) Le Berre, M.; Chen, Y.; Baigl, D. From Convective Assembly to Landau−Levich Deposition of Multilayered Phospholipid Films of Controlled Thickness. *Langmuir* **2009**, *25* (5), 2554–2557. https://doi.org/10.1021/la803646e.

(241) Landau, L.; Levich, B. Dragging of a Liquid by a Moving Plate; Pelcé, P. B. T.-D. of C. F., Ed.; Academic Press: San Diego, 1988; pp 141–153. https://doi.org/https://doi.org/10.1016/B978-0-08-092523-3.50016-2.

(242) Yu, L.; Portale, G.; Stingelin, N. Solution-Processing of Semiconducting Organic Small Molecules: What We Have Learnt from 5,11-Bis(Triethylsilylethynyl)Anthradithiophene. *J. Mater. Chem. C* **2021**, *9* (33), 10547–10556. https://doi.org/10.1039/d1tc01418h.

(243) Lee, S. B.; Kang, B.; Kim, D.; Park, C.; Kim, S.; Lee, M.; Lee, W. B.; Cho, K. Motion-Programmed Bar-Coating Method with Controlled Gap for High-Speed Scalable Preparation of Highly Crystalline Organic Semiconductor Thin Films. *ACS Appl. Mater. Interfaces* **2019**, *11* (50), 47153–47161. https://doi.org/10.1021/acsami.9b17044.

(244) Yi, H. T.; Gartstein, Y. N.; Podzorov, V. Charge Carrier Coherence and Hall Effect in Organic Semiconductors. *Sci. Rep.* **2016**, *6* (March), 1–11. https://doi.org/10.1038/srep23650.

(245) D'Innocenzo, V.; Luzio, A.; Petrozza, A.; Fazzi, D.; Caironi, M. Nature of Charge Carriers in a High Electron Mobility Naphthalenediimide Based Semiconducting Copolymer. *Adv. Funct. Mater.* **2014**, *24* (35), 5584–5593. https://doi.org/10.1002/adfm.201400394.

(246) Meneau, A. Y. B.; Olivier, Y.; Backlund, T.; James, M.; Breiby, D. W.; Andreasen, J. W.; Sirringhaus, H. Temperature Dependence of Charge Localization in High-Mobility, Solution-Crystallized Small Molecule Semiconductors Studied by Charge Modulation Spectroscopy. *Adv. Funct. Mater.* **2016**, *26* (14), 2326–2333. https://doi.org/10.1002/adfm.201502502.

(247) Scaccabarozzi, A. D.; Scuratti, F.; Barker, A. J.; Basu, A.; Paterson, A. F.; Fei, Z.; Solomeshch, O.; Petrozza, A.; Tessler, N.; Heeney, M.; Anthopoulos, T. D.; Caironi, M. Understanding Charge Transport in High-Mobility P- Doped Multicomponent Blend Organic Transistors. *Adv. Electron. Mater.* **2020**, *6* (10), 2000539. https://doi.org/10.1002/aelm.202000539.

(248) Pace, G.; Bargigia, I.; Noh, Y. Y.; Silva, C.; Caironi, M. Intrinsically Distinct Hole and Electron Transport in Conjugated Polymers Controlled by Intra and Intermolecular Interactions. *Nat. Commun.* **2019**, *10* (1). https://doi.org/10.1038/s41467-019-13155-9.

(249) Zorn, N. F.; Berger, F. J.; Zaumseil, J. Charge Transport in and Electroluminescence from Sp 3 -Functionalized Carbon Nanotube Networks. *ACS Nano* **2021**, *15* (6), 10451–10463. https://doi.org/10.1021/acsnano.1c02878.

(250) Sciascia, C.; Martino, N.; Schuettfort, T.; Watts, B.; Grancini, G.; Antognazza, M. R.; Zavelani-Rossi, M.; McNeill, C. R.; Caironi, M. Sub-Micrometer Charge Modulation Microscopy of a High Mobility Polymeric n-Channel Field-Effect Transistor. *Adv. Mater.* **2011**, *23* (43), 5086–5090. https://doi.org/10.1002/adma.201102410.

(251) Chin, X. Y.; Pace, G.; Soci, C.; Caironi, M. Ambipolar Charge Distribution in Donor–Acceptor Polymer Field-Effect Transistors. *J. Mater. Chem. C* **2017**, *5* (3), 754–762. https://doi.org/10.1039/C6TC05033F.

(252) Martino, N.; Fazzi, D.; Sciascia, C.; Luzio, A.; Antognazza, M. R.; Caironi, M. Mapping Orientational Order of Charge-Probed Domains in a Semiconducting Polymer. *ACS Nano* **2014**, *8* (6), 5968–5978. https://doi.org/10.1021/nn5011182.

Appendix A: Supporting Information for "Effects of Molecular Encapsulation on the Photophysical and Charge Transport Properties of a Naphthalene Diimide Bithiophene Copolymer"

Supporting Information

Effects of Molecular Encapsulation on the Photophysical and Charge Transport Properties of a Naphthalene Diimide Bithiophene Copolymer

Stefano Pecorario[‡,1,2], Jeroen Royakkers[‡,3,4,5], Alberto D. Scaccabarozzi[1], Francesca Pallini[6], Luca Beverina[6], Hugo Bronstein*[,4,5], Mario Caironi*[,1]

[1] Center for Nano Science and Technology@PoliMi, Istituto Italiano di Tecnologia, via Giovanni Pascoli 70/3, Milan 20133, Italy

[2] Department of Energy, Micro and Nanostructured Materials Laboratory - NanoLab, Politecnico di Milano, Via Ponzio 34/3, Milano, 20133, Italy.

[3] Sensor Engineering Department, Faculty of Science and Engineering, Maastricht University, P.O. Box 616, 6200 MD Maastricht, The Netherlands

[4] Department of Chemistry, University of Cambridge, Lensfield Road, Cambridge, CB2 1EW UK

[5] Cavendish Laboratory, University of Cambridge, Cambridge, CB3 0HE UK

[6] Department of Materials Science, Università di Milano-Bicocca, via Cozzi 55, 20125 Milan, Italy

[‡] These authors contributed equally

* Corresponding authors

Table of Contents:

1) Synthesis

- **General Experimental Information**

All reactions were performed in oven-dried glassware under argon atmosphere and magnetic stirring, unless stated otherwise. The reactions were protected from light using aluminum foil. Chemicals and solvents were purchased from chemical suppliers (Sigma-Aldrich, TCI, Fluorochem, Acros Organics, Alfa Aesar, SLS, Fisher Scientific) and used as received unless stated otherwise. The Br_2-NDI-2OD co-monomer was prepared according to our previous literature procedure.[1] Reactions were monitored through thin layer chromatography (TLC) using DC Fertigfolien ALUGRAM aluminium sheets coated with silica gel. Column chromatography was carried out on a Biotage® Isolera™ Four with Biotage® SNAP or Sfar cartridges (10 g, 20 g, 50 g or 100 g). ^{1}H NMR spectra were recorded on a 400 MHz Avance III HD Spectrometer, 400 MHz Neo Prodigy Spectrometer, 400 MHz Smart Probe Spectrometer or a 500 MHz DCH Cryoprobe Spectrometer in the stated solvent using residual protic solvent $CHCl_3$ (δ = 7.26 ppm, s) or DMSO (δ = 2.50 ppm, s) as the internal standard. ^{1}H NMR chemical shifts are reported to the nearest 0.01 ppm. ^{13}C NMR spectra were recorded on the 500 MHz DCH Cryoprobe Spectrometer in the stated solvent using the residual protic solvent $CHCl_3$ (δ= 77.16 ppm, t) or DMSO (δ = 39.52 ppm, s) as the internal standard. ^{13}C NMR chemical shifts are reported to the nearest 0.01 ppm. Mass spectra were obtained using a Waters LCT Premier, Waters Vion IMS Qtof, Finnigan MAT 900XP or Waters MALDI micro MX spectrometer at the Department of Chemistry, University of Cambridge. The number-average (Mn) and weight-average (Mw) molecular weights were determined against a polystyrene standard using an Agilent Technologies 1200 Series GPC-SEC System in chlorobenzene at 80 °C.

- **Monomers Synthesis**

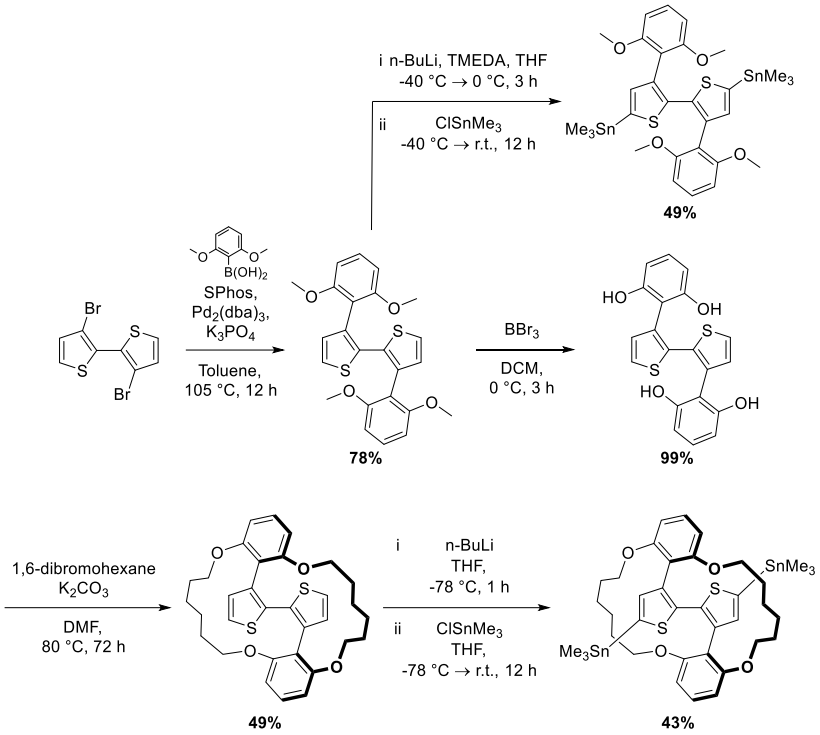

3,3'-bis(2,6-dimethoxyphenyl)-2,2'-bithiophene (DMP-BT)[2]

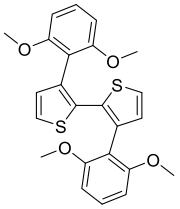

Under argon, a solution of 3,3'-dibromo-2,2'-bithiophene (2.2321 g, 6.8879 mmol), 2,6-dimethoxyphenylboronic acid (5.0 g, 27.4755 mmol), SPhos (283.5 mg, 0.6906 mmol), $Pd_2(dba)_3$ (198.7 mg, 0.2170 mmol) and K_3PO_4 (7.0982 g, 33.4395 mmol) in toluene (25 mL) and water (5 mL) was stirred at 105°C for 12 h. The reaction mixture was cooled to room temperature, washed with water and extracted with toluene (1x). The organic phase was concentrated *in vacuo* and the residue was sonicated in methanol. The resulting white solids were collected by filtration. Next, the product was further purified using silica column chromatography (loaded with 100% hexane, eluted with 50% DCM). The product fractions were concentrated *in vacuo* to afford the product as a white solid (2.3491 g, 5.3564 mmol, 78%).

^{1}H NMR (400 MHz, CDCl3) δ 7.14 (d, J = 5.2 Hz, 1H), 7.10 (t, J = 8.3 Hz, 1H), 6.87 (d, J = 5.2 Hz, 1H), 6.36 (d, J = 8.3 Hz, 2H), 3.50 (s, 6H). **HRMS** (ASAP-TOF): Calculated for $C_{24}H_{23}O_4S_2^+$: 439.1038. Found *m/z* 439.1029 $[M+H]^+$.

2,2'-Bis(trimethylstannyl)-3,3'-bis(2,6-dimethoxyphenyl)-2,2'-bithiophene (DMP-BT-SnMe$_3$)

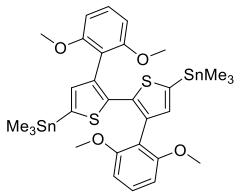

Under argon, n-BuLi (3.84 mL, 1.6 M, 6.1440 mmol) was added dropwise at -40 °C to a solution of DMP-BT (1.0 g, 2.2802 mmol) in dry THF (100 mL) and TMEDA (0.95 mL). The reaction was stirred at this temperature for 5 minutes, after which it was warmed to 0 °C and left stirring for 3 h. Next, it was cooled back to -40 °C and trimethyltinchloride solution (7 mL, 1.0 M in THF, 7.0 mmol) was added. The reaction was left to warm to room temperature and it was stirred for 12 h. Next, water (~50 mL) was added and the organic layer was separated. The aqueous layer was then extracted with DCM (2 x) and the combined organic layer was dried over $MgSO_4$, filtered and concentrated *in vacuo*. The resulting solid was sonicated in methanol and collected by filtration to afford 1.4 g of crude material. The crude was recrystallized twice from acetonitrile (First recrystallization: dissolve crude in 250 mL ACN, add a spoon of charcoal, filter through celite, reduce volume to ~100 mL and let it cool down. The same procedure was followed for the second recrystallization, but this time it was reduced to 50-60 mL). The desired product was obtained as a white crystalline solid (854.3 mg, 1.1179 mmol, 49%).

^{1}H NMR (700 MHz, CD_2Cl_2) δ 7.09 (t, *J* = 8.3 Hz, 2H), 6.94 – 6.83 (m, 2H), 6.36 (d, *J* = 8.3 Hz, 4H), 3.47 (s, 12H), 0.46 – 0.16 (s+d, 18H).**^{13}C NMR** (176 MHz, CD_2Cl_2) δ 158.37, 140.63, 140.22, 134.68, 131.82, 128.62, 114.78, 104.52, 55.63, -8.05. **HRMS** (ASAP-TOF): Calculated for $C_{30}H_{39}O_4S_2Sn_2^+$: 765.0323. Found *m/z*: 765.0289 $[M]^+$.

3,3'-bis(2,6-dihydroxyphenyl)-2,2'-bithiophene (DHP-BT)[2]

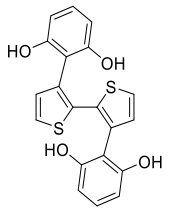

Under argon, a 1M BBr_3 solution (in DCM, 27.4 mL, 27.4 mmol) was added dropwise at – 10 °C to a solution of 3,3'-bis(2,6-dimethoxyphenyl)-2,2'-bithiophene (3.0 g, 6.8406 mmol) in DCM (29 mL). The reaction was stirred for 6 h at – 10 °C. Next, the reaction mixture was poured into 100 mL of 1M $NaHCO_3$ solution and the white solids were collected by filtration. The solids were re-dissolved in EtOAc, dried over $MgSO_4$ and concentrated *in vacuo*. The solids were then sonicated in DCM (2x) and collected by filtration to afford the product as a white solid (2.61 g, 6.8245 mmol, >99%).

^{1}H NMR (400 MHz, DMSO) δ 8.86 (s, 4H), 7.27 (d, *J* = 5.1 Hz, 2H), 6.97 (t, *J* = 8.1 Hz, 2H), 6.83 (d, *J* = 5.1 Hz, 2H), 6.36 (d, *J* = 8.1 Hz, 4H). **HRMS** (ASAP-TOF): Calculated for $C_{20}H_{15}O_4S_2^+$: 383.0412. Found *m*/*z* 383.0410 $[M+H]^+$.

Encapsulated Bithiophene (E-BT)[2]

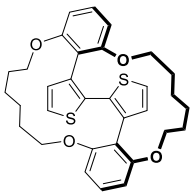

Under argon, 3,3'-bis(2,6-dihydroxyphenyl)-2,2'-bithiophene (1.0 g, 2.6147 mmol), K_2CO_3 (2.4213 g, 17.5190 mmol) and dry DMF (300 mL) were added to a 500 mL round-bottomed flask and it was heated at 50 °C for 1 h. To this, a solution of 1,6-dibromohexane (0.8044 mL, 5.2294 mmol) in dry DMF (300 mL) was added dropwise over 1 h. The mixture was heated to 80 °C and stirred for 48 h. The reaction mixture was concentrated *in vacuo*, re-dissolved in the minimal amount of chloroform and hexane and purified by silica column chromatography, using 50-70% chloroform in hexane. The product fractions were concentrated *in vacuo*, sonicated in methanol, collected by filtration and dried under high vacuum to afford the product as a white solid (704.3 mg, 1.2882 mmol, 49%).

^{1}H NMR (400 MHz, CDCl3) δ 7.38 (t, J = 8.3 Hz, 2H), 6.98 (d, J = 5.1 Hz, 2H), 6.75 (d, J = 5.1 Hz, 2H), 6.69 (d, J = 8.3 Hz, 4H), 4.12 – 3.97 (m, 4H), 3.75 (ddd, J = 9.1, 7.7, 5.1 Hz, 4H), 1.52 – 1.39 (m, 8H), 1.26 – 1.07 (m, 4H), 0.93 (ddd, J = 14.2, 12.2, 6.9 Hz, 4H). **^{13}C NMR** (176 MHz, $CDCl_3$) δ 159.10, 133.51, 131.20, 130.16, 129.52, 122.73, 117.62, 107.26, 69.90, 30.43, 27.40. **HRMS** (ASAP-TOF): Calculated for $C_{32}H_{35}O_4S_2^+$: 547.1977. Found *m*/*z* 547.1967 $[M+H]^+$.

Encapsulated Bithiophene Monomer (E-BT-SnMe$_3$)

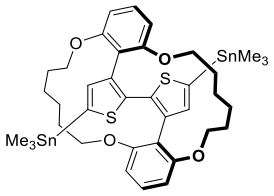

Under argon, n-BuLi (0.85 mL, 1.6 M, 1.3632 mmol) was added dropwise at -40 °C to a solution of E-BT (300 mg, 0.6214 mmol) in dry THF (5 mL) and TMEDA (0.26 mL). The reaction was stirred at this temperature for 5 minutes, after which it was warmed to 0 °C and left stirring for 3 h. Next, it was cooled back to -40 °C and trimethyltinchloride solution (1.5 mL, 1.0 M in THF, 1.50 mmol) was added. The reaction was left to warm to room temperature and it was stirred for 12 h. Next, water (~50 mL) was added and the organic layer was separated. The aqueous layer was then extracted with DCM (2 x) and the combined organic layer was dried over $MgSO_4$, filtered and concentrated *in vacuo*. The resulting

solid was sonicated in methanol and collected by filtration. The crude was recrystallized from acetonitrile (and a small amount of $CHCl_3$) to afford the desired product as a white crystalline solid (235.7 mg, 0.2702 mmol, 43%).

^{1}H NMR (700 MHz, $CDCl_3$) δ 7.34 (t, *J* = 8.3 Hz, 2H), 6.80 – 6.74 (s, 2H), 6.68 (d, *J* = 8.3 Hz, 4H), 4.00 (dt, *J* = 8.7, 4.2 Hz, 4H), 3.69 (td, *J* = 9.4, 2.9 Hz, 4H), 1.49 (d, *J* = 10.3 Hz, 4H), 1.42 (dd, *J* = 11.8, 8.2 Hz, 4H), 1.09 (dd, *J* = 17.0, 6.9 Hz, 4H), 0.91 – 0.84 (m, 4H), 0.35 – 0.15 (m, 18H). **^{13}C NMR** (176 MHz, CD_2Cl_2) δ 159.49, 140.16, 138.36, 134.21, 132.88, 130.23, 118.48, 107.90, 70.37, 30.68, 27.64, -8.18. **HRMS** (ASAP-TOF): Calculated for $C_{38}H_{50}O_4S_2Sn_2^+$: 872.1189 Found *m/z* 872.1221 $[M]^+$.

- **Polymers Synthesis**

PNDIT2[3]

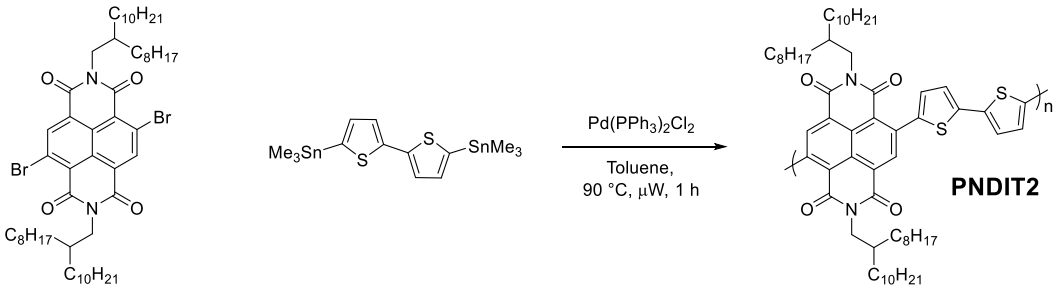

Under argon, a mixture of Br_2-NDI-2OD (120 mg, 0.1218 mmol), 5,5'-bis(trimethylstannyl)-2,2'-bithiophene (60.6 mg, 0.1218 mmol), $Pd(PPh_3)_2Cl_2$ (4.5 mg, 0.0064 mmol) and anhydrous toluene (3 mL) was stirred at 90 °C under microwave irradiation for 1 h. The resulting blue viscous liquid was precipitated into stirring methanol (~150 mL) and the polymer was collected by filtration and subjected to soxhlet extraction in acetone, hexane and $CHCl_3$. The $CHCl_3$ fraction was concentrated *in vacuo*, precipited in methanol (~150 mL), collected by filtration and dried under high vacuum to afford the polymer as a blue-green plastic (118.5 mg, 0.1195 mmol, 98%); Mn = 45.0 kDa, Mw = 136.1 kDa, PDI = 3.02.

DMP-PNDIT2

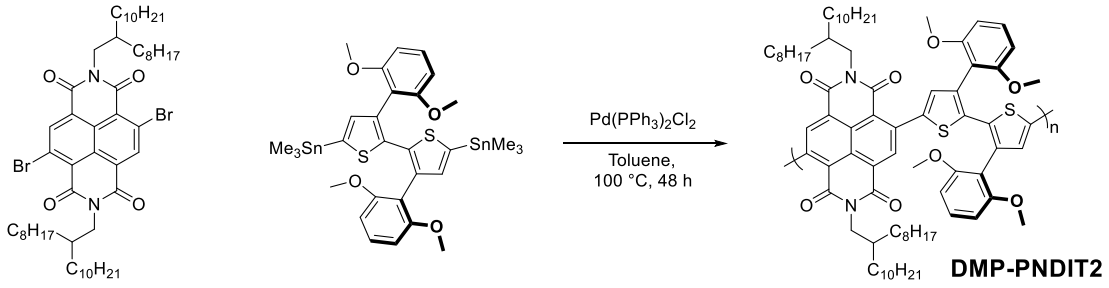

Under argon, a mixture of Br_2-NDI-2OD (150 mg, 0.1523 mmol), DMP-BT-$SnMe_3$ (116.4 mg, 0.1523 mmol), $Pd(PPh_3)_2Cl_2$ (5.57 mg, 0.0079 mmol) and anhydrous toluene (4 mL) was stirred at 100 °C for

48 h. The resulting blue-green liquid was precipitated into stirring methanol (~150 mL) and the polymer was collected by filtration and subjected to soxhlet extraction in acetone, hexane and $CHCl_3$. The $CHCl_3$ fraction was concentrated *in vacuo*, precipited in methanol (~150 mL), collected by filtration and dried under high vacuum to afford the polymer as a blue-green solid (215.4 mg, 0.1431 mmol, 94%); Mn = 19.4 kDa, Mw = 37.1 kDa, PDI = 1.91.

E-PNDIT2

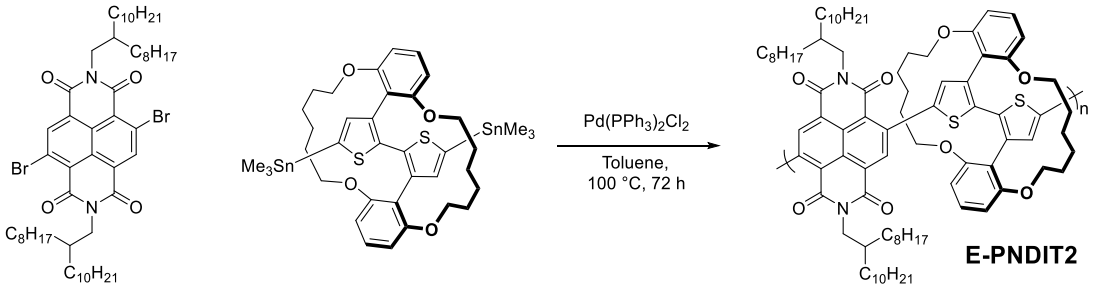

Under argon, a mixture of Br_2-NDI-2OD (70 mg, 0.0711 mmol), E-BT-$SnMe_3$ (62 mg, 0.0711 mmol), $Pd(PPh_3)_2Cl_2$ (2.6 mg, 0.0037 mmol) and anhydrous toluene (1.7 mL) was stirred at 90 °C for 72 h. The resulting blue-green liquid was precipitated into stirring methanol (~150 mL) and the polymer was collected by filtration and subjected to soxhlet extraction in acetone, hexane and $CHCl_3$. The $CHCl_3$ fraction was concentrated *in vacuo*, precipited in methanol (~150 mL), collected by filtration and dried under high vacuum to afford the polymer as a blue-green solid (59.9 mg, 0.0437 mmol, 61%); Mn = 19.9 kDa, Mw = 46.4 kDa, PDI = 2.33.

- **NMR Spectra**

3,3'-bis(2,6-dimethoxyphenyl)-2,2'-bithiophene (DMP-BT)[2]

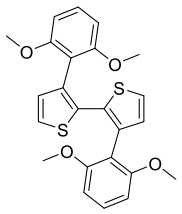

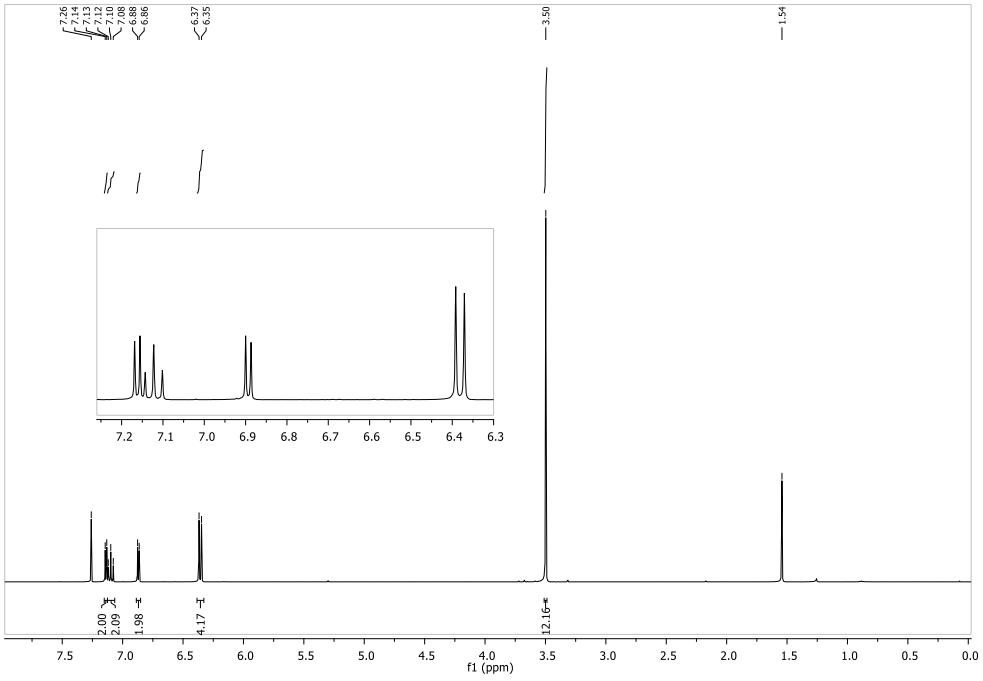

2,2’-Bis(trimethylstannyl)-3,3'-bis(2,6-dimethoxyphenyl)-2,2'-bithiophene (DMP-BT-SnMe$_3$)

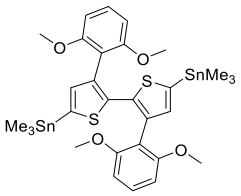

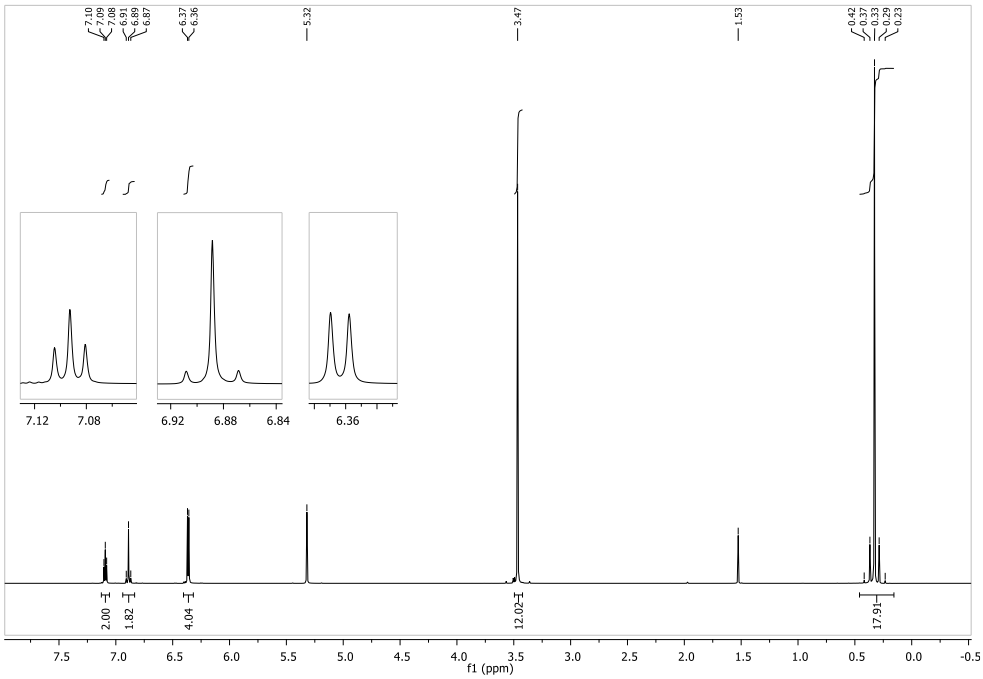

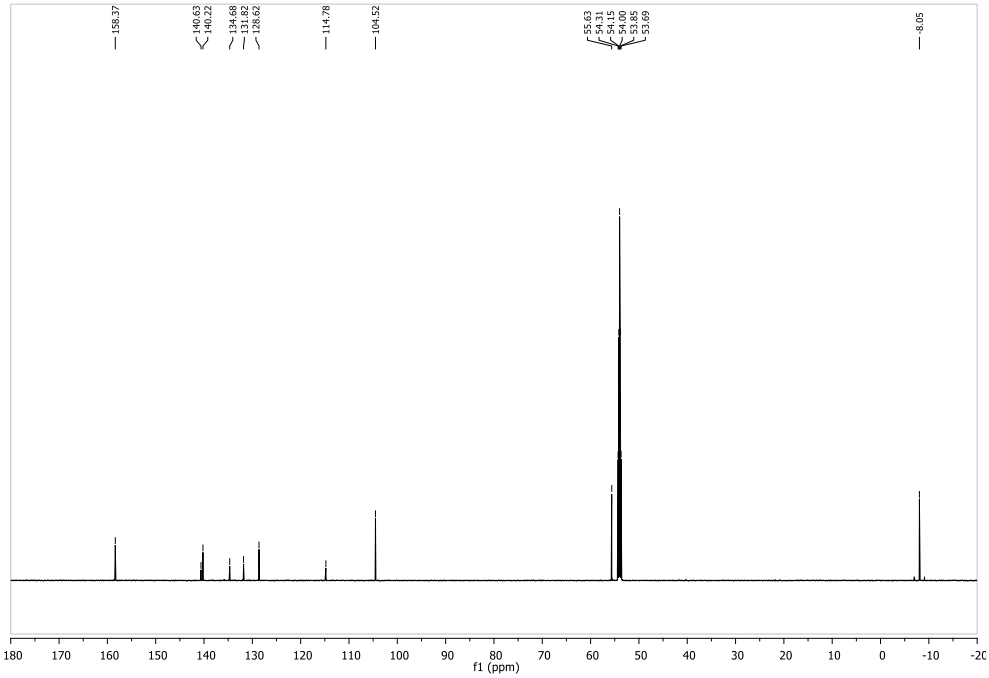

3,3'-bis(2,6-dihydroxyphenyl)-2,2'-bithiophene (DHP-BT)[2]

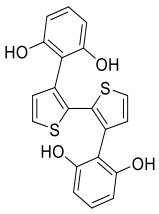

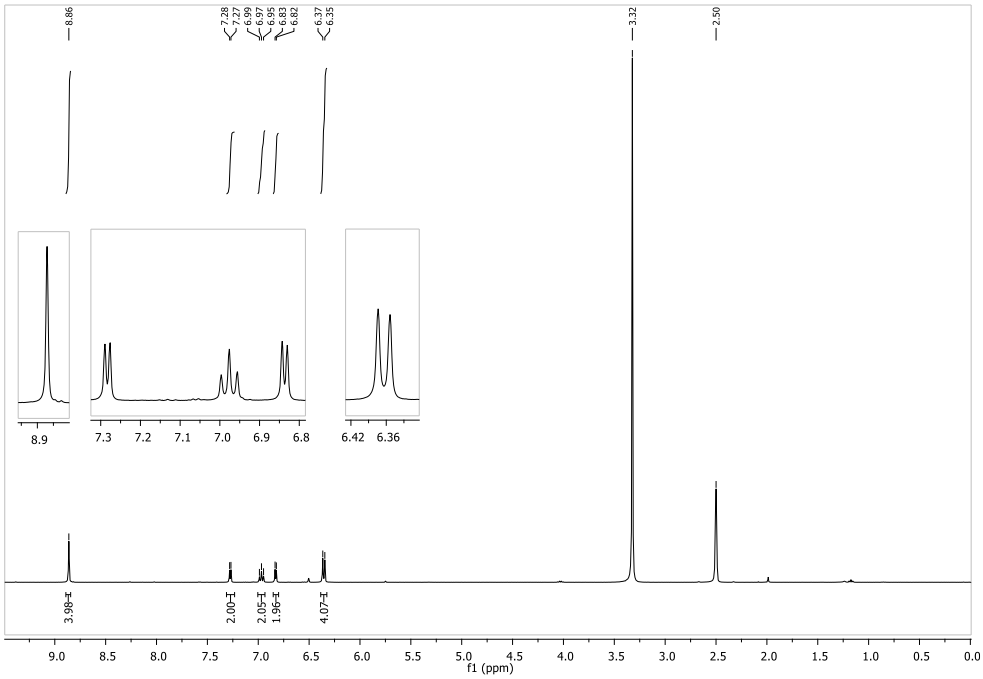

Encapsulated Bithiophene (E-BT)[2]

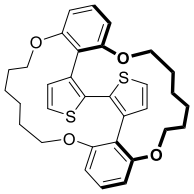

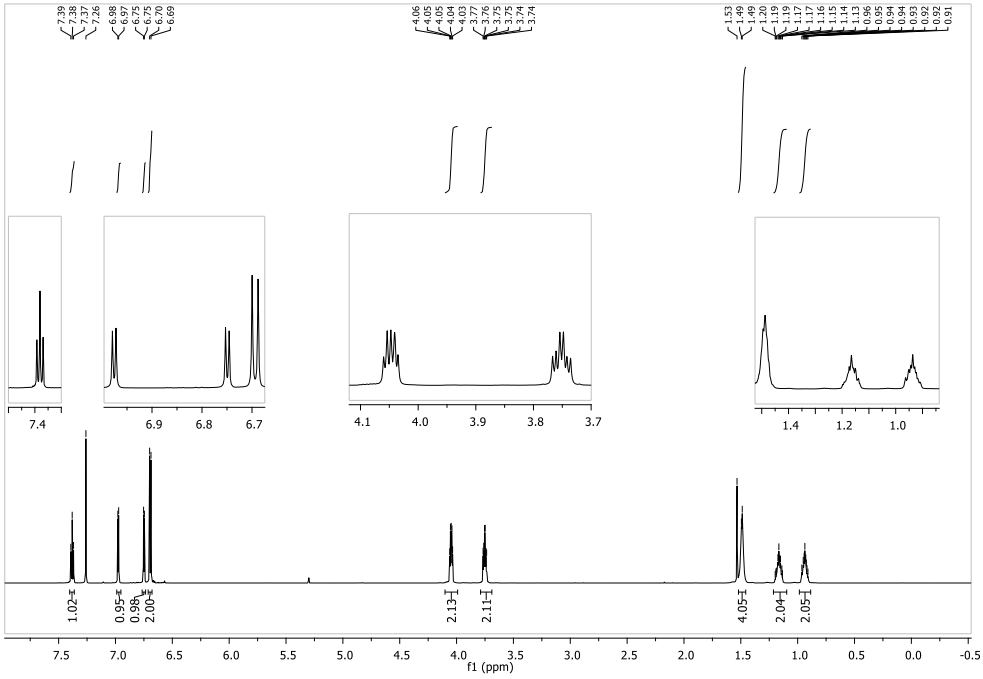

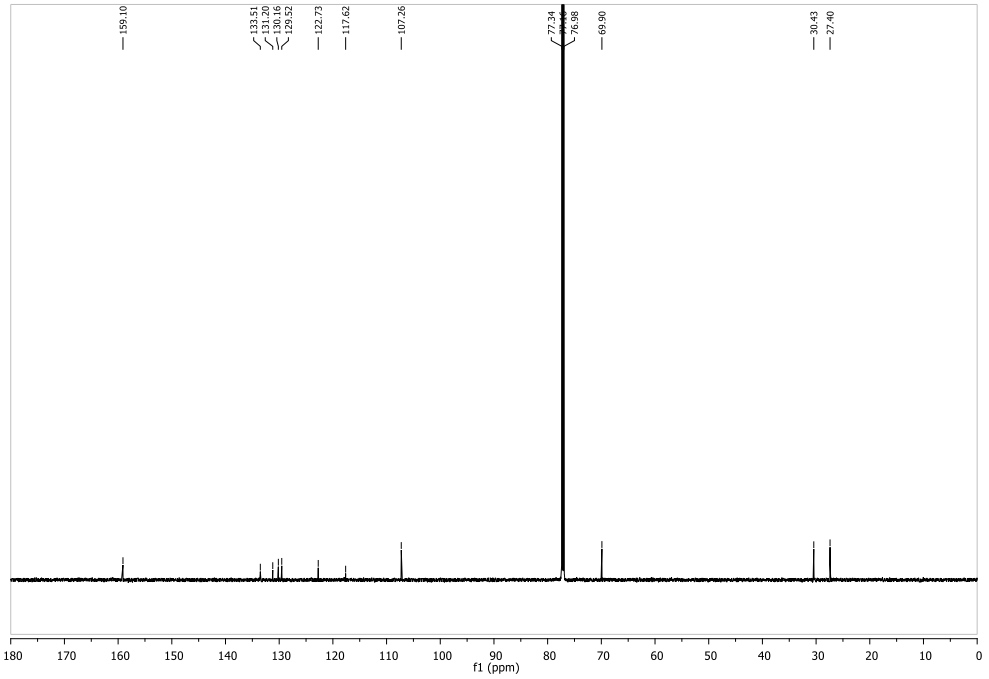

Encapsulated Bithiophene Monomer (E-BT-$SnMe_3$)

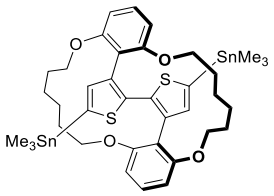

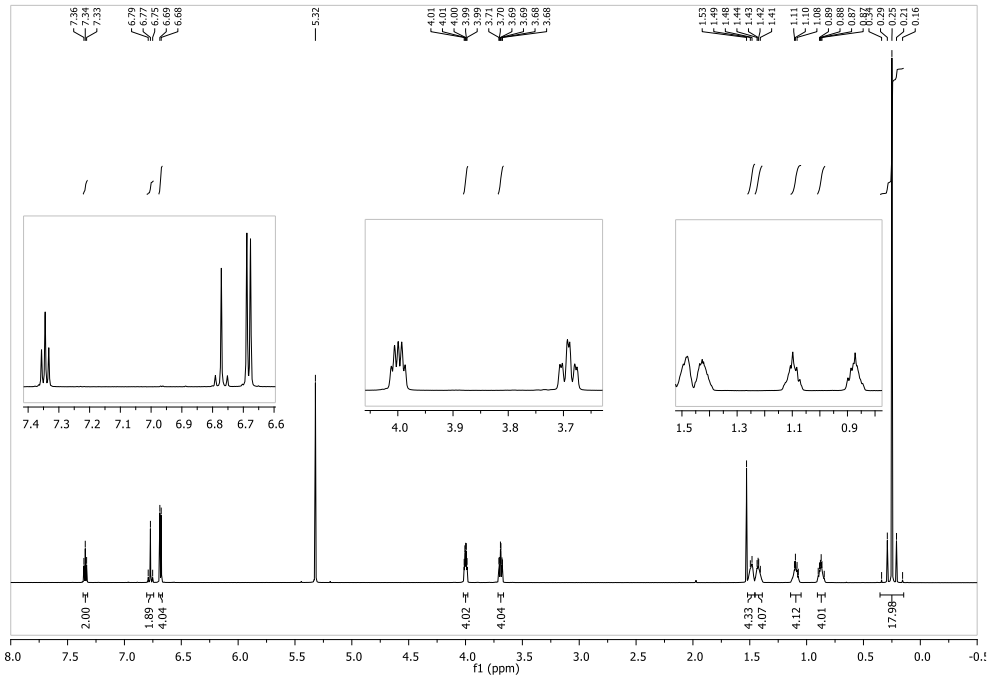

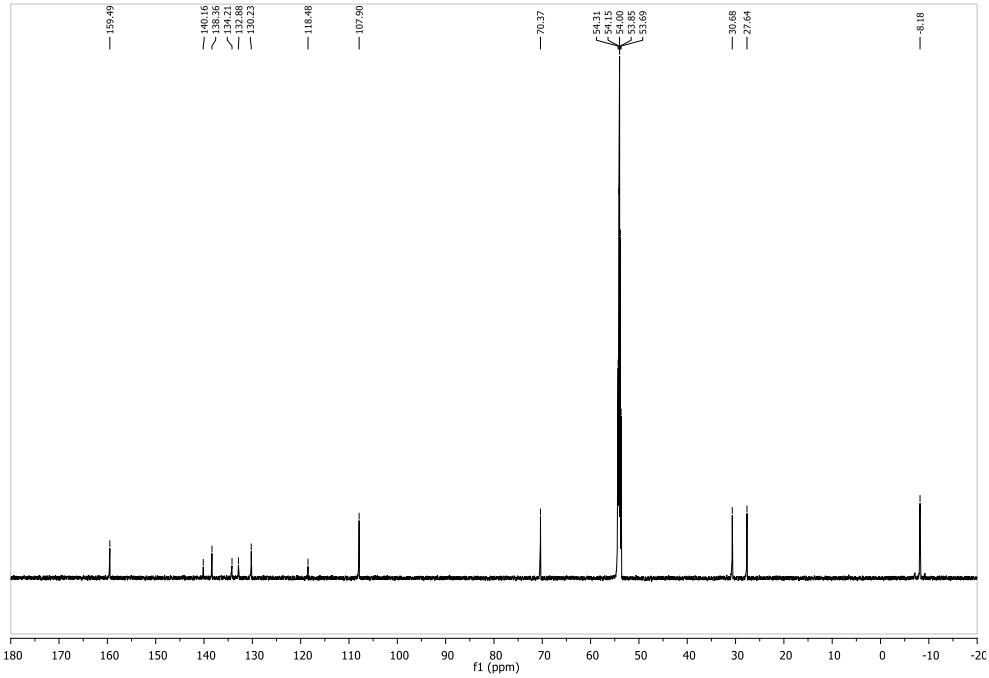

PNDIT2

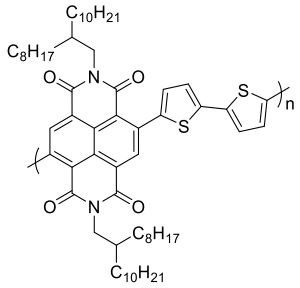

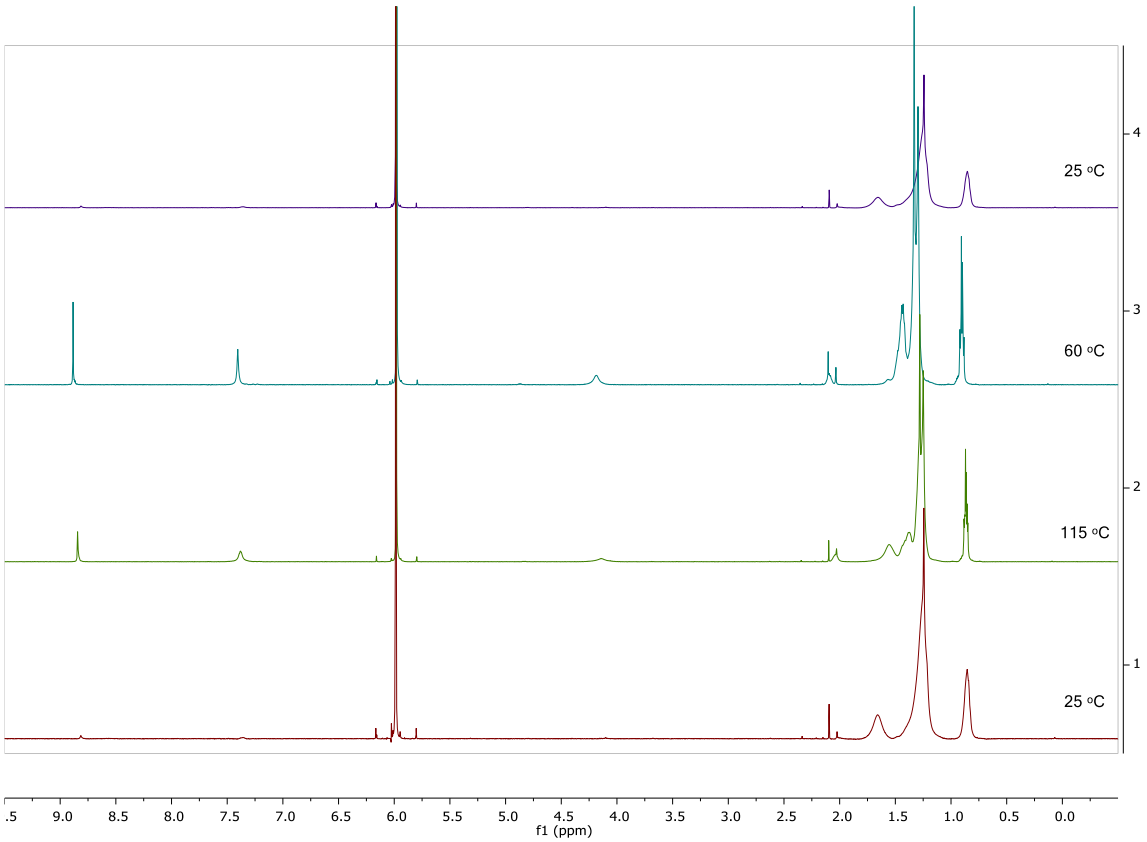

NMR spectrum of PNDIT2 in 1,1,2,2-Tetrachloroethane-d2 at 25 °C (purple; 4), 60 °C (blue; 3), 115 °C (green; 2), and back at 25 °C (red; 1).

DMP-PNDIT2

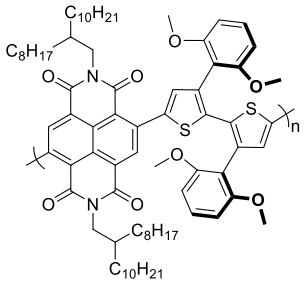

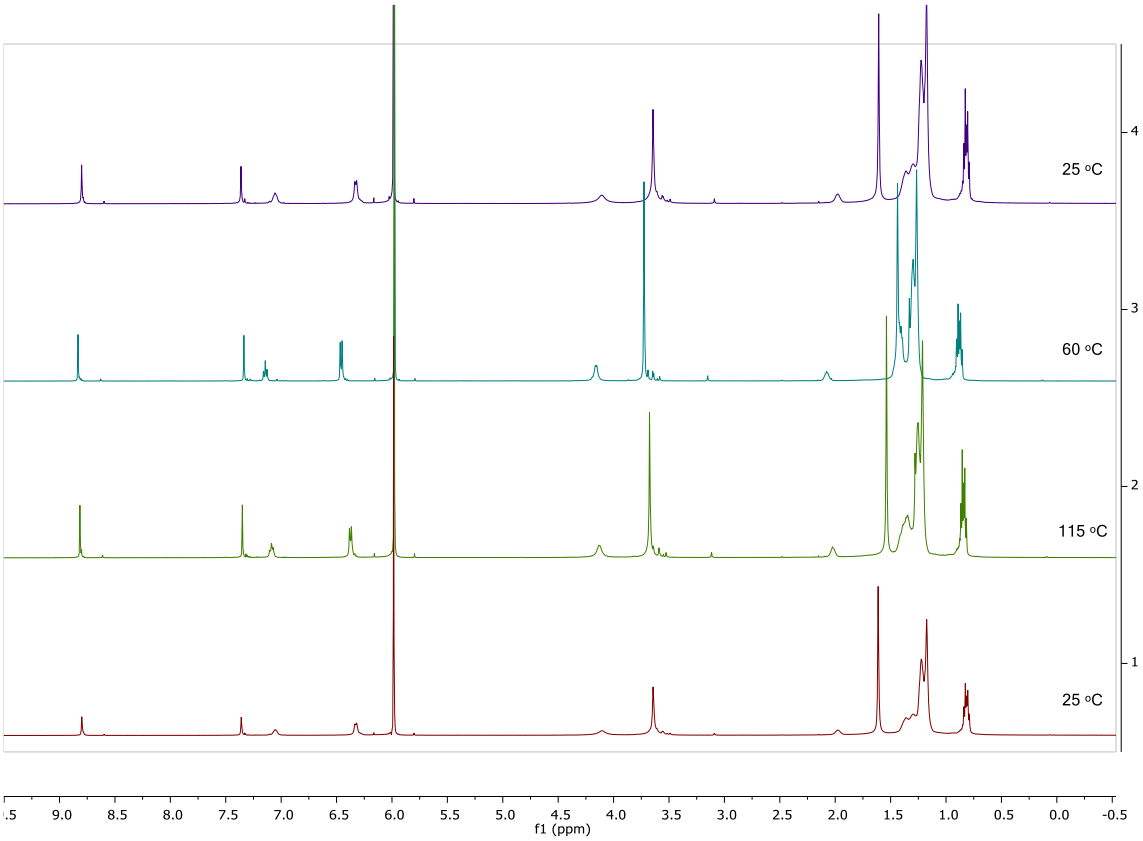

NMR spectrum of DMP-PNDIT2 in 1,1,2,2-Tetrachloroethane-d2 at 25 °C (purple; 4), 60 °C (blue; 3), 115 °C (green; 2), and back at 25 °C (red; 1).

E-PNDIT2

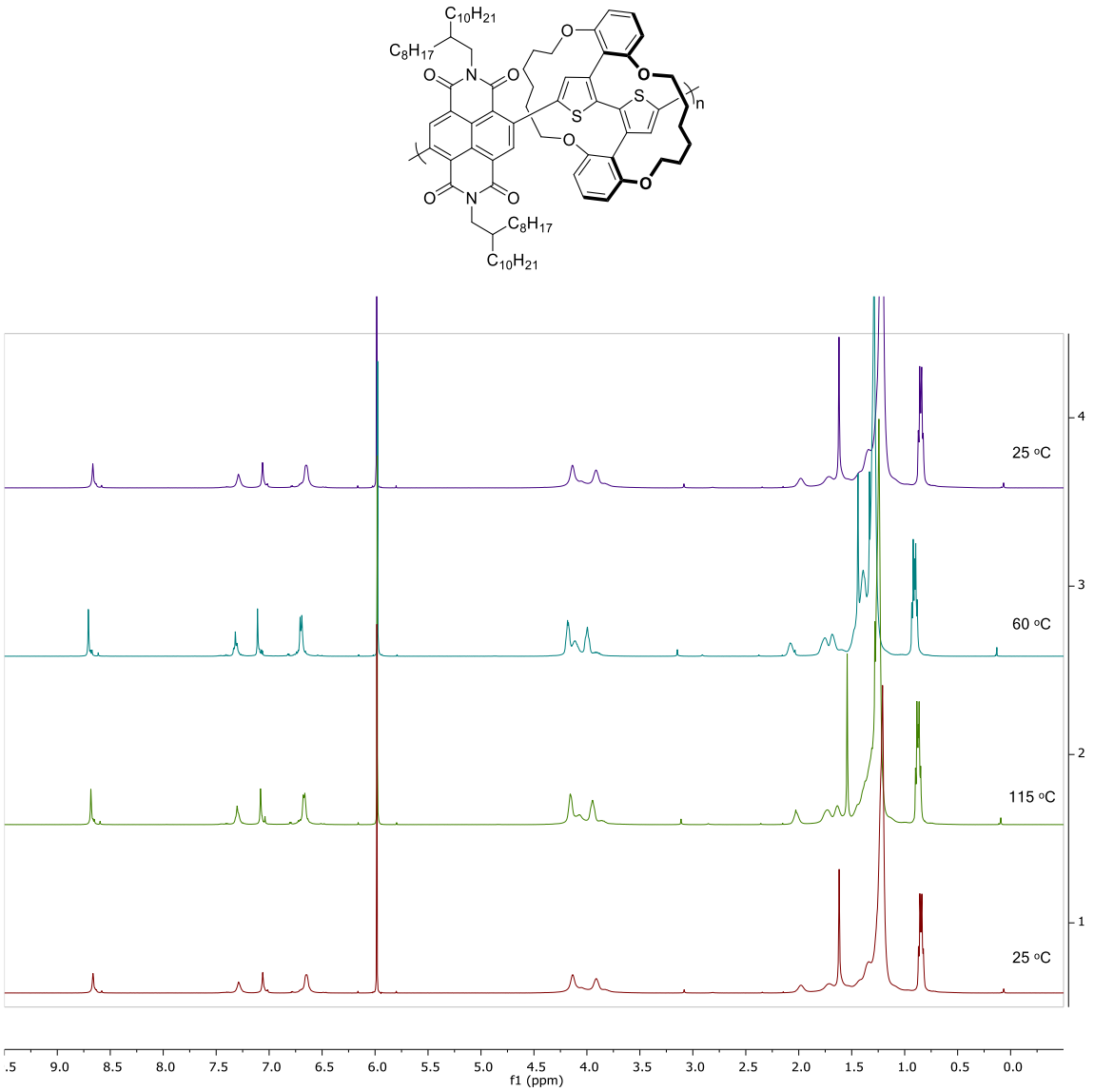

NMR spectrum of E-PNDIT2 in 1,1,2,2-Tetrachloroethane-d2 at 25 °C (purple; 4), 60 °C (blue; 3), 115 °C (green; 2), and back at 25 °C (red; 1).

2) DFT Calculations

- **Dihedral angles** - Calculated using b3lyp/6-31g*

PNDIT2

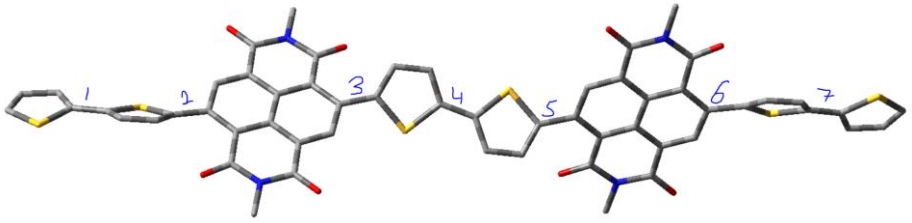

Position #	1	2	3	4	5	6	7
Angle °	161.5 (18.5)	142.9 (37.1)	134.7 (45.3)	163.4 (16.6)	133.2 (46.8)	135.5 (44.5)	161.5 (18.5)

Average dihedral angle between thiophenes (#1,4,7) = 162.13 (or 18.87).
Average dihedral angle between thiophene and NDI (#2,3,5,6) = 136.575 (or 43.425).

DMP-PNDIT2

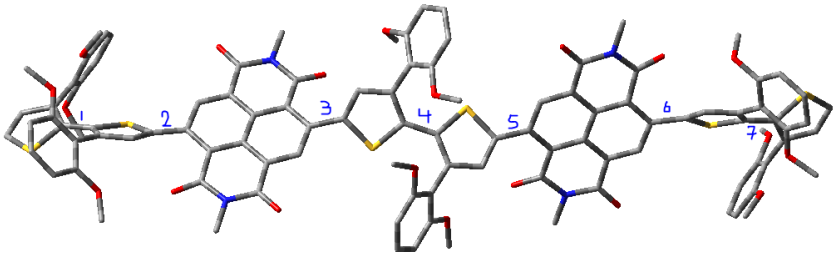

Position #	1	2	3	4	5	6	7
Angle °	150.95 (29.05)	130.53 (49.47)	126.78 (53.22)	152.46 (27.54)	131.02 (49.98)	133.60 (46.40)	150.37 (29.63)

Average dihedral angle between thiophenes (#1,4,7) = 151.26 (or 28.74).
Average dihedral angle between thiophene and NDI (#2,3,5,6) = 130.48 (or 49.52).

E-PNDIT2

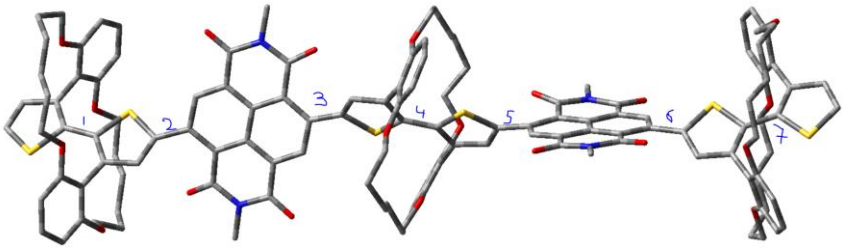

Position #	1	2	3	4	5	6	7
Angle °	177.7 (2.3)	128.8 (51.2)	135.3 (44.7)	177.5 (2.5)	130.3 (49.7)	133.4 (46.6)	176.4 (3.6)

Average dihedral angle between thiophenes (#1,4,7) = 177.2 (or 2.8).
Average dihedral angle between thiophene and NDI (#2,3,5,6) = 131.95 (or 48.05).

- **HOMO/LUMO Levels** - Calculated using b3lyp/6-31g*

PNDIT2

Eg = 1.98 eV

LUMO (-3.42 eV)

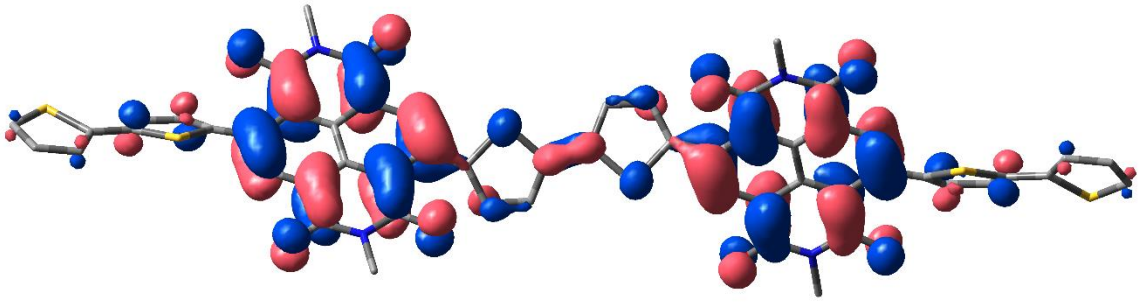

HOMO (-5.40 eV)

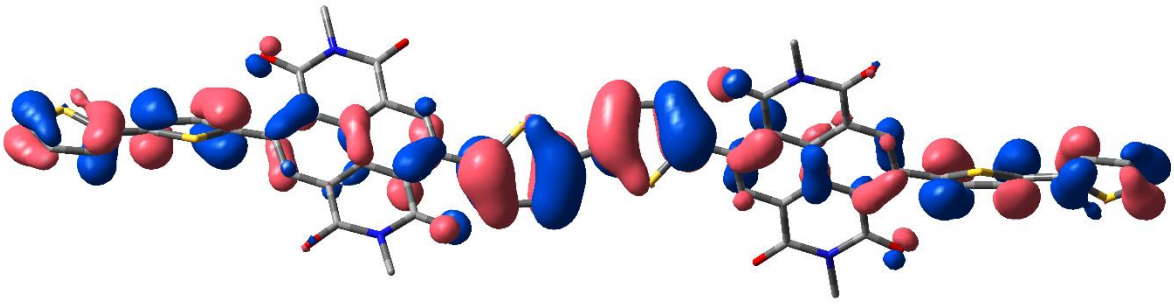

DMP-PNDIT2

Eg = 1.85 eV

LUMO (-3.12 eV)

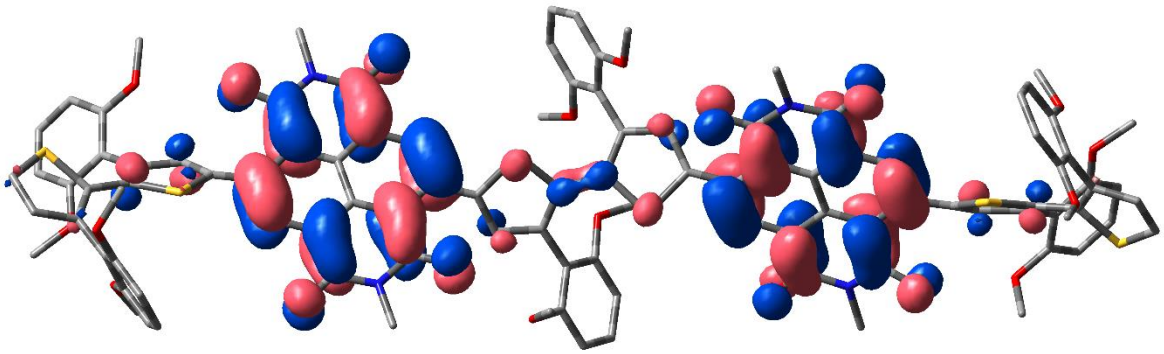

HOMO (-4.97 eV)

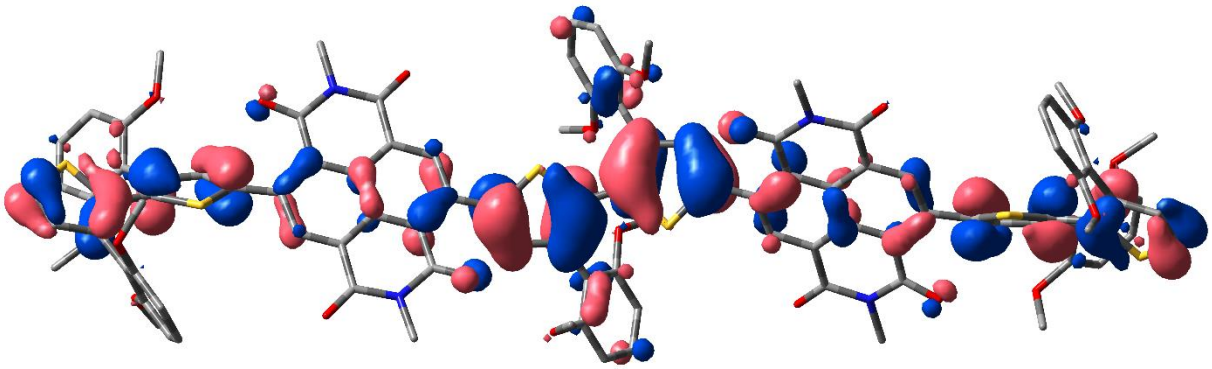

E-PNDIT2

Eg = 1.80 eV

LUMO (-3.12 eV)

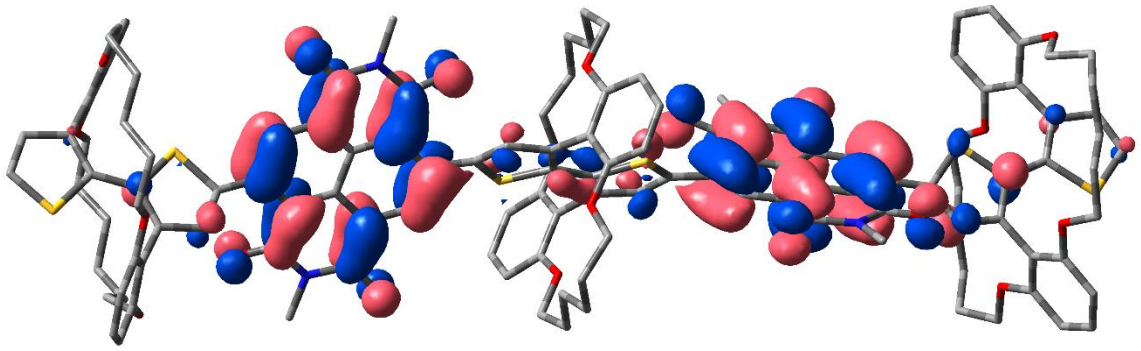

HOMO (-4.92 eV)

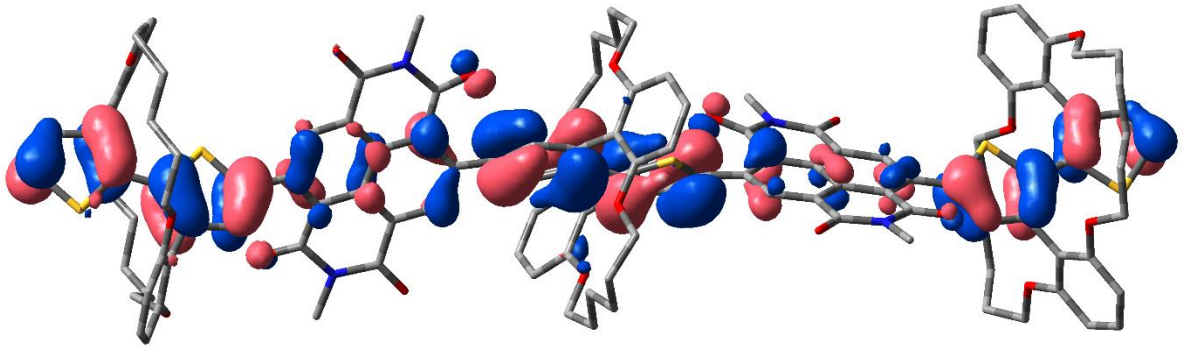

3) Thermal Characterization

Thermogravimetric Analysis (TGA) measurements (Figure S1) were performed with a TGA/DSC 1 STAR^e System from Mettler Toledo, using alumina crucibles. All measurement were performed following the same TGA method: heating from 30°C to 600 °C with a 10°C/min rate. The measurements were performed under 50 mL/min N_2 flow.

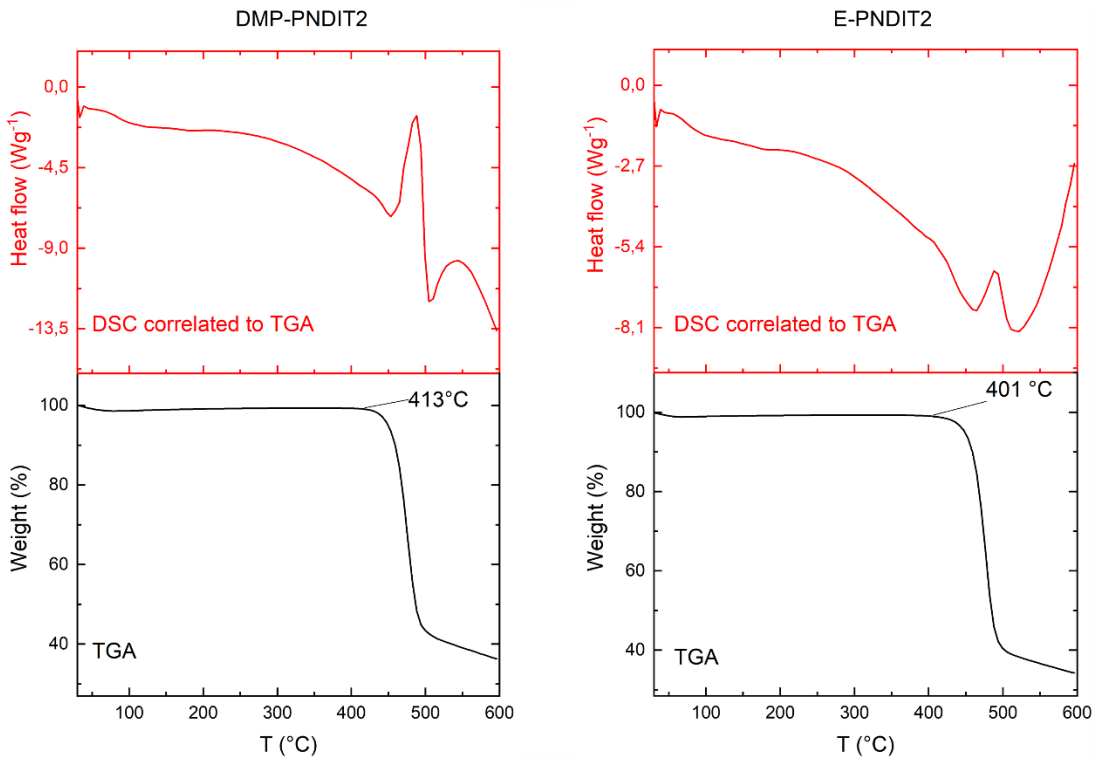

Figure S1. Thermogravimetric Analysis (TGA)

DMP-PNDIT2

Sample weight: 4.5047 mg

The thermogram shows significant weight loss and degradation after 413 °C. DSC analysis correlated to TGA shows no evident sign of decomposition before 400 °C as well.

Total weight loss at 600 °C: 64%

E-PNDIT2

Sample weight: 5.1840 mg

The thermogram shows significant weight loss and degradation after 401 °C. DSC analysis correlated to TGA shows no evident sign of decomposition before 400 °C as well.

Total weight loss at 600 °C: 66%

Differential Scanning Calorimetry (DSC) measurements (Figure S2) were performed on the polymers in powder form with a DSC 1 STAR^e System from Mettler Toledo, using aluminum crucibles. Calibration was performed with an Indium standard. All DSC measurements were performed following the same thermal treatment:

- 1st heating cycle: from 0 °C to 300 °C, 10°C/min
- isotherm at 300°C for 2 min.
- cooling: from 300 °C to 0°C, 10°C/min
- isotherm at 0°C for 2 min
- 2nd heating cycle: from 0 °C to 350°C, 10°C/min

The measurements were performed under 80 mL/min N_2 flow.

DMP-PNDIT2

Sample weight: 4.000 mg

Two endothermic peaks are present around 65 °C and 110 °C in the 1st heating cycle. Correspondent exothermic features are observed during the cooling cycle, suggesting melting and recrystallization processes during heating and cooling of the sample.

The transitions present above 240 °C in the heating cycles are probably related to instrumental artifacts. No sign of these features is present in DSC related to TGA, which support this hypothesis.

E-PNDIT2

Sample weight: 7.500 mg

A broad exothermic peak (result of peak integration: 37.77 mJ) is present between 140 °C and 250 °C in the first heating cycle. This feature is likely related to crystallization phenomena corresponding to the microstructural evolution seen in GIWAXS measurements (Figure S11 and Figure S12). No evident melting peak is present below 300 °C during the first heating cycle, which is compatible with GIWAXS data showing stable diffraction patterns till 300 °C. Similarly to DMP-PNDIT2, two endothermic features are present around 65 °C and 100 °C in the first heating cycle. These peaks are not present in the 2nd heating cycle, probably because a stable crystalline phase is formed with annealing above 140 °C, which is driven by inter-locking of the encapsulating rings (see discussion in the main text). Two noisy transitions around 255 °C and 325 °C are visible in the second heating cycle. These two features are probably instrumental artifacts. No sign of these features is present in DSC correlated to TGA (Figure S1), which support this hypothesis.

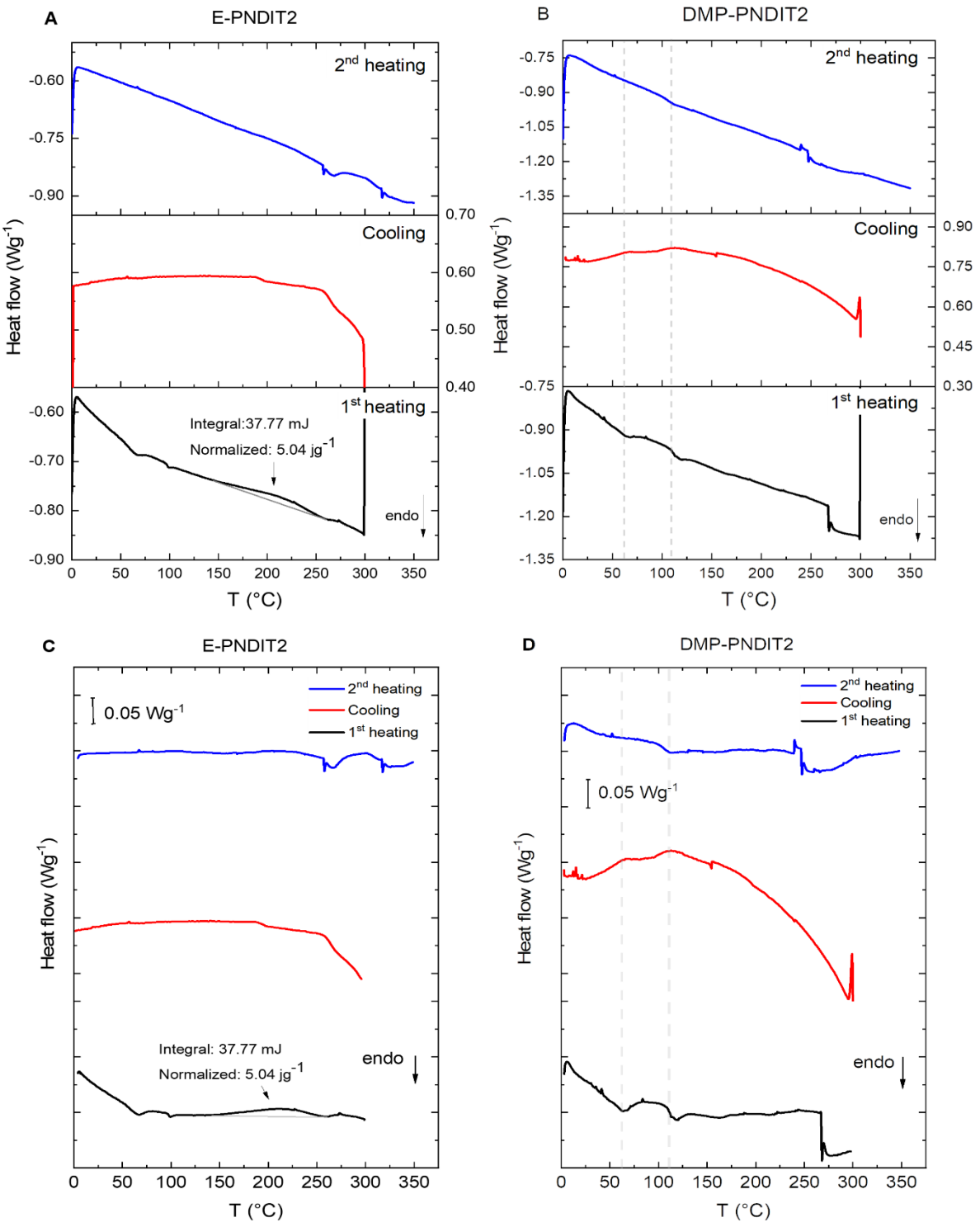

Figure S2. Differential Scanning Calorimetry (DSC). Top Graphs (A, B) show heating and cooling original cycles. Bottom graphs (C, D) show the same thermograms with horizontal baseline.

4) Optical Properties

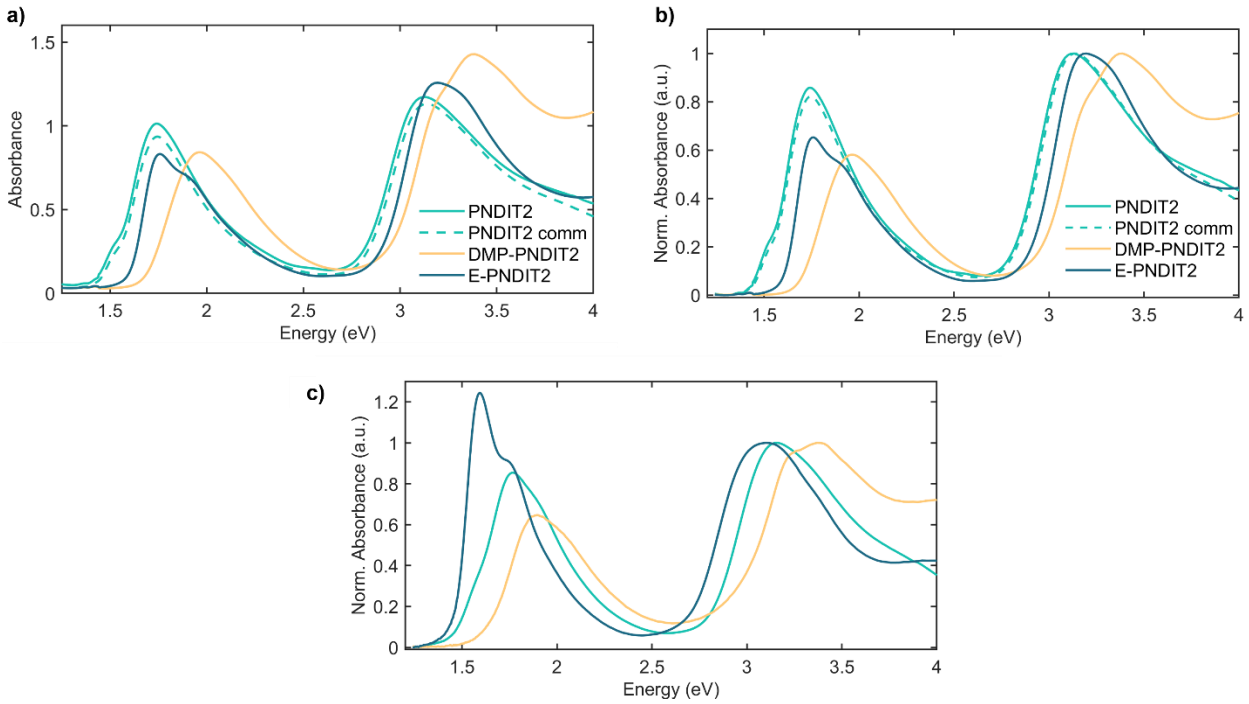

Figure S3. (a,b) UV-Vis absorption spectra of PNDIT2, DMP-PNDIT2 and E-PNDIT2 dissolved in toluene at a concentration of 0.1 g/L, and (c) in thin film. The spectra in (b) and (c) are normalized at the π-π* transition peaks.

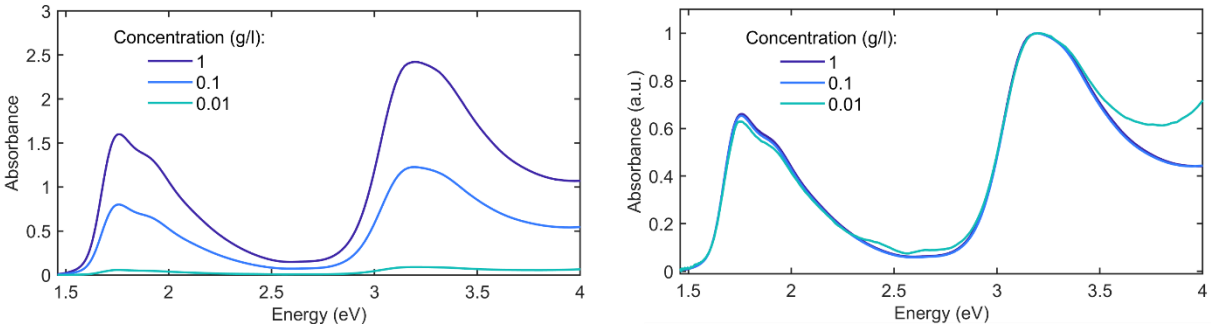

Figure S4. (a) Concentration dependent absorbance of E-PNDIT2 in toluene. (b) Normalization of the absorption spectra at the maximum of the high-energy absorption band (π-π* band).

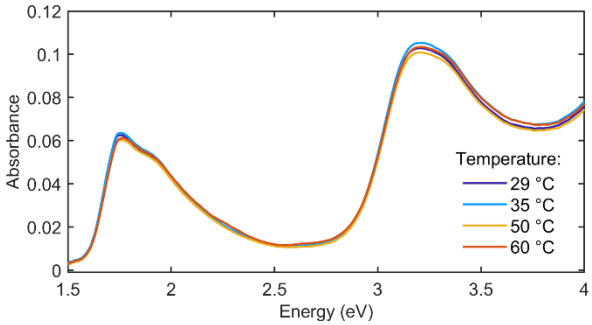

Figure S5. UV-Vis absorption of E-PNDIT2 (0.01 g/l in toluene) as function of the solution temperature.

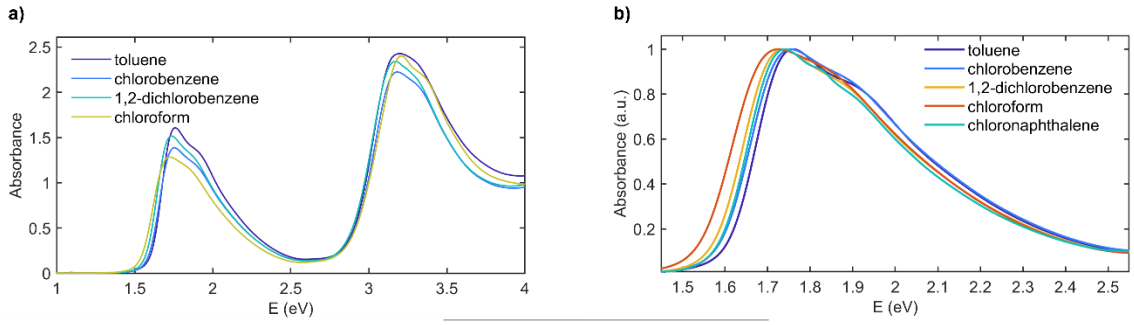

c)

Solvent	E_T (30) (kcal mol^{-1})
Toluene	33.9
Chlorobenzene	36.8
Chloronaphthalene	37.0
1,2-dichlorobenzene	38.0
Chloroform	39.1

Figure S6. (a) UV-Vis absorption spectra of E-PNDIT2 in solutions 1 g/l of various organic solvents. (b) Normalization of the absorption spectra at the maximum of the low energy absorption band (CT band). The redshift of the main peak and of the absorption tail are clear indication of solvatochromism. (c) Solvent polarity parameters $E_T(30)$ for the employed solvents (from Ref. [4]).

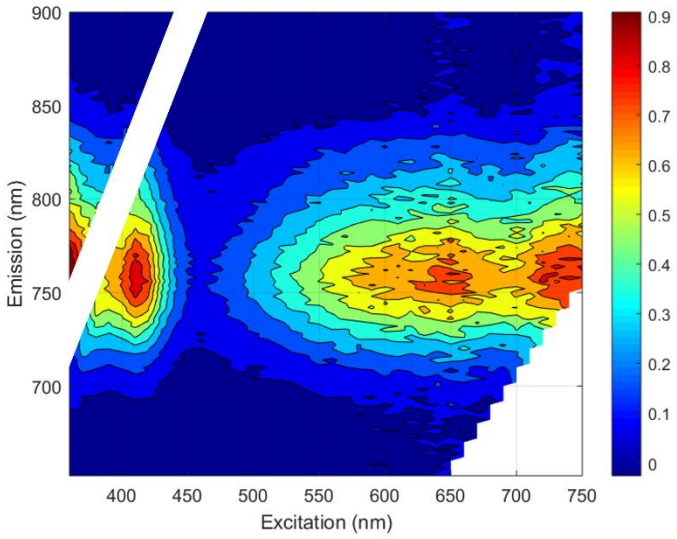

Figure S7. Excitation/emission map of E-PNDIT2 0.1 g/L in toluene.

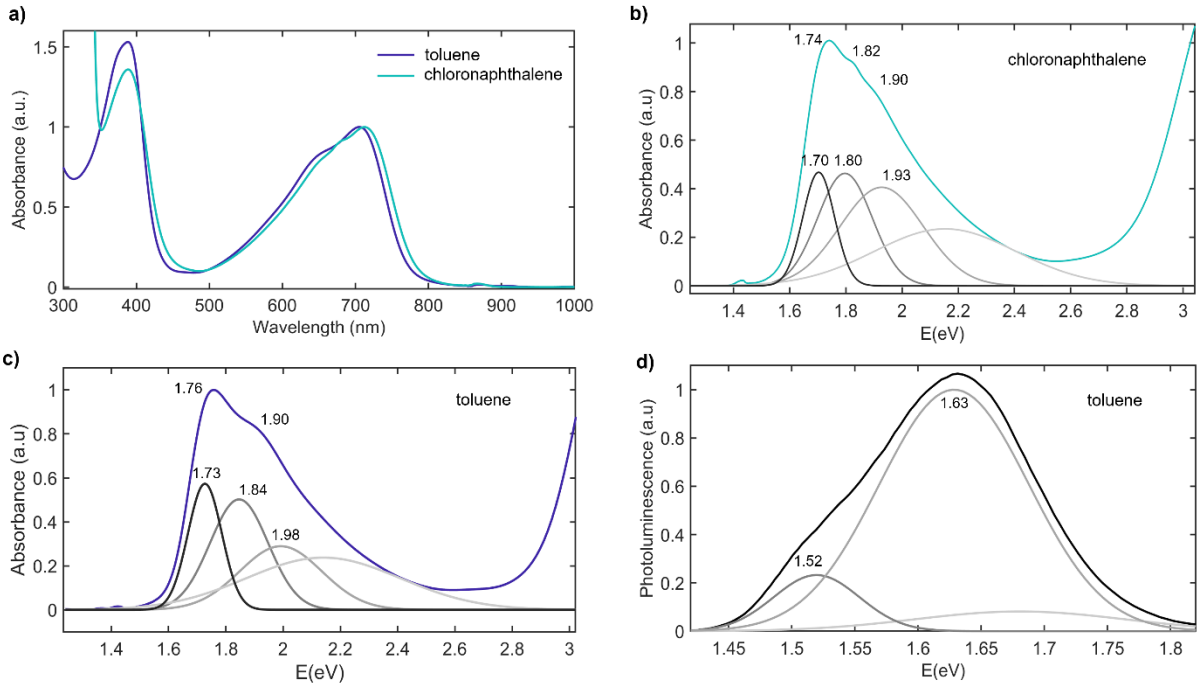

Figure S8. a) Comparison of the UV-Vis absorption spectra of E-PNDIT2 in toluene and in chloronaphthalene solutions (1 g/L), plotted as a function of the incident wavelength. **b,c)** Deconvolution with four gaussians of the absorption spectra in chloronaphthalene and toluene solutions, respectively. While the CT band of E-PNDIT2 in chloronaphthalene displays a fine structure with a main peak at 1.74 eV and two evident shoulders, a peak at 1.76 eV and only one shoulder are present in toluene solution. However, the deconvolution analysis shows that the best fit of the absorption

spectrum in both the solvents is described by three gaussians spaced of ~0.12 eV (compatible with vibronic coupling involving collective stretching modes found in virtually all π-conjugated systems[5,6]). **d)** Emission spectrum (excitation wavelength: 650 nm) of E-PNDIT2 in toluene (0.1 g/L), and its deconvolution with three gaussians. Two gaussians at 1.52 eV and 1.63 eV mainly contribute to the emission spectrum. The energy spacing between the peaks is of 0.11 eV, in good agreement with the spacing derived by deconvolution of the absorption spectra. Therefore, such a fine structure both in the absorption and emission spectra clearly indicates vibronic progression of unaggregated chains, as opposed to different aggregates.

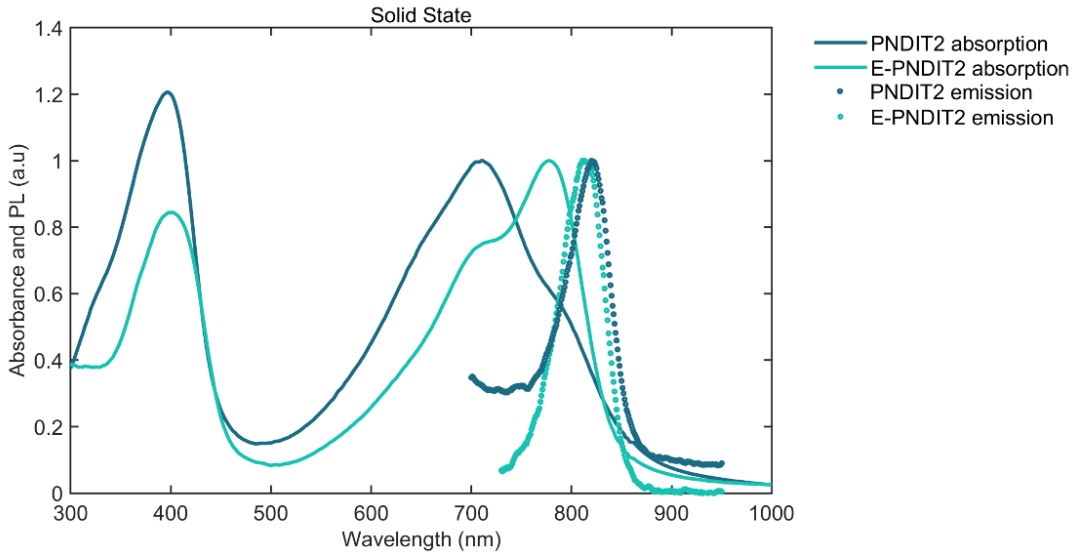

Figure S9. Comparison of the normalized absorption and photoluminescence (PL) spectra of thin films of PNDIT2 and E-PNDIT2.

5) Thin Film Microstructure

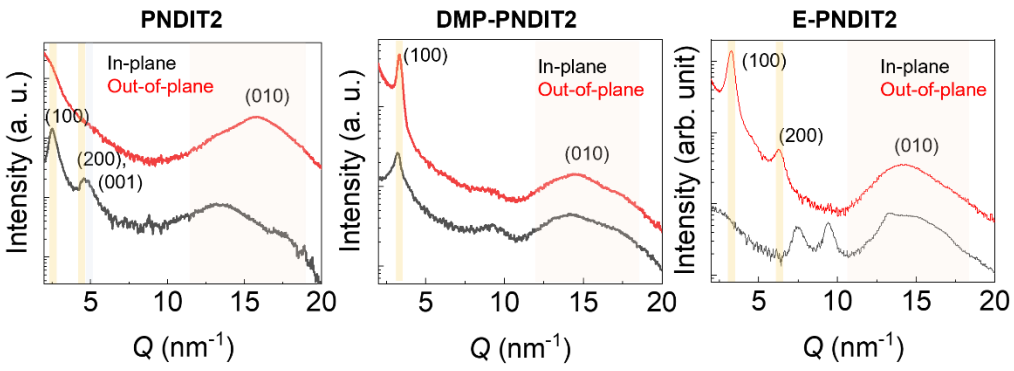

Figure S10. In-plane/out-of-plane integrated diffraction patterns of PNDIT2, DMP-PNDIT2 and E-PNDIT2**.**

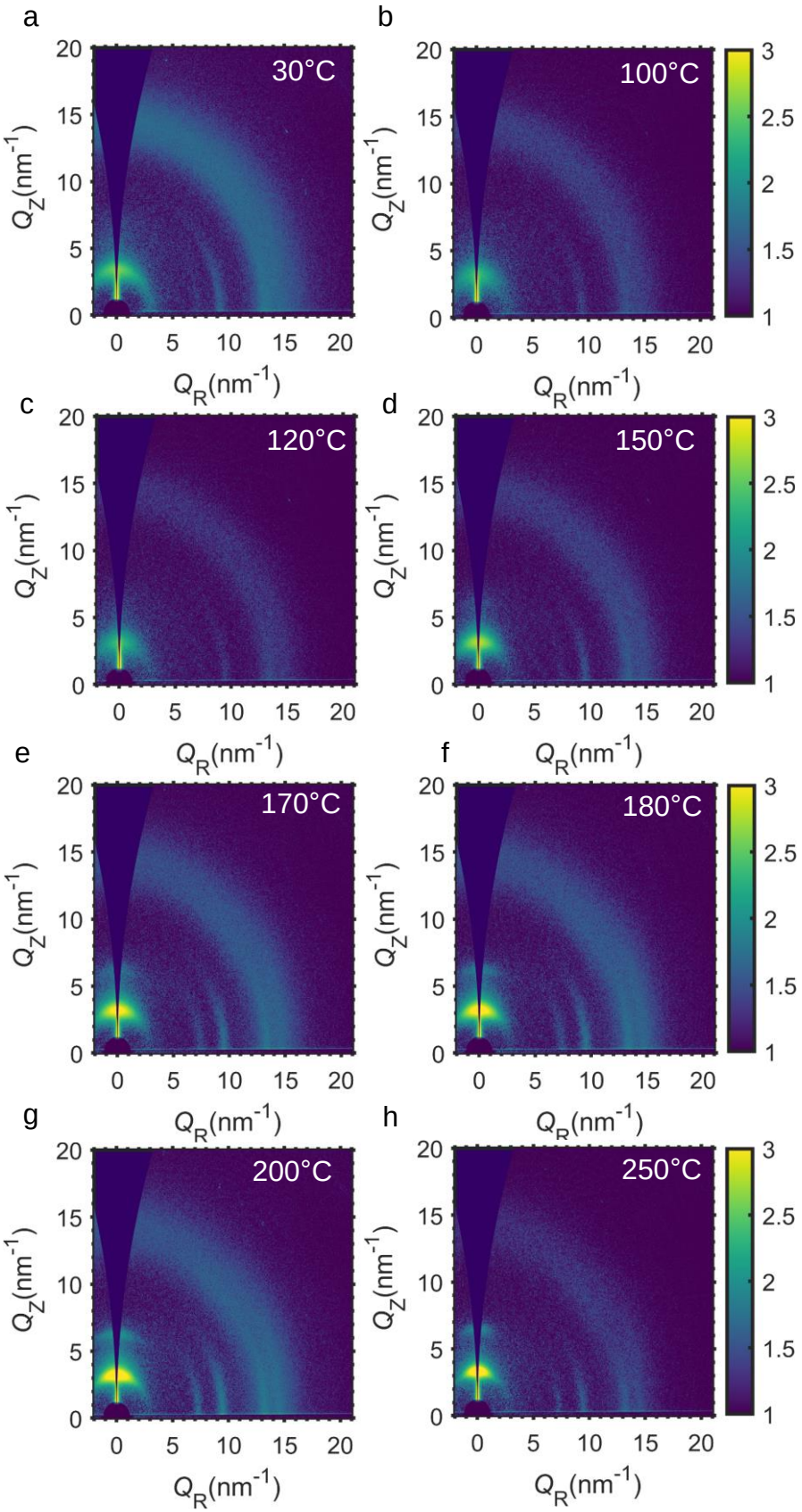

Figure S11. *In-situ* GIWAXS while annealing a film of E-PNDIT2, which has not been previously annealed.

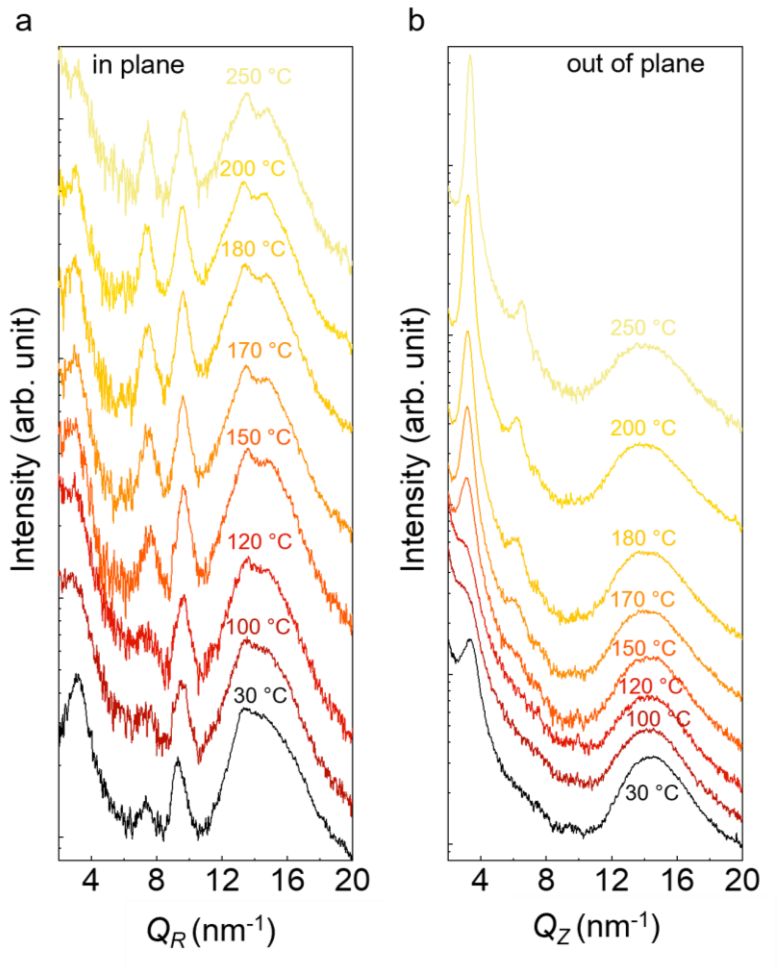

Figure S12. In-plane/out-of-plane integrated diffraction patterns of E-PNDIT2 (from 2D patterns of Figure S11).

6) Charge Transport

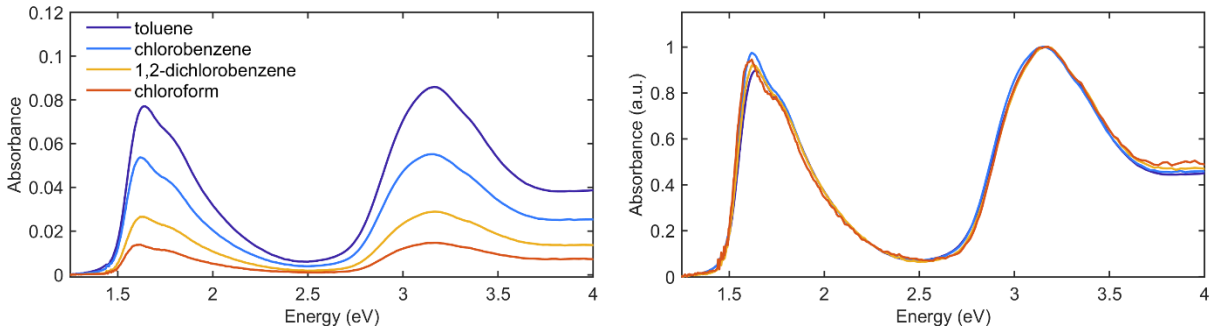

Figure S13. UV-Vis absorption of thin films of E-PNDIT2 deposited from various solvent solutions at a concentration of 5 g/L

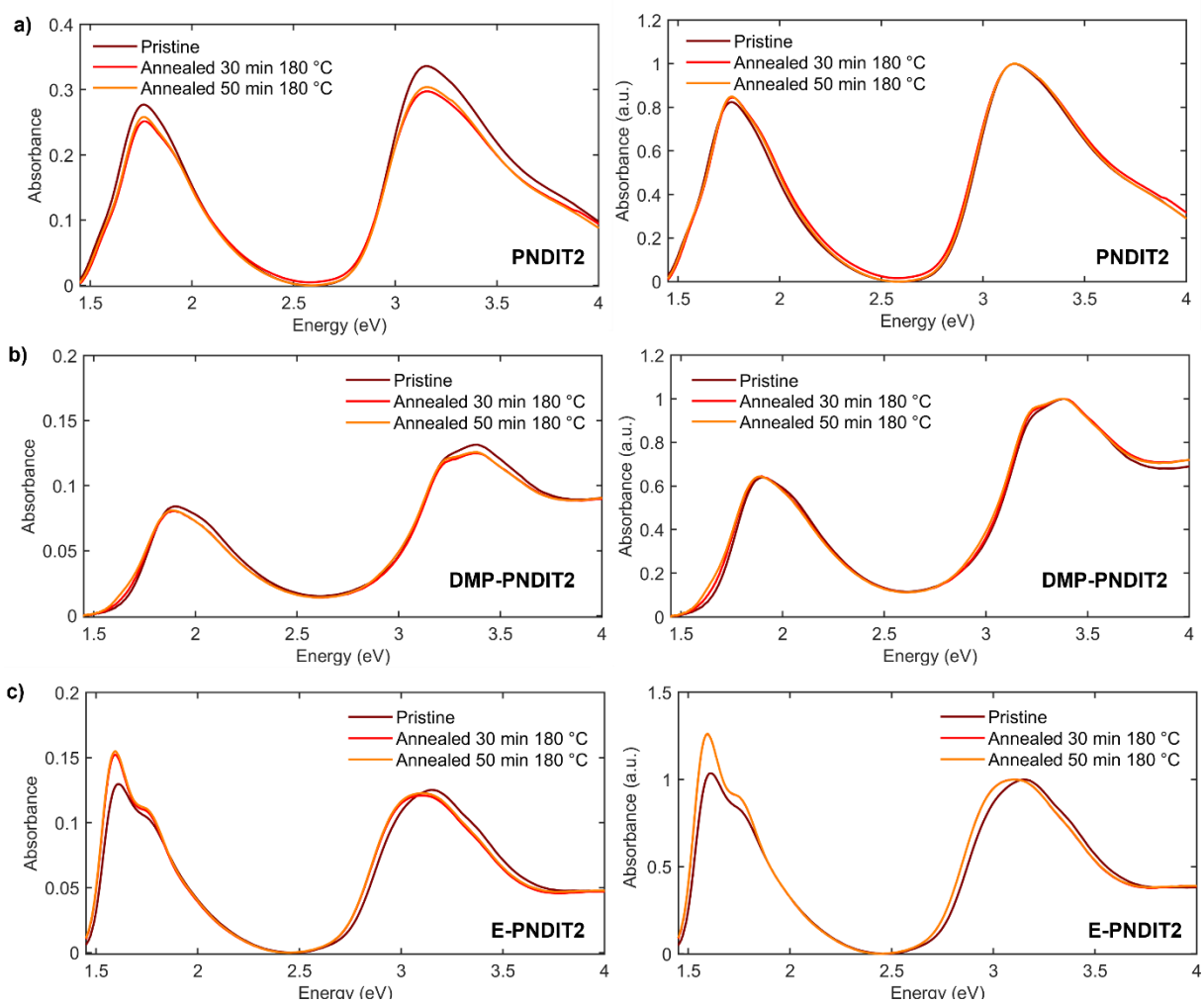

Figure S14. Effect of the annealing temperature on the UV-Vis absorption spectra of (a) PNDIT2, (b) DMP-PNDIT2 and (c) E-PNDIT2.

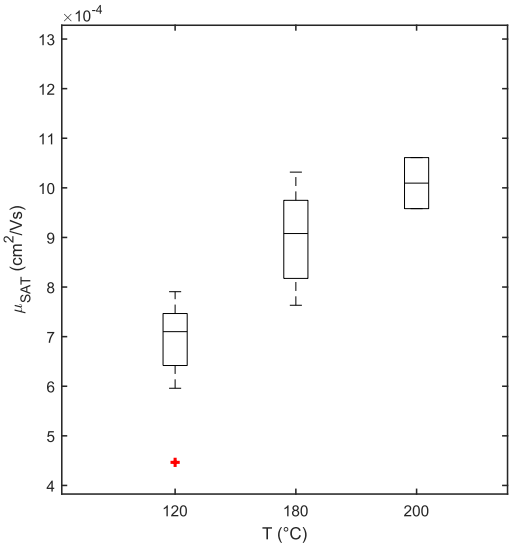

Figure S15. Box-plot of the saturation mobility of devices based on E-PNDIT2 films annealed for 30 min at different temperatures (spin-casted from toluene solution at a concentration of 10 g/L).

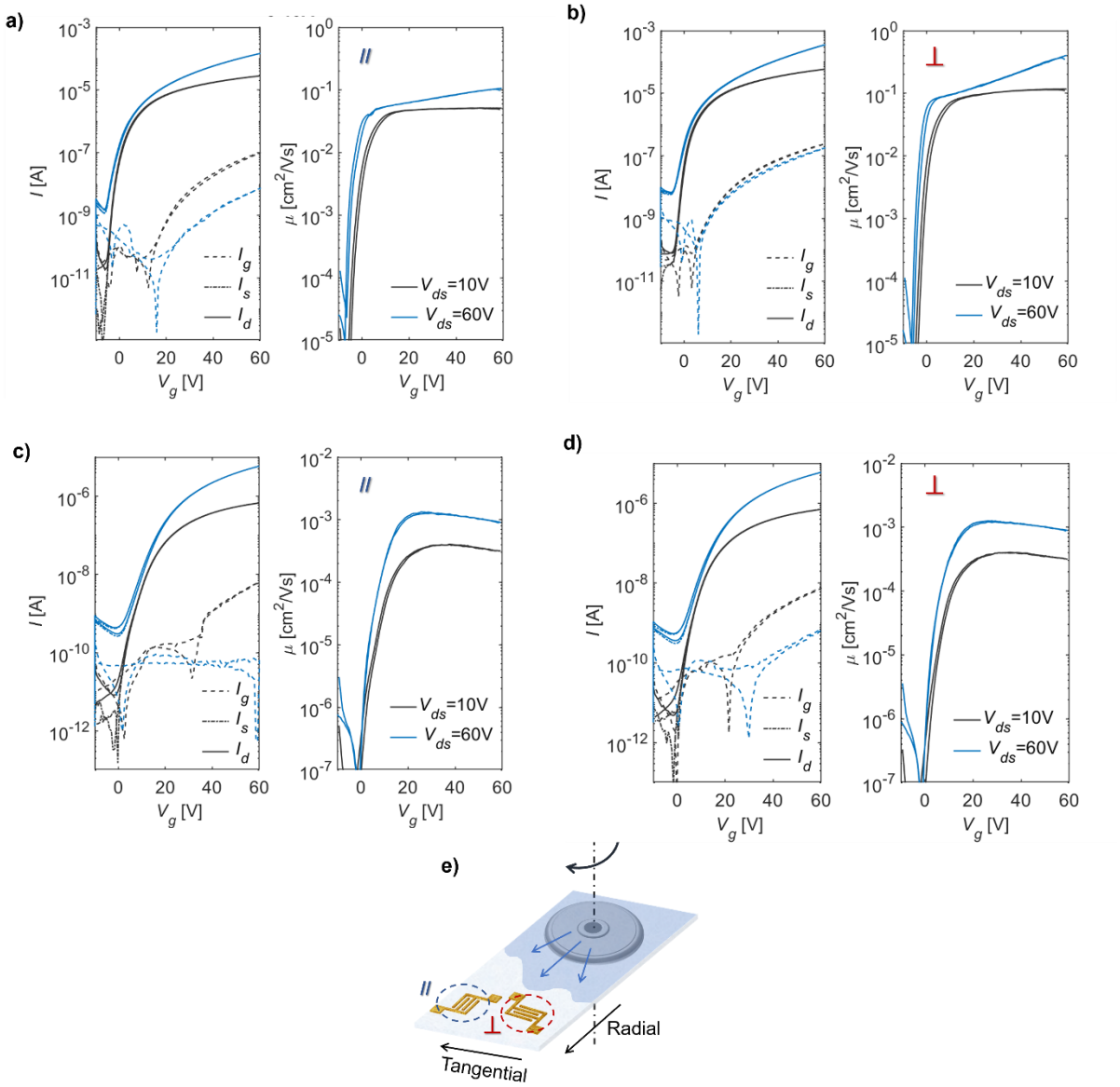

Figure S16. Transfer curves, and related mobility curves as a function of the gate potential, of devices based on PNDIT2 (a,b) and on E-PNDIT2 (c, d). Source and drain contacts are oriented parallel to the alignment direction in panels (a,c), and perpendicularly in panels (b,d). PNDIT2-based devices have L = 10 μm and W = 2 mm, E-PNDIT2-based devices L = 2.5 μm and W = 2 mm. e) Scheme of the off-center spin-coating.

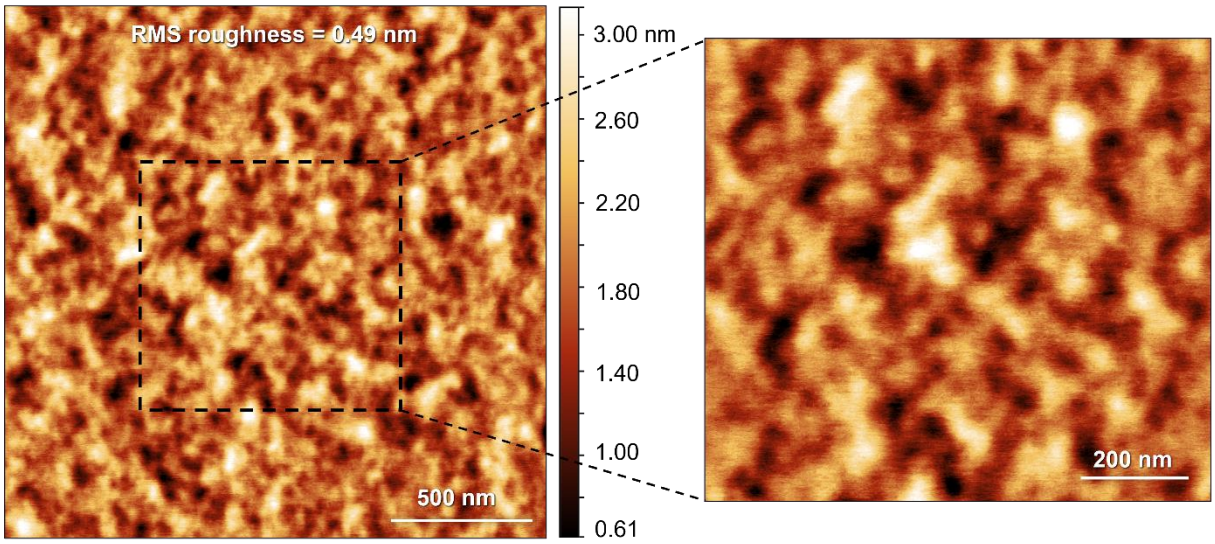

Figure S17. AFM topography of E-PNDIT2 thin-film.

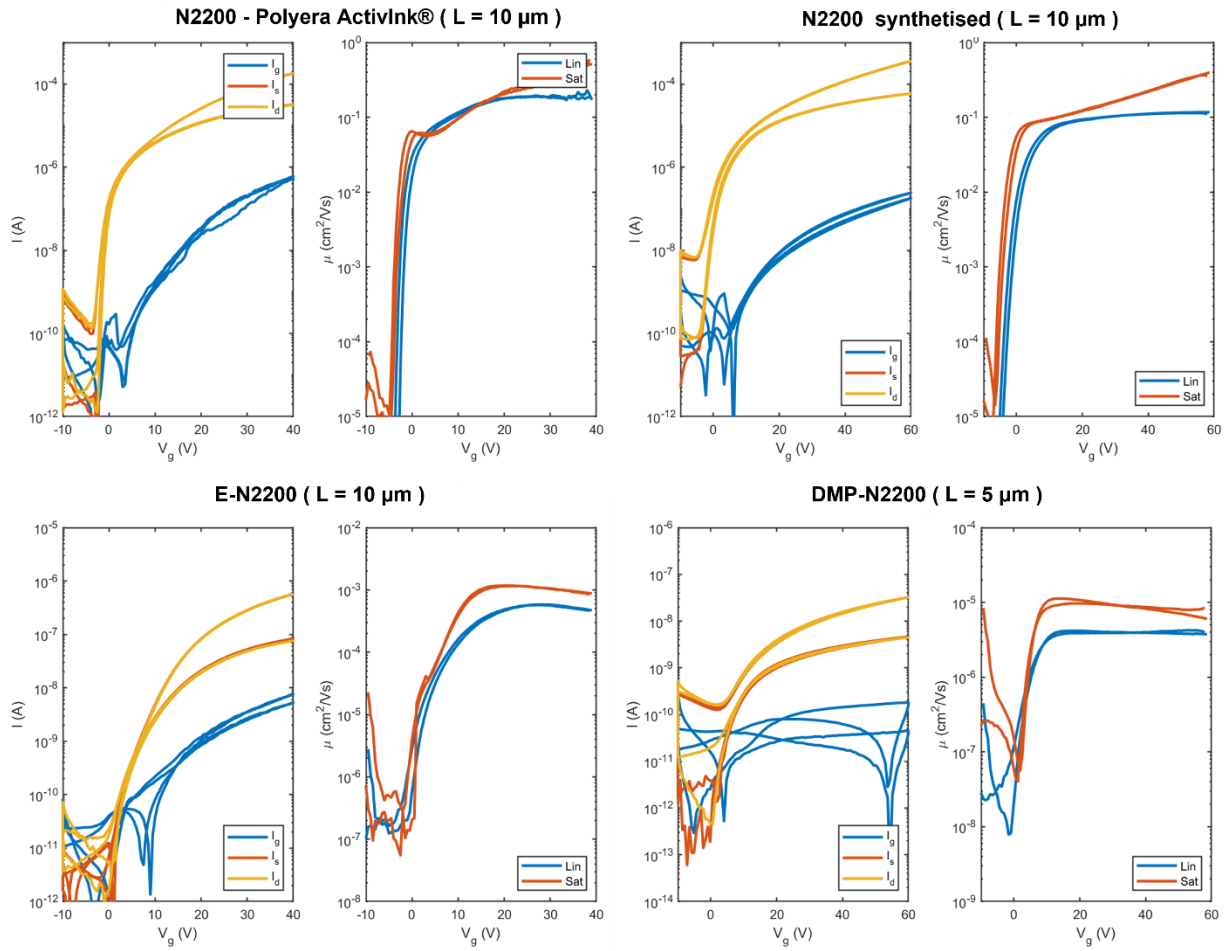

Figure S18. Transfer curves, and related mobility curves as a function of the gate potential, of devices based on PNDIT2 (both commercial ink and synthesized in this work), E-PNDIT2 and DMP-PNDIT2.

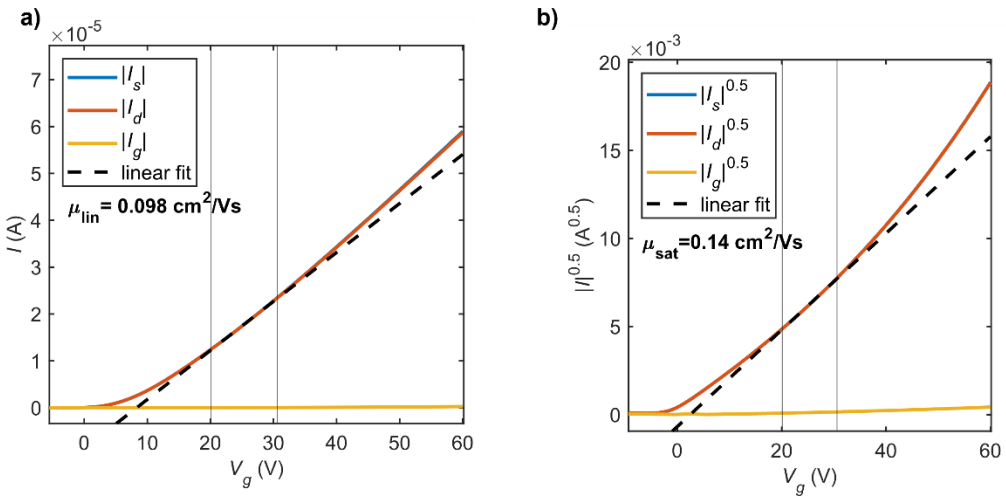

Figure S19. Mobility extraction from the linear slope of the transistors transfer curves a) in linear regime (V_{ds} = 10 V), and b) in saturation regime (V_{ds} = 60 V). The slope is obtained by fitting the curves in the range V_g = 20 - 30 V.

References

(1) Royakkers, J.; Guo, K.; Toolan, D. T. W.; Feng, L. W.; Minotto, A.; Congrave, D. G.; Danowska, M.; Zeng, W.; Bond, A. D.; Al-Hashimi, M.; Marks, T. J.; Facchetti, A.; Cacialli, F.; Bronstein, H. Molecular Encapsulation of Naphthalene Diimide (NDI) Based π-Conjugated Polymers: A Tool for Understanding Photoluminescence. *Angew. Chemie - Int. Ed.* **2021**, *60* (47), 25005–25012. https://doi.org/10.1002/anie.202110139.

(2) Sugiyasu, K.; Honsho, Y.; Harrison, R. M.; Sato, A.; Yasuda, T.; Seki, S.; Takeuchi, M. A Self-Threading Polythiophene: Defect-Free Insulated Molecular Wires Endowed with Long Effective Conjugation Length. *J. Am. Chem. Soc.* **2010**, *132* (42), 14754–14756. https://doi.org/10.1021/ja107444m.

(3) Chen, Z.; Zheng, Y.; Yan, H.; Facchetti, A. Naphthalenedicarboximide- vs Perylenedicarboximide-Based Copolymers. Synthesis and Semiconducting Properties in Bottom-Gate N-Channel Organic Transistors. *J. Am. Chem. Soc.* **2009**, *131* (1), 8–9. https://doi.org/10.1021/ja805407g.

(4) Reichardt, C. Solvatochromic Dyes as Solvent Polarity Indicators. *Chem. Rev.* **1994**, *94* (8), 2319–2358. https://doi.org/10.1021/cr00032a005.

(5) Qarai, M. B.; Chang, X.; Spano, F. C. Vibronic Exciton Model for Low Bandgap Donor-Acceptor Polymers. *J. Chem. Phys* **2020**, *153*, 244901. https://doi.org/10.1063/5.0029193.

(6) Denti, I.; Cimò, S.; Brambilla, L.; Milani, A.; Bertarelli, C.; Tommasini, M.; Castiglioni, C. Polaron Confinement in N-Doped P(NDI2OD-T2) Unveiled by Vibrational Spectroscopy. *Chem. Mater.* **2019**, *31* (17), 6726–6739. https://doi.org/10.1021/acs.chemmater.9b01218.

Appendix B: Supporting Information for "Investigating Charge Transport in Semiconducting Single-Walled Carbon Nanotube Networks by Charge Modulation Microscopy"

ADVANCED MATERIALS INTERFACES

Supporting Information

for *Adv. Mater. Interfaces,* DOI: 10.1002/admi.202202454

Investigating Charge Transport in Semiconducting Single-Walled Carbon Nanotube Networks by Charge Modulation Microscopy

Mengting Jiang, Stefano Pecorario, Nicolas F. Zorn, Jana Zaumseil, and Mario Caironi**

WILEY-VCH

Supporting Information

Investigating Charge Transport in Semiconducting Single-Walled Carbon Nanotube Networks by Charge Modulation Microscopy

Mengting Jiang[1,#], Stefano Pecorario[1,2,#], Nicolas F. Zorn[3], Jana Zaumseil[3,], Mario Caironi[1,*]*

[1] Center for Nano Science and Technology@PoliMi, Istituto Italiano di Tecnologia, via Giovanni Pascoli 70/3, Milan 20133, Italy

[2] Department of Energy, Micro and Nanostructured Materials Laboratory - NanoLab, Politecnico di Milano, Via Ponzio 34/3, Milano, 20133, Italy.

[3] Institute for Physical Chemistry, Universität Heidelberg, D-69120 Heidelberg, Germany.

[#] These authors contributed equally

* Corresponding authors

Table of Contents:

Table S1. Chiral indices, diameter, and absorption wavelength (E_{11} and trion absorption peaks) of the SWCNTs species used in this work.

Chiral indices	D (nm)	E_{11} (eV)	Trion (eV)	E_{11} (nm)	Trion (nm)
(6,5)	0.76	1.23	1.06	1005	1165
(7,5)	0.83	1.19	1.02	1045	1213
(7,6)	0.90	1.09	0.95	1135	1312
(8,6)	0.97	1.03	0.91	1200	1361
(8,7)	1.03	0.96	0.85	1285	1464
(9,7)	1.11	0.92	0.82	1350	1521

Figure S1.

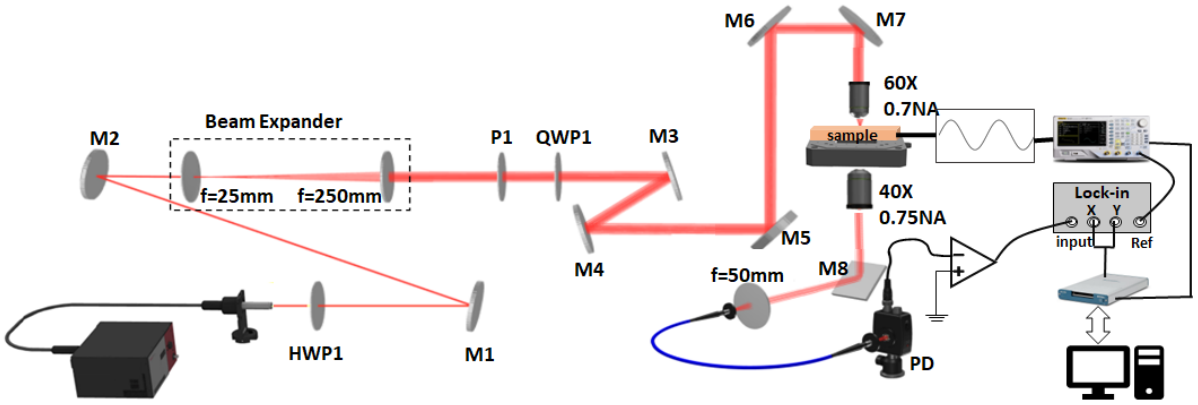

a) Scheme of the CMM setup:

- Variable λ source, covering the 900-1500 nm range: supercontinuum white laser (SuperK Extreme, NKT photonics) coupled with Acousto-Optic Tunable Filters (SuperK IR-AOTF, NKT photonics).
- Optical fiber: single model fiber P3-1064Y-FC-5 for the wavelength range 980-1650 nm.
- HWP1: achromatic half-waveplate integrated to shift the polarization direction.
- QWP1: two achromatic quarter waveplates (for the 690-1200 nm and 1100-1800 nm wavelength ranges) used to manipulate the polarization.
- LP1: linear polarizer used to polarize the beam in the measurements performed to detect the local degree of orientational order (Figure S7).
- M1, 2…, 8: metallic mirrors.
- Beam Expander (10×): it is needed to fill up the objective numerical aperture (NA).
- Confocal microscope: the beam is focused on the sample by a 0.7 NA objective (S Plan Fluor 60×, Nikon), and collected by the bottom 0.75 NA objective (CFI Plan Apochromat VC 20×, Nikon). The sample is scanned by means of a PZT stage (E-517.i3).
- Signal generation: the gate potential is modulated by supplying the DC and AC components using a Keithley 3390 waveform generator.
- Signal detection: the signal is detected through a silicon photodiode coupled with a transimpedance amplifier (FEMTO DHPCA 100) and a SR830 DSP Lock-In Amplifier (Stanford Research Systems). The data are acquired with a NIDAQ.

To ensure the device stability during the experiment, the SWCNTs FET is placed inside a custom case with continuous nitrogen fluxing.

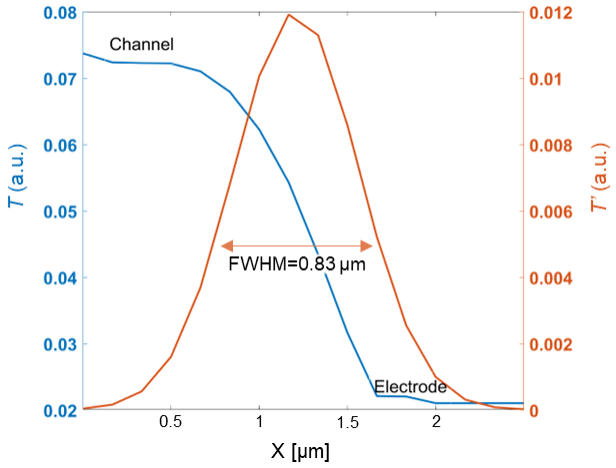

b) Spatial resolution assessment.

Since the electrodes are fabricated by photolithography, they present a sharp edge. The transmission at 1005 nm (blue curve) is measured at the interface between the channel (high transmission) and the electrode (nearly zero transmission). The spatial resolution is calculated as the FWHM of the gaussian obtained by computing the first derivative of the transmission curve (orange curve), and it is ~ 0.8 µm.

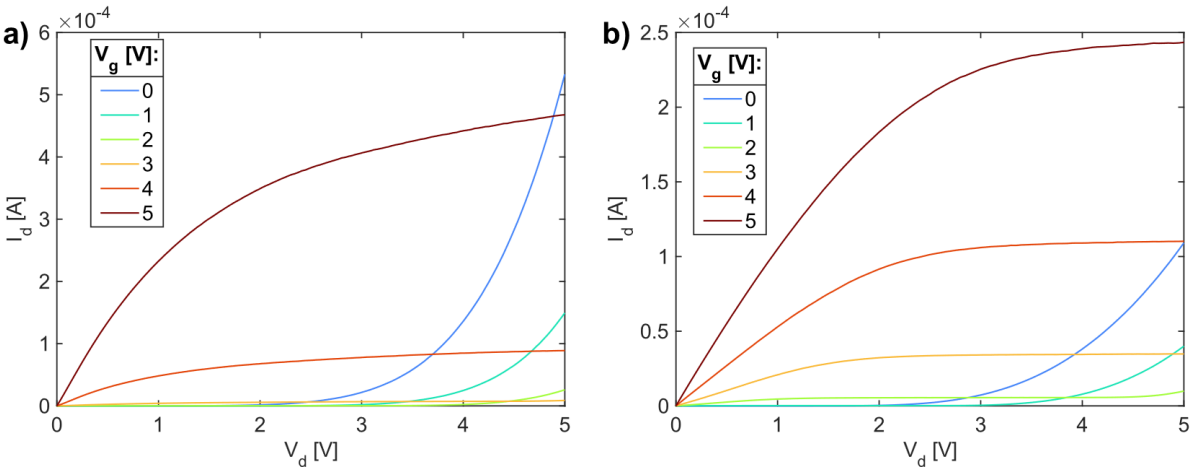

Figure S2. Output curves (electron accumulation) of representative FETs based on **a)** monochiral (6,5) SWCNT network and **b)** multichiral SWCNT network.

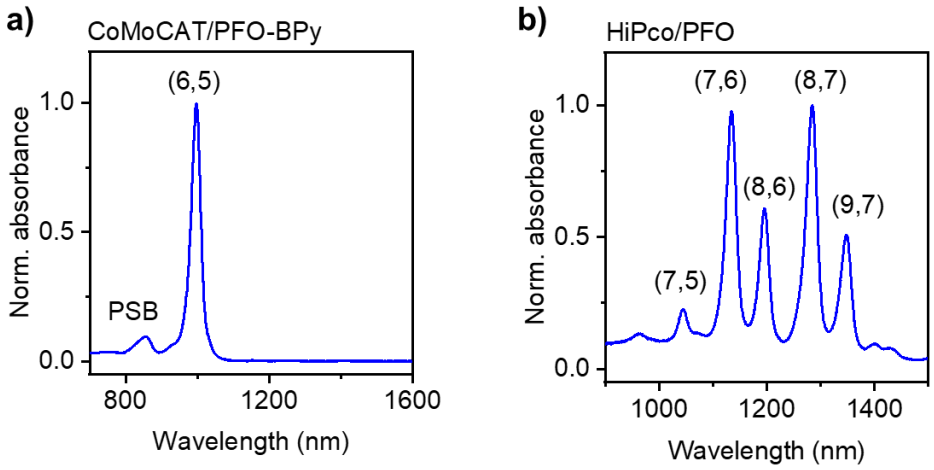

Figure S3. a) Absorption spectra of a CoMoCAT/PFO-BPy dispersion (*i.e*, monochiral (6,5) SWCNTs) and **b)** a HiPco/PFO (*i.e.* multichiral SWCNTs) dispersion. The E_{11} transitions are labelled with the chiral indices of the corresponding SWCNT species. PSB denotes the phonon side band of the (6,5) SWCNT E_{11} peak.

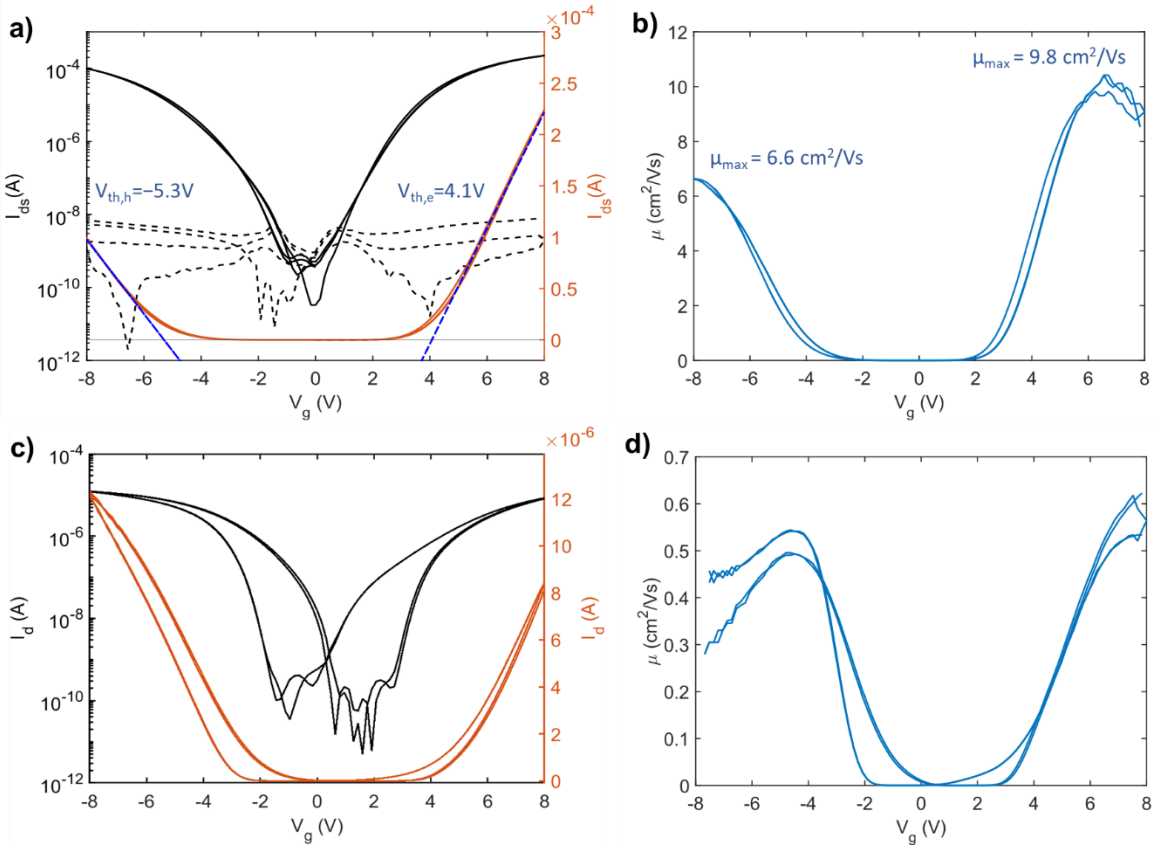

Figure S4. Transfer curve and threshold voltage extraction for **a)** the monochiral network and **c)** the multichiral network. V_g-dependent field-effect mobility for **b)** the monochiral network and **d)** the multichiral network.

Figure S5

a) CMS spectrum on the entire device *vs* **b)** local CMS spectrum acquired with the confocal microscope.

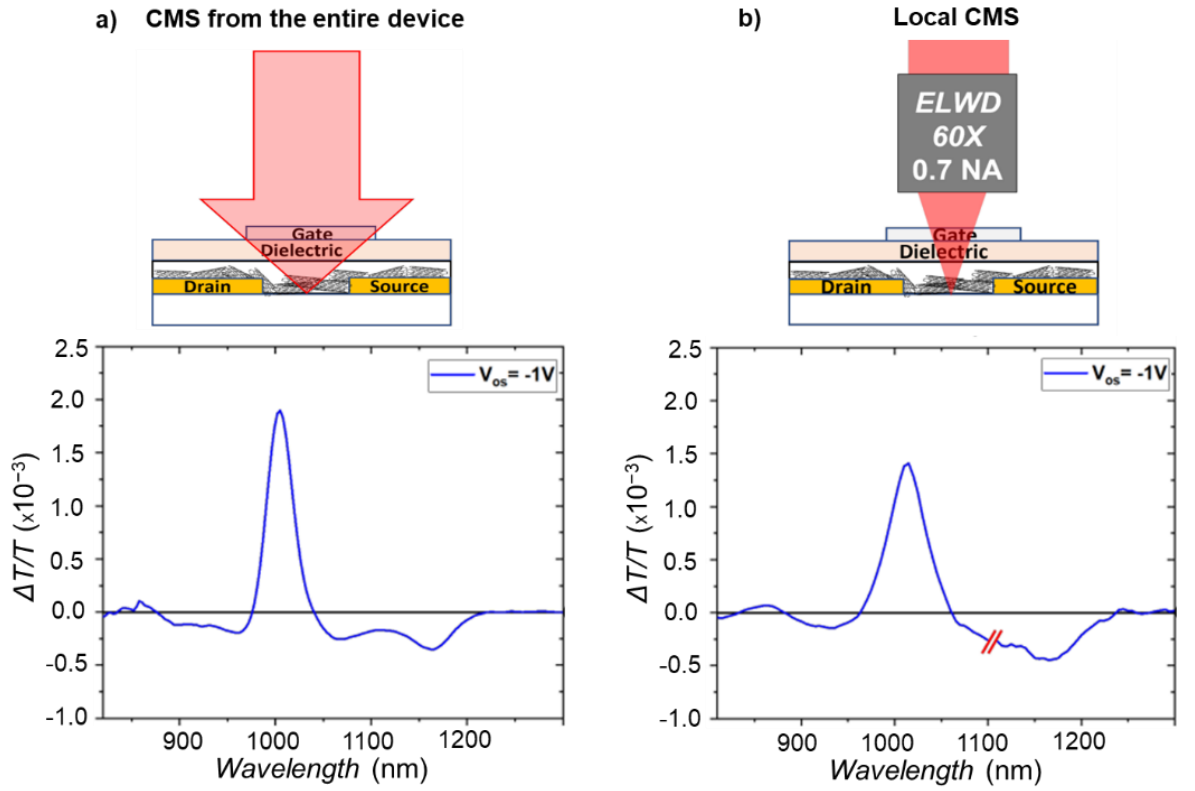

c) Local CMS spectra in different locations within the device channel.

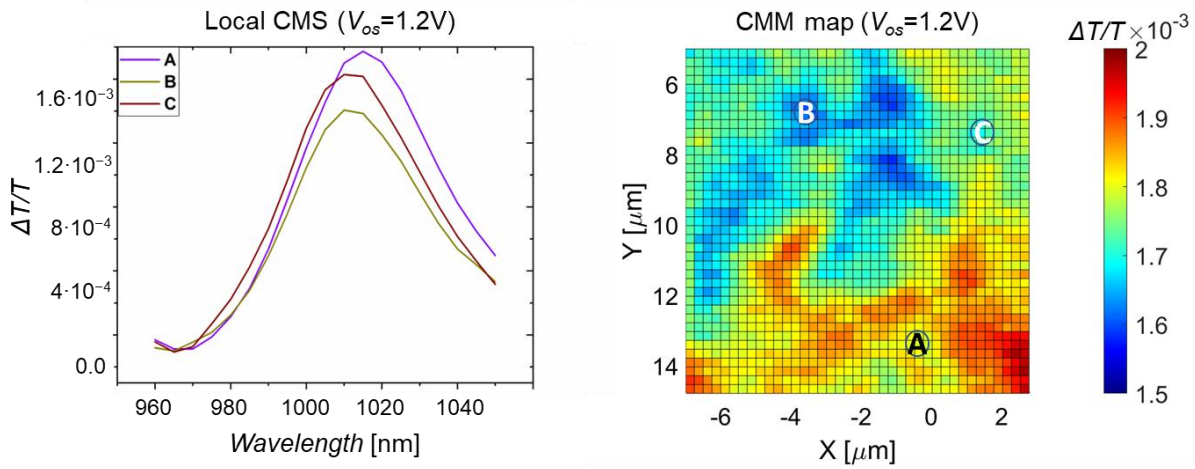

d) Comparison of the local CMS spectra at the center of channel and at the contact edge.

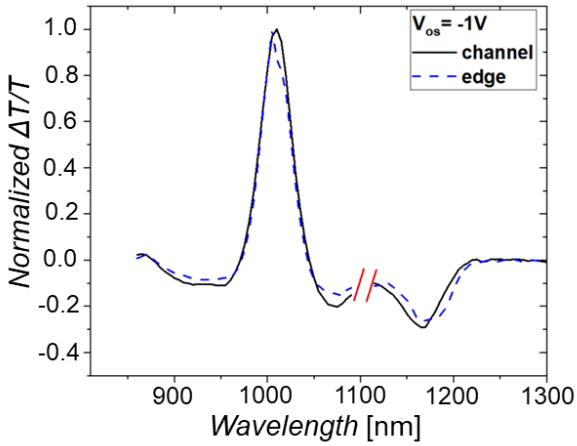

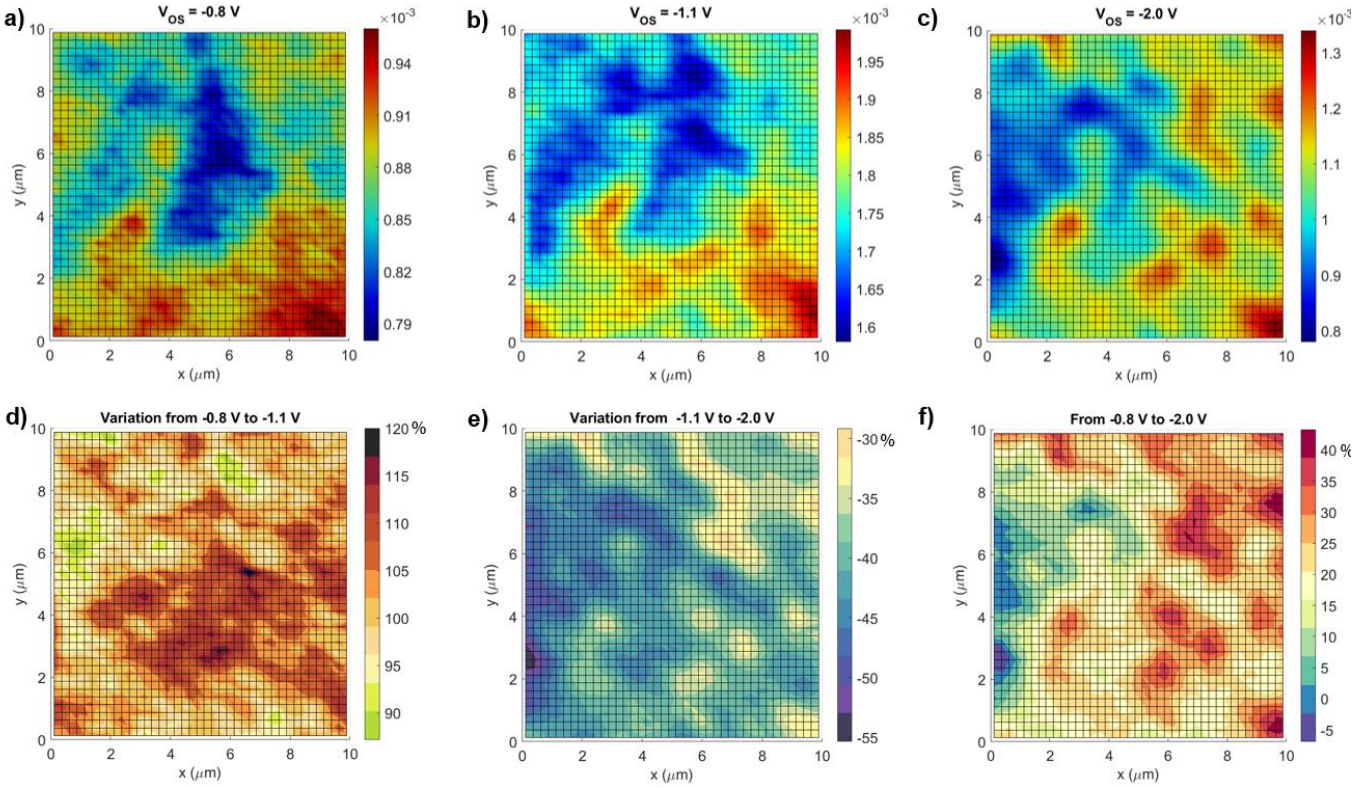

Figure S6. CMM maps of a (6,5) monochiral SWCNT network, corresponding to the E_{11} bleaching peak at 1005 nm, acquired in hole accumulation at **a)** V_{os} = −0.8 V, **b)** V_{os} = −1.1 V, **c)** V_{os} = −2.0 V. Percentage variation of the CMS signal when passing **d)** from V_{os} = −0.8 to −1.1 V, **e)** from V_{os} = −1.1 to −2.0 V and **f)** from V_{os} = −0.8 to −2.0 V. Consistently with the trend of ΔT/T *vs* V_{os} shown in Figure 1f, the mean CMS signal increases from the map at V_{os} = −0.8 V to the one at V_{os} = −1.1 V and then it drops in the map at V_{os} = −2.0 V.

Polarized-CMM analysis (Figure S7)

Using a polarizer to tune the linear polarization of the probing beam, it is possible to perform polarized charge modulation microscopy (p-CMM). As reported by Martino and co-authors[39], this technique allows to map selectively the orientational order of the part of the active layer probed by mobile charge carriers. p-CMM maps acquired with linear polarization of 0°, 30°, 60°, 90°, 120° and 150° are shown in Figure S7a, while a map acquired with circular polarization is reported in Figure S7b.

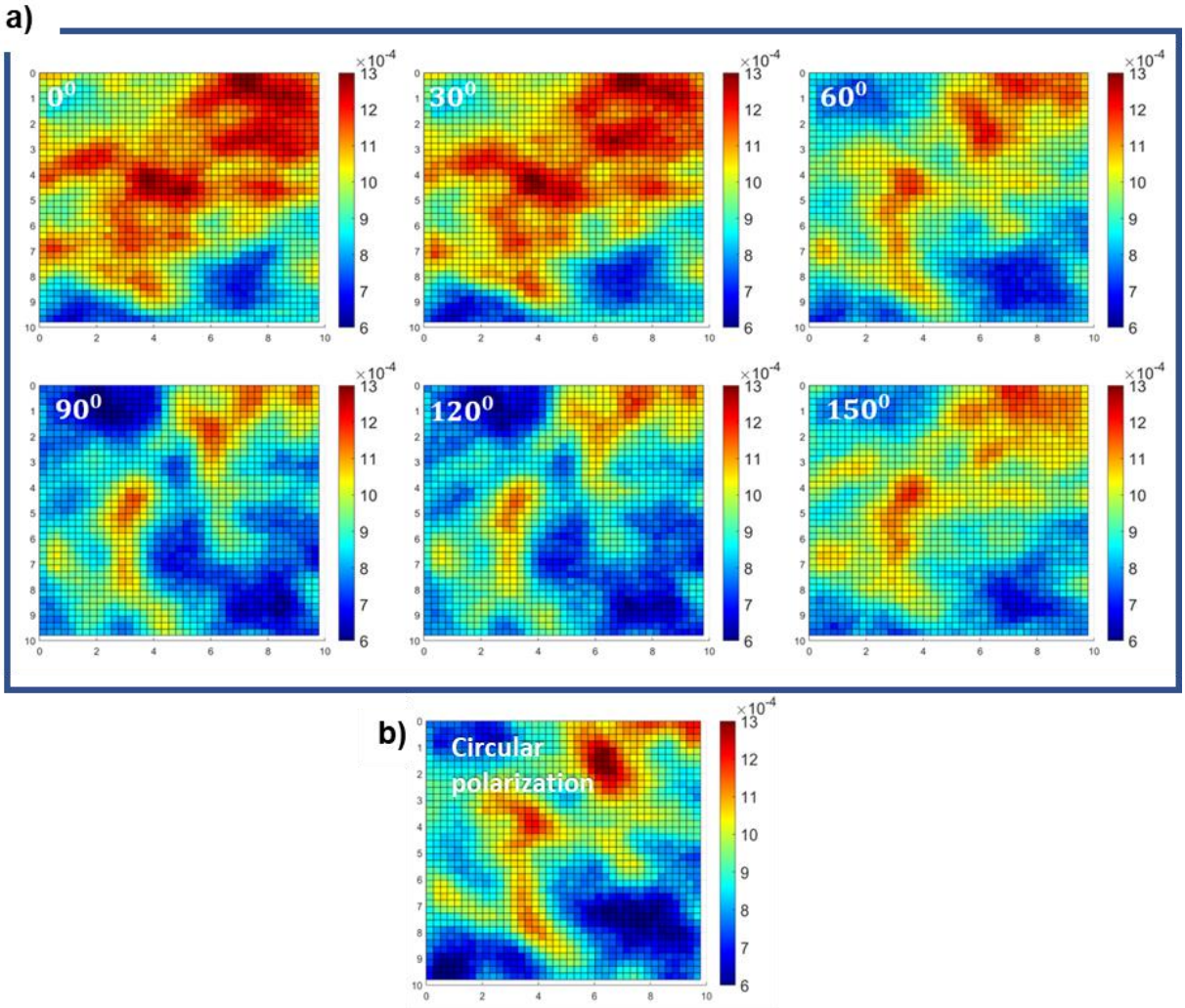

Figure S7. a) p-CMM maps of the monochiral (6,5) SWCNT network ($V_g = -2 \pm 0.1$ V, $\lambda = 1005$ nm) with probing beam linearly polarized at 0, 30, 60, 90, 120, 150° with respect to the direction of the y axis.

We applied the same procedure implemented by Martino et. al. to calculate the local degree of orientational order (O) of the (6,5) SWCNTs. For every pixel with (x,y) coordinates, the trend of the CMS signal as a function of the polarization is fitted with the following equation:

$$CMS_{(x,y)} = M_{(x,y)} \cos^2(\beta_{(x,y)} - \theta) + C_{(x,y)}, \qquad \text{(Eq. S1)}$$

where θ is the polarization angle of the probing beam (θ = 0° when the polarization is parallel to the electrodes), while $M_{(x,y)}$, $C_{(x,y)}$ and $\beta_{(x,y)}$ are fitting parameters. $M_{(x,y)}$ and $C_{(x,y)}$ correspond, respectively, to the polarization dependent and independent parts of the CMS signal amplitude (Figures S7c,d). $\beta_{(x,y)}$ indicates the average SWCNTs direction in the pixel with the assumption that charge transport occurs preferentially along the SWCNT direction (Figure S7e). Figure S7h depicts the R^2 parameter from the fit, which confirms the reliability of the procedure.

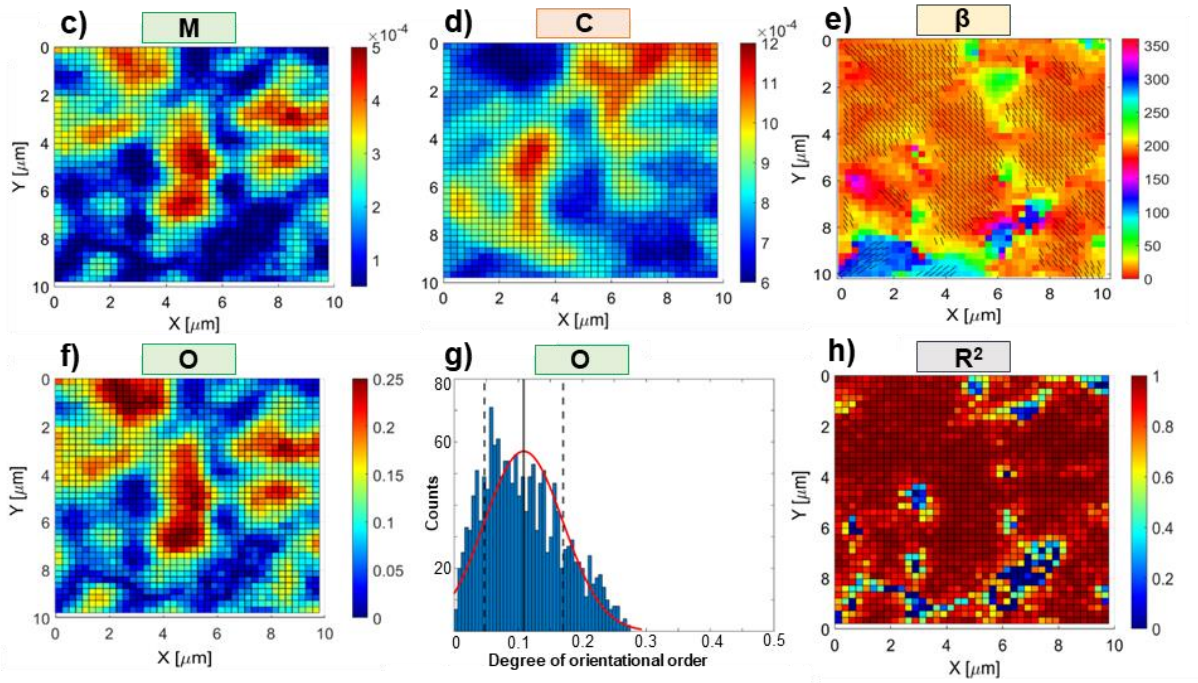

Figure S7. c) Map of the polarization dependent signal amplitude (M). **d)** Map of the polarization independent signal amplitude (C). **e)** Map of the average SWCNTs direction (β). **f)** Map of the orientational order (O), and **g)** the corresponding histogram. **h)** Fitting accuracy (R^2 parameter).

From the knowledge of the M and C parameters, the local degree of orientational order $O_{(x,y)}$ is calculated pixel by pixel as:

$$O_{(x,y)} = \frac{M_{(x,y)}}{M_{(x,y)} + 2C_{(x,y)}} \qquad \text{(Eq. S2)}$$

The map corresponding to the O parameter is shown in Figure S7f, while Figure S7g reports the histogram with the frequencies of the O parameter from the Figure S7f map. As expected for randomly distributed networks deposited by spin coating, the degree of orientational order at the micrometric scale is poor (average degree of order O ~ 10%). Moreover, there is no significant correlation between the degree of orientational order map and the CMM map obtained with circular polarization (Figure S7b). Hence, we can exclude the local orientational order at the micrometric scale as a drive for the accumulation of free carriers in the studied networks.

Reliable measurement of optical density maps for the (6,5) network (Figure S8)

Due to the high transparency (~95%) of the SWCNT network and to the possible fluctuations of the laser beam intensity, the optical density (OD) maps must be measured with great care averaging over several scans. OD is derived from:

$$OD = \log_{10} \frac{T_0}{T} \qquad \text{(Eq. S3)}$$

by measuring both the transmission through the FET channel (T) and the blank transmission (T_0), which is obtained from a region on the sample where the PMMA, HfO_x and Ag layers are present, but not the SWCNT network.

The T_0 and T transmission maps (Figure S8a,b) result from the average over 20 scans with probing laser wavelength of 1005 nm (E_{11} peak of (6,5) SWCNTs):

$$< T_0(x,y) >= \frac{\sum_{i=1}^{20} T_0(x,y)}{20}, < T(x,y) >= \frac{\sum_{i=1}^{20} T(x,y)}{20} \qquad \text{(Eq. S4a,b)}$$

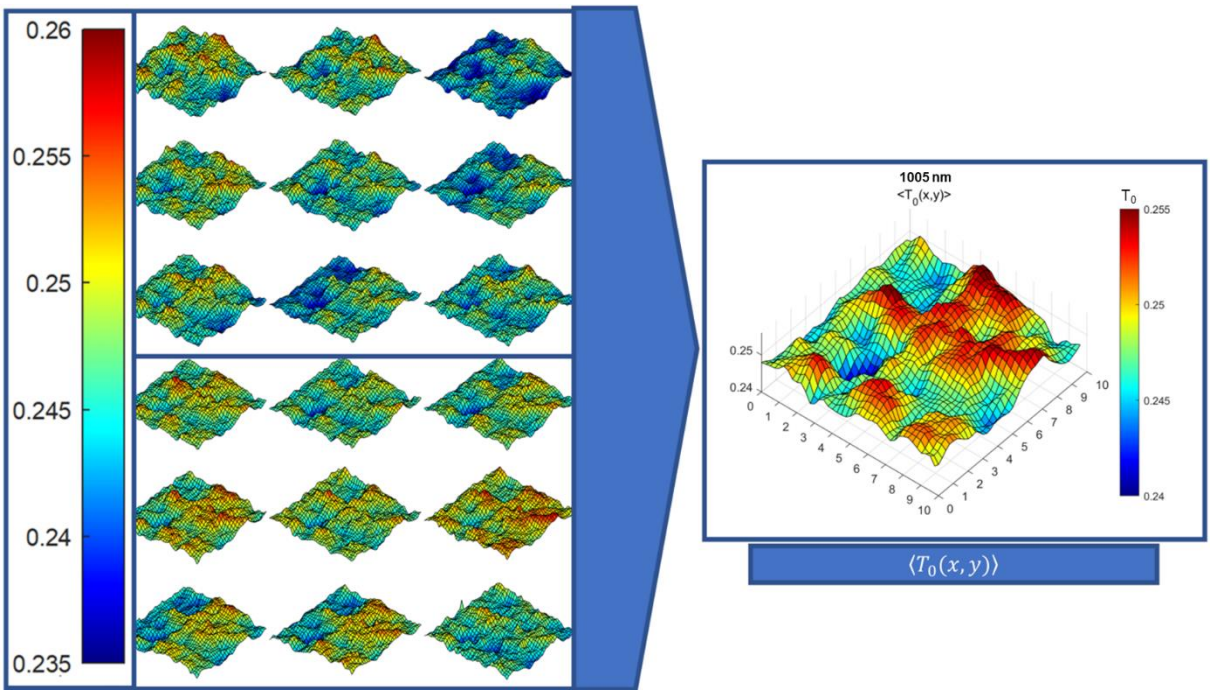

Figure S8a. Blank transmission T_0 at 1005 nm measured by averaging 20 scans on the same area without SWCNTs.

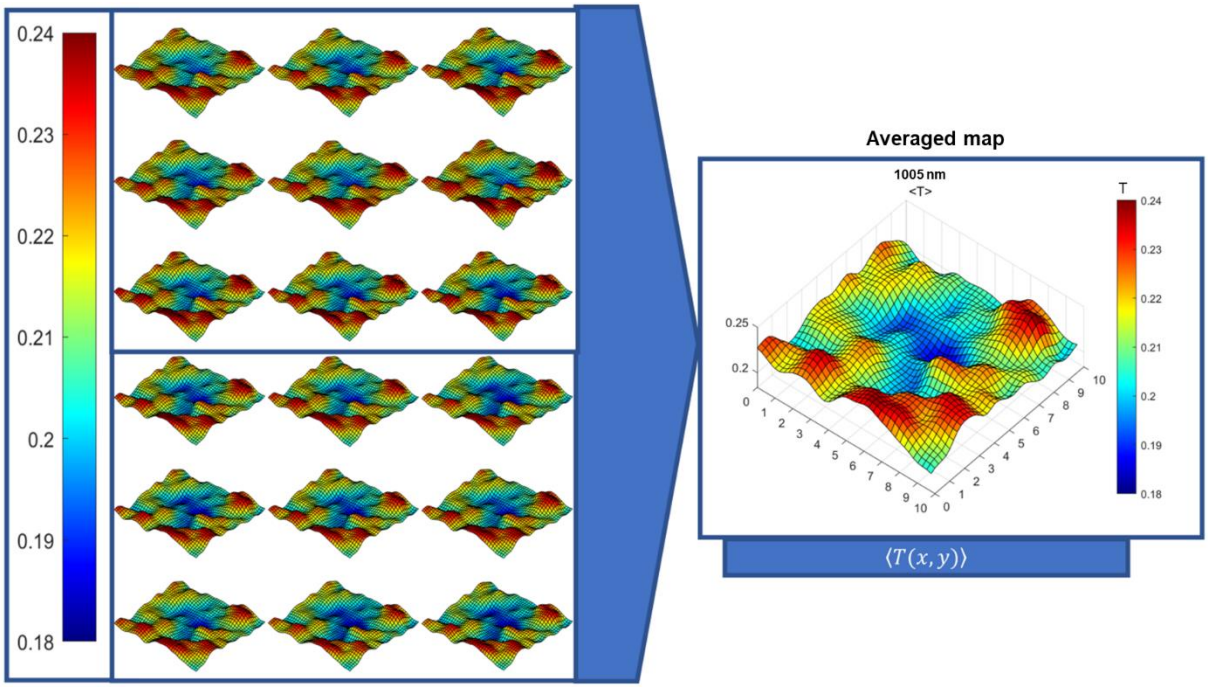

Figure S8b. Transmission T measured by averaging 20 scans on the same area with SWCNTs.

The T_0 value used to derive the OD maps is further obtained by taking the mean value of the 1600 pixels of the $<T_0(x,y)>$ map. The distributions of T_0 and T from the averaged scans is represented with histograms in Figure S8c.

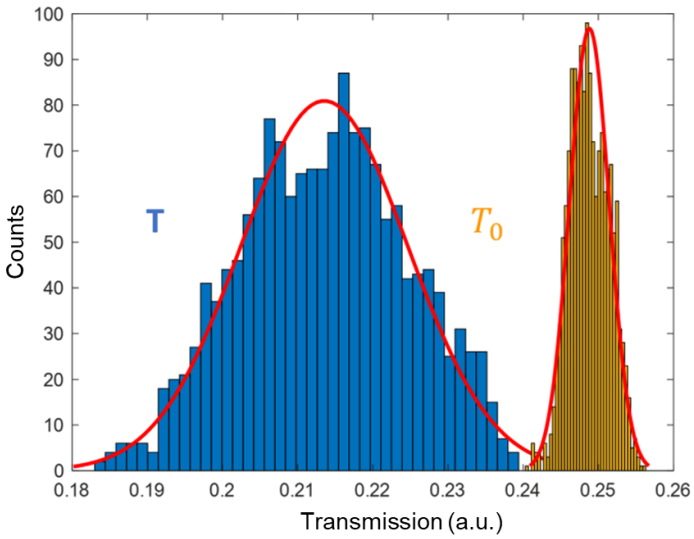

Figure S8c. Histograms counting the number of pixels having a given transmission in the averaged maps of T_0 and T.

The fluctuation of the blank transmission is low ($\frac{std(T_0)}{\langle T_0 \rangle}$ =1.04%), therefore we can assume a constant blank transmission. The histogram of T confirms that in presence of carbon nanotubes the transmission at 1005 nm is always lower than the blank transmission T_0.

Finally, the OD map is derived by applying Eq. S3, and the standard deviation of the OD value for each pixel is calculated according to the error propagation arithmetic. The results are shown in Figure S8d and demonstrate that the uncertainty of the measured OD can be considered negligible.

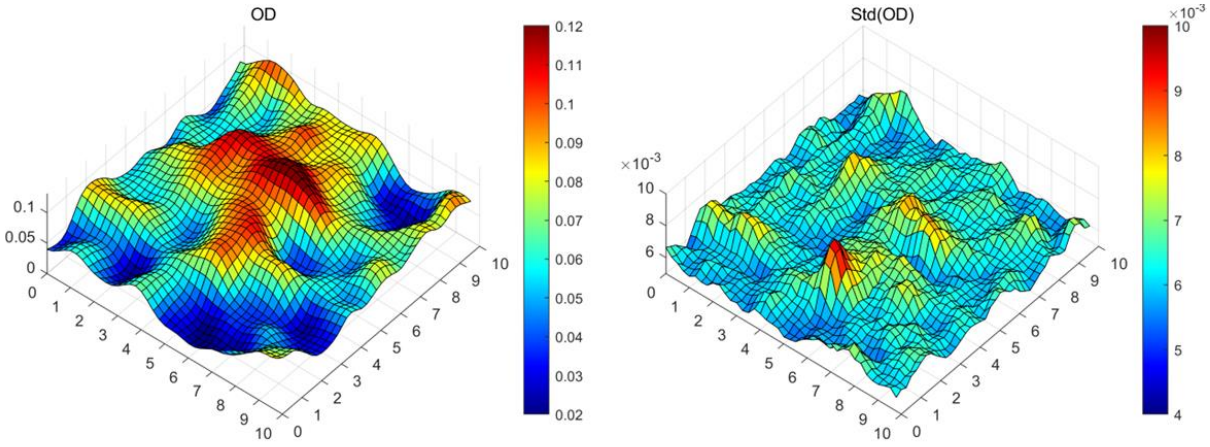

Figure S8d. OD and std(OD) maps derived measuring T and T_0 over 20 scans on the same area.

Distribution of ΔT/T *vs* OD from the maps in Figure 3

Plotting the distribution for each scanned pixel of the CMS signal as a function of the standardized OD (Figures S9a-c), a sounding growing trend of the CMS with OD is observed. Moreover, the analysis of the variation of the CMS signal from V_{os} = −0.6 to −0.8 V (Figures S9d,g) shows that, by increasing $|V_{os}|$, the highest growth of the signal (hence the charge density) happens in the regions with the lowest network density, which matches also those having the lowest CMS signal at −0.6 V. Diversely, from V_{os} = −0.8 to −1.0 V (Figures S9e,f) the CMS signal grows proportionally more in pixels where there is the lowest charge density at V_{os} = −0.8 V, but there is not a significative correlation with the OD, namely with the network density. In conclusion, by increasing the offset potential, the charge density grows and distribute more uniformly in the whole active area. At low V_{os} the regions with the highest network density have also a higher probability to present more effective connections among tubes that favour charge tunnelling. As the potential grows further, the dependence with the network density becomes less relevant.

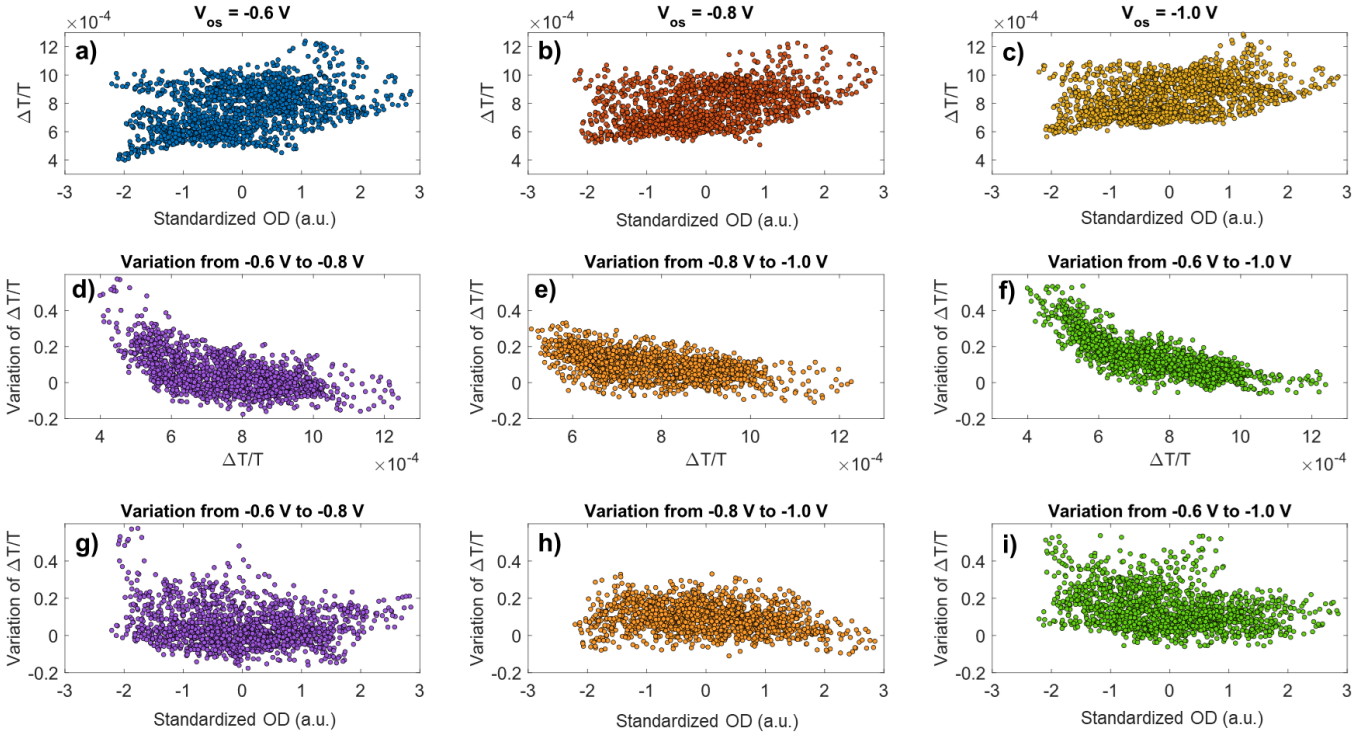

Figure S9. a-c) Distribution of the CMS signal (ΔT/T) *vs* standardized OD for all the 1600 pixels in the CMM maps of Figure 3a-c, *i.e.*, for the (6,5) monochiral network at V_{os} = −0.6, −0.8, −1.0 V. The standardized optical density OD for the i-th pixel of the map is computed

from the measured optical density OD as follows: $OD(i) = \frac{OD_m(i)-\mu}{\sigma}$, where μ is the average OD_m of the whole map and σ the standard deviation. **d-e)** Distribution of the variation of the CMS signal from $V_{os|i}$ to $V_{os|f}$ *vs* the CMS signal at $V_{os|i}$ (corresponding to the maps in Figure 3d-f). **d-e)** Distribution of the variation of the CMS signal from $V_{os|i}$ to $V_{os|f}$ *vs* the standardized OD (corresponding to the maps in Figure 3d-f).

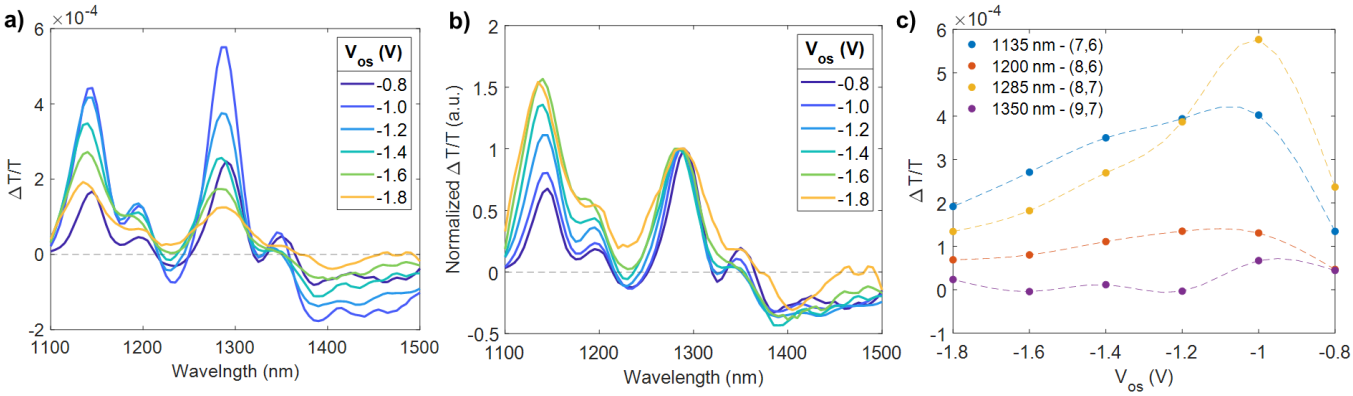

Figure S10. a) Local CMS spectra in hole accumulation regime at varying V_{os}. **b)** Spectra of panel a) normalized at the (8,7) E_{11} bleaching peak (1285 nm). **c)** Maximum of the E_{11} bleaching peaks of the (7,6), (8,6), (8,7) and (9,7) species as a function of the offset potential V_{os} (the dashed lines serve as guide to the eye).

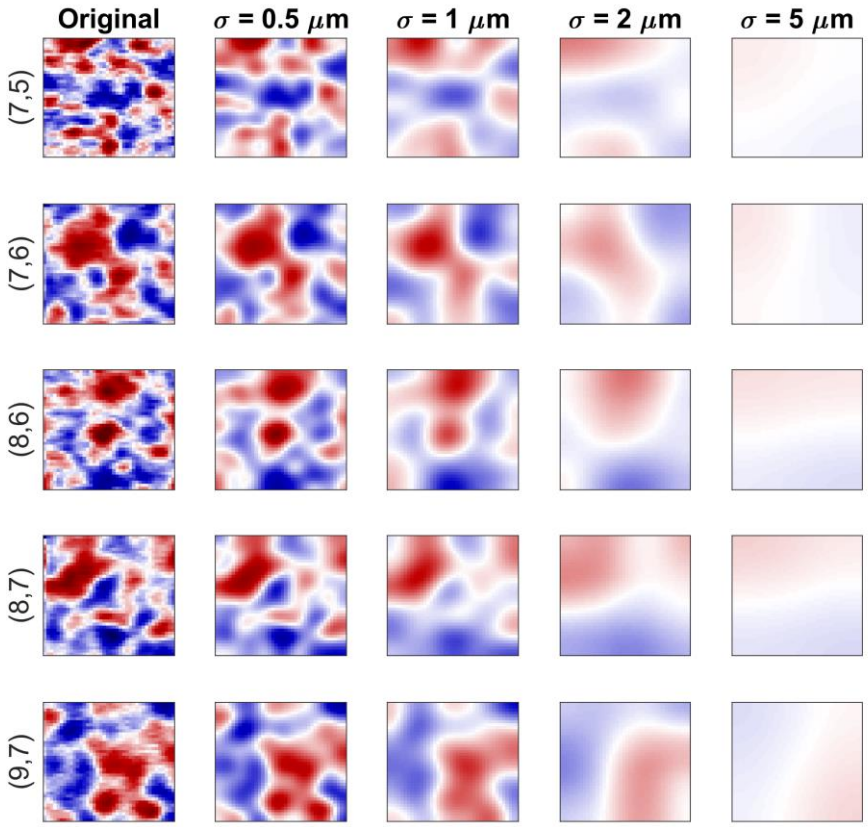

Figure S11a. Convolution of the CMM maps with a gaussian kernel having a standard deviation σ. This is equivalent to blurring progressively the image, substituting the signal of each pixel with the average signal in its neighborhood. The wider is the gaussian function, the larger is the neighborhood included in the average, and the more the local information becomes smoothed. Loosing local information, the signal converges towards the average value, which also correspond to the "macroscopic CMS" acquired from the entire device.

The CMM maps have been previously standardized as follows:

$$\overline{\mathrm{CMS}}(\mathrm{i}) = \frac{\mathrm{CMS}(\mathrm{i}) - \mu}{\mathrm{std}(\mathrm{CMS})},$$

where μ is the average signal of the whole CMM map and $\mathrm{std}(\mathrm{CMS})$ the standard deviation. In this way, the standardized maps (first column of Figure S11a) have zero mean and unitary standard deviation and can be easily compared to each other without concerns from factors affecting the intensity of the signal but not the spatial distribution, such as their different oscillator strength and dependence on $|V_{os}|$.

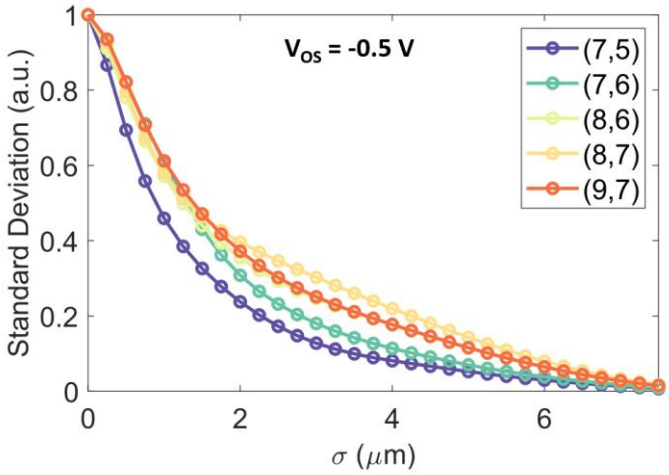

Figure S11b. By increasing progressively the standard deviation of the gaussian kernel σ, the results of the convolution are blurred maps with lower and lower contrast among the values in every pixel (Figure S11a). Here we plot a trend of the signal standard deviation of the convoluted maps as σ increases. Interestingly, the CMM map of the (7,5) SWCNTs (those with the largest bandgap) blurs at lower σ values than all the others. This is consistent with the presence of more fragmented percolation paths, as seen in Figure S4f. In general, for long enough σ, the low-bandgap SWCNTs, *i.e.* (8,7) and (9,7), have CMM maps that preserve better the local information, which can be associated with more extended percolation paths.

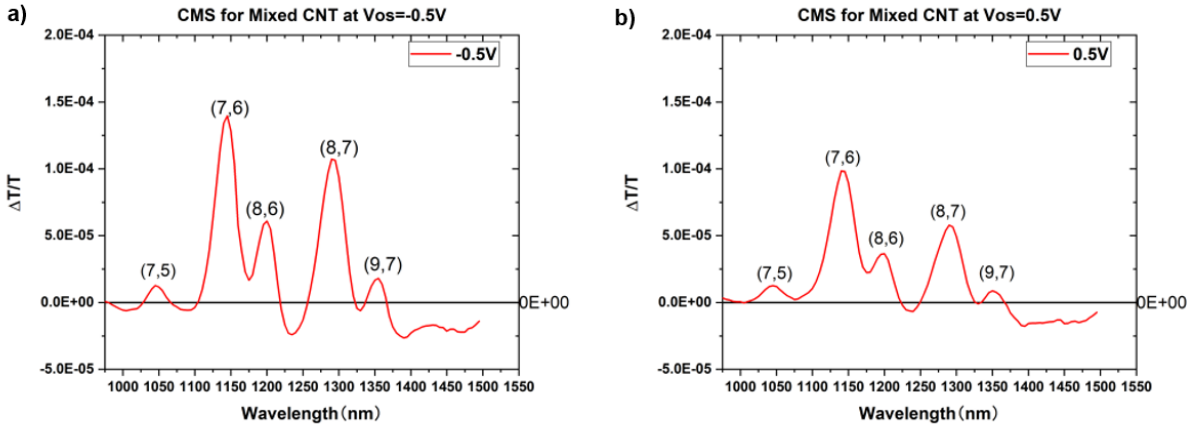

Figure S12. CMS spectra from the entire device in **a)** hole (V_{os} = −0.5V) and **b)** electron (V_{os} = 0.5V) accumulation regimes.

Cross-correlation analysis of OD and CMM maps for the five (n, m) species present in the multichiral SWCNT network

Calculating the zero-mean normalized cross correlation (ZNCC) coefficients of two images is useful to estimate in a quantitative way if they present patterns which are similar (positive correlation, ZNCC close to 1) or complementary (negative correlation, ZNCC close to -1).
In Figure S13a we apply systematically this procedure to compare the OD distributions of the five (n, m) SWCNT species among each other. Similarly, we compare the OD distributions with the CMM maps in Figure S13b, and the CMM maps among each other in Figure S13c.

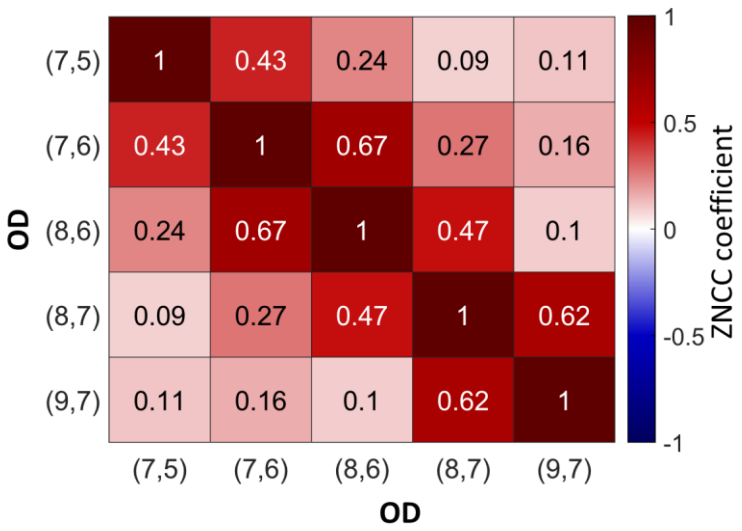

Figure S13a. Table collecting the ZNCC coefficients among the OD maps (Figures 5f-l) corresponding to the E_{11} absorption peak of all the five SWCNTs species contained in the multichiral network. The diagonal represents the zero-lag autocorrelation function (identically equal to 1). A strong correlation exists between the OD maps of first-neighbour chiralities.

Figure S13b. Table collecting the ZNCC coefficients obtained by the cross-correlation of the CMM maps of Figures 5a-e with the OD maps of Figures 5f-l. No sounding correlations are detected among the network density of every SWCNTs species and the CMS signal distribution of any chirality.

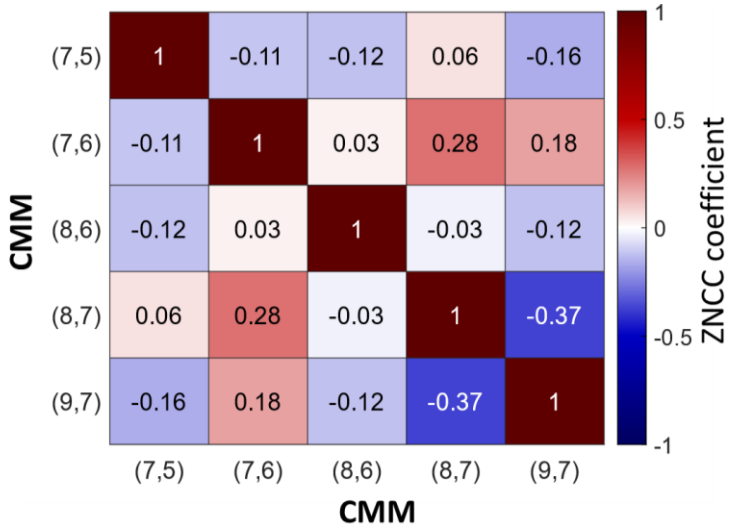

Figure S13c. Table collecting the ZNCC coefficients among the CMM maps of Figures 5a-e with the OD maps of Figures 5f-l. This graph suggests a moderate negative correlation between the (8,7) and (9,7) CMM maps (ZNCC coefficient of -0.37), suggesting a certain degree of complementary in the spatial distribution of charge carriers on the two chiral species with the lowest bandgaps.

Computational details for the cross-correlation analysis (*Matlab* script)

```
% Standardization
A=A-mean(A(:),'all');
A=A/sqrt(sum(A(:).^2));
B=B-mean(B(:),'all');
B=B/sqrt(sum(B(:).^2));
% Cross-correlation
fft_A=fft2(A); % 2D Fourier Transform of the matrix A
fft_B=fft2(B); % 2D Fourier Transform of the matrix B
C=real(fftshift(ifft2(conj(fft_A).*fft_B))); % 2D cross-correlation
```

Appendix C: Supporting Information for "Stable and Solution-Processable Cumulenic sp-Carbon Wires: A New Paradigm for Organic Electronics"

ADVANCED MATERIALS

Supporting Information

for *Adv. Mater.,* DOI: 10.1002/adma.202110468

Stable and Solution-Processable Cumulenic sp-Carbon Wires: A New Paradigm for Organic Electronics

*Stefano Pecorario, Alberto D. Scaccabarozzi, Daniele Fazzi, Edgar Gutiérrez-Fernández, Vito Vurro, Lorenzo Maserati, Mengting Jiang, Tommaso Losi, Bozheng Sun, Rik R. Tykwinski, Carlo S. Casari, and Mario Caironi**

WILEY-VCH

Supporting Information

Stable and Solution-Processable Cumulenic sp-Carbon Wires: A New Paradigm for Organic Electronics

*Stefano Pecorario, Alberto D. Scaccabarozzi, Daniele Fazzi, Edgar Gutiérrez-Fernández, Vito Vurro, Lorenzo Maserati, Mengting Jiang, Tommaso Losi, Bozheng Sun, Rik R. Tykwinski, Carlo S. Casari and Mario Caironi**

Table of contents

A) HOMO/LUMO gap and optical absorption in solution vs solid-state

Table S1

Electrochemical[a]						Optical[b]		
E_{red}^1 (V)	E_{red}^2 (V)	E_{ox}^1 (V)	E_{gap} (eV)	E_{HOMO} [c] (eV)	E_{LUMO} [c] (eV)	λ_{max} (nm)	λ_{onset} (nm)	E_{gap} (eV)
–1.94	–2.25	0.68	2.62	-5.48	-2.86	418	454	2.73

[a] Cyclic voltammetry (CV) performed in dry, deoxygenated CH_2Cl_2 solutions using 0.1 M nBu$_4$NPF$_6$ as supporting electrolyte and a scan rate of 100 mV/s. Pt wire was used as counter electrode, and a glassy carbon disc was used as working electrode. Potentials are referenced to the ferrocene/ferrocenium (Fc/Fc^+) couple used as an internal standard (from reference [S1]). [b] Spectra were obtained in CH_2Cl_2. The optical HOMO-LUMO gap was estimated from the intersection of the x-axis and a tangent line passing through the inflection point of the lowest energy absorption. [c] The HOMO and LUMO energy values were estimated considering the Fc/Fc^+ redox potential of –4.8 eV with respect to the vacuum level.[S2]

[S1] S. N. Spisak, M. U. Bühringer, Z. Wei, Z. Zhou, R. R. Tykwinski, M. A. Petrukhina, *Angew. Chemie - Int. Ed.* **2019**, *58*, 2023.

[S2] J. Pommerehne, H. Vestweber, W. Guss, R. F. Mahrt, H. Bässler, M. Porsch, J. Daub, *Adv. Mater.* **1995**, *7*, 551.

Figure S1

Comparison of the UV-Vis absorption spectra of [3]Ph in 1,2-dichlorobenzene solution (10^{-4} M) and of thin films deposited at different temperature. The panel on the right details the wavelengths corresponding to the low-energy absorption peaks.

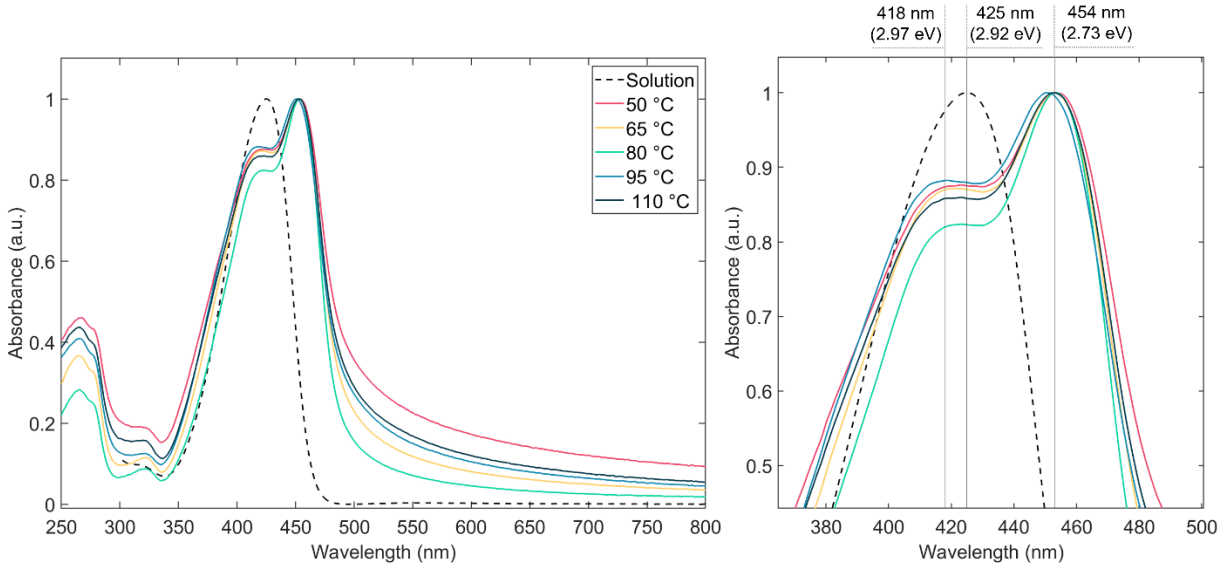

Discussion:

The solution presents a unique band peaked at 425 nm (2.92 eV), assigned to the HOMO-LUMO optical transition of [3]Ph single molecules (unaggregated). Diversely, the thin films are characterized by two bands: a sharp one at 454 nm (2.73 eV) and a blunt band at about 418 nm (2.97 eV). The former is assigned to J-type aggregates and is red-shifted with respect to the band in solution. The latter results from the convolution of transitions assigned to the single-molecule and to H-type aggregates (see discussion in paragraph 2.2 of the main body). Moreover, we noticed a trend in the intensity ratio between these two bands as a function of the deposition temperature. The intensity of the 418 nm band is decreasing with respect to the one at 454 nm passing from films deposited at 50 °C to 65 °C and 80 °C, then it increases again in films deposited at 110 °C and 95 °C. Supposing that the relative intensity of the J-type and H-type transitions is constant in crystalline phases, such trend can be rationalized by a variation of the unaggregated phase (single molecule contributions). The presence of the single molecule-like contribution would derive from regions of high defectiveness, like at the grain boundaries, where the crystalline packing is disrupted. In this regard, the lower the abundance of defects, the lower would be the relative intensity of the 418 nm band. This interpretation is consistent with the information on the surface roughness and defectivity recorded by atomic force microscopy (Figure S4-S6). Indeed, we observed marked grain boundaries and cracks in the

films deposited at 50 °C and 110 °C, while the deposition at 80 °C provides the smoothest crystalline grains surface. Consistently, the same behavior described for the relative intensity of the peaks at 454 nm and 418 nm is retrieved in the trend of the long tail absorption: the film deposited at 80 °C presents the sharpest absorption onset, sign of high crystalline order, while at the other deposition temperatures the absorption tail is blunter. Hence, we suggest this feature as a possible signature of the superior quality and lower defectiveness of the crystalline domains forming at 80 °C.

Finally, this finding correlates well with the trend of mobility in devices based on thin films of [3]Ph deposited at different temperatures. Indeed, the mobility increases passing from deposition temperature of 50 °C to 80 °C and it decreases at higher temperature (Figure 4d).

B) Polarized optical microscopy images

Figure S2

a) Polarized optical microscopy images of [3]Ph films deposited with coating speed v = 30 mm/s at 50 °C, 80 °C, and 110 °C on glass substrates with interdigitated gold source and drain electrodes (top) and on silicon substrates used to perform the GIWAXS measurements (bottom). The scalebar is 100 µm.

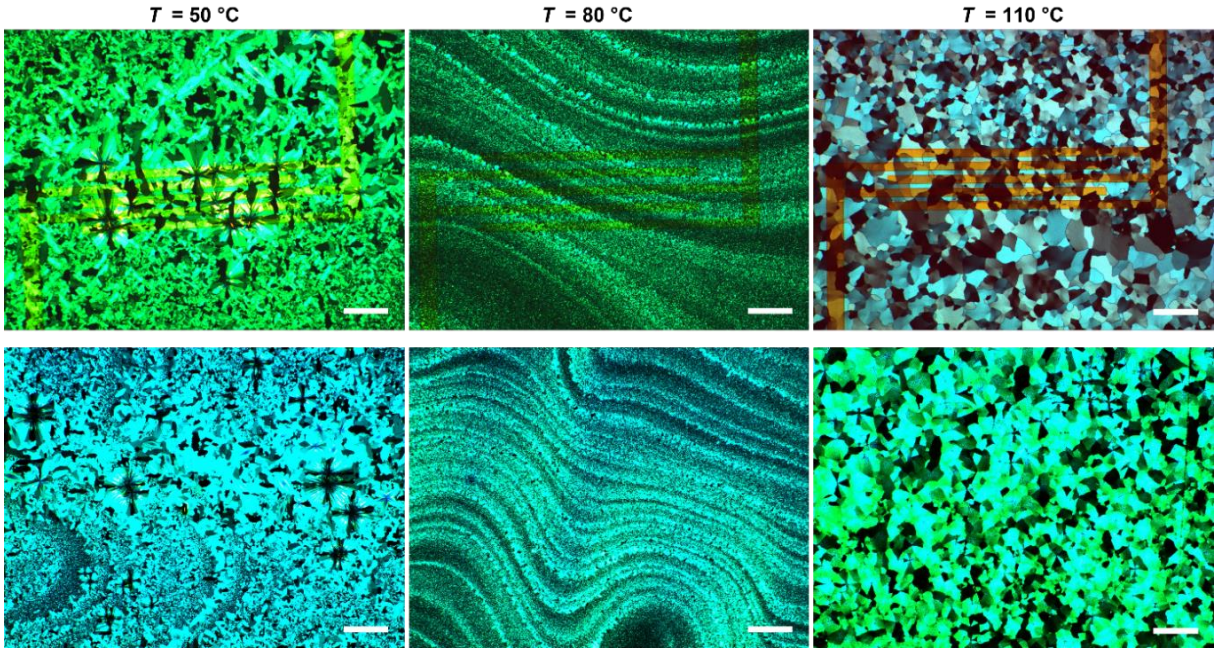

b) Polarized optical microscopy images of [3]Ph films deposited with coating speed v = 5 mm/s and v = 100 mm/s at 50 °C, 80 °C, and 110 °C on glass substrates. The scalebar is 100 µm. The shape and size homogeneity of the crystalline structures achieved with these coating speeds is lower than with v = 30 mm/s.

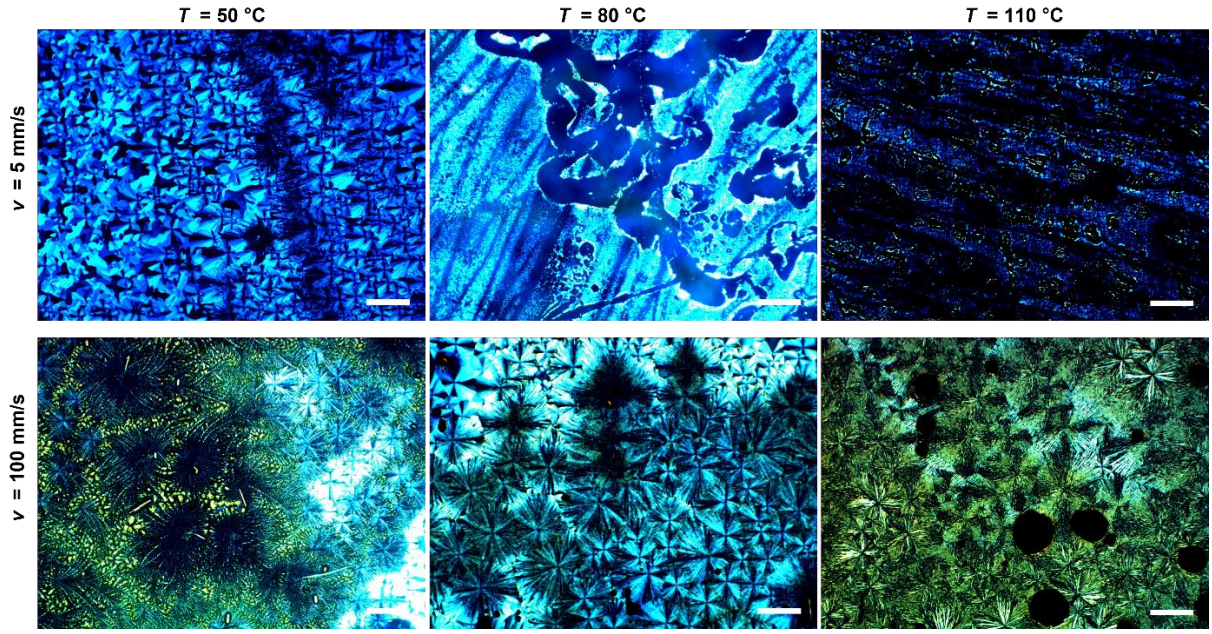

Figure S3

Dark-field optical microscopy image of long needle-like [3]Ph crystals formed by drop casting at 50 °C from a solution (10 g/L) in 1,2-dichlorobenzene. The scalebar is 300 µm.

C) Atomic force microscopy imaging and surface roughness extraction

The AFM topographies of films deposited at 50 °C, 80 °C, and 110 °C were analyzed with *Gwyddion* to extract the root mean square roughness (RMS). The following figures show next to the original AFM topography (left), the same image with an overlayed mask in violet (right). Such mask identifies regions with abrupt change in the film height distribution due to the presence of defects (grain boundaries, cracks, pits, small crystallites on the surface of the thin film). In this way, it is possible to extract roughness parameters of the ordered crystalline grains (unmasked) and compare it with the roughness of the entire scanned region including defects (entire).

Figure S4

AFM topography of a thin film of [3]Ph deposited at 50°C. The film is characterized by rough grains with a petal-like shape, suggesting a radial growth of the crystalline grains from a central nucleation point. The grain boundaries are highlighted in green in the image on the right. Hundreds of micrometers long cracks run parallel to the grain growth direction. Furthermore, several small crystallites lay on top of the film and accumulate preferentially in correspondence of the grain boundaries.

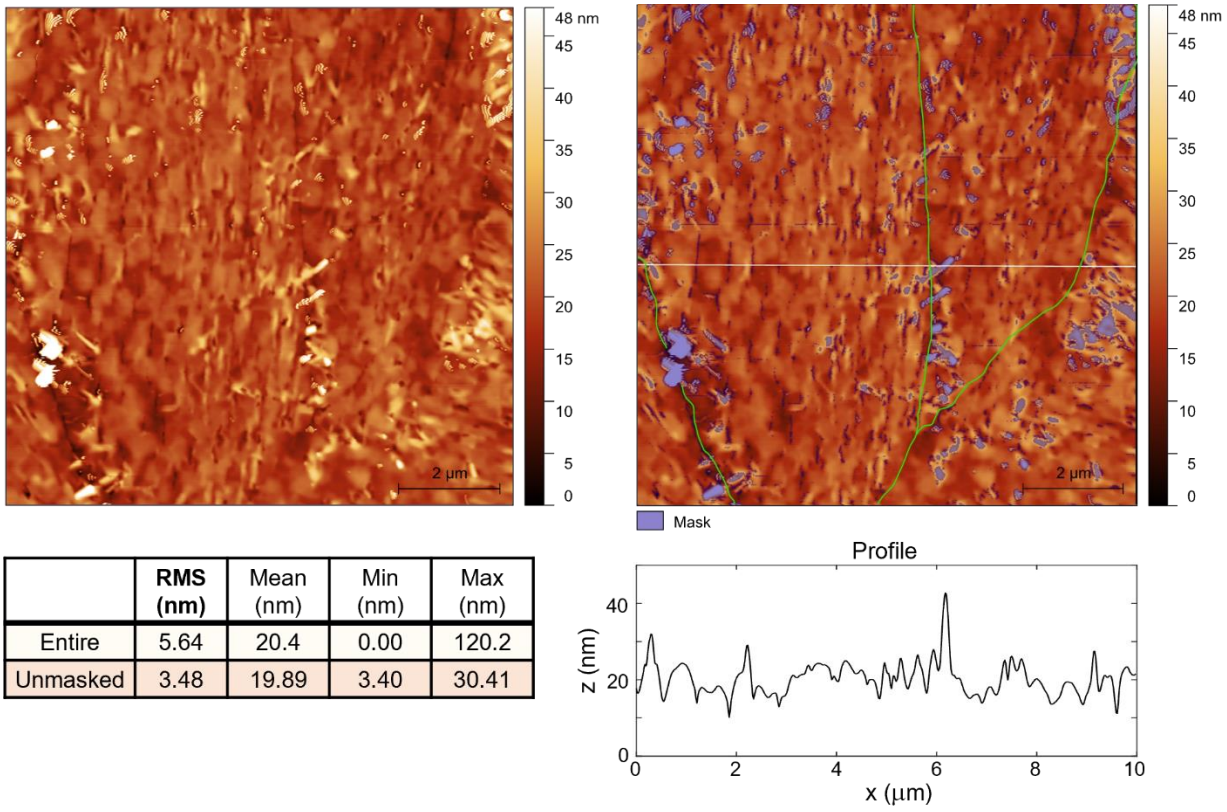

	RMS (nm)	Mean (nm)	Min (nm)	Max (nm)
Entire	5.64	20.4	0.00	120.2
Unmasked	3.48	19.89	3.40	30.41

Figure S5

AFM topography of a thin film of [3]Ph deposited at 80 °C. The crystalline grains are few microns large, however they display much lower cracks and crystallites on the surface compared to the films deposited at higher or lower temperature. The grain boundaries, highlighted by the violet mask, are compact and affect the total roughness of the film only slightly. Within the grains, it is possible to see terraces with one-monolayer thickness (~ 1 nm). Overall, the RMS roughness is lower than in the films deposited at 50 °C and 110 °C, both considering the unmasked regions and the entire film.

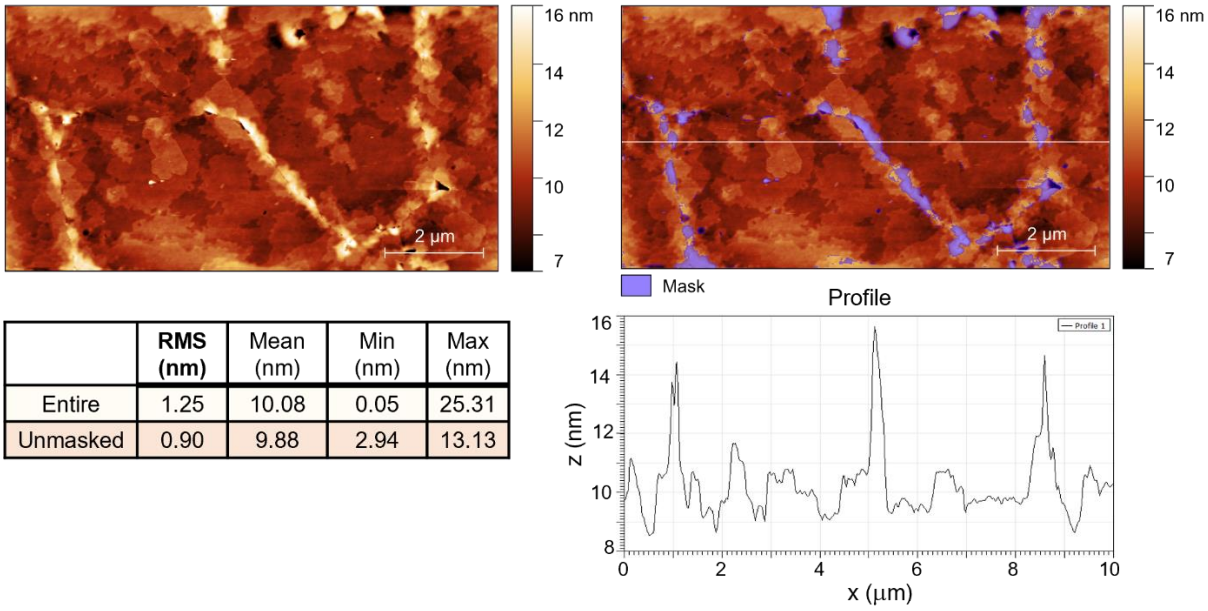

	RMS (nm)	Mean (nm)	Min (nm)	Max (nm)
Entire	1.25	10.08	0.05	25.31
Unmasked	0.90	9.88	2.94	13.13

Figure S6a

AFM topography of a thin film of [3]Ph deposited at 110°C. The crystalline grains in this film are tens of micrometers large. Therefore, the AFM image corresponds to a scan within a single crystalline grain. The film is characterized by micrometers long parallel cracks, with large pits having a depth of 16 nm, which likely corresponds to the thickness of the film.

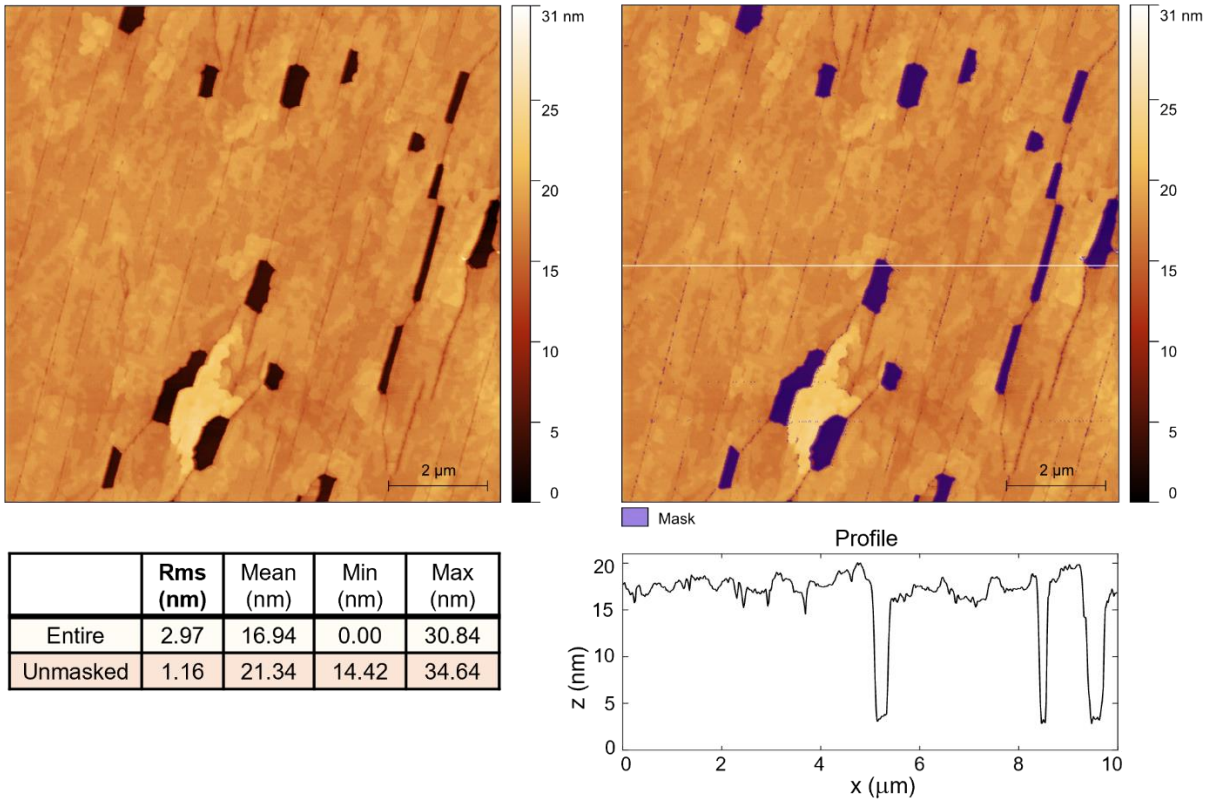

	Rms (nm)	Mean (nm)	Min (nm)	Max (nm)
Entire	2.97	16.94	0.00	30.84
Unmasked	1.16	21.34	14.42	34.64

Figure S6b

Additional AFM scans spanning larger areas of a thin film of [3]Ph deposited at 110 °C, accompanied by the POM images of the characterized devices. Grain boundaries are characterized by an increased density of pits with respect to within the grains. Moreover the direction of the cracks (lines of defects) change from grain to grain, suggesting that tensional stresses arise in one particular direction of the crystal.

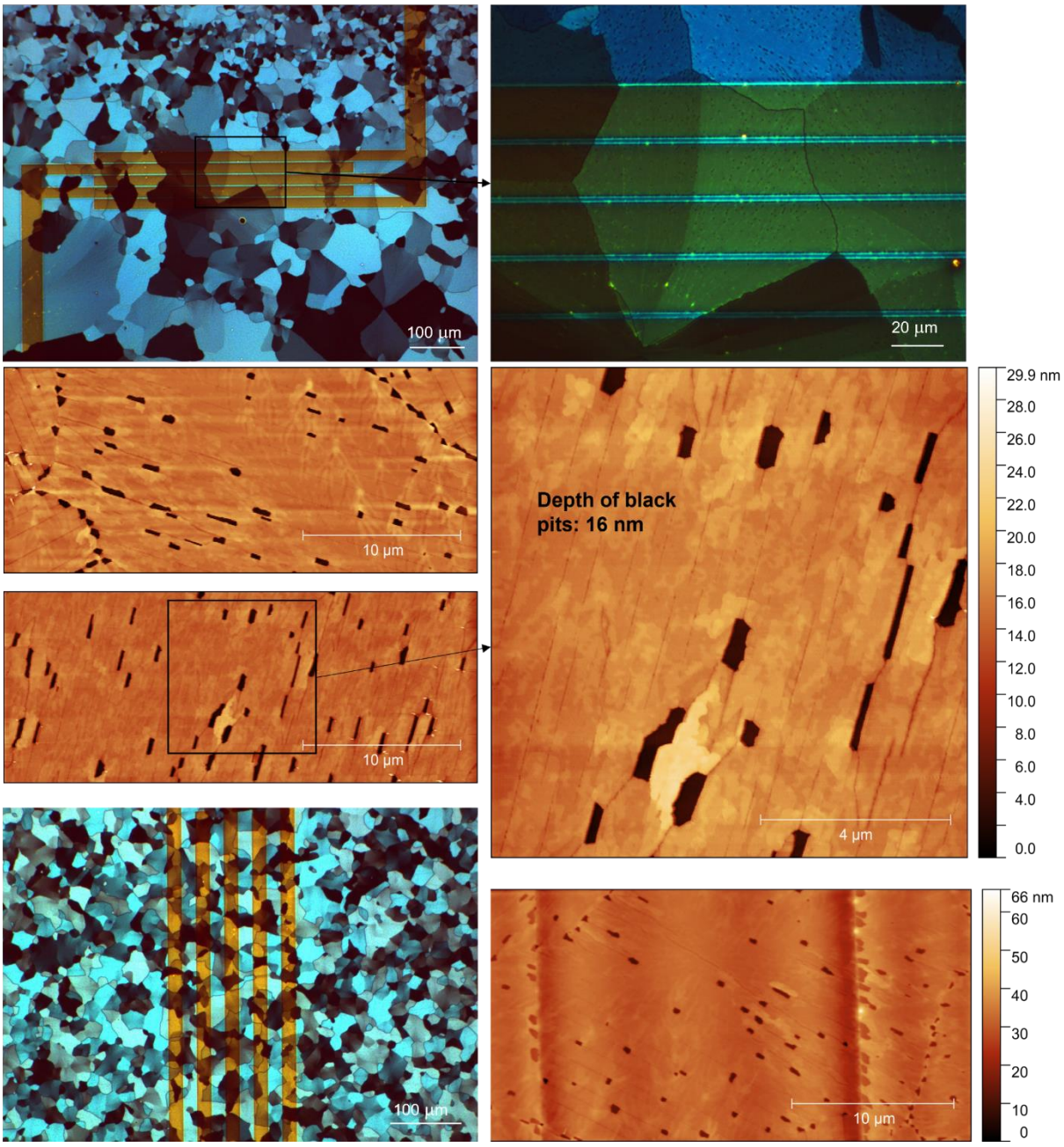

D) GIWAXS analysis

Figure S7

X-ray diffraction pattern of single-crystalline [3]Ph.

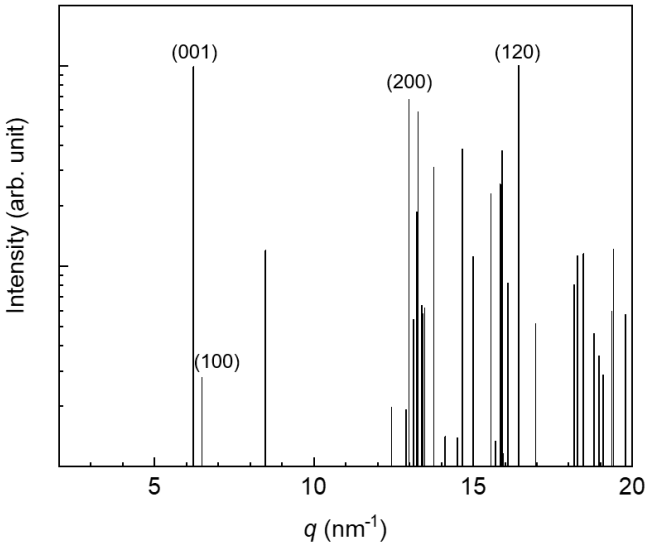

Figure S8

In-plane (IP) and out-of-plane (OOP) integrations of the GIWAXS patterns of thin films of [3]Ph deposited at 50 °C, 80 °C, and 110 °C.

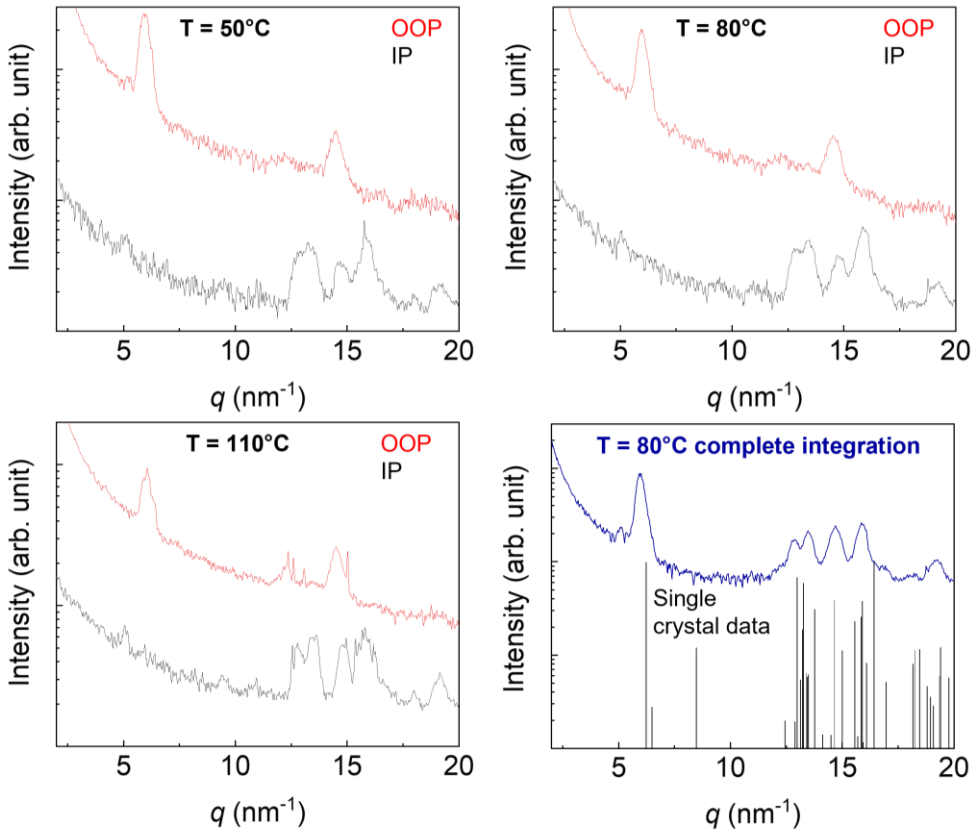

Figure S9

GIWAXS patterns of thin films of [3]Ph deposited at 50 °C, 80 °C, and 110 °C measured under an incident angle of 0.14°, with all the Miller indexes obtained by simulations with the GIWAXS SIIRkit package. [S3] Applying the same fitting routes to achieve the lowest errors, we detect an increase of the volume of the cell at higher deposition temperatures, associated with a deformation in the *ab* plane. Table S2 summarizes the lattice parameters associated with the three samples deposited at different temperatures. It is important to mention that, due to the intrinsic imperfections of the material in the film, the GIWAXS patterns show only a partial number of Bragg reflections, and the fitted lattice unit cannot be compared directly with the single crystal in terms of lattice parameters and Miller indexes. Therefore, the simulated unit cell from the GIWAXS patterns is probably oversized. Though, it can be useful to detect quantitative changes between the patterns from the different samples.

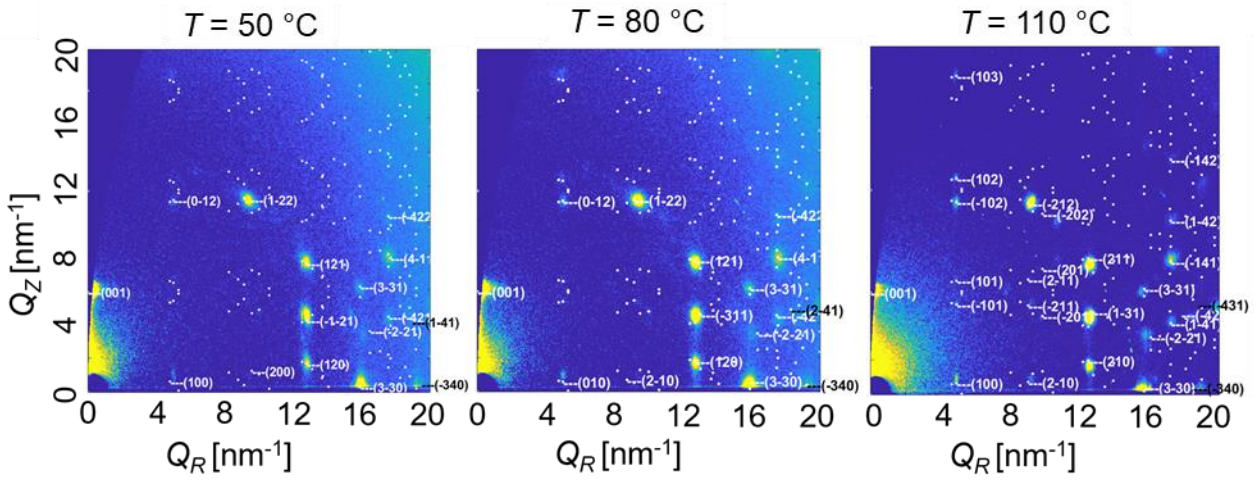

Table S2

Parameters of the fitted lattice units by GIWAXS-SIIRkit package [S3] for thin films of [3]Ph deposited at 50 °C, 80 °C, and 110 °C. The lattice parameters of the [3]Ph single crystal are reported for comparison.

Lattice parameters	**50 °C – 0.14°**	**80 °C – 0.14°**	**110 °C – 0.14°**	**Single Crystal**
a (Å)	14.42	14.51	13.92	10.035
b (Å)	13.81	13.77	14.75	9.978
c (Å)	10.82	10.84	10.83	10.458
Alpha (°)	93.14	93.84	94.63	74.960
Beta (°)	95.44	95.44	95.22	92.170
Gamma (°)	114.55	114.15	113.93	74.730
Volume (Å^3)	1940.46	1953.66	2007.67	969.22

[S3] V. Savikhin, H. G. Steinru ck, R. Z. Liang, B. A. Collins, S. D. Oosterhout, P. M. Beaujuge, M. F. Toney, *J. Appl. Crystallogr.* **2020**, *53*, 1108.

E) TD-DFT//DFT computed electronic transitions and transfer integrals

Figure S10

Scheme of H-type (D1) and J-type (D4) molecular aggregates with the associated TD-DFT computed electronic transitions (energies not rescaled). Molecules of [3]Ph present a computed HOMO-LUMO transition at 3.13 eV. Exciton splitting occurs upon formation of molecular dimers, resulting in a higher and a lower optical transition. Given the J- and H-type nature of the excitonic interactions, D1 transition is blue-shifted with respect to the single molecule (active high-energy transition and forbidden low-energy transition forbidden), while D4 transition is red-shifted (active low-energy transition and forbidden high-energy transition).

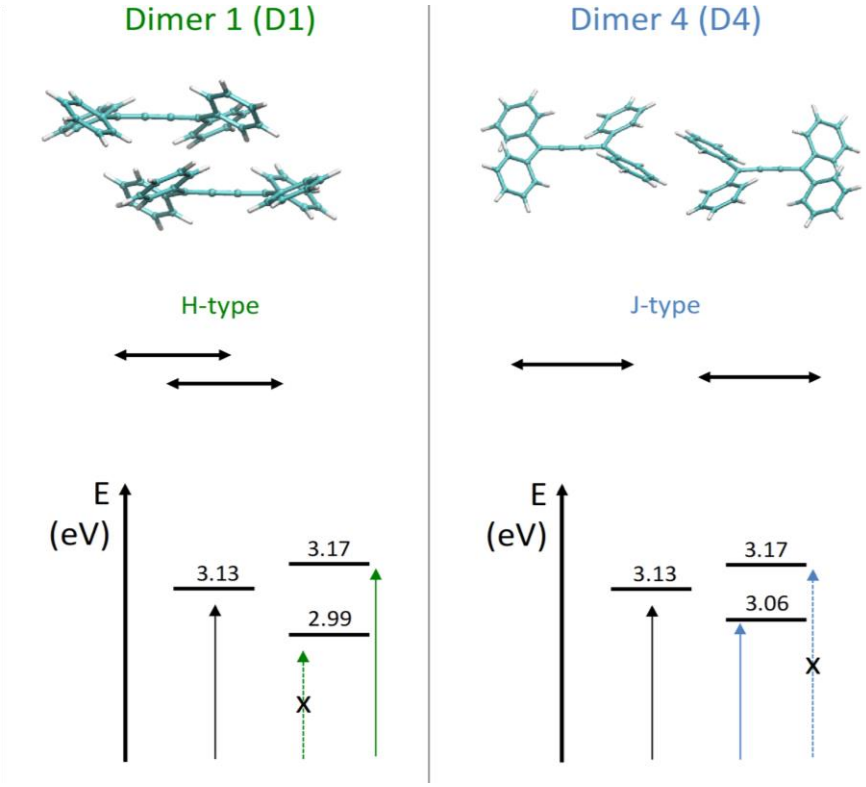

Table S3

TD-DFT computed electronic transitions for the [3]Ph single molecule (S) and for the molecular dimers (D1-4) extrapolated from the crystal structure as shown in Figure 3.

	S		**D1**		**D2**		**D3**		**D4**	
	E (eV)	*f*	*E* (eV)	*f*	*E* (eV)	*f*	*E* (eV)	*f*	*E* (eV)	*f*
Low	3.1313	0.9528	2.9963	0.0000	3.1313	0.9528	3.0735	2.0796	3.0693	2.2260
High			3.1695	1.6051	3.1513	0.7528	3.1629	0.0001	3.1749	0.0000

f : oscillator strength

Table S4

Charge transfer integrals (electronic couplings), V_{ij}, computed at the DFT level for a hole transport mechanism.

	D1	D2	D3	D4
V_{ij} (eV)	0.045890	0.012913	0.012897	-0.001000

Figure S11

Polarized absorption spectra of a single crystalline grain of a thin film deposited at 80°C.

The measures were recorded with a homemade setup where the polarization of a white light beam is controlled by rotating a linear polarizer. The beam is focused on the sample with a confocal microscope reaching micrometric resolution.

Being the two absorption bands around 418 nm and 454 nm assigned to two types of aggregate oriented in different crystallographic directions, their relative intensity is changing as a function of the polarization of the light beam.

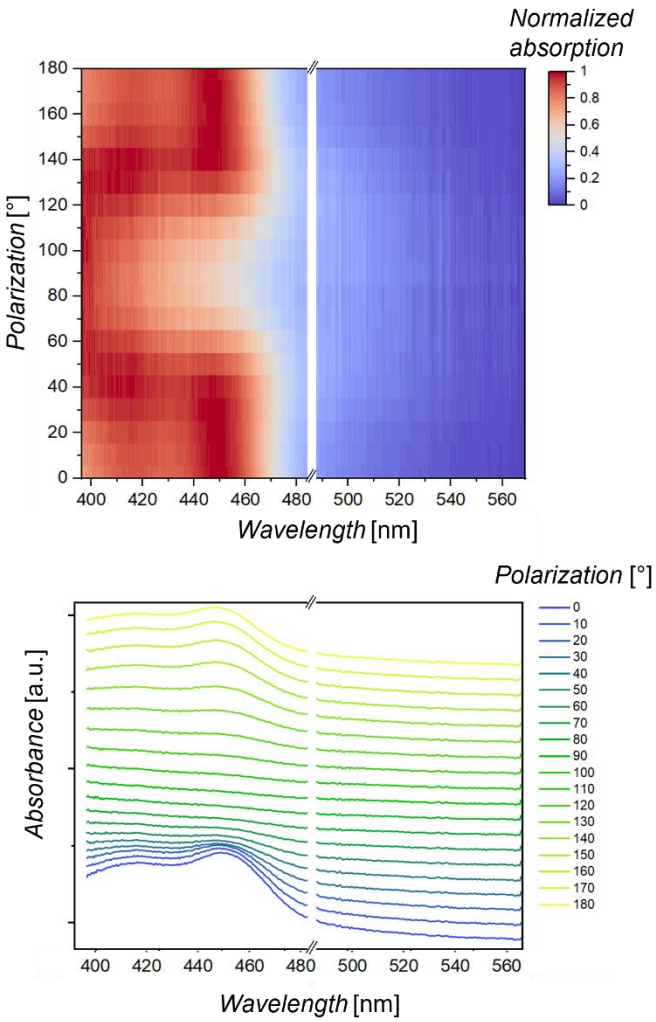

Figure S12

a) Computed DFT (wB97XD3/6-31G*) highest/lowest occupied molecular orbital (HOMO/LUMO) for [3]Ph.

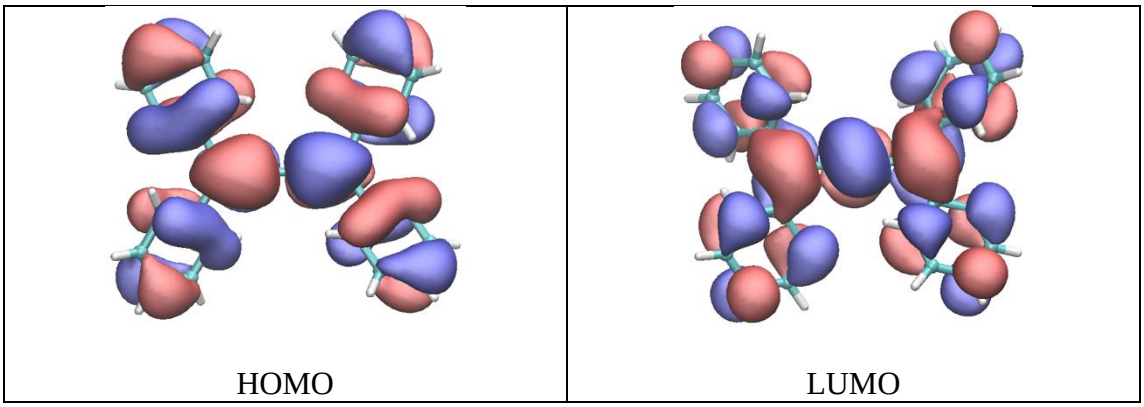

b) Carbon-carbon bond lengths of the [3]Ph sp-chain computed at the wB97X-D3/cc-pVTZ level of theory. Purple line (neutral species), red line (charged - hole - species).

Upon charging, the carbon bonds close to the end-group increase their bond length, while the central carbon-carbon bond shrinks, leading to a more alternated structure for the charged species than the neutral one.

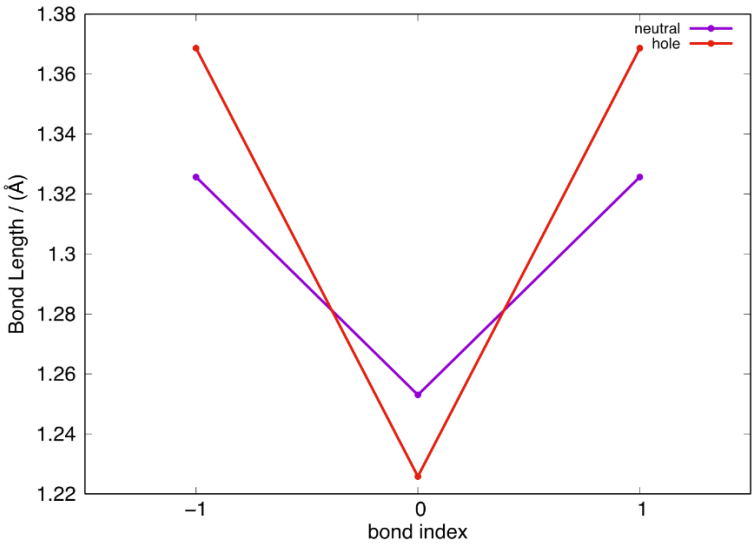

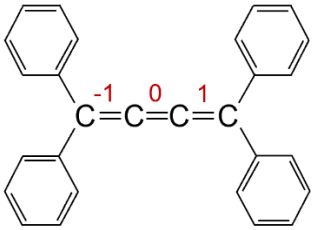

F) Electrical characterization

Figure S13

Transfer characteristics plotted in linear scale, mobility extraction from linear fit, mobility extraction with the Y-function method (same device of Figure 4b–c with L = 40 µm, W = 0.2 mm, deposition temperature T = 80 °C).

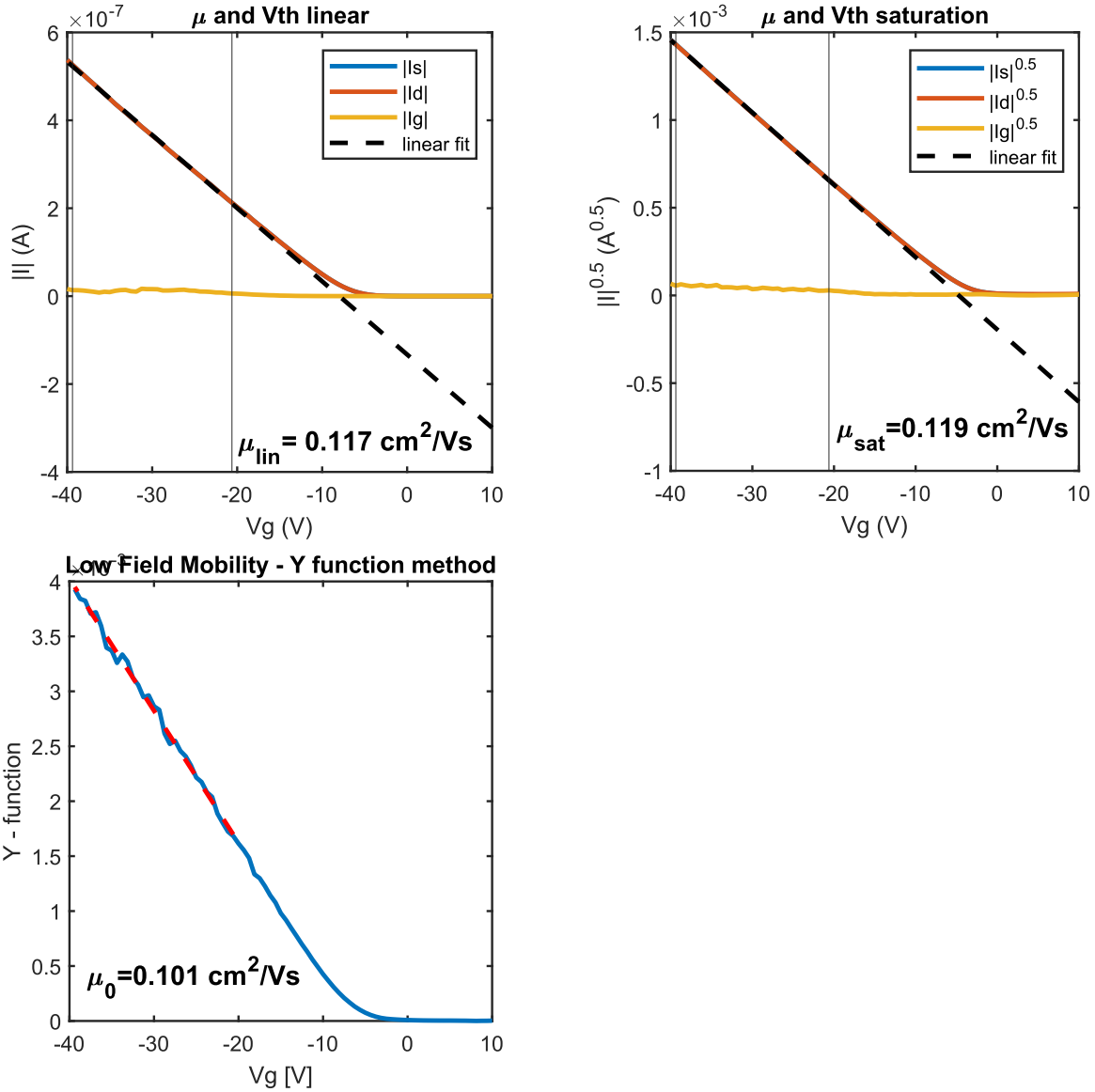

Figure S14

Transfer characteristics and plots of mobility as function of V_g of transistors with different channel length (L). [3]Ph deposited at 80 °C.

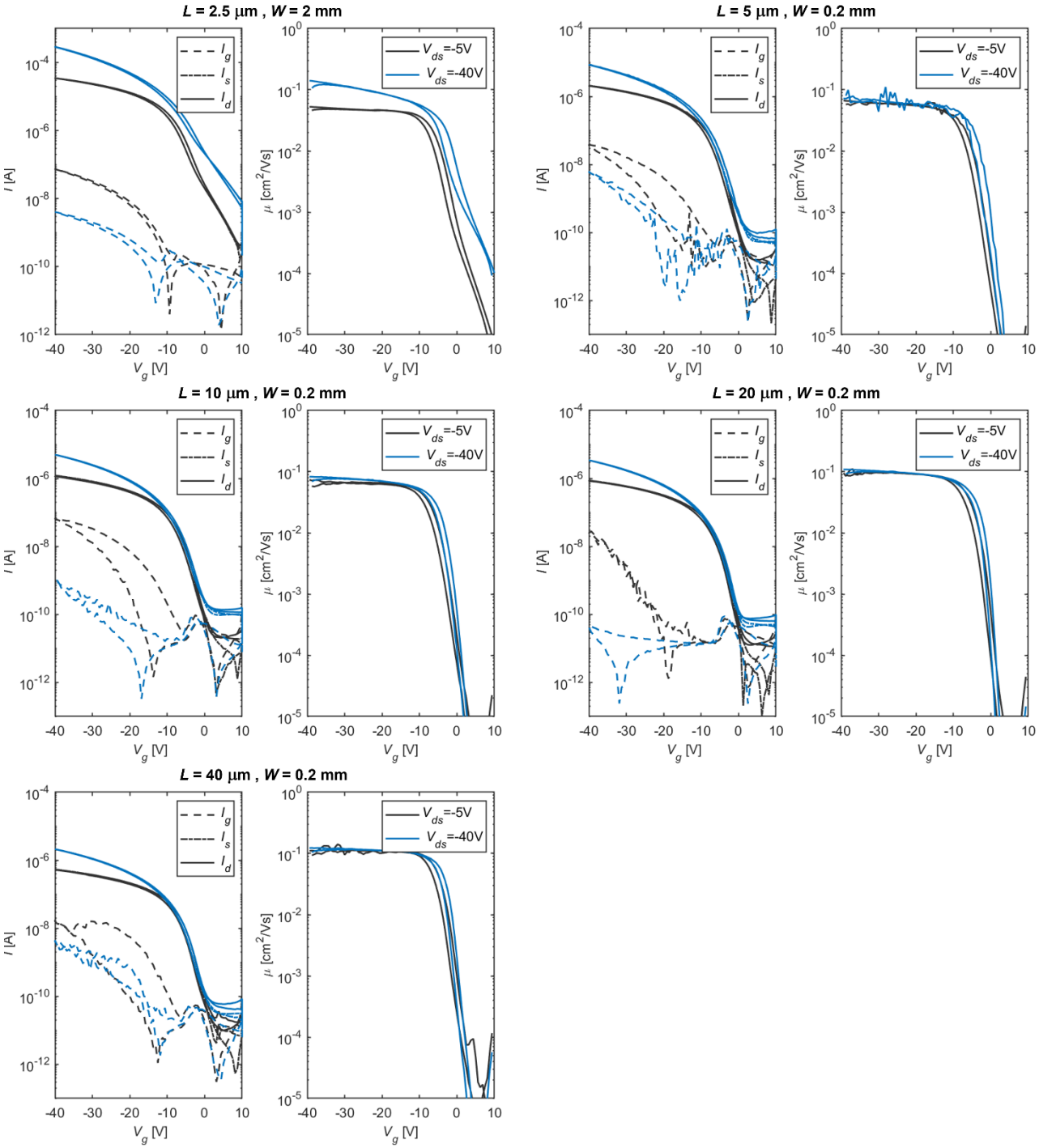

Table S5

Summary of the main figures of merit of optimized [3]Ph-based OFETs (T = 80 °C). The first line refers to the device with transfer characteristic and mobility trend plotted in Figure 4b-c. We also report the average, minimum and maximum values of the parameters from the whole set of tested devices.

	Linear (V_{ds} = −5V)				**Saturation (V_{ds} = −40V)**			
	μ [cm^2 V^{-1} s^{-1}]	r	V_{th} [V]	I_{on}/I_{off}	μ [cm^2 V^{-1} s^{-1}]	R	V_{th} [V]	I_{on}/I_{off}
Device of Figure 3b-c	$1.1 \cdot 10^{-1}$	0.992	–7.2	$5.3 \cdot 10^{4}$	$1.1 \cdot 10^{-1}$	0.953	–4.2	$5.1 \cdot 10^{4}$
Mean	$5.7 \cdot 10^{-2}$	0.998	–8.6	$2.1 \cdot 10^{5}$	$7.8 \cdot 10^{-2}$	0.918	–6.1	$2.8 \cdot 10^{5}$
Min	$1.7 \cdot 10^{-2}$	0.964	–10.9	$1.5 \cdot 10^{4}$	$2.1 \cdot 10^{-2}$	0.789	–8.4	$1.9 \cdot 10^{4}$
Max	$1.1 \cdot 10^{-1}$	1.083	–3.7	$1.5 \cdot 10^{6}$	$1.9 \cdot 10^{-1}$	0.990	–4.2	$3.3 \cdot 10^{6}$

Figure S15

a) Contact resistance extraction by Transmission Line Method (TLM). The contact resistance per unit width ($R_c\ W$) is obtained as the y-intercept of the linear fit of the total resistance per unit width ($R_{tot}\ W$) as function of the channel length (L):

$$R_{tot}\ W\ (L) = R_{ch}\ (L)\ W + R_c\ W$$

Here, the total resistance (R_{tot}) is derived from the transistors transfer curves in linear regime (averaged over three devices with the same channel length), thus it is dependent on the gate potential (V_g):

$$R_{tot} = V_{ds} / I_{ds}\ (V_g)$$

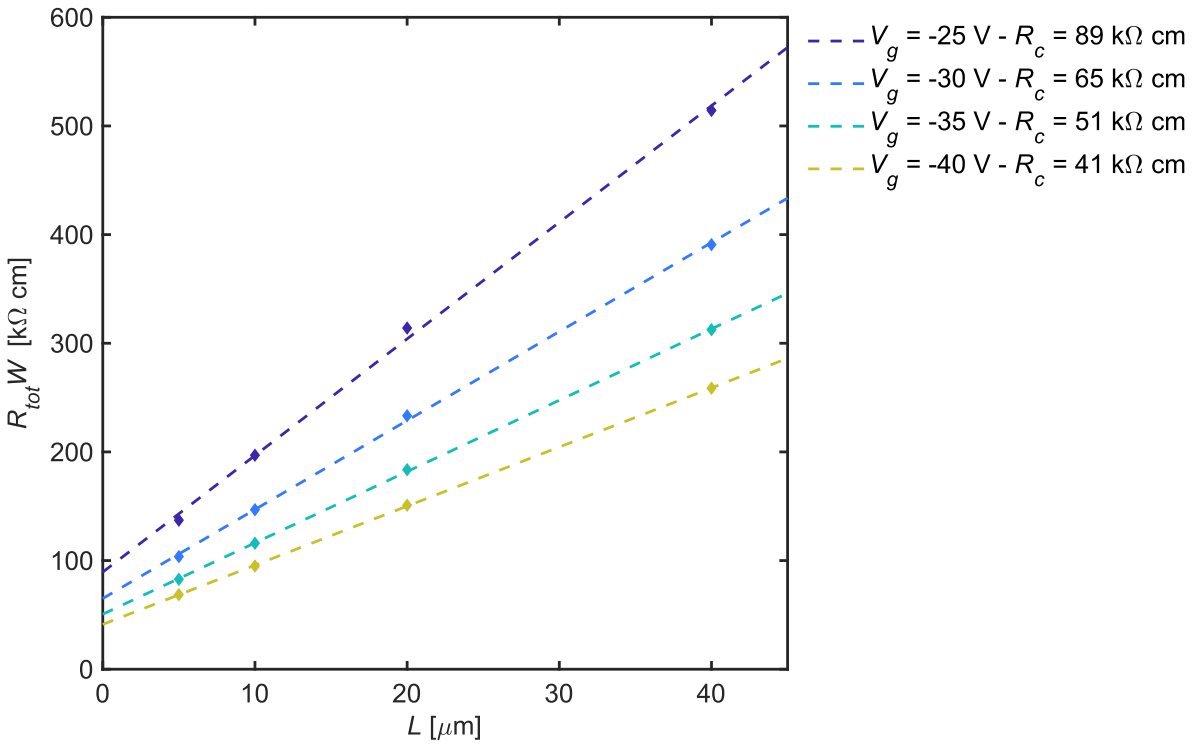

Table S6

TLM extracted R_c values as function of V_g together with 95% confidence bounds and R^2 factor of the linear fit.

V_g [V]	$Rc\ W$ [kΩ·cm] (with 95% confidence bounds)	R^2
–25	89.42 (56.98, 121.8)	0.99815
–30	65.09 (51.06, 79.11)	0.99940
–35	50.64 (45.37, 55.91)	0.99987
–40	41.28 (38.24, 44.32)	0.99994

b) Histograms comparing the contact resistance per unit width ($R_c\,W$), as extracted by TLM, with the channel resistance per unit width ($R_{ch}\,(L)\,W$). The color code accounts for the dependence of the channel and contact resistance on the applied gate voltage.

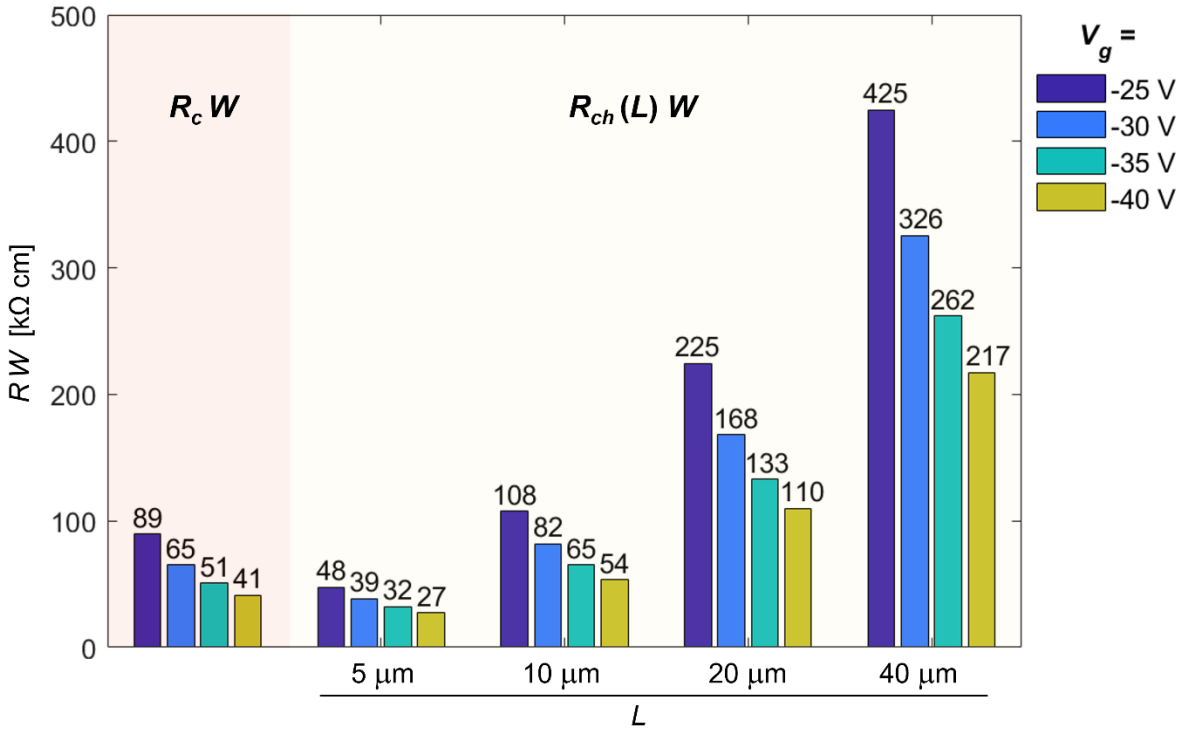

c) Once the contributions of the contact and channel resistance are known, it is possible to estimate the effective linear mobility that the devices would display in the case of zero contact resistance (*i.e.*, considering only the voltage drop along the channel), according to:

$$\mu_{eff} = \mu_{lin} \cdot (1 + R_c / R_{ch})$$

The impact of the contact resistance is dominant for the devices with the shortest channel length (L = 5 µm) and becomes lower and lower with increasing L. By removing the contribution of R_c, the estimated FET effective mobility results to be about 0.13 $cm^2\,V^{-1}\,s^{-1}$ irrespectively of the channel length.

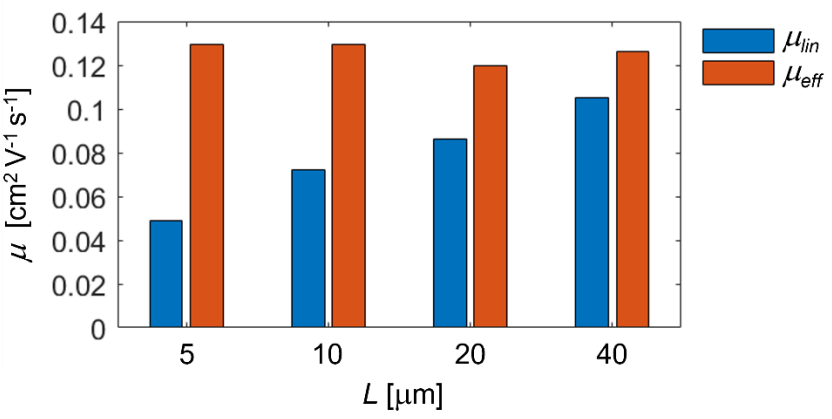

Figure S16

Output characteristic curves of devices with [3]Ph thin films deposited at T = 80 °C

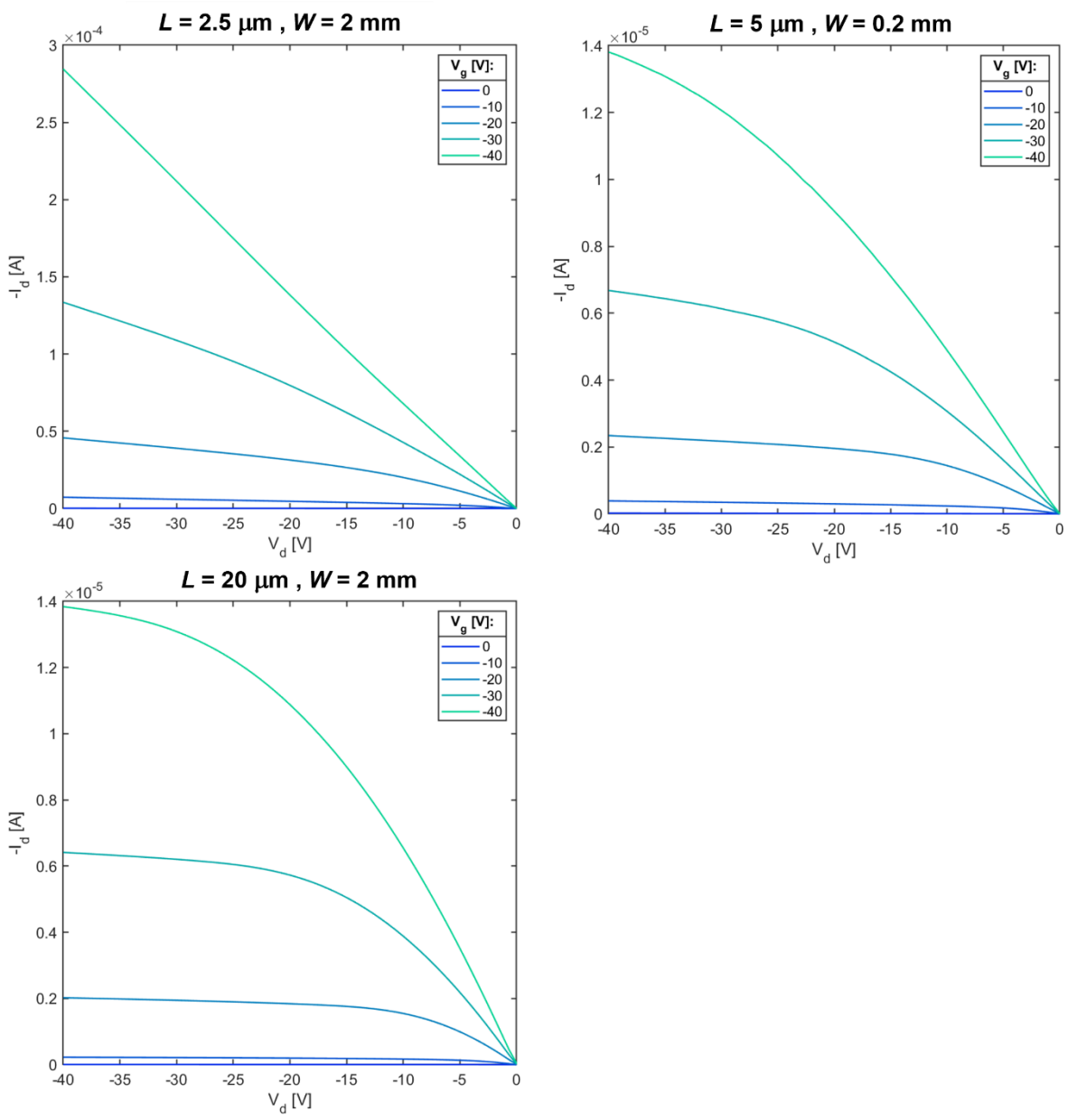

G) Degradation of thin films upon light-exposure

Figure S17

Light-induced UV-Vis absorption evolution during irradiation of a thin film of [3]Ph with 405 nm LED. The significant and homogeneous bleaching of the absorption spectrum already after 2s of exposure testifies the degradation of the [3]Ph film.

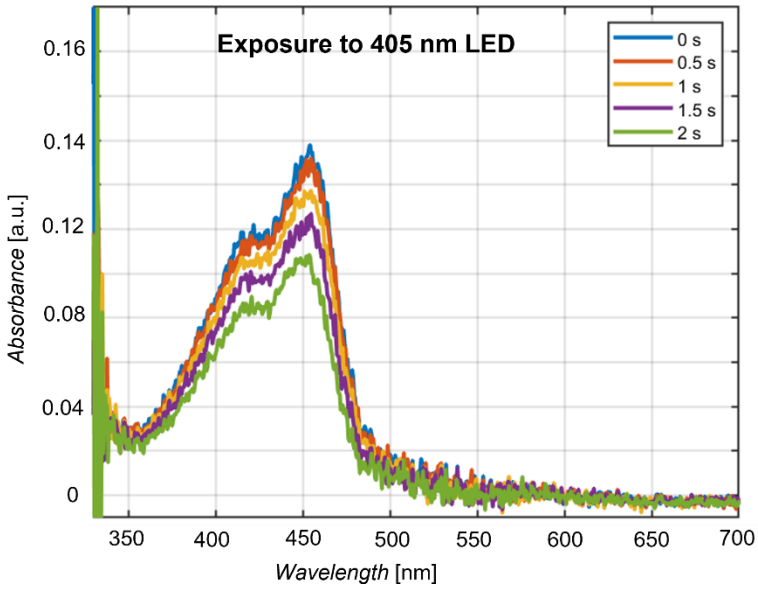

Figure S18

Electrical transport worsening due to exposure to white-light, demonstrated by measurement of the transistors transfer curves with and without illumination.

The transfer curves 1–5 refer to successive measurements in darkness obtained by varying the applied V_{ds} potential and the gate voltage V_g range. No degradation of the transistor performance occurs from one measurement to the other. Finally, the transfer curve 5 (in green) was recorded with the white lamp of the probe station microscope turned on. In this case, a clear degradation of the transistor performance occurs, marked by the lower on-currents and by a considerable hysteresis.

The measurements were performed in a controlled nitrogen atmosphere ($[0_2] < 4$ ppm, $[H_2O] < 1$ ppm), hence demonstrating that the photodegradation mechanism takes place even at negligible concentration of oxygen and humidity.